KARAGANDA
BUKETOV
B
UNIVERSITY

BULLETIN
OF THE KARAGANDA UNIVERSITY

PHYSICS
Series

ҚАРАҒАНДЫ УНИВЕРСИТЕТІНІҢ ХАБАРШЫСЫ

ВЕСТНИК
КАРАГАНДИНСКОГО УНИВЕРСИТЕТА

BULLETIN
OF THE KARAGANDA UNIVERSITY

ФИЗИКА сериясы

Серия ФИЗИКА

PHYSICS Series

2025

30-том • 4(120)-шығарылым
Том 30 • Выпуск 4(120)
Volume 30 • Issue 4(120)

МАЗМҰНЫ – СОДЕРЖАНИЕ – CONTENTS

КОНДЕНСАЦИЯЛАНҒАН КҮЙДІҢ ФИЗИКАСЫ
ФИЗИКА КОНДЕНСИРОВАННОГО СОСТОЯНИЯ
PHYSICS OF THE CONDENSED MATTER

ТЕХНИКАЛЫҚ ФИЗИКА
ТЕХНИЧЕСКАЯ ФИЗИКА
TECHNICAL PHYSICS

ЖЫЛУФИЗИКАСЫ ЖӘНЕ ТЕОРИЯЛЫҚ ЖЫЛУТЕХНИКАСЫ
ТЕПЛОФИЗИКА И ТЕОРЕТИЧЕСКАЯ ТЕПЛОТЕХНИКА
THERMOPHYSICS AND THEORETICAL THERMOENGINEERING

CORRIGENDUM

МЕРЕЙТОЙ ИЕСІ
НАШИ ЮБИЛЯРЫ
OUR ANNIVERSARIES

D. Soldatkhan[1], A. Morzabayev[1✉], B. Mauyey[1, 2]

[1]L.N. Gumilyov Eurasian National University, Astana, Kazakhstan;
[2]Joint Institute for Nuclear Research, Dubna, Russia

The analysis of the elastic scattering of the ^{6}He+^{208}Pb nuclear system using the new B3Y-Fetal potential

At energies close to the Coulomb barrier, a semi-microscopic analysis of the angular distribution of elastic scattering of the halo nucleus ^{6}He on the heavy nucleus ^{208}Pb was performed. In this analysis, the effectiveness of the new B3Y-Fetal folding potential for the large asymmetric ^{6}He+^{208}Pb system was investigated. The effective NN interactions, M3Y and B3Y potentials, were constructed taking into account the distribution features of the weakly bound neutrons of the ^{6}He halo nucleus in the strong Coulomb field of the ^{208}Pb nucleus. These density-dependent folding potentials were used as the real part of the optical model potential. The obtained results successfully reproduce the experimental data on elastic scattering. The new B3Y-Fetal potential provides a more accurate description of the NN interaction at large distances in highly asymmetric systems, thereby yielding a more precise prediction of the angular distributions of elastic scattering. The density-dependent modified CDM3Y6-Paris and CDB3Y6-Fetal potentials offer a more realistic description of NN interactions in nuclear matter, since the density-dependent parameters C, α, β, and γ were chosen based on the value of the incompressibility coefficient K calculated at the saturation point. For the ^{6}He+^{208}Pb system at energies E_{lab} = 22 and 27 MeV, a set of optimal parameters for elastic scattering cross sections near the Coulomb barrier was determined. The effectiveness of the new B3Y-Fetal potential in describing the angular distribution of elastic scattering was confirmed. The results of the semi-microscopic analysis are characterized by the renormalization factor N_r and the χ^2/N coefficients. The obtained results may contribute to nuclear astrophysics, particularly to studies of halo nuclei structures and the mechanisms of nuclear interaction processes.

Keywords: elastic scattering, ^{6}He — halo nucleus, ^{208}Pb — heavy nucleus, folding potential, B3Y-Fetal, K — incompressibility coefficient

✉*Corresponding author*: Morzabayev, Aidar, morzabayev_ak@enu.kz

Introduction

The ^{6}He+^{208}Pb system is one of the widely studied topics in modern nuclear physics. Such investigations are important for understanding the structure of exotic nuclei and the mechanisms of their interactions. The ^{6}He+^{208}Pb system also aids in modeling nucleosynthesis processes occurring in stars, which is essential in nuclear astrophysics. Studies involving the ^{6}He nucleus make a significant contribution to understanding neutron density distributions (neutron halo), particularly in providing deeper insight into the r-process [1].

In systems with large asymmetry, effects such as the nuclear rainbow, weak absorption, and pronounced oscillations in the scattering cross section can be observed. The strong Coulomb field of the heavy ^{208}Pb nucleus, along with the ability to incorporate the density distribution of weakly bound halo nuclei (such as ^{6}He,

[11]Be, and [8]B), plays an important role in studying their breakup into fragments. This is due to the fact that their neutron halo structure differs significantly from that of standard nuclei [2]. In this regard, a microscopic investigation of the breakup of the ^{6}He nucleus scattered from a ^{208}Pb target is of great interest.

The elastic scattering of the ^{6}He+^{208}Pb system was studied using a microscopic analysis based on the newly developed B3Y(Botswana-3 Yukawa)-Fetal folding potential [2]. We aimed to investigate this system using the double folding model (DFM), which accounts for the nucleon densities of both interacting nuclei. The microscopic effective nucleon-nucleon (NN) interactions, such as the M3Y (Michigan-3-Yukawa) realistic potentials, are constructed by taking into account the nucleon density distributions [3]. Additionally, we aimed to comparatively evaluate our results obtained using the B3Y-Fetal potential against the data reported by other authors [4]. In the folding model, the effective NN interaction potential is constructed microscopically by taking into account the density distribution of nucleons. This approach makes it possible to integrate over the interactions of each nucleon, providing a more accurate description of the mean field inside the nucleus. As a result, the obtained folding potential accounts for the saturation properties of nuclear matter and the density distribution at the nuclear surface. Such features allow for more reliable predictions of the angular distribution in elastic scattering, refinement of nuclear characteristics, and more accurate calculations of reactions. Therefore, the results of such an analysis are of great importance in nuclear astrophysics and thermonuclear energy research.

The halo structure of the ^{6}He nucleus, characterized by a wide spatial distribution of neutrons, was calculated in the strong field of the heavy ^{208}Pb nucleus, and the results were tested against experimental data. In the study of the ^{6}He+^{208}Pb system, the M3Y-Reid, M3Y-Paris, and B3Y-Fetal potentials are modified to more accurately describe the NN interactions within nuclear matter [5].

The delicate balance between the Coulomb and nuclear potentials is clearly manifested in the DFOM (Double Folding Optical Model) framework. The M3Y-Reid, M3Y-Paris, and B3Y-Fetal potentials allow these processes to be described based on realistic density distributions and NN interactions [6]. The approach of using density-dependent potentials is well-suited for the the^{6}He+^{208}Pb system, as it provides a better opportunity to account for the diffuse density characteristic of the halo structure [7]. In the folding model, realistic NN interactions are combined with accurate nuclear matter density functions, offering a more precise description [8]. The difference between this work and the studies by Khoa et al. lies in the use of the new B3Y-Fetal potential for the NN interaction and the introduction of density-dependent parameters into this potential.

The new B3Y-Fetal potential differs from the traditional M3Y-Reid and M3Y-Paris potentials in that it is derived from the calculation of nuclear matrix elements of the two-body interaction within the variational method with lowest-order constraints (LOCV) [2]. In semi-microscopic analysis, the accuracy of the folding potential is determined by the renormalization coefficient Nr. The coefficient Nr is obtained during calculations with the FRESCO code by comparing theoretical cross sections with experimental data. The closer the value of N_r is to 1, the more accurately the applied folding potential describes the real nuclear force. Meanwhile, the χ^2/N comparison coefficient reflects the degree of agreement between the calculated and experimental cross sections. The combination of these two parameters makes it possible to assess the reliability of the folding potential.

The main reason why the B3Y-Fetal potential provides good results is that, when introducing corrections to the density-dependent formula, it takes into account the saturation density of the binding forces in the nuclear medium, namely the incompressibility coefficient K. From a physical point of view, this model can be explained as follows: first, the calculation is performed from the center of the ^{6}He nucleus based on the nucleon density distribution of the ^{208}Pb nucleus. Second, the calculation is performed from the center of the ^{208}Pb nucleus based on the nucleon density distribution of the ^{6}He nucleus. For this reason, the method is called the double-folding model

The two-parameter density model (Fermi or Woods–Saxon) describes the nucleus in a simple form through the central density distribution and the surface thickness (radius, diffuseness). In contrast, in the DFM, the nucleon density distributions of two nuclei ($\rho_1(r_1)$, $\rho_2(r_2)$) are taken and folded with the effective NN interaction to construct a fully microscopic potential. In other words, this is a more complex microscopic method that takes into account the complete density distribution of both nuclei, rather than just one. Cluster models (for example, α-cluster models) play an important role in describing the correlation of nucleons inside the nucleus and their grouped interactions. For instance, DWBA is used in reaction theory models to describe inelastic processes (transfer reactions) in nuclear reactions. In the future, just as we have applied this approach to other systems, we will also apply it to the ^{6}He+^{208}Pb system.

As a result of this study, the elastic scattering of the ^{6}He+^{208}Pb system is successfully described based on density-dependent folding potentials. The weakly bound nature of the halo-structured 6He nucleus provides deeper insight into the specific features of nucleus–nucleus interactions. This not only expands the boundaries of nuclear physics but also enhances the accuracy of astrophysical models.

Theoretical formalisms and procedures

Based on the DFM, a modified effective NN interaction potential (M3Y) is obtained by taking into account the nucleon density distributions of the ^{6}He+^{208}Pb system. The resulting folding potential constitutes the real part of the optical potential (OP). Using this OP, we evaluate the accuracy of the theoretical model by describing the angular distribution of elastic scattering in comparison with experimental data on nucleus–nucleus interactions.

Since 6He is a weakly bound nucleus prone to breakup, it induces a pronounced cluster structure of neutrons and alpha particles at energies near the strong Coulomb barrier of the ^{208}Pb nucleus [9]. Therefore, to clarify the pure elastic scattering cross sections of neutrons, an analysis was carried out at near-barrier energies of E_{lab} = 22 and 27 MeV. The nucleus–nucleus realistic potential is obtained in the following form [10].

$$V(R) = \iint \rho_{6He}(\vec{r}_1)\rho_{208Pb}(\vec{r}_2)\vartheta_{NN}\left(\left|\vec{R}+\vec{r}_2-\vec{r}_1\right|\right)d^3r_1d^3r_2 \tag{1}$$

Here, ϑ_{NN} is the effective NN interaction potential of the M3Y type.

The formula for calculating the direct and exchange parts of the NN effective interaction based on the M3Y-Reid potential is given in [11].

$$\upsilon_D(s) = 7999.0\frac{e^{-4s}}{4s} - 2134.25\frac{e^{-2,5s}}{2,5s} \tag{2}$$

$$\upsilon_{EX}(s) = 4631.4\frac{e^{-4s}}{4s} - 1787.1\frac{e^{-2,5s}}{2,5s} - 7.8474\frac{e^{-0,7072s}}{0,7072s} \tag{3}$$

for M3Y-Paris potential [11]:

$$\upsilon_D(s) = 11061.6\frac{e^{-4s}}{4s} - 2537.5\frac{e^{-2,5s}}{2,5s} \tag{4}$$

$$\upsilon_{EX}(s) = -1524.0\frac{e^{-4s}}{4s} - 518.8\frac{e^{-2,5s}}{2,5s} - 7.8474\frac{e^{-0,7072s}}{0,7072s} \tag{5}$$

for the new B3Y-Fetal potentials [12]:

$$\upsilon_D(s) = 10472.13\frac{e^{-4S}}{4s} - 2203.11\frac{e^{-2,5S}}{2,5s} \tag{6}$$

$$\upsilon_{EX}(s) = 499.63\frac{e^{-4S}}{4s} - 1347.77\frac{e^{-2,5S}}{2,5s} - 7.8474\frac{e^{-0,7072S}}{0,7072s} \tag{7}$$

The B3Y and M3Y type potentials are modified to be dependent on both energy and density [13].

$$\upsilon_{D(EX)}(\rho,r,s) = F(E,\rho)g(E)\upsilon'_{D(EX)}(s) \tag{8}$$

The density-dependent function ($F(\rho)$) is given as [14]:

$$F(\rho) = C\left(1+\alpha e^{-\beta\rho}\right)--\gamma\rho) \tag{9}$$

The energy-dependent factor ($g(E)$) is given as [14]:

$$g(E) = (1-0.003E/A) \tag{10}$$

The density-dependent parameters are chosen to reduce the K-value in accordance with the saturation property of nuclear matter (as shown in Table 1). The CDM3Y6 parameters were applied to the B3Y-Fetal potential to construct the CDB3Y6-Fetal version.

The parameters of the M3Y-Reid, M3Y-Paris, and B3Y-Fetal potentials are presented [10]

Density dependence	C	α	β (fm³)	γ (fm³)	K (MeV)
CDM3Y6-Reid CDM3Y6-Paris CDB3Y6-Fetal	0.2658	3.8033	1.4099	4.0	252

In the region near the saturation point, the curvature of the binding energy per nucleon curve depends on the K — incompressibility of nuclear matter [10].

The nuclear compressibility coefficient is calculated using the following equation [11]:

$$K_\infty = -\frac{3\hbar^2 k_F^3}{5m} + 5J_D C\beta(\varepsilon)\rho^{5/3}\Big|_{\rho=\rho_0} \tag{11}$$

The dependence curve of the binding energy per nucleon on the nuclear matter density allows for the determination of the actual saturation density ρ_0 of the nucleus [15]. The saturation density ρ_0 represents the density per unit volume that characterizes the "natural" arrangement of nucleons inside the nucleus where the binding energy reaches its maximum value. In this case, the binding energy of nuclear matter can be approximated in the following form [16].

$$\frac{B}{A}(\rho) = a_V\left(1 - \frac{1}{2}\left(\frac{\rho - \rho_0}{\rho_0}\right)^2\right), \tag{12}$$

where $\frac{B}{A}$ is the binding energy per nucleon; ρ is the nuclear matter density; ρ_0 is the saturation density, and a_V is the volume binding energy coefficient. To find the point where the binding energy reaches its maximum, we write it in the following form.

$$\frac{d\left(\frac{B}{A}\right)}{d\rho} = 0. \tag{13}$$

For the ^{208}Pb nucleus, the normal saturation density has a value of approximately $\rho_0 \approx 0.16$ fm^{-3}, according to both experimental and theoretical studies [17].

Determining the exact saturation density for the ^{6}He nucleus is a special case, as it has a halo structure composed of $6He \to 4He + 2n$. The two neutrons are spatially extended away from the core, meaning its structure is characterized by a broadly distributed, diffuse density. This expands its overall density distribution, reduces the average density, and the corresponding calculated results can be approximated using the following formula [18].

$$\rho_{6He} = \frac{A}{\frac{4}{3}\pi R^3} \approx 0.09 \text{ fm}^{-3} \tag{14}$$

Here, R is the mean radius of the nucleus. For ^{6}He, the experimental radius is approximately $R \approx 2.5$ fm, with mass number $A = 6$.

We express the nucleon density distribution of each colliding nucleus using the two-parameter Fermi (2pF) model [19] and the result of the calculation is shown in the following Table 2:

$$\rho(r) = \frac{\rho_0}{1 + \exp\left(\frac{r - c}{z}\right)}. \tag{15}$$

2pF-model, c, z, <r²>^{1/2}, ρ_o — parameters of the distribution of substance density of the nucleus [19]

Nuclear	c, fm	z, fm	<r²>^{1/2}, fm	ρ_o, fm⁻³
^{6}He	1.8	0.75	2.5	0.08
^{208}Pb	6.624	0.549	5.521	0.16

Analysis Section

Folding potentials were calculated in the DFPOT code. Semi-microscopic analysis was carried out using the FRESCO code [20]. For the ^{6}He+^{208}Pb system at E_{lab}=22.0 MeV, the calculated DF potentials using CDM3Y6-Reid, CDM3Y6-Paris, and CDB3Y6-Fetal interactions are shown in Figure 1.
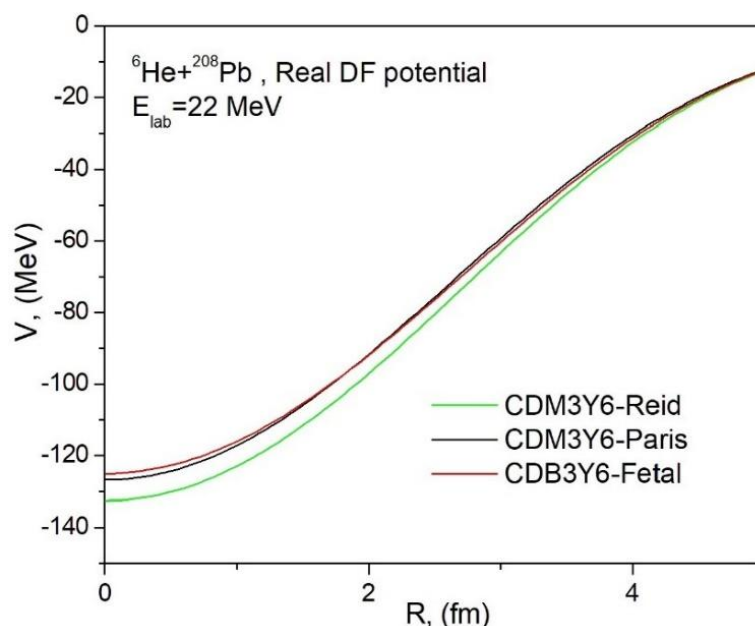
Figure 1. The generated real DF potentials for the ^{6}He+^{208}Pb system at E_{lab} = 22.0 MeV

The depth and characteristics of the DF microscopic potentials obtained for our ^{6}He+^{208}Pb system are consistent with the results reported in the literature [21]. Due to the large asymmetry in the ^{6}He+^{208}Pb system, constructing the CDM3Y6-Reid, CDM3Y6-Paris, and CDB3Y6-Fetal potentials within the DFM was challenging. It was observed that the CDM3Y6-Paris and CDB3Y6-Fetal potentials, being density-dependent, are noticeably deeper in the radial regions up to 3 fm.

T a b l e 3

OM and DFOM parameters for the ^{6}He+^{208}Pb elastic scattering
at E_{lab} = 22.0 MeV and E_{lab} = 27.0 MeV energy, r_c = 1.25 fm

E MeV	Model	Type of real potential				Imaginary potential parameter (WS)				σ_R mb
		V_0 MeV	Rv fm	av fm	N_r	W_0 MeV	r_W fm	a_W fm	χ^2/N	
22.0	OM Exp: [22, 23,24]	170.7	0.9	0.55	–	20.4	1.4	0.74	0.77 2.0 2.89	1099
	DFOM	CDM3Y6- Reid			0.79	20.4	1.4	0.74	-	1357
	DFOM	CDM3Y6-Paris			0.8	20.4	1.4	0.74	-	1378
	DFOM	CDB3Y6- Fetal			0.85	20.4	1.4	0.74	-	1365
27.0	OM (для exp: [25])	170.7	0.9	0.55	–	20.4	1.4	0.74	0.06	1940
	DFOM	CDM3Y6-Paris			0.8	20.4	1.4	0.74	-	1876
	DFOM	CDB3Y6- Fetal			0.84	20.4	1.4	0.74	-	2011

Based on the experimental data at E_{lab} = 22 MeV from references [22–24], a common optimal set of parameters was obtained within the framework of the OM analysis (Table 3). The value of χ^2/N-indicates the relative error between the theoretical calculation and the experimental data of the angular distribution for elastic scattering.

The result of the OM analysis is shown in the following Figure 2.
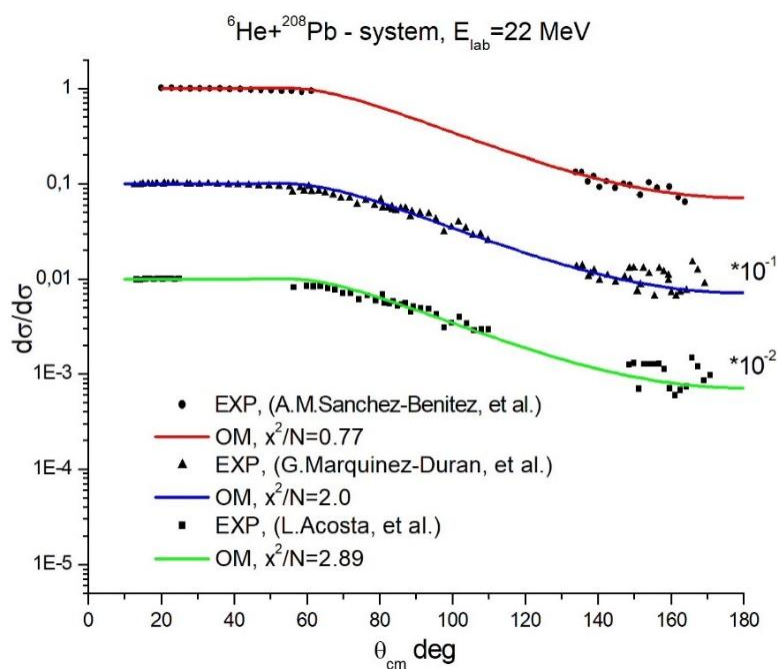
Figure 2. OM results of the ^{6}He+^{208}Pb system at E_{lab} = 22 MeV

In the following analysis, we replace only the real part of these refined OM parameters with a microscopic folding potential. In this semi-microscopic analysis, the parameters of the imaginary part (W_0, r_W, a_W) remain in the Woods–Saxon form. The stability of the imaginary parameters in the DFOM analysis confirms the reliability of the tested DF real potential. The results of the DFOM model analysis for the experimental data at E_{lab} = 22 MeV [22] and E_{lab} = 27 MeV [25] are presented in Figure 3.
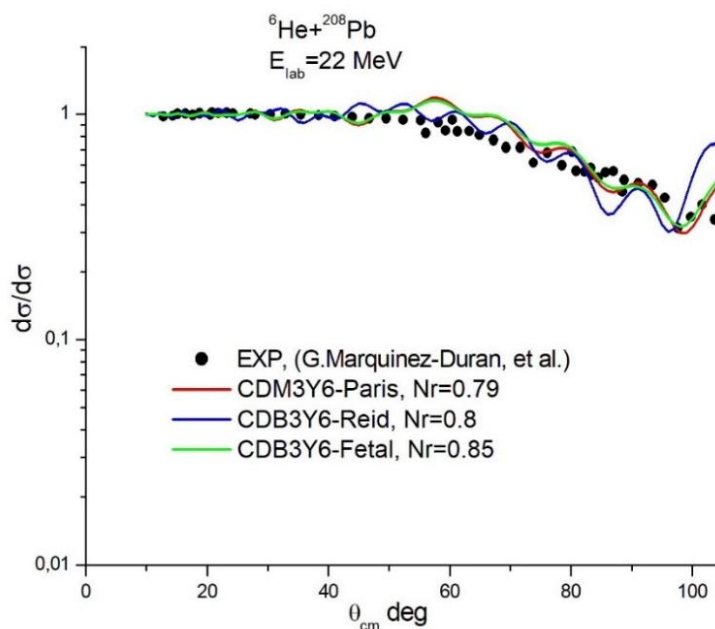
Figure 3. DFOM results of the ^{6}He+^{208}Pb system at E_{lab} = 22 MeV
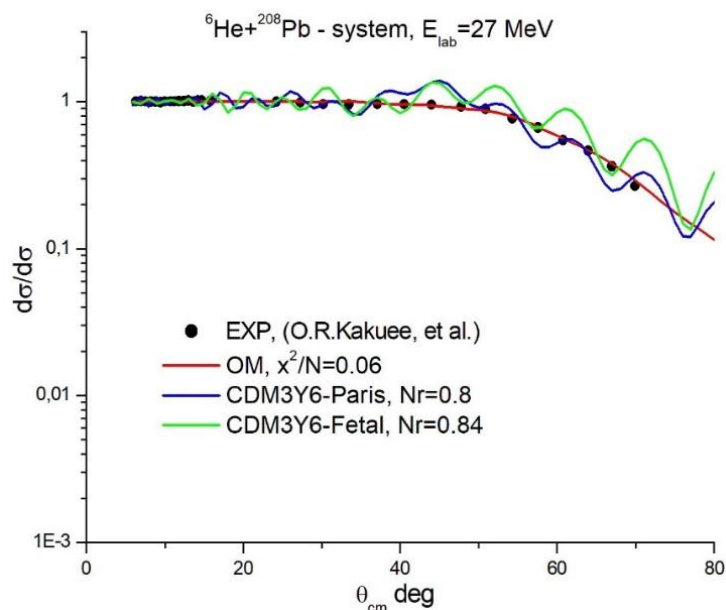
Figure 4. OMand DFOM results of the ^{6}He+^{208}Pb system at E_{lab} = 27 MeV

In the semi-microscopic analysis, the DF real potential primarily influences the angular distribution of elastic scattering at forward angles (up to 90°). At energies near the Coulomb barrier, cluster transfer effects in the elastic scattering distribution are clearly observed at angles between 60° and 80°. Correspondingly, the density-dependent CDM3Y6-Paris and CDB3Y6-Fetal potentials provided a successful description of this behavior (Figs. 3 and 4).To characterize nuclear reactions and to verify the accuracy of the performed calculations, the σ_R- total reaction cross-sections were determined.

Conclusion

The angular distributions of elastic scattering for the ^{6}He+^{208}Pb system near the Coulomb barrier at E_{lab} = 22 and 27 MeV were analyzed using the DFOM model. Real folding potentials CDM3Y6-Paris and CDB3Y6-Fetal were constructed based on neutron density distributions for this system. The obtained potentials account for the density distribution of the weakly bound neutrons in the ^{6}He halo nucleus in the presence of the strong Coulomb field of the ^{208}Pb nucleus.

The density-dependent modified M3Y-Paris and B3Y-Fetal potentials contribute to a more accurate description of nucleon-nucleon interactions in nuclear matter. The structures observed in the angular distributions were successfully explained by the characteristics of these potentials and were evaluated using adjustable normalization coefficients — Nr. A distinctive feature of the DF real potentials was their consideration of the asymmetric nature of the studied system and the calculation at energies near the Coulomb barrier.

In this study, the newly developed CDB3Y6-Fetal potential was successfully applied to the ^{6}He+^{208}Pb nuclear system, which exhibits significant asymmetry in terms of mass and isotopic composition. The effectiveness of this new potential in describing the angular distribution of elastic scattering was demonstrated. Such research results can contribute to nuclear astrophysics, particularly in studying the structure of halo nuclei and the mechanisms of nuclear interaction processes.

Acknowledgment

References

1   Arnould, M., Goriely, S., & Takahashi, K. (2007). The r-process of stellar nucleosynthesis: Astrophysics and nuclear physics achievements and mysteries. *Physics Reports, 450*(4–6), 97–213. https://doi.org/10.1016/j.physrep.2007.06.002

2   Fiase, J.O., Devan, K.R.S., & Hosaka, A. (2002). Mass dependence of M3Y-type interactions and the effects of tensor correlations. *Physical Review C, 66*(1), 014004. https://doi.org/10.1103/PhysRevC.66. 014004.

3   Khoa, D.T., et al. (2007). Folding model analysis of elastic and inelastic ^{6}He+^{208}Pb scattering and the halo structure of ^{6}He. *Nuclear Physics A, 759*, 3–30.

4   Khoa, D.T., Cuong, D.C., & Loan, D.T. (2023). New density-dependent M3Y interactions for nucleus–nucleus optical potentials and elastic scattering of ^{6}He on ^{208}Pb. *Nuclear Physics A, 1035*, 122717.

5   Amangeldi, et al. (2024). Efficiency of the new B3Y-fetal potential in the analysis of the elastic and inelastic angular distributions for the ^{10}B+^{12}C system. *Pramana, 98*(3), 106. https://doi.org/10.1007/s12043-024-02760-z.

6   Soldatkhan, D., Amangeldi, N., Makhanov, K.M., & Smagulov, Zh.K. (2023). Application of the new B3Y-Fetal potential in the semi-microscopic analysis of the scattering of accelerated ^{6}Li — lithium and ^{16}O — oxygen nuclei from the ^{12}C — carbon nucleus. *Eurasian Physical Technical Journal, 25*, 4(46), 22–30. https://doi 10.31489/2023No4/17-22

7   Keeley, N., Alamanos, N., Lapoux, V., & Rusek, K. (2009). Review of reactions with light exotic nuclei. *Progress in Particle and Nuclear Physics, 63*(2), 396–447. https://doi.org/10.1016/j.ppnp.2009.05.001

8   Amangeldi, N., et al. (2024). Recent Measurement and Theoretical Analysis for the Elastic Scattering of the ^{15}N+^{11}B System. *Brazilian Journal of Physics, 54*(5), 169. https://doi.org/10.1007/s13538-024-01547-2

9   Descouvemont, P. & Hussein, M.S. The cluster structure of ^{6}He and reactions with heavy targets. *Physics Letters B, 693*(6), 568–572 (2010). https://doi.org/10.1016/j.physletb.2010.09.011

10   Kyoungsu Heo et al. (2024). Folding potential with modern nuclear density functionals and application to ^{16}O+^{208}Pb reaction. *Phys. Rev. C, 110*(3), 034616. DOI: https://doi.org/10.1103/PhysRevC.110.034616

11   Soldatkhan, D., Yergaliuly, G., Amangeldi, N., Mauyey, B., Odsuren, M., Awad, Ibraheem A., & Hamada, Sh. (2022). New Measurements and theoretical analysis for the ^{16}O+^{12}C Nuclear System. *Brazilian Journal of Physics, 52*(152), 1–10. https://doi.org/10.1007/s13538-022-01153-0.

12   Soldatkhan, D., Amangeldi, N., Baltabekov, A., & Yergaliuly, G. (2022). Investigation of the energy dependence of the interaction potentials of the ^{16}O+^{12}C nuclear system with a semi-microscopic method. *Eurasian Physical Technical Journal, 19*, 3(41), 39–44. https://doi 10.31489/2022No3/39-44

13   AA, B. (2025). Analysis of the effect of the B3Y-fetal potential on energy near the coulomb barrier for the ^{9}Be+^{12}C system. *Eurasian Physical Technical Journal, 22*(1).

14   Soldatkhan, D., Mauyey, B., Baratova, A.A., & Makhanov, K.M. (2025). Introduction of a New B3Y-Fetal Potential in the Semimicroscopic Analysis of the ^{15}N+^{27}Al Nuclear System. *Bulletin of the University of Karaganda — Physics, 117*(1), 29–36.

15   Khoa, D.T., von Oertzen W., Bohlen, H.G., & Ohkubo, S. (2007). Nuclear rainbow scattering and nucleus–nucleus potential. *Journal of Physics G: Nuclear and Particle Physics, 34*(5), R111. https://doi.org/10.1088/0954-3899/34/5/R01

16   Khoa, D.T., Satchler, G.R., & von Oertzen, W. (1997). Nuclear incompressibility and density dependent nucleon–nucleon interaction. *Physics Review C, 56*, 954. https://doi.org/10.1103/PhysRevC.56.954

17   Ring, P. & Schuck, P. (1980). *The Nuclear Many-Body Problem.* Springer-Verlag, ISBN: 978-3-540-21206-5

18   Jensen, A.S., Riisager, K., Fedorov, D.V., & Garrido, E. (2004). Structure and reactions of quantum halos. *Rev. Mod. Phys. 76*, 215. https://doi.org/10.1103/RevModPhys.76.215

19   de Vries, H., de Jager, C. W., & de Vries, C. (1987). Nuclear charge-density-distribution parameters from elastic electron scattering. *Atomic Data and Nuclear Data Tables, 36*, 495–536.

20   Thompson, I.J. (1988). Coupled reaction channels calculations in nuclear physics. *Computer Physics Reports, 7*, 167–212.

21   Awad, A. Ibraheem, El-Azab, M.A., & El-Ghafar, H.H. (2021). Analysis of ^{4,6,8}He+^{208}Pb elastic scattering using different density-dependent interactions within the double-folding optical model. *International Journal of Modern Physics E, 30*(12), 2150105. https://doi.org/10.1142/S0218301321501057

22   Sánchez-Benítez, A.M., et al. (2008). Study of the elastic scattering of ^{6}He on ^{208}Pb at energies around the Coulomb barrier. *Nuclear Physics A, 803*(1–2), 30–45. https://doi.org/10.1016/j.nuclphysa.2008.01.015

23   Marquínez-Durán, et al. (2016). Precise measurement of near-barrier ^{8}He+^{208}Pb elastic scattering: Comparison with ^{6}He. *Physical Review C, 94*(6), 064618. https://doi.org/10.1103/PhysRevC.94.064618

24   Acosta, L., et al. (2011). Elastic scattering and α-particle production in ^{6}He+^{208}Pb collisions at 22 MeV. *Physical Review C, 84*(4), 044604. https://doi.org/10.1103/PhysRevC.84.04460

25   Kakuee, O. R., et al. (2004). Long range absorption in the scattering of ^{6}He on ^{208}Pb and ^{197}Au at 27 MeV. *Nuclear Physics A, 735*(3–4), 321–340. https://doi.org/10.1016/j.nuclphysa.2004.01.139

Д. Солдатхан, А.К. Морзабаев, Б. Мауей

^{6}He+^{208}Pb ядролық жүйесінің серпімді шашырауын жаңа B3Y-Fetal потенциалы арқылы талдау

Кулондық тосқауылға жақын энергияларда ^{6}He гало ядроның ^{208}Pb ауыр ядросымен серпімді шашырауының бұрыштық таралуына жартылай микроскопиялық талдау жүргізілді. Талдау барысында жаңа B3Y-Fetal фолдинг потенциалдың ^{6}He+^{208}Pb асимметриясы үлкен жүйе үшін тиімділігі зерттелді. Тиімді NN өзара әрекеттесу M3Y және B3Yпотенциалдары ^{208}Pb ядроның күшті кулондық өрісіндегі

^{6}He гало ядроның әлсіз байланысқан нейтрондар тығыздығының таралу ерекшелігін ескеру негізінде құрылды. Тығыздыққа тәуелді бұл фолдинг потенциалдар оптикалық модельдің нақты бөлігі ретінде қолданылды. Алынған талдау нәтижелер серпімді шашыраудың эксперименттік деректерін сәтті сипаттай алды. Жаңа B3Y-Fetal потенциалы асимметриясы үлкен жүйелердегі үлкен қашықтықтарда ядролар арасындағы өзара әрекеттесуді дәлірек сипаттап, серпімді шашыраудың бұрыштық таралуын нақты болжауға мүмкіндік береді. Тығыздыққа тәуелді модификацияланған CDM3Y6-Paris, CDB3Y6-Fetal потенциалдары ядролық материя нуклондарының өзара әсерін барынша нақты сипаттауға үлес қосады. Себебі тығыздығына тәуелді C, α, β, γ — параметрлер қанықтылық нүктесіне қатысты есептелген K сығылмаушылық коэффициенті мәніне байланысты таңдалды. Кулондық тосқауылға жақын $E_{lab} = 22$ және 27 MeV энергияларда ^{6}He+^{208}Pb жүйесі үшін серпімді шашырау қимасына арналған оңтайлы параметрлер жиынтығы анықталды. Серпімді шашыраудың бұрыштық таралуын сипаттауда жаңа B3Y-Fetal потенциалдың тиімділігі айқындалды. Жартылай микроскопиялық талдау нәтижесін N_r — ренормализация факторы мен χ^2/N — коэффициенттері көрсетеді. Алынған нәтижелері ядролық астрофизикада, әсіресе гало ядроларының құрылымын және ядролық өзара әрекеттесу процестерінің механизмдерін зерттеуге үлес қоса алады.

Кілт сөздер: серпімді шашырау, ^{6}He — гало ядро, ^{208}Pb — ауыр ядро, фолдинг потенциалы, B3Y-Fetal, K — сығылмаушылық коэффициенті

Д. Солдатхан, А.К. Морзабаев, Б. Мауей

Анализ упругого рассеяния ядерной системы ^{6}He+^{208}Pb с использованием нового потенциала B3Y-Fetal

При энергиях, близких к кулоновскому барьеру, проведён полумикроскопический анализ угловых распределений упругого рассеяния ядра-гало ^{6}He на ядре ^{208}Pb. В рамках исследования применён новый фолдинговый потенциал B3Y-Fetal для описания асимметричной системы ^{6}He+^{208}Pb. Эффективные нуклон-нуклонные взаимодействия в потенциалах M3Y и B3Y построены с учётом распределения плотности слабо связанных нейтронов в ^{6}He в кулоновском поле ядра ^{208}Pb. Зависимые от плотности фолдинговые потенциалы использовались в качестве реальной части оптической модели и позволили успешно воспроизвести экспериментальные данные по упругому рассеянию. Показано, что новый потенциал B3Y-Fetal обеспечивает более точное описание взаимодействия ядер на больших расстояниях в сильно асимметричных системах и даёт надёжное предсказание угловых распределений упругого рассеяния. Модифицированные потенциалы CDM3Y6-Paris и CDB3Y6-Fetal вносят вклад в более корректное описание нуклон-нуклонных взаимодействий в ядерной материи, поскольку параметры C, α, β, γ выбирались в зависимости от коэффициента сжимаемости K, рассчитанного вблизи точки насыщения. Для системы ^{6}He+^{208}Pb при энергиях $E_{lab} = 22$ и 27 МэВ определены оптимальные параметры сечения упругого рассеяния, что подтвердило эффективность потенциала B3Y-Fetal. Результаты полумикроскопического анализа отражаются коэффициентами перенормировки N_r и χ^2/N. Полученные результаты могут внести вклад в ядерную астрофизику, в частности в изучение структуры гало-ядер и механизмов процессов ядерного взаимодействия.

Ключевые слова: упругое рассеяние, ^{6}He — гало-ядро, ^{208}Pb — тяжелое ядро, фолдингпотенциал, B3Y-Fetal, K — коэффициент несжимаемости

Information about the authors

Soldatkhan, Dauren — PhD, Senior Teacher, L.N. Gumilyov Eurasian National University, Astana, Kazakhstan; e-mail: soldathan.dauren@gmail.com. SCOPUS Author ID: 57768566200; ORCID ID https://orcid.org/0000-0001-7981-4100

Morzabayev, Aidar (*corresponding author*) — Candidate of Physico-Mathematical Sciences, Associate Professor, L.N. Gumilyov Eurasian National University, Astana, Kazakhstan; e-mail: morzabayev_ak@enu.kz; SCOPUS Author ID 26531512300; ORCID ID: https://orcid.org/record/DJU-9592-2022

Mauyey, Bahytbek — PhD, Senior Teacher, Joint Institute for Nuclear Research, Dubna, Russia; L.N. Gumilyov Eurasian National University, Astana, Kazakhstan; e-mail: bahytbek01@yandex.kz. SCOPUS Author ID: 57193847043; ORCID ID: https://orcid.org/0000-0003-4301-1327

G.A. Bakalbayeva[1, 2], A.A. Baratova[1, 2✉], N.K. Aidarbekov[1, 2], M.M. Kubenova[1, 2],
A.N. Amangozhayeva[2], R.S. Bisseken[2]

[1]Caspian University of Technology and Engineering named after Sh. Yessenov, Aktau, Kazakhstan;
[2]L.N. Gumilyov Eurasian National University, Astana, Kazakhstan

Investigation of the Functional Characteristics of $Pr_{1-x}Sr_xFe_{1-\gamma}Co_\gamma O_{3-\delta}$ Perovskite Cathodes for Reversible Solid Oxide Fuel Cells

A systematic investigation was conducted on perovskite-type cathode materials of the composition $Pr_{1-x}Sr_xFe_{1-\gamma}Co_\gamma O_{3-\delta}$, synthesized via self-propagating high-temperature synthesis, with the aim of optimizing their performance in reversible solid oxide fuel cells (RSOFCs). Particular attention was given to the influence of Sr and Co substitution on thermal expansion, electrical conductivity, and polarization resistance under operating conditions. Detailed analyses using dilatometry, four-probe conductivity measurements, and electrochemical impedance spectroscopy revealed that moderate strontium substitution ($x = 0.2$–0.3) provides the most favorable balance between enhanced oxygen vacancy concentration, optimized lattice parameters, and structural stability. These factors jointly promote higher conductivity while maintaining low polarization resistance. The incorporation of cobalt was shown to boost electronic transport, although excessive Co levels (e.g., $y = 0.5$) resulted in increased thermal expansion and interfacial resistance due to phase interactions with the electrolyte. Among the studied compositions, PSFC-2020, PSFC-3020, and PSFC-4020 demonstrated superior electrochemical performance, with conductivities up to ~186 S·cm^{-1} and polarization resistances as low as 1.9 Ω·cm^2 at 850 °C. The findings confirm the potential of Pr–Sr–Fe–Co perovskites as high-performance cathode candidates for advanced RSOFCs systems, combining favorable thermomechanical compatibility, efficient charge transport, and long-term durability.

Keywords: reversible solid oxide fuel cells (RSOFCs), perovskite cathodes, Pr–Sr–Fe–Co oxides, thermal expansion, electrical conductivity, polarization resistance, electrochemical performance

✉*Corresponding author*: Baratova, Aliya, baratova_aa@enu.kz

Introduction

Reversible Solid Oxide Fuel Cells (RSOFCs), which can also operate in reverse as solid oxide fuel cells, are increasingly regarded as one of the most promising technologies for high-temperature energy conversion. These systems are not only capable of efficiently generating electricity from hydrogen and a variety of hydrocarbon fuels, but can also be employed for their electrochemical synthesis through steam electrolysis. The combination of high efficiency, flexibility in fuel choice, and significant environmental advantages positions RSOFCs as a key avenue for the advancement of hydrogen-based energy solutions [1–3].

The durability and long-term stability of such devices are largely governed by the properties of the cathode materials. These materials must combine high mixed ionic-electronic conductivity with resistance to chemical interactions and thermomechanical stresses under conditions of cyclic temperature fluctuations and varying gas atmospheres. Equally critical is their compatibility with solid electrolytes, the most widely employed of which are yttria-stabilized zirconia (YSZ) and gadolinium-doped ceria (GDC) [4–6].

Among the wide range of oxide compounds, particular attention has been drawn to complex perovskite-type materials based on rare-earth ferrite-cobaltites with the general formula $Pr_{1-x}Sr_xFe_{1-\gamma}Co_\gamma O_{3-\delta}$. Their distorted perovskite lattice with $GdFeO_3$-type orthorhombic symmetry provides a unique combination of high electrical conductivity and pronounced catalytic activity in oxygen reduction processes. The partial substitution of strontium and cobalt into the crystal structure enables deliberate tuning of oxygen non-stoichiometry, unit cell parameters, thermal expansion coefficients, and overall electrophysical properties. This flexibility offers valuable opportunities for tailoring such materials to the specific operating conditions of RSOFCs [7–9].

One of the major challenges lies in ensuring the long-term stability of cathodes under high-temperature electrolysis and repeated reversible cycling, which inherently involves alternating oxidation and reduction processes. Addressing this issue requires a comprehensive investigation of how cation composition influences the crystal structure, thermal expansion behavior, electrical conductivity, polarization resistance, and chemical compatibility of cathodes with solid electrolytes [10–12].

The present study is devoted to a comprehensive investigation of cathode materials with the composition $Pr_{1-x}Sr_xFe_{1-\gamma}Co_\gamma O_{3-\delta}$ synthesized by the self-propagating high-temperature synthesis (SHS) method. The primary objective is to identify the optimal ratios of Sr and Co that ensure maximum electrocatalytic activity, low polarization resistance, and strong resistance to degradation within high-performance RSOFCs systems. In addition, the work aims to determine the key factors governing the long-term durability and operational characteristics of these cathodes [13–15].

Materials and methods

In this work, a series of praseodymium ferrite–cobaltite perovskites with the general formula $Pr_{1-x}Sr_xFe_{1-\gamma}Co_\gamma O_{3-\delta}$ ($0 \leq x \leq 0.4$; y = 0.2; 0.5) was prepared using high-purity reagents to ensure accurate stoichiometry and reproducibility. The starting chemicals were praseodymium nitrate hexahydrate $Pr(NO_3)_3 \cdot 6H_2O$, iron nitrate nonahydrate $Fe(NO_3)_3 \cdot 9H_2O$, cobalt nitrate hexahydrate $Co(NO_3)_2 \cdot 6H_2O$ (purity $\geq$ 98–99 %), and strontium carbonate $SrCO_3$ (purity $\geq$ 98 %). All components were used without further purification [16–18].

The stoichiometric proportions of the precursors were calculated for each target composition, after which the reagents were dissolved in 0.1 M nitric acid (HNO_3) under continuous stirring until complete dissolution. The neutralization of $SrCO_3$ by nitric acid yielded soluble strontium nitrate with CO_2 release, while the other nitrates dissolved without secondary reactions.

The resulting homogeneous nitrate solution was evaporated to dryness, producing a mixed salt residue. This residue was dispersed in ethylene glycol ($HOCH_2CH_2OH$, $\geq$ 99 %) at a molar ratio of 2:1 relative to the total nitrate ion content. Ethylene glycol served simultaneously as a solvent and a fuel for the subsequent self-propagating high-temperature synthesis (SHS). Upon heating, an intense exothermic redox reaction occurred, accompanied by rapid temperature rise and the formation of finely dispersed oxide powders. Nitrogen was identified as the main gaseous by-product, indicating the high selectivity and cleanliness of the synthesis process [19–20].

The as-combusted powders underwent multi-stage heat treatment: first at 400 °C and 700 °C to remove organics and promote initial crystallization, then at 900 °C for phase development, and finally calcined at 1100 °C for 30 min to achieve complete crystallization of the perovskite structure. X-ray diffraction confirmed the high phase purity and orthorhombic $GdFeO_3$-type symmetry (*Pbnm*) for all samples.

The synthesized compositions and their corresponding abbreviations are as follows:

* PFC-20: $PrFe_{0.8}Co_{0.2}O_3$ ($x = 0$, $y = 0.2$)
* PSFC-1020: $Pr_{0.9}Sr_{0.1}Fe_{0.8}Co_{0.2}O_{3-\delta}$ ($x = 0.1$, $y = 0.2$)
* PSFC-2020: $Pr_{0.8}Sr_{0.2}Fe_{0.8}Co_{0.2}O_{3-\delta}$ ($x = 0.2$, $y = 0.2$)
* PSFC-3020: $Pr_{0.7}Sr_{0.3}Fe_{0.8}Co_{0.2}O_{3-\delta}$ ($x = 0.3$, $y = 0.2$)
* PSFC-4020: $Pr_{0.6}Sr_{0.4}Fe_{0.8}Co_{0.2}O_{3-\delta}$ ($x = 0.4$, $y = 0.2$)
* PSFC-3050: $Pr_{0.7}Sr_{0.3}Fe_{0.5}Co_{0.5}O_{3-\delta}$ ($x = 0.3$, $y = 0.5$)

In the sample code, the first two digits represent the molar fraction of Sr ($x \times 100$) and the last two digits correspond to the molar fraction of Co ($y \times 100$) in the perovskite lattice. This designation provides a clear link between composition and the measured physicochemical properties.

Table 1 presents the nomenclature and key physicochemical parameters of the synthesized $Pr_{1-x}Sr_xFe_{1-\gamma}Co_\gamma O_{3-\delta}$ perovskite powders, including specific surface area (S_{BET}), equivalent particle size (d_{BET}), and theoretical density (γ_{theo}). The series encompasses both the undoped composition (PFC-20) and Sr-, Co-substituted variants (PSFC), enabling the assessment of how A- and B-site cation substitutions influence powder characteristics.

The S_{BET} values lie in the range of 4.8–6.4 m^2/g, which is relatively high for oxide materials obtained by SHS. A gradual increase in specific surface area is observed with the introduction and growth of Sr content, as well as with partial substitution of Fe by Co. This trend may be associated with the impact of heterova-

lentcation substitution on the combustion process during SHS, where changes in thermal release and diffusion rates can limit particle coarsening and promote the formation of a more developed surface morphology.

The equivalent particle sizes (d_{BET}), calculated from BET data, range from 65 nm in PFC-20 to 50 nm in PSFC-3050, confirming the nanoscale nature of the powders. The observed reduction in particle size for Co-rich compositions can be linked to the higher exothermicity of the reaction and shortened grain growth stage, leading to enhanced dispersion. These fine particle dimensions are expected to facilitate improved contact area with the electrolyte and more efficient gas diffusion in the cathode layer.

T a b l e 1

Nomenclature and key physicochemical parameters of $Pr_{1-x}Sr_xFe_{1-\gamma}Co_\gamma O_{3-\delta}$ perovskite powders

Sample composition	$S_{BET}(m^2/g)$	$d_{BET}(nm)$	γ_{theor}, g/sm^3
PFC-20	4.8	65	6.36
PSFC-1020	5.2	60	6.29
PSFC-2020	5.6	56	6.22
PSFC-3020	5.9	54	6.16
PSFC-4020	6.1	52	6.09
PSFC-3050	6.4	50	6.21

where:
– S_{BET} — specific surface area determined by the Brunauer–Emmett–Teller (BET) method;
– d_{BET}– equivalent particle diameter, calculated from S_{BET} data assuming spherical particles;
– γ_{theor} — theoretical density of the bulk perovskite phase, calculated from crystallographic parameters.

Theoretical density values (γ_{theor}) vary only slightly (6.09–6.36 g/cm^3) across the series, reflecting the fact that density is primarily determined by the crystal structure and average atomic mass of the constituent elements. Minor variations arise from the substitution of Pr^{3+} by Sr^{2+} in the A-site and Fe^{3+} by Co^{3+} in the B-site, which slightly modify the lattice parameters.

Overall, the powders synthesized via SHS demonstrate a combination of high surface area, nanoscale particle size, and phase purity, all of which are advantageous for cathode applications in RTFCs. The interplay between composition and microstructural characteristics revealed in Table 1 provides a basis for correlating synthesis conditions, structural parameters, and functional performance in subsequent electrochemical testing.

Table 2 summarizes the key ionic characteristics of the cations incorporated into the synthesized perovskites $Pr_{1-x}Sr_xFe_{1-\gamma}Co_\gamma O_{3-\delta}$, including their valence states, coordination numbers (CN), ionic radii (r), and electronegativities (χ) according to the Pauling scale. These parameters determine the strength and nature of cation–anion bonding within the crystal lattice, which in turn directly governs the coefficient of thermal expansion (CTE), electrical conductivity, and the overall electrochemical performance of the cathode materials. In particular, variations in these ionic properties critically influence lattice stability, conductivity, and the resistance of the materials under operating conditions.

A comparison of the ionic parameters of the A-site cations (Pr^{3+} and Sr^{2+}) reveals that Sr^{2+} possesses a significantly larger ionic radius (1.44 Å vs. 1.179 Å) and a lower electronegativity (0.99 vs. 1.13). Substituting Pr^{3+} with Sr^{2+} enhances the ionic character of the A–O bond and leads to an expansion of the A-site sublattice, which can contribute to an increase in the coefficient of thermal expansion by weakening the covalent component of the bonding. Moreover, the incorporation of Sr^{2+}requires charge compensation through the formation of oxygen vacancies. These vacancies not only enlarge the lattice parameters but may also strongly influence the transport properties of the material.

For the B-site cations ($Fe^{3+}$and Co^{3+}), smaller ionic radii are characteristic (0.645 Å for Fe^{3+} and 0.545–0.61 Å for Co^{3+}, depending on the spin state), along with higher electronegativity values (1.83–1.88). Incorporation of Co^{3+} not only alters the size and symmetry of the BO_6 octahedra but can also induce spin-state transitions at elevated temperatures. These transitions result in the elongation of B–O bonds and consequently contribute to an increased coefficient of thermal expansion (CTE). At the same time, such effects influence electronic and mixed ionic–electronic conductivity by modifying the orbital overlap between O 2p and B 3d states.

Ionic parameters of cations $Pr_{1-x}Sr_xFe_{1-\gamma}Co_\gamma O_{3-\delta}$ perovskites

Sample composition	Oxidation state	Coordination Number (CN)	Ionic radius r (Å)	Electronegativity χ (Pauling)	Structural influence
Pr^{3+}	+3	9	1.179	1.13	Larger CN reduces bond distortion; higher χ leads to stronger A–O covalency
Sr^{2+}	+2	12	1.44	0.89	Lower χ increases A–O ionicity; larger radius expands lattice, affects CTE
Fe^{3+}	+3	6	0.645	1.83	Small radius stabilizes octahedral B–O bonds; higher χ strengthens covalency
Co^{3+}	+3 (low-spin/high-spin)	6	0.545 (low-spin) / 0.61 (high-spin)	1.88	Spin-state transitions at high T lengthen B–O bonds, increasing CTE

where:

– CN (Coordination Number) — the number of nearest neighboring oxygen ions bonded to a given cation within the crystal lattice;

– r(Å) — the ionic radius corresponding to the specific coordination;

– χ — the Pauling electronegativity, reflecting the ability of an ion to attract electrons.

Thus, the values presented in Table 2 provide a fundamental basis for interpreting the experimental results. They clarify why the $Pr_{1-x}Sr_xFe_{1-\gamma}Co_\gamma O_{3-\delta}$ $Pr_{1-x}Sr_xFe_{1-\gamma}Co_\gamma O_{3-\delta}$ series exhibits a nonlinear dependence of the CTE on Sr content, along with a steady increase in CTE as the Co fraction rises. Moreover, these parameters offer a physicochemical rationale for the observed trends in electrical conductivity and polarization resistance.

Results and discussion

To establish the correlation between chemical composition, structural features, thermal expansion, electrical transport behavior, and polarization resistance of the cathode materials, a series of experiments was carried out on synthesized perovskites $Pr_{1-x}Sr_xFe_{1-\gamma}Co_\gamma O_{3-\delta}$ with controlled Sr and Co contents.

The linear CTE was measured using a Netzsch DIL 402C dilatometer over the temperature range from room temperature up to 1000 °C at a heating rate of 5 °C/min. The influence of Sr and Co on the CTE can be explained by their ionic characteristics (Table 2):

– substitution of Pr^{3+} (χ = 1.13, r = 1.179 Å, CN = 9) with Sr^{2+} (χ = 0.99, r = 1.44 Å, CN = 12) enlarges the A-site sublattice and modifies the strength of the A–O bond, which can either increase or decrease the CTE.

– the incorporation of Sr^{2+} requires charge compensation through the formation of oxygen vacancies, which expand the lattice and promote higher CTE values.

– doping with Co^{3+} (particularly in its high-spin state) leads to elongation of the B–O bonds at elevated temperatures due to spin-state transitions, thereby producing a consistent increase in the CTE.

Electrical conductivity was measured on rectangular bars (3×2×30 mm) prepared by uniaxial pressing followed by sintering at 1100 °C for 4 h. Platinum electrodes (0.2 mm) were applied with platinum paste and subsequently fired at 900 °C for 1 h. Measurements were carried out in air using a four-probe DC technique (Solartron SI-1260/1287) over the temperature range of 300–950 °C with 50 °C increments. Increasing the Sr content up to $x = 0.2$ reduced the activation energy (E_a) and enhanced the conductivity due to a higher carrier concentration and reduced lattice distortions. At higher Sr levels ($x \geq 0.3$), the conductivity effect tended to stabilize, indicating saturation of the defect structure.

Polarization resistance (Rη) was determined by electrochemical impedance spectroscopy (EIS) using symmetric cells with dense YSZ and GDC electrolytes. Electrolyte discs (~12 mm in diameter, 0.3 mm thick) were pressed at 300 MPa and sintered at 1450 °C (YSZ) or 1350 °C (GDC). Cathode layers with a thickness of 20–30 μm were deposited by screen printing from a slurry composed of perovskite powder, iso-

propanol, polyvinyl butyral, and triethylene glycol dimethacrylate. The firing process was carried out at 1050 °C (for PSFC-3020) to optimize adhesion to the electrolyte and minimize the formation of secondary phases.

Impedance measurements were conducted in the frequency range of 0.1 Hz to 1 MHz with an amplitude of 10 mV in air at 600–900 °C, using 50 °C increments. By combining thermomechanical, electrical transport, and electrochemical characterization with an analysis of the cationic ionic parameters, it was possible to establish a balance between structural stability, high electrical conductivity, and low polarization resistance. Among the investigated compositions, PSFC-2020, PSFC-3020, and PSFC-4020 demonstrated the most promising performance as cathode materials for RSOFCs when paired with YSZ and GDC electrolytes.

Figure 1 illustrates the variation of the linear thermal expansion coefficient (CTE, α) in the low-temperature region for the $Pr_{1-x}Sr_xFe_{1-\gamma}Co_\gamma O_{3-\delta}$ (PSFC-x20) series with different molar fractions of Sr ($x = 0$–0.4), as well as for the specific composition $Pr_{0.7}Sr_{0.3}Fe_{0.5}Co_{0.5}O_{3-\delta}$ (PSFC-3050).

The PSFC-x20 curve exhibits a distinctly nonlinear behavior. In the range $0 < x \leq 0.1$, a slight increase in α is observed, followed by a decrease at $x = 0.2$ and 0.3. The lowest CTE values are recorded at $x = 0.3$, indicating an optimal balance between lattice parameters and defect concentration in this compositional region. With further Sr substitution up to $x = 0.4$, a sharp rise in α occurs.

This behavior can be explained by the competition of two mechanisms:

– the enhancement of the ionic character of the A–O bond when Pr^{3+} ($\chi = 1.13$) is substituted with the less electronegative Sr^{2+} ($\chi = 0.99$) increases lattice rigidity and reduces its tendency toward thermal expansion.

– at the same time, the growth in oxygen vacancy concentration, required for charge compensation upon Sr^{2+} incorporation, weakens interstitial bonding and promotes higher CTE values.

For compositions with $x \leq 0.3$, the first mechanism dominates, resulting in a reduction of α, whereas for $x > 0.3$ the second mechanism prevails, leading to an increase.

The specific composition PSFC-3050, which contains a higher Co fraction ($y = 0.5$), exhibits a markedly higher CTE compared with PSFC-3020 at the same Sr content ($x = 0.3$). This behavior is consistent with the well-documented effect of spin-state transitions of Co^{3+} upon heating, which are accompanied by the elongation of Co–O bonds and, consequently, an increase in thermal expansion.
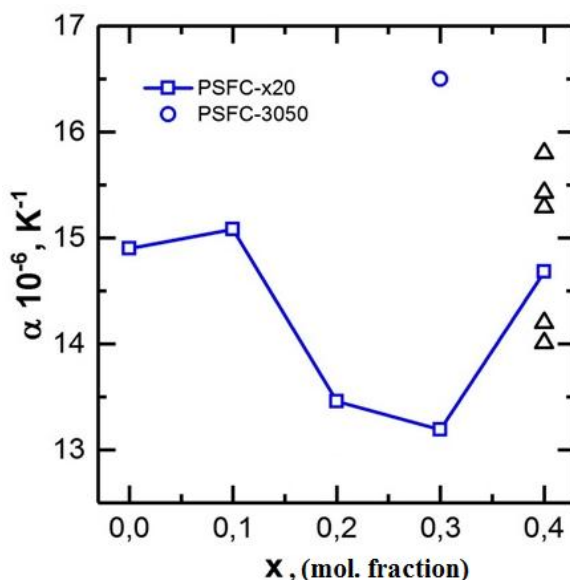
Figure 1. Dependence of the linear thermal expansion coefficient (α) of $Pr_{1-x}Sr_xFe_{1-\gamma}Co_\gamma O_{3-\delta}$ and $Pr_{0.7}Sr_{0.3}Fe_{0.5}Co_{0.5}O_{3-\delta}$ compositions on Sr molar fraction (x) in the low-temperature range

From the standpoint of minimizing the CTE and achieving better thermomechanical compatibility with solid electrolytes (YSZ and GDC), the most promising compositions are those with moderate Sr content ($x = 0.2$–0.3) and reduced Co content, particularly PSFC-2020 and PSFC-3020.

Figure 2 presents the temperature dependence of the electrical conductivity (σ) for a series of perovskite compositions with varying Sr and Co contents in the range of 350–950 °C.

For the PFC-20 composition ($x = 0$, $y = 0.2$), which does not contain Sr, an exponential increase in conductivity with temperature was recorded, showing no indication of saturation-behavior typical of thermally activated charge transport. A similar trend is observed for PSFC-1020 ($x = 0.1$, $y = 0.2$), though at a noticeably higher conductivity level. This enhancement is attributed to the effect of Sr^{2+}, which promotes the formation of oxygen vacancies and increases the concentration of mobile charge carriers.

Compositions with higher Sr contents ($x = 0.2$–0.4) exhibit nontrivial temperature-dependent behavior: in the conductivity curves of PSFC-2020, PSFC-3020, PSFC-4020, and particularly PSFC-3050, a distinct maximum is observed, followed by a decline at elevated temperatures. Such behavior is characteristic of mixed-conducting oxides, where increasing temperature enhances oxygen release. The resulting oxygen loss reduces the concentration of hole carriers (e.g., Fe^{4+}), thereby disturbing the balance between ionic and electronic conductivity.

The temperatures corresponding to the conductivity maxima (T_{max}) systematically shift toward lower values with increasing Sr content. This trend reflects the role of oxide non-stoichiometry: higher Sr^{2+} concentrations accelerate the generation of oxygen vacancies, lowering the lattice stability against thermal degradation. At the same time, varying the Co fraction for instance, in PSFC-3050 with $y = 0.5$ leads to a significant increase in the absolute conductivity values, while exerting only a minor effect on the position of T_{max}.
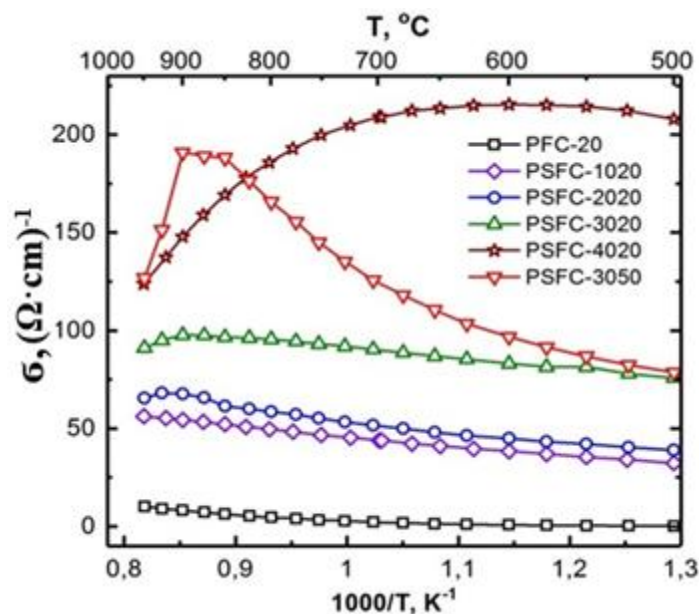
Figure 2. Dependence of the linear thermal expansion coefficient (α)
of temperature-dependent electrical conductivity of $Pr_{1-x}Sr_xFe_{1-\gamma}Co_\gamma O_{3-\delta}$

The coincidence of T_{max} with the inflection points in the CTE curves—as demonstrated earlier—highlights the close relationship between the electrophysical and structural properties of the investigated materials. Among the studied compositions, PSFC-2020 and PSFC-3020 exhibit the most stable conductivity within the operating temperature range, maintaining a balance between sufficient mobile carrier concentration and resistance to oxygen-related degradation. These materials are therefore particularly promising for cathode applications in RSOFCs operating under high-temperature conditions.

Of particular interest is the PSFC-3050 composition, which exhibits an anomalous temperature dependence of conductivity. This behavior necessitated the calculation of two distinct activation energy values: 16.0 kJ·mol^{-1} in the 300–600 °C range and 30.5 kJ·mol^{-1} in the 600–850 °C range. Such a distinction suggests a change in the dominant charge-transport mechanisms across different temperature intervals.

The polarization resistance values also clearly highlight the advantage of Sr-rich compositions. The lowest Rη values (1.9–2.5 Ω·cm^2) were recorded for PSFC-2020, PSFC-3020, and PSFC-4020, indicating high-quality cathode/electrolyte interfaces and reduced losses associated with electrode reactions.

Thus, the most promising candidates for application as dense cathodes in RSOFCs are PSFC-4020 and PSFC-3050, which combine high electrical conductivity, reduced polarization resistance, and acceptable thermal stability.

21

Figure 3 illustrates the dependence of the polarization resistance (Rη) of the PSFC-3020 cathode material on the sintering temperature applied to bond it with the YSZ solid electrolyte, measured at an operating temperature of 850 °C. The results clearly show that the polarization resistance reaches its minimum when sintering is carried out at 1050 °C.
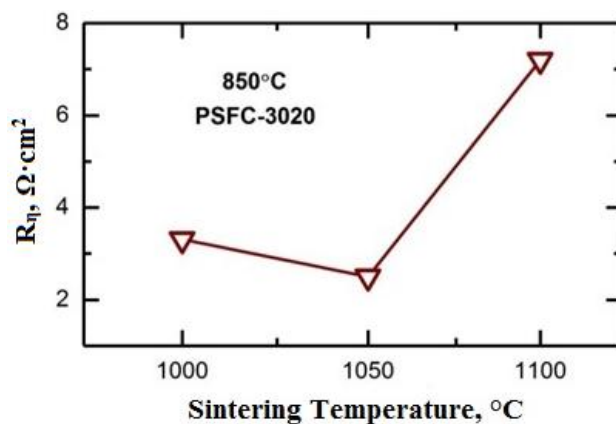
Figure 3. Influence of the sintering temperature on the polarization resistance
of the PSFC-3020 cathode in contact with a YSZ electrolyte

Figure 4 presents the dependencies of electrical conductivity (σ) and polarization resistance (Rη) for cathode materials of the composition $Pr_{1-x}Sr_xFe_{0.8}Co_{0.2}O_{3-\delta}$ as a function of the Sr molar fraction (x) at 850 °C.
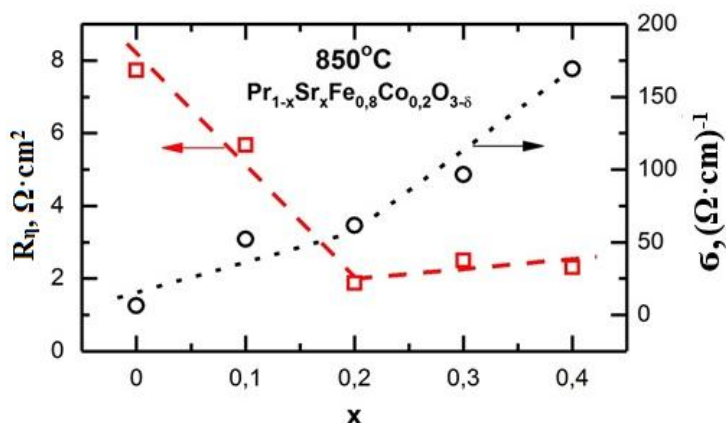
Figure 4. Effect of Sr Content on the Electrical Conductivity and Polarization Resistance
of $Pr_{1-x}Sr_xFe_{0.8}Co_{0.2}O_{3-\delta}$ Cathodes at 850 °C

Up to $x = 0.2$, a clear correlation is observed between the two parameters: as electrical conductivity increases, polarization resistance decreases significantly. This relationship indicates improved kinetics of oxygen electrochemical processes, driven by a higher density of charge carriers and enhanced interfacial charge transfer.

However, for $x > 0.2$, the trend changes: despite the continued rise in electrical conductivity, polarization resistance begins to increase. This discrepancy is most likely associated with chemical interactions between Sr-enriched cathodes and the YSZ electrolyte during thermal treatment, leading to the formation of low-conductivity secondary phases at the electrode/electrolyte interface. This effect is particularly pronounced in the PSFC-3050 sample, which exhibits high Rη despite its relatively high σ, supporting the above interpretation.

Therefore, the optimal balance between high electrical conductivity and low polarization resistance is achieved at Sr concentrations in the range of 0.2–0.3 molar fraction. Within this composition window, PSFC-2020, PSFC-3020, and PSFC-4020 show the most favorable electrochemical performance among the studied materials.

Conclusion

This work presents an in-depth study of the structural, electrical, and electrochemical characteristics of perovskite-type cathode materials based on $Pr_{1-x}Sr_xFe_{0.8}Co_{0.2}O_{3-\delta}$, synthesized via a self-propagating high-temperature synthesis route. By systematically varying the Sr and Co content, a series of compositions was prepared and thoroughly evaluated in terms of thermal expansion behavior, electrical conductivity, and polarization resistance under conditions relevant to reversible solid oxide fuel cells (RSOFCs).

It was shown that moderate strontium substitution ($x = 0.2$–0.3) leads to improved electrochemical performance due to enhanced oxygen vacancy concentration and optimized lattice parameters, which facilitate effective charge transport. The incorporation of cobalt further promotes electronic conductivity and structural flexibility, though excessive Co levels (e.g., in PSFC-3050) were found to negatively impact polarization resistance, likely due to undesirable interfacial phase formation with the YSZ electrolyte.

Among the studied compositions, PSFC-2020, PSFC-3020, and PSFC-4020 demonstrated a balanced combination of high electrical conductivity (up to ~186 S·cm^{-1} at 800 °C) and low polarization resistance (as low as 1.9 Ω·cm^2 at 850 °C), along with favorable thermal compatibility with common electrolytes. Notably, PSFC-3020 exhibited optimal performance at a sintering temperature of 1050 °C, minimizing interfacial degradation and ensuring good adhesion to the YSZ substrate.

These findings confirm that tailored A-site (Sr) and B-site (Co) substitution within the Pr-based perovskite structure enables precise control over the functional properties of cathode materials. The study highlights the potential of PSFC-type materials as high-performance cathodes for advanced RSOFCs systems, offering improved energy efficiency, electrochemical stability, and long-term durability.

Acknowledgment

References

1   Minh, N. & Williams, M. C. (2015). Electrolysis operating mode for reversible solid oxide fuel cells. *ECS Transactions, 68*(1), 3301–3305. https://doi.org/10.1149/06801.3301ecst

2   Yoon, K.J., Lee, S., Park, S.-Y., & Minh, N.Q. (2025). Advances in high-temperature solid oxide electrolysis technology for clean hydrogen and chemical production: Materials, cells, stacks, systems and economics. *Progress in Materials Science, 154*, 101520. https://doi.org/10.1016/j.pmatsci.2025.101520

3   Liang, Z., Wang, J., Ren, K., & Jiao, Z. (2024). Discovering two general characteristic times of transient responses in solid oxide cells. *Nature Communications, 15*(1), 4587. https://doi.org/10.1038/s41467-024-48785-1

4   Yerofeev, V., Goncharova, M., Smirnov, V., Rodin, A., & Volkov, A. (2025). Bio-resistant cement composites with active mineral additive. *International Journal for Computational Civil and Structural Engineering, 21*(3), 33–40. https://doi.org/10.22337/2587-9618-2025-21-3-33-40

5   Güneş, F. & Korkmaz, T. (2025). Comparison of the mechanical properties of polyetheretherketone and polyphenylenesulfone produced by fused filament fabrication and conventional manufacturing methods for dental applications: An in vitro study. *BMC Oral Health, 25*, 1455. https://doi.org/10.1186/s12903-025-06851-0

6   Zhang, Z., Wang, X., & Yan, Y. (2021). A review of the state-of-the-art in electronic cooling. *e-Prime Advances in Electrical Engineering, Electronics and Energy, 1*, 100009. https://doi.org/10.1016/j.prime.2021.100009

7   Zheng, H., Li, W., Ma, S., Li, Z., Chen, Z., Zhang, L., Hu, J., & Liu, T. (2025). Perovskite oxides for electrocatalytic nitrogen/carbon fixation. *Chemical Science.* Advance Article. https://doi.org/10.1039/D5SC05965H

8   Assirey, E.A. (2019). Perovskite synthesis, properties and their related biochemical and industrial application. *Saudi Pharmaceutical Journal, 27*(6), 817–829. https://doi.org/10.1016/j.jsps.2019.05.003

9   Wang, J., Chao, G., Zong, W., Chu, K., Zhu, J., Chen, R., Zheng, Y., Zhang, L., & Liu, T. (2024). Efficient nitrate electroreduction to ammonia over copper catalysts supported on electron-delocalized covalent organic frameworks. *Chemical Engineering Journal, 499*, 156343. https://doi.org/10.1016/j.cej.2024.156343

10   Mirza, M., Abdulaziz, R., Maskell, W. C., Wilcock, S., Jones, A. H., Woodall, S., Jackson, A., Shearing, P.R., & Brett, D.J.L. (2023). Electrochemical processing in molten salts — a nuclear perspective. *Energy & Environmental Science, 16*, 952–982. https://doi.org/10.1039/D2EE02010F

11   Zong, S., Zhao, X., Jewell, L.L., Zhang, Y., & Liu, X. (2024). Advances and challenges with SOEC high temperature co-electrolysis of CO_2/H_2O: Materials development and technological design. *Carbon Capture Science & Technology, 12*, 100234. https://doi.org/10.1016/j.ccst.2024.100234

12 Franco, A. (2025). Green hydrogen and the energy transition: Hopes, challenges, and realistic opportunities. *Hydrogen, 6*(2), 28. https://doi.org/10.3390/hydrogen6020028

13 Nikolaev, K.G., Wu, J., Leng, X., Vazquez, R.J., McCuskey, S.R., Bazan, G.C., Novoselov, K.S., & Andreeva, D.V. (2025). A single-material strategy: Graphene sponge bioanode and cathode for Shewanellaoneidensis MR-1 microbial fuel cells. *RSC Sustainability*. Advance online publication. https://doi.org/10.1039/D5SU00629E

14 Wang, X., Zhang, Y., Zhang, H., & Han, M. (2024). Mechanism analysis of the reduction process of the NiO–YSZ anode of a solid oxide fuel cell by hydrogen. *Journal of The Electrochemical Society, 171*(9), 091501. https://doi.org/10.1149/1945-7111/ad1649.

15 Bekmyrza, K.Zh., Kuterbekov, K.A., Kabyshev, A.M., Kubenova, M.M., Baratova, A.A., Aidarbekov, N., Chaka, M.D., & Benti, N.E. (2025). High-performance hydrogen energy generation via innovative metal-organic framework catalysts and integrated system design. *Scientific Reports, 15*, 28418. https://doi.org/10.1038/s41598-025-08306-6

16 Kuterbekov, K.A., Bekmyrza, K.Zh., Kabyshev, A.M., Kubenova, M.M., Aidarbekov, N.K., & Nurkenov, S.A. (2022). Investigation of the Characteristics of Materials with the Ruddlesden-Popper Structure for Solid Oxide Fuel Cells. *Bulletin of the University of Karaganda — Physics, 108*(4), 32–47. https://doi.org/10.31489/2022ph4/32-47.

17 Nikonov, A.V., Pavzderin, N.B., Khrustov, V.R., Semenova, I.V., Demidova, K.I., Kuterbekov, K.A., Bekmyrza, K.Zh., Nurakov, S.N., Koketay, T.A., & Gyrdasova, O.I. (2021). Investigation of thermal, electrical, and electrochemical properties of $Pr_{1-y}Sr_xFe_{1-y}Co_yO_3$ $(0 < x < 0.4;$ $y = 0.2,$ $0.5)$ cathode materials for SOFC. *Journal of Alloys and Compounds, 865*, 158898, https://doi.org/10.1016/j.jallcom.2021.158898.

18 Rakhadilov, B.K., Berdimuratov, N.E., Zhurerova, L.G., Bayatanova, L.B., Kurbanbekov, Sh.R., & Satbayeva, Z.A. (2023). Study of the VAC of the EPCTT process with varying electrode parameters. *Bulletin of the University of Karaganda — Physics, 111*(3), 13632–142.https://doi.org/10.31489/2023ph3/136-142.

19 Li, X., Li, Y., Ren, L., Zhu, K., Zhao, Y., & Yuan, X.-Y. (2017). Self-crosslinking coatings of fluorinated polysiloxanes with enhanced icephobicity. *Thin Solid Films, 638*, 383–390. https://doi.org/10.1016/j.tsf.2017.08.034

20 Zhi, J.H., Zhang, L., Yan, Y.Y., & Zhu, J. (2017). Mechanical durability of superhydrophobic surfaces: The role of surface modification technologies. *Applied Surface Science, 389*, 7–24. https://doi.org/10.1016/j.apsusc.2016.09.049

Г.А. Бакалбаева, А.А. Баратова, Н.К. Айдарбеков,
М.М. Кубенова, А.Н. Амангожаева, Р.С. Бисекен

$Pr_{1-x}Sr_xFe_{1-\gamma}Co_\gamma O_{3-\delta}$ негізіндегі перовскит катодтарының функционалдық қасиеттерін реверсивті қатты оксидті отын элементтері үшін зерттеу

$Pr_{1-x}Sr_xFe_{1-\gamma}Co_\gamma O_{3-\delta}$ құрамындағы перовскиттік катодты материалдардың функционалдық қасиеттері өздігінен таралатын жоғары температуралық синтез әдісі арқылы зерттелді. Зерттеудің негізгі мақсаты — реверсивті қатты оксидті отын элементтерінде (RSOFCs) олардың жұмыс тиімділігін арттыру. Sr және Co изоморфтық орын басуының жылулық ұлғаю коэффициентіне, электрөткізгіштікке және поляризациялық кедергіге әсері қарастырылды. Дилатометриялық талдау, төрт-зондты өлшеу әдісі және электрхимиялық импеданс спектроскопия нәтижелері Sr-дың орташа мөлшері ($x = 0.2$–0.3) ең тиімді теңгерімді қамтамасыз ететінін көрсетті: құрылымдық тұрақтылық сақталады, оттектік вакансиялардың концентрациясы артады және тор параметрлері оңтайланады. Бұл факторлар жоғары электрөткізгіштікке және төмен поляризациялық кедергіге қол жеткізуге мүмкіндік береді. Кобальт қосудың электрондық тасымалдауды күшейтетіні анықталды, алайда оның шамадан тыс мөлшері ($y = 0.5$) жылулық ұлғаю коэффициентін жоғарылатып, электролитпен әрекеттесудің нәтижесінде интерфазалық кедергіні арттырады. Зерттелген үлгілер ішінде PSFC-2020, PSFC-3020 және PSFC-4020 ең жоғары электрхимиялық сипаттамаларды көрсетті: электрөткізгіштік шамамен ~186 S·см$^{-1}$ және поляризациялық кедергі 1.9 Ом·см^2-қа дейін төмен 850 °C температурада. Бұл нәтижелер Pr–Sr–Fe–Co негізіндегі перовскиттердің жоғары термомеханикалық үйлесімділігімен, тиімді заряд тасымалдауымен және ұзақ мерзімді тұрақтылығымен RSOFCs катодтары ретінде перспективалы екенін дәлелдейді.

Кілт сөздер: реверсивті қатты оксидті отын элементтері (RSOFCs), перовскит катодтары, Pr–Sr–Fe–Co оксидтері, жылулық ұлғаю, электрөткізгіштік, поляризациялық кедергі, электрхимиялық өнімділік

Г.А. Бакалбаева, А.А. Баратова, Н. К. Айдарбеков,
М.М. Кубенова, А.Н. Амангожаева, Р.С. Бисекен

Исследование функциональных свойств перовскитных катодов $Pr_{1-x}Sr_xFe_{1-\gamma}Co_\gamma O_{3-\delta}$ для реверсивных твёрдооксидных топливных элементов

Проведено комплексное исследование перовскитных катодных материалов состава $Pr_{1-x}Sr_xFe_{1-\gamma}Co_\gamma O_{3-\delta}$, синтезированных методом самораспространяющегося высокотемпературного синтеза, с целью оптимизации их эксплуатационных характеристик в реверсивных твёрдооксидных топливных элементах (RSOFCs). Особое внимание уделялось влиянию замещения Pr стронцием и кобальтом на коэффициент теплового расширения, электропроводность и поляризационное сопротивление в условиях работы элемента. Дилатометрические исследования, измерения проводимости четырёхзондовым методом и электрохимическая импедансная спектроскопия показали, что умеренное содержание Sr ($x = 0.2$–0.3) обеспечивает оптимальное сочетание структурной стабильности, высокой концентрации кислородных вакансий и благоприятных параметров решётки. Эти факторы способствуют росту электропроводности при сохранении низкого поляризационного сопротивления. Введение кобальта усиливает электронный транспорт, однако его избыточное количество (например, $y = 0.5$) вызывает рост коэффициента теплового расширения и увеличение межфазного сопротивления вследствие взаимодействия с электролитом. Наилучшие электрохимические характеристики продемонстрировали составы PSFC-2020, PSFC-3020 и PSFC-4020, обеспечившие проводимость до ~186 $S \cdot см^{-1}$ и поляризационное сопротивление не более 1.9 $Ом \cdot см^2$ при 850 C. Полученные результаты подтверждают перспективность перовскитов Pr–Sr–Fe–Co в качестве эффективных катодов для RSOFCs благодаря их высокой термомеханической совместимости, улучшенной проводимости и долговечности.

Ключевые слова: реверсивные твёрдооксидные топливные элементы (RSOFCs), перовскитные катоды, оксиды Pr–Sr–Fe–Co, тепловое расширение, электропроводность, поляризационное сопротивление, электрохимическая эффективность

Information about the authors

Bakalbayeva, Gulshat — Researcher of the scientific and technical program of the Caspian University of Technology and Engineering named after Sh. Yessenov, Aktau, Kazakhstan; PhD student, L.N. Gumilyov Eurasian National University, Astana, Kazakhstan; e-mail: bakalbayaeva_ga@enu.kz

Baratova, Aliya (*corresponding author*) — Leading researcher of the scientific and technical program of the Caspian university of Technology and Engineering named after Sh. Yessenov, Aktau, Kazakhstan; Candidate of Physical and Mathematical Sciences, Associate Professor, L.N. Gumilyov Eurasian National University, Astana, Kazakhstan; SCOPUS Author ID 55221822500; ORCID ID: 0000-0002-7015-3657; e-mail: baratova_aa@enu.kz

Aidarbekov, Nursultan — Leading researcher of the scientific and technical program of the Caspian university of Technology and Engineering named after Sh. Yessenov, Aktau, Kazakhstan; PhD, Senior Teacher, L.N. Gumilyov Eurasian National University, Astana, Kazakhstan; SCOPUS Author ID: 57222254501; ORCID ID 0000-0002-1981-5416; e-mail: nursultan02_22.10.92@mail.ru

Kubenova, Marzhan — Leading researcher of the scientific and technical program of the Caspian university of Technology and Engineering named after Sh. Yessenov, Aktau, Kazakhstan; PhD, teacher-researcher, L.N. Gumilyov Eurasian National University, Astana, Kazakhstan; SCOPUS Author ID 57197744698; ORCID ID: 0000-0002-7015-3657; e-mail: kubenova_mm_1@enu.kz

Amangozhayeva Arailym — Master student, L.N. Gumilyov Eurasian National University, Astana, Kazakhstan; e-mail: Arai.86-33@mail.ru

Bisseken, Rizabek — Student of 4th course, L.N. Gumilyov Eurasian National University, Astana, Kazakhstan; e-mail: rizabekbisekenov@gmail.ru

ТЕХНИКАЛЫҚ ФИЗИКА
ТЕХНИЧЕСКАЯ ФИЗИКА
TECHNICAL PHYSICS

I.I. Sadikov[1], T.B. Fayziyev[1], S.A. Baytelesov[1], F.R. Kungurov[1],
Sh.A. Alikulov[1], D.P. Tadjibaev[1], D.E. Uskenbaev[2✉], A.S. Kudussov[3]

[1]Institute of Nuclear Physics of Uzbekistan Academy of Sciences, Ulugbek, Tashkent, Uzbekistan;
[2]S. Seifullin Kazakh Agrotechnical Research University, Astana, Kazakhstan;
[3]Buketov Karaganda National Research University, Karaganda, Kazakhstan

Determination of the Neutron Fluxes Energy Spectrum
of the WWR-SM Reactor of the INP AS RU

The article presents the results of analyzing the energy spectrum and spatial distribution of neutrons in the core of the WWR-SM (Water-Water Reactor, Serially Modernized) research reactor after switching to low-enriched fuel (19.75 % ^{235}U). The increase in the number of fuel assemblies (FAs) from 18 to 24 altered the neutron characteristics of the reactor. A combination of computational methods (IRT-2D and WIMS codes) and experimental data obtained from neutron activation analysis enabled a detailed study of flux distribution. Fast neutrons dominate in the central part of the core, while the proportion of thermal neutrons increases significantly in the beryllium reflectors. Measurements showed that in vertical channels, the thermal neutron flux density is 2.3 times higher than that of fast neutrons. In horizontal experimental channels, values up to $1.8 \cdot 10^{12}$ neutrons/(cm^2·s) with a cadmium ratio of 28 were recorded, confirming their suitability for research. Analysis of the thermal power of FAs revealed its maximum values in the center of the core with a gradual decrease toward the periphery, correlating with the ^{235}U burnup distribution. The obtained results have practical significance for optimizing fuel loading, planning refueling campaigns, and testing prospective fuel compositions (UO$_2$+Al, U$_3$Si$_2$+Al). The study emphasizes the need for further verification of computational models and more detailed investigation of neutron spectra under various core configurations. The presented data contribute to enhancing the efficiency and safety of WWR-SM reactor operation while expanding its research potential in nuclear physics and materials science.

Keywords: nuclear fuel, energy spectrum, fast neutrons, thermal neutrons, reactor core, neutron activation analysis, WWR-SM reactor, fuel burnup

✉*Corresponding authors*: Uskenbaev Daniyar, usdan@mail.ru

Introduction

In the field of research related to radiation: processes of interaction of radiation with matter [1–3], processes of material production using radiation of different spectral composition [4–7], and others are widely applied and studied. In this area, the processes related to radiation in nuclear reactors are of particular interest. In the core of a research reactor, the energy spectrum of radiation (neutrons) is a key characteristic that determines the efficiency and safety of nuclear experiments.

The energy spectrum of neutrons in the core of a research reactor is a key characteristic that determines the effectiveness and safety of nuclear experiments.

Knowledge of the spectrum is necessary for accurate planning of neutron physics studies, assessment of fuel burnout, dose loads on materials, and accuracy of activation analysis [8–10].

Classification of neutron spectra.

In research reactors operating primarily with thermal neutrons, the spectrum is conventionally divided into three regions [10, 11]:

Thermal range ($E < 0.5$ eV);

Epithermal region (0.5 eV $< E < 100$ keV);

Fast range ($E > 100$ keV).

Methods for determining the neutron spectrum.

Experimental methods:

Activation methods using standard foils (Au, Mn, Co, etc.) [12];

The method of responses and convolution [13];

The TOF (time-of-flight) method [14].

Calculation methods:

Montecarlo programs: MCNP, SERPENT [15];

Deterministic codes: WIMS, DRAGON, IRT-2D [16–18];

The use of ENDF/B-VII, JENDL, JEFF, and others nuclear data libraries [19].

The features of the spectrum in research reactors are determined by the moderator, reflector and configuration of the core. In the VVR-SM reactor, for example, there is a pronounced predominance of thermal neutrons in the central core zone and an increase in the proportion of fast neutrons in the periphery [20]. The spectra significantly depend on the degree of fuel burnout and loading of experimental devices [21].

Application of spectral analysis data:

Calculation of reactivity and fuel burnout [22];

Planning of radiation testing of materials [23];

Preparation of macroscopic constants [24];

Activation analysis and isotope production [25].

The WWR-SM research reactor is a key facility for fundamental and applied research in nuclear physics. Since 2009, the reactor has been using low-enriched IRT-4M fuel (19.75 % uranium-235) with a uranium concentration of 2.8 g/cm³ [26]. In the near future, it is planned to test new types of fuel: UO_2+Al (3.3 g/cm³) and U_3Si_2+Al (3.6 g/cm³) [27], which requires a detailed study of the neutron-physical characteristics of the core. Previously, studies of neutron fluxes in WWR-type reactors were carried out in works [28–30], where methods for calculating and measuring neutron spectra were developed. However, for the WWR-SM reactor with its unique core configuration and beryllium reflectors, such studies require updating. This work uses modern calculation methods, including the IRT-2D code and the ASTRA program [31], as well as neutron activation analysis to verify the results [32].

The purpose of the work is to determine the energy spectrum of neutron fluxes, the distribution of neutron density in the core and channels of the reactor, and to analyze the thermal power of the FA. The data obtained will help optimize the operation of the reactor and prepare for the use of new types of fuel.

The analysis of the neutron energy spectrum is a fundamental part of neutron physics calculations. Combining experimental data with numerical simulation results provides the most accurate representation of neutron fields in the core and contributes to improving the reliability and efficiency of nuclear installations.

Calculations of neutron fluxes in vertical channels

The IRT-2D code was used to calculate the neutron flux density distribution in the WWR-SM reactor core. Two-group macroscopic cross-sections for each FA obtained using the WIMS code [33] were used.

The reactor core is loaded with 24 FAs with different degrees of uranium-235 burnup. Fresh FAs with minimal burnups are located in the central part of the core, and fuel assemblies with high burnups are located on the periphery. Beryllium reflectors are placed around the 24 FAs.

Figure 1 shows the results of calculating the distribution of thermal and fast neutron fluxes in the core of the WWR-SM research reactor.
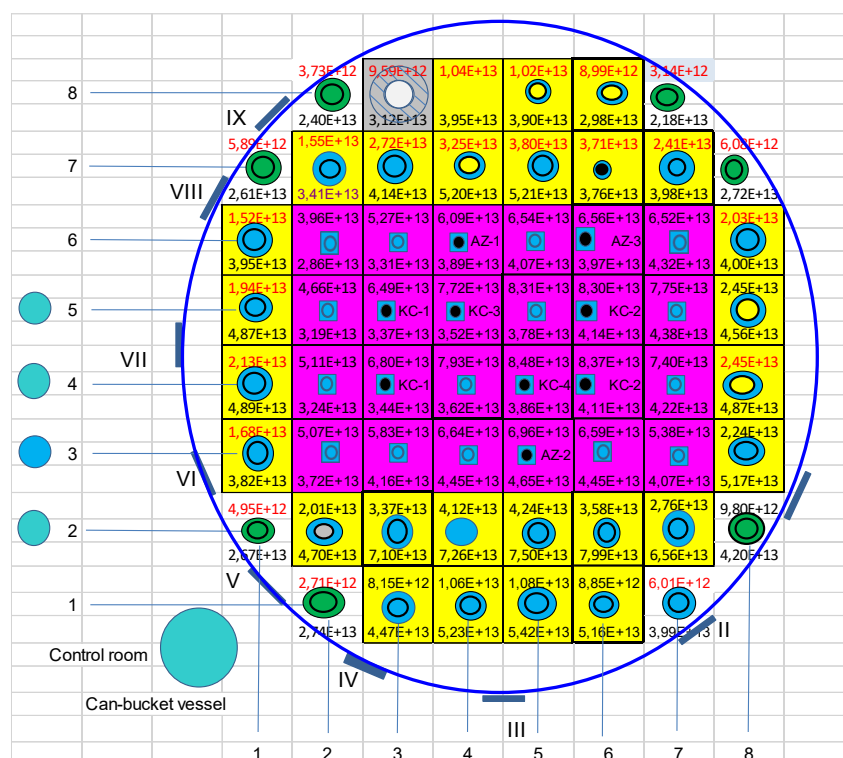
Figure 1. Distribution of thermal and fast neutron fluxes in the WWR-SM research reactor's core.
The upper row in red shows the results of calculations of fast neutron fluxes with energy $E > 0.1$ MeV,
and the lower row shows the results of calculations of thermal neutron fluxes with energy $E < 0.625$ MeV

Figures 2 and 3 show the distribution of fast and thermal neutron fluxes in the WWR-SM reactor core. As can be seen from the figures, in the center of the core, where the FAs are located, there is an increase in the number of fast neutrons, which is 2 times greater than the number of thermal neutrons. On the periphery of the core, where the beryllium reflectors are located, the number of thermal neutrons exceeds the number of fast neutrons. It is also clear that the thermal neutron flux density is greater where 6FAs are located in series (column index), compared to the section where 4 FAs are located in a row (row index).
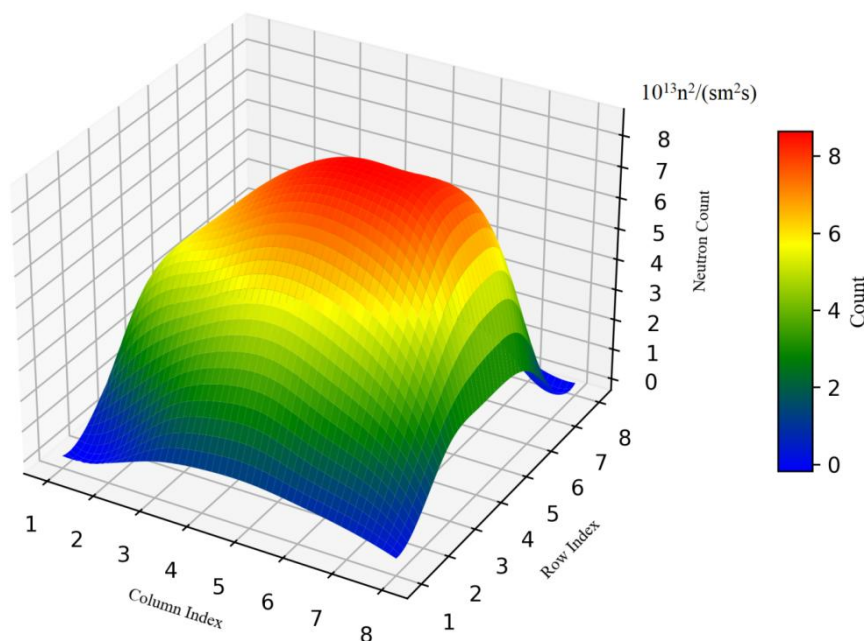
Figure 2. Distribution of fast neutron flux in the WWR-SM reactor's core
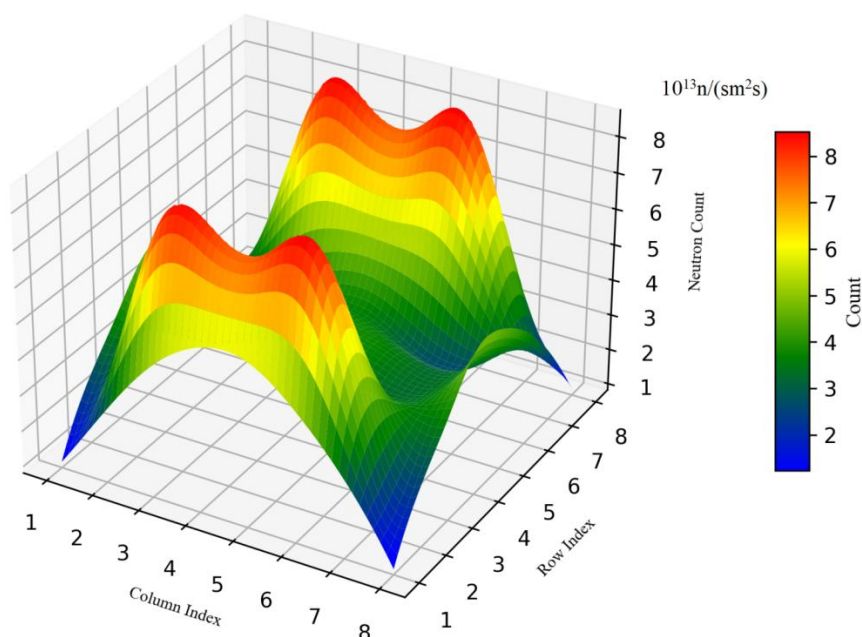
Figure 3. Distribution of thermal neutron flux in the WWR-SM reactor's core

Measurement of neutron fluxes in the core and vertical channels

The measurement of the neutron flux density in the core and in the beryllium reflector of the WWR-SM reactor was carried out using the well-known method of neutron activation analysis of samples (foils) introduced into the neutron flux. The activity of the irradiated sample was determined by the formula

$$A_0 = 1.628 * 10^{-15} \Phi \sigma \textit{мp} \left(1 - \exp\left(\frac{-0.693t}{T} \right) \right) * \exp\left(\frac{-0.693t_1}{T} \right) A^{-1}, \tag{1}$$

where Φ — neutron flux, neutron/(cm^2*s); σ — activation cross section, mbarn; $\textit{м}$ — weight of activated sample, mg; p — isotope abundance, %; A — atomic weight of the irradiated isotope; T — half-life of the product isotope, seconds; t, t_1 — irradiation time and cooling time (in the same units as T), seconds.

And was measured using a GC1020 germanium detector with a diameter of 46 mm, a length of 29 mm and an efficiency of 10 % with a GENIE 2000 spectrometric system from CANBERRA. The spectrometer resolution for the ^{60}Co γ-radiation line $E\gamma = 1332$ keV was 1.8 keV, and the calibration accuracy in the 0–1500 keV γ-radiation energy range was ±2 keV.

In measurements of the thermal neutron flux in the channels of the WWR-SM reactor, an aluminum-cobalt alloy containing 0.1 % ^{59}Co with a mass of 2 mg was used as a sample. A comparison of the results of measurements and calculations of the thermal neutron flux density for different vertical channels is presented in Table 1.

T a b l e 1

Thermal neutron flux densities in the WWR-SM reactor core

Channel number according to Fig. 2	Monitor weight, mg	Result of measurements of thermal neutron flux density, (10^{13} n/cm2 s)	Calculation result of thermal neutron flux density, (10^{13} n/cm2 s)
2-4	2.1	7.41	7.26
2-5	2.3	7.62	7.50
3-1	2.8	3.9	3.82
3-8	3.3	5.28	5.17
4-1	2.4	5.07	4.89
5-1	2.2	4.92	4.87
6-8	3.0	4.19	4.00
7-1	2.5	2.69	2.61

Energy spectrum of neutrons in the WWR-SM reactor core

The energy spectrum of neutrons was calculated depending on their energy in the WWR-SM reactor core. Using a program written in PYTHON, the energy spectrum of neutrons was constructed on a logarithmic scale.

Figure 4 shows the energy spectrum of neutrons in the vertical channel 4-1 of the WWR-SM reactor. As can be seen from the figure, in the vertical channel 4-1, where the beryllium reflector is located, there are 2.3 times more thermal neutrons than fast neutrons. This is due to the fact that most neutrons are slowed down in distilled water, which is located in the gaps of the beryllium reflector.

As can be seen from Figure 5, the vertical channel 4-2 is located inside the fuel assembly in the reactor core, so the fast neutron flux density is 1.6 times greater than the thermal neutron flux density. This is due to the fact that during the fission of uranium-235, neutrons with an average energy of 2 MeV are born, and they do not have time to slow down inside the nuclear fuel.

The obtained neutron spectra are in good agreement with the results obtained at the VVR-K reactor [34].
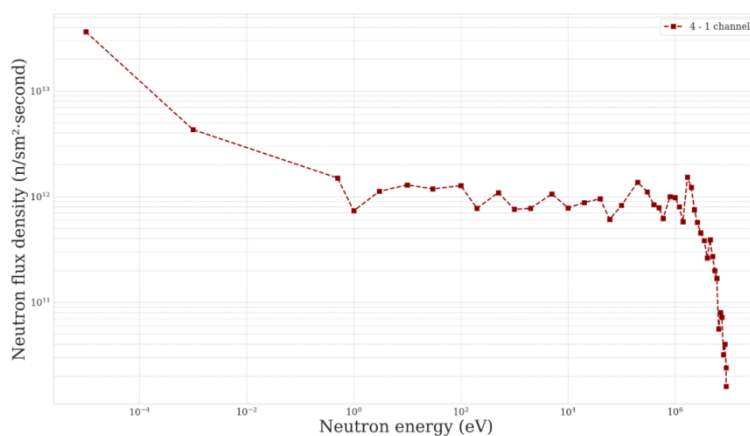
Figure 4. Neutron flux density depending on neutron energy in vertical channel 4-1 of the WWR-SM reactor

Figure 5 shows the neutron spectrum in channel 4-2.
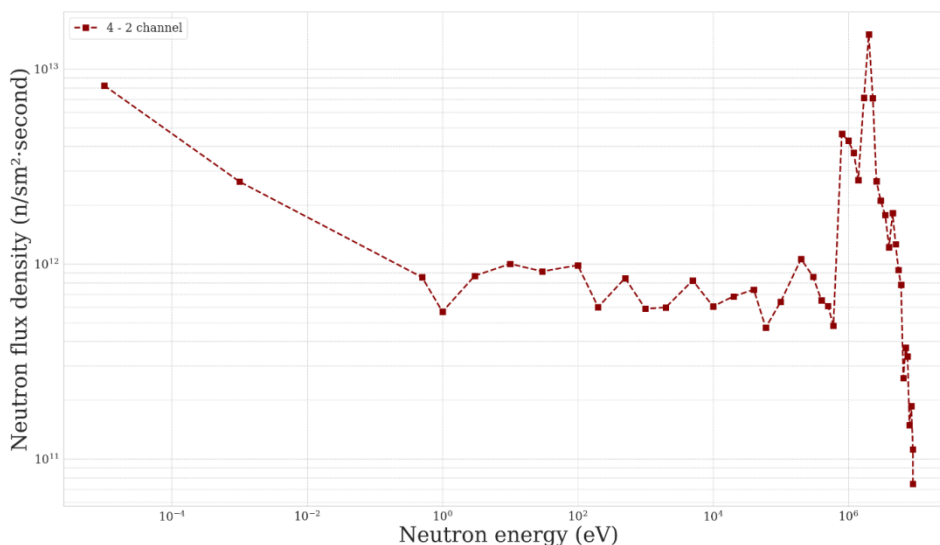
Figure 5. Neutron flux density depending on neutron energy in vertical channel 4-2 of the WWR-SM reactor

Measurement of neutron fluxes and cadmium ratio in the horizontal channel and thermal column

To determine the neutron flux values in the horizontal channel of the reactor, a mass spectrometric measurement technique was used. For this purpose, gold foils 10–20 μm thick and weighing 1–5 mg were placed in pairs in the mass spectrometer input arm near the bottom of the channel, in the middle, and at the output in the mass spectrometer. One of the gold foils in each pair was placed in a 0.5 mm thick cadmium case. Irradiation was carried out for 10 minutes, and then the samples were kept for 24 hours in the biological shield of the mass spectrometer. Before measuring the activity of the sample, the background NΦ of the set-up was measured. The exposure time was selected based on the condition of collecting sufficient statistics.

The measured number of N decays was determined by the formula

$$N = (N - N\Phi)\cdot n/(W\cdot S\cdot K\cdot Q\cdot \varepsilon), \tag{2}$$

where n — correction for the resolution of the installation; W — solid angle correction; S — attenuation adjustment; K — self-shielding correction; Q — backscatter correction; ε — efficiency of the measuring setup.

The resolving power R of the installation was determined by the formula:

$$R = \frac{1}{1 - 10^{-6}\,N}\,. \tag{3}$$

Here the following values were used: $n = 1.005$, $W = 0.95$, $\varepsilon = 1$, and due to the small thickness of the gold foils, corrections for backscattering, attenuation and self-shielding were neglected.

The measurements and calculations carried out showed that the thermal neutron flux inside the 6th horizontal channel is:

$$\Phi_T = 1{,}8\cdot 10^{12}\,n/(\text{cm}^2\ \text{s}) \pm 12\ \%. \tag{4}$$

Cadmium ratio:

$$R_{Cd} = 28 \pm 3. \tag{5}$$

At the exit of the channel:

$$\Phi_T = 1{,}1\cdot 10^{10}\,n/(\text{cm}^2\ \text{s}) \pm 12\ \%. \tag{6}$$

At the outlet of the thermal column:

$$\Phi_T = 1{,}3\cdot 10^{10}\,n/(\text{cm}^2\ \text{s}) \pm 12\ \%. \tag{7}$$

Calculation of the thermal power distribution of the IRT-4M type FA
in the WWR-SM reactor core

There are several types of application programs for calculating certain reactor parameters. One of them is the IRT-2D program, developed by the staff of the Kurchatov Institute of Atomic Energy of the Russian Academy of Sciences. Calculations according to this program are carried out in a 2-group approximation on a plane in two-dimensional geometry.

The IRT-2D program was used to calculate the thermal power for 24 IRT-4M fuel assemblies with different uranium-235 burnup values. The results of the IRT-2D program are in good agreement with the experimental data [9].

The results of calculations of power distribution in the active zone with 24 fuel assemblies (FA) are given in Table 2.

T a b l e 2

Results of calculations of thermal power for 24 cells of the WWR-SM reactor core

It is evident from the data presented in Table 2 that the maximum power is observed in the central section of the reactor core, and the minimum is at the edges of the core.

The center of the table shows the vertical channels inside the fuel assemblies (FA). The FAs with black circles in the center represent the emergency protection rods (AP-1, AP-2, AP-3) and the compensating rods (KS-1, KS-2, KS-3, KS-4).

The top row of cells in the table shows the fuel assembly power in percent, and the bottom row of cells shows the uranium-235 burnup in percent.

Conclusion

A comprehensive study of neutron fluxes in the WWR-SM research reactor core of the INP AS RU is carried out in this work. The main attention is paid to determining the energy spectrum of neutrons, their flux density distribution in vertical and horizontal channels, as well as the analysis of the influence of the core configuration on the neutron-physical characteristics of the reactor.

As a result of the analysis of the neutron flux distribution and its energy spectrum in the reactor core, the following was established:

The calculated and experimental data showed good agreement, which confirms the correctness of using the IRT-2D and WIMS codes for modeling neutron fluxes and thermal modes of the reactor.

It was found that the neutron fluxes distribution in the core depends on the location of the FAs and the fuel burnup degree: fast neutrons predominate in the central part, while the proportion of thermal neutrons increases in the beryllium reflectors.

Measurements in the vertical channels demonstrated that the thermal neutron flux density in the reflector zone exceeds that for fast neutrons by 2.3 times, which is due to the effective moderation of neutrons in water.

In the horizontal channels and the thermal column, thermal neutron flux values of up to $1.8 \cdot 10^{12}$ $n/(\text{cm}^2 \text{ s})$ with a cadmium ratio of $R_{Cd} = 28$ were recorded, which confirms the suitability of these channels for experiments.

The thermal power of the FA is maximum in the center of the core and decreases towards the periphery, which is consistent with the distribution of uranium-235 burnup.

The results obtained are of great practical importance for:

Optimization of fuel loading and planning of refuelling campaigns.

Efficient use of experimental reactor channels for applied and fundamental research.

Preparation for testing new types of fuel (UO_2+Al, U_3Si_2+Al) with increased uranium concentration.

Further research prospects may include:

In-depth study of neutron spectra for various core configurations.

Verification of calculation models for new types of fuel.

Development of methods for improving the accuracy of neutron flux measurements in reactor channels.

Thus, the work carried out confirms the uneven distribution of neutron flux and power in the WWR-SM reactor core, which must be taken into account when operating reactor installations to ensure their efficient and safe operation.

References

1   Islamov, A.K., Ibragimova, E.M., Kudratov, K.N., Khayitov, I.A., & Vildanov, R.R. (2023). Effects of fast neutrons and gamma components on color centers and activator glow in Lu_2SiO_5:Ce scintillator crystals. *Optical Materials, 145*, 114459.

2   Alikulov, Sh.A., Baytelesov, S.A., Kungurov, F.R., Sadikov, I.I., Tojiboev, D.D., Shaimerdenov, A.A., Nogai, A.S., & Uskenbaev, D.E. (2024). Electrical conductivity of GMZ grade graphite as a function of fast neutron fluence. *Eurasian Journal of Physics and Functional Materials, 8*(3), 105–110.

3   Mussaeva, M.A., Ibragimova, E.M., & Buzrikov, S.N. (2018). Optical Spectra of Gamma-Irradiated LiF Crystals with Anisotropic Lithium Nanoparticles. *Optics and Spectroscopy, 124*(5), 644–648.

4   Uskenbaev, D., Nogai, A., Uskenbayev, A., Zhetpisbayeva, A., Nogai, A., et al. (2023). Synthesis and Research of Critical Parameters of Bi-HTSC Ceramics Based on Glass Phase Obtained by IR Heating. *ChemEngineering, 7*(5), 95.

5   Uskenbaev, D.E., Nogai, A.S., Uskenbayev, A.D., Nogai, E.A., Kudusov, A.S., & Khamzina, B.E. (2024). Critical current density of high-temperature superconducting ceramics BSCCO Bi-2234. *Bulletin of the University of Karaganda – Physics, 3*(115), 65–70.

6   Nogai, A.S., Nogai, A.A., Uskenbaev, D.E., et al. (2023). Features of Structures and Ionic Conductivity of $Na_3Fe_2(PO_4)_3$ Polycrystals Obtained by Solid Phase and Melt Methods. *Ceramics, 6*(4), 2295–2306.

7   Uskenbaev, D.E., Nogai, A.S., Uskenbaev, A.D., & Nogai, E.A. (2023). Effects of conditions on the synthesis and properties of Bi-2234 HTSC ceramic produced from the melt. *Bulletin of the University of Karaganda – Physics, 3*(111), 163–170.

8   Glasstone, S. & Sesonske, A. (1994). *Nuclear Reactor Engineering*, 4th ed., Vol. 1, Springer.

9   Yuldashev, B.S., Salikhbaev, U.S., Dosimbaev, A.A. et al. (2005). Operation of VVR-SM with 36%enrichment uranium-dioxide fuel. *Bulletin of the Institute of Atomic Physics of the Russian Academy of Sciences, 99*(2), 147–152.

10 Lamarsh, J.R. & Baratta, A.J. (2001). Introduction to Nuclear Engineering, 3rd ed., Prentice Hall. chrome-extension://efaidnbmnnnibpcajpcglclefindmkaj/https://www.engr.psu.edu/conedmat/courses/nuce497a/lamarsh_baratta-introduction_to_nuclear_engineering_textbook_3rd_edition.pdf

11 Koning, A.J. & Rochman, D. (2012). Modern Nuclear Data Evaluation with the TALYS Code System. *Nuclear Data Sheets, 113*(12), 2841–2934. https://doi.org/10.1016/j.nds.2012.11.002

12 IAEA TECDOC-1743. Compendium of Neutron Beam Facilities for High Precision Nuclear Data Measurements, IAEA, 2014. https://www-pub.iaea.org/MTCD/Publications/PDF/TE-1743_web.pdf

13 Gold, R. (1964). Activation Analysis, ORNL Report.

14 Litvintsev, Yu.A. (1983). *Methods of Measuring Neutron Spectra*. Moscow: Energoatomizdat.

15 Knoll, G.F. (2010). *Radiation Detection and Measurement*, 4th ed., Wiley.

16 Pelowitz, D.B. MCNPX User's Manual, LA-CP-05-0369, LANL, 2005.

17 Leppänen, J. (2015). Serpent — A Continuous-energy Monte Carlo Reactor Physics Burnup Calculation Code, VTT Tech. Research Centre of Finland. chrome-extension://efaidnbmnnnibpcajpcglclefindmkaj/https://serpent.vtt.fi/download/Serpent_manual.pdf

18 Stamm'ler, R.J.J. & Abbate M.J. (1983). *Methods of Steady-State Reactor Physics in Nuclear Design*. Academic Press.

19 Arkhangelsky, N.V. (1972). *IRT-2D Program*. Moscow.

20 Salomon, S. & Hébert, A. (2013). *DRAGON: A Collision Probability Transport Code for Cell and Supercell Calculations*. ÉcolePolytechnique de Montréal.

21 Chadwick, M.B. et al. (2011). ENDF/B-VII.1 Nuclear Data for Science and Technology: Cross Sections, Covariances, Fission Product Yields and Decay Data, Nuclear Data Sheets. https://doi.org/10.1016/j.nds.2011.11.002

22 Bytelesov, S.A. et al. (2008). Neutron-physical calculations of VVER-SM, Atomic Energy. DOI: 10.1007/s10512-008-9039-4

23 Alikulov, Sh.A., Baytelesov S.A., et al. (2014). Experimental studies of spent fuel burn-up in WWR-SM reactor. *Journal of Nuclear Engineering and Design, 277*, 63–165. https://doi.org/10.1016/j.nucengdes.2014.06.020

24 Ivanov, K.N. & Karpov, S.A. (2012). *Theory and calculation of active zones of nuclear reactors*. Moscow.

25 IAEA TRS-437. (2006). Fuel Modelling at Extended Burnup, IAEA.

26 Drozdov, V.N. et al. (1987). *Calculation of neutron reaction constants in reactors*. Moscow, Energoatomizdat.

27 IAEA TECDOC-1215. (2001). Practical Use of Research Reactors: Operation, Utilization and Applications, IAEA.

28 Heat-emitting assemblies IRT-4M. Catalog description 0019.20.00.000. Novosibirsk, 2004.

29 Smith, J. et al. (2018). Advanced Nuclear Fuel for Research Reactors. *Nuclear Engineering*, 45, 112–120.

30 Ivanov, A.P. (1985). *Neutron spectra in research reactors*. Moscow: Energoatomizdat.

31 Petrov, V.G. (1992). *Methods for calculating neutron fluxes*. Kyiv: Naukova Dumka.

32 Brown, R. (2010). *Neutron Activation Analysis in Reactor Physics*. Springer.

33 Taliev, A.V. (2006). *ASTRA program for calculating thermal modes*. Moscow.

34 Deen, J.R. & Woodruff, W.L. (1995). WIMS–ANL User Manual. Rev. 6 ANL/TD/TM99-07. — Argonne National Laboratory 9700 South Cass Avenue Argonne, Illinois 60439-4841, P. 95.

35 Koltochnik, S. N., Sairanbayev, D. S., Chekushina, L. V., Gizatulin, Sh. Kh., & Shaimerdenov, A.A. (2018). Comparison of neutron spectrum in the WWR-K reactor with leu fuel against heu one. *NNC RK Bulletin, 4*, 14–17. https://doi.org/10.52676/1729-7885-2018-4-14-17.

И.И. Садиков, Т.Б. Файзиев, С.А. Байтелесов, Ф.Р. Кунгуров,
Ш.А. Аликулов, Д.П. Таджибаев, Д.Е. Таджибаев, А.С. Кудусов

Нейтрон ағындарының энергетикалық спектрін анықтау ӨзР ҒА ЯФИ ССР-СМ реакторлары

Бұл зерттеуде (Өзбекстан Ядролық физика институты) ССР-СМ реакторының белсенді аймағында нейтрон ағындарының спектрі мен таралуы қарастырылды (19,75 % U-235 аз байытылған отынға көшкеннен кейін, отындық жинақтар саны 18-ден 24-ке дейін өсті). IRT-2D және WIMS

программалары мен нейтрондық-активациялық талдау деректері пайдаланылып, нейтрон ағынының тығыздығы және энергетикалық спектрі зерттелді. Нәтижелер реактордың орталық бөлігінде жылдам нейтрондар басым екенін, ал бериллий рефлекторларында жылу нейтрондарының үлесі артатындығын көрсетті. Тік каналдардағы өлшемдер рефлектордағы жылу нейтрондарының ағыны жылдам нейтрондарға қарағанда 2,3 есе жоғары екенін анықтады. Көлденең каналдарда кадмий коэффициенті 28 болатын $1,8 \cdot 10^{12}$ н/(см²·с) дейінгі жылу нейтрон ағындары тіркелді, бұл оларды тәжірибелер үшін қолайлы етеді. Отынды жинақтардың жылу қуаты орталықта максималды болып, перифериялға қарай азаяды, бұл U-235-тің жануына сәйкес келеді. Алынған нәтижелер отынды тиімді пайдалану, оны ауыстыруды жоспарлау және жаңа отын түрлерін (UO₂+Al, U₃Si₂+Al) сынау үшін маңызды.

Кілт сөздер: ядролық отын, энергетикалық спектр, жылдам нейтрондар, жылу нейтрондары, реактордың белсенді аймағы, нейтрондық-активациялық талдау, ССР-СМ реакторы, отынның жануы

И.И. Садиков, Т.Б. Файзиев, С.А. Байтелесов, Ф.Р. Кунгуров,
Ш.А. Аликулов, Д.П. Таджибаев, Д.Е. Таджибаев, А.С. Кудусов

Определение энергетического спектра нейтронных потоков реактора ВВР-СМ ИЯФ АН РУ

В данном исследовании изучены спектры и распределение нейтронных потоков в активной зоне реактора ВВР-СМ (Институт ядерной физики, Узбекистан) после перехода на низкообогащенное топливо (19,75 % U-235) с увеличением числа тепловыделяющих сборок (ТВС) с 18 до 24. С применением кодов IRT-2D и WIMS, а также данных нейтронно-активационного анализа исследованы плотность потока нейтронов и их энергетический спектр. Результаты показали, что в центральной части активной зоны преобладают быстрые нейтроны, тогда как в бериллиевых отражателях возрастает доля тепловых нейтронов. Измерения в вертикальных каналах выявили, что поток тепловых нейтронов в отражателе в 2,3 раза выше, чем поток быстрых нейтронов. В горизонтальных каналах зафиксированы тепловые потоки до $1,8 \cdot 10^{12}$ н/(см²·с) с кадмиевым отношением 28, что делает их пригодными для экспериментов. Тепловая мощность ТВС достигает максимума в центре и снижается к периферии, что коррелирует с выгоранием U-235. Полученные данные важны для оптимизации загрузки топлива, планирования перегрузок и испытания новых видов топлива (UO₂+Al, U₃Si₂+Al).

Ключевые слова: ядерное топливо, энергетический спектр, быстрые нейтроны, тепловые нейтроны, активная зона реактора, нейтронно-активационный анализ, реактор ВВР-СМ, выгорание топлива

Information about the authors

Sadikov, Ilkhom — DcS, Academician, Professor, Director, Institute of Nuclear Physics, Academy of Sciences of Uzbekistan, Ulugbek, Tashkent, Uzbekistan; email: ilkham@inp.uz, ORCID ID: https://orcid.org/0000-0002-9779-370X

Fayziyev, Temur — PhD student, Institute of Nuclear Physics, Uzbekistan Academy of Sciences, Ulugbek, Tashkent, Uzbekistan; e-mail: temurfayziyev@outlook.com; Scopus ID: 58427407800; ORCID ID: https://orcid.org/0000-0002-8824-5488

Baytelesov, Sapar — DcS, Professor, Head of laboratory, Institute of Nuclear Physics, Academy of Sciences of Uzbekistan, Ulugbek, Tashkent, Uzbekistan, e-mail: bytel@inp.uz; ORCID ID: https://orcid.org/0000-0003-3926-9579

Kungurov, Fakhrulla — DcS, Senior Researcher, Deputy Director, Institute of Nuclear Physics, Academy of Sciences of Uzbekistan, Ulugbek, Tashkent, Uzbekistan, e-mail: fkungurov@inp.uz; ORCID ID: https://orcid.org/0000-0003-4359-3523

Alikulov, Sherali — PhD, Senior Researcher, Institute of Nuclear Physics, Academy of Sciences of Uzbekistan, Ulugbek, Tashkent, Uzbekistan, email: alikulov@inp.uz ORCID ID: https://orcid.org/0000-0003-4028-6501

Tadjibaev, Diyer — PhD, Senior Researcher, Institute of Nuclear Physics, Uzbekistan Academy of Sciences, Ulugbek, Tashkent, Uzbekistan; e-mail: tadjibaev@inp.uz: Scopus ID: 35305693000; ORCID ID: https://orcid.org/0009-0001-9782-8079

Uskenbaev, Daniyar (*corresponding author*) — PhD, Associate Professor, S. Seifullin Kazakh Agrotechnical Research University, Astana, 010001, Kazakhstan, e-mail: usdan@mail.ru, ORCID ID: http://orcid.org/0000-0001-6265-1376

Kudussov, Arystan — Candidate of Physical and Mathematical Sciences, Buketov Karaganda National Research University, University str., 28, Karaganda, Kazakhstan; 100028; e-mail: akudusov@mail.ru; ORCID ID: https://orcid.org/0009-0006-2821-6446

Sh.M. Kazhykenov[1✉], G.U. Yerbolatova[1], A.K. Tussupbekova[2]

[1]D. Serikbayev East Kazakhstan Technical University, Ust-Kamenogorsk, Kazakhstan;
[2]Buketov Karaganda National Research University, Karaganda, Kazakhstan

Application of numerical methods to determine some parameters of radiation embrittlement of borosilicate glass

In this paper, a numerical method for determining the parameters of radiation embrittlement in borosilicate glass is proposed. The method is based on analyzing the changes in the mechanical properties of the material under radiation exposure, using known irradiation parameters: the total interaction cross section σ_{tot} of glass atoms, the fluence Φ and the energy E of protons. To quantitatively assess the accumulated damage, the DPA (displacements per atom) model is used, and numerical calculations are performed in LAMMPS (molecular dynamics) and COMSOL (analysis of mechanical properties). The obtained results allow us to predict structural changes in glass and to design materials with enhanced resistance to radiation damage. The particle energy range of 1–10 MeV is considered, a correlation is established between radiation defects and a decrease in the elastic modulus. The threshold value of radiation damage (DPAcr), the change in the elastic modulus and the ultimate strength of glass depending on the radiation dose were determined. The effective elastic modulus after irradiation was calculated, which quantitatively describes the change in the material properties. It was determined at what fluence value the critical destruction of the glass structure begins.

Keywords: radiation embrittlement, total interaction cross section, DPA, elastic modulus, radiation resistance, nuclear materials, modeling

✉*Corresponding author*: Kazhykenov, Shalkar, nuclearshalkar@gmail.com

Introduction

Borosilicate glass is a key material in nuclear technologies due to its high chemical durability, low thermal expansion coefficient, and resistance to radiation damage. It is widely used in the storage of radioactive waste (vitrification of high-level residues); in the production of shielding screens for nuclear reactors and particle accelerators; as components of fuel assemblies and in the structures of fusion reactors. However, despite its stability, prolonged radiation exposure leads to the accumulation of damage within the glass structure, causing mechanical embrittlement. This manifests as deformation and reduced strength of the glass; the appearance of microcracks and a decrease in the elastic modulus; the breakdown of the silicate network and changes in interatomic bonding. Previous studies [1–4] have shown that the primary mechanism of borosilicate glass degradation is the accumulation of radiation-induced defects, such as displaced atoms and interstitial defects [5, 6]. However, the quantitative assessment of this damage and its impact on the mechanical properties of the glass remains insufficiently investigated.

The aim of this study is to determine the parameters of radiation-induced embrittlement of borosilicate glass based on the modeling of radiation defects (DPA — displacements per atom) and numerical analysis of mechanical properties. This will help compare the results with experimental data and confirm the applicability of numerical methods in the design of containers for long-term storage of nuclear waste. To achieve this: 1. Molecular dynamics simulations will be performed in LAMMPS to evaluate the formation of defects under proton irradiation in the energy range of 1–10 MeV. 2. A mechanical analysis will be conducted in COMSOL to establish the relationship between accumulated defects and changes in the elastic properties of the glass 3. Dependencies of Young's modulus, tensile strength, and fracture toughness on DPA will be obtained. The results will allow for the prediction of the radiation resistance of borosilicate glass and the development of new compositions with improved mechanical properties.

Materials and Methods

To model radiation-induced damage in borosilicate glass, proton irradiation in the energy range of 1–10 MeV is used. This range was chosen based on the spectrum of secondary protons generated in nuclear reactors and particle accelerators [7]; the peak contribution to radiation defect formation (DPA — displacements per atom) [8, 4]; and the ability to model structural changes in the glass at different depths [9, 10]. To determine the effect of radiation exposure on the structure and mechanical properties of borosilicate glass, a two-level modeling approach is applied: 1. Atomic-scale modeling — analysis of defect structures and their formation using molecular dynamics simulations (LAMMPS). 2. Macroscopic modeling of mechanical properties — calculation of changes in the elastic characteristics of the glass using COMSOL Multiphysics.

Atomic-Scale Modeling in LAMMPS

To evaluate the formation of radiation-induced defects at the atomic level, it was first necessary to reconstruct the atomic structure of borosilicate glass. In this study, the melting-quenching method was used to generate an amorphous structure representative of the glassy state. Model of Borosilicate Glass: The irradiated geometry is modeled as a rectangular solid with dimensions:
– Width: 40 mm,
– Length: 200 mm,
– Thickness: $d = 5$ mm.
The chemical composition of borosilicate glass is shown in Table 1.

T a b l e 1

Chemical composition of borosilicate glass

SiO_2 (silicate matrix)	80–85 %
B_2O_3 (boron trioxide)	10–15 %
Na_2O, Al_2O_3, K_2O (network modifiers)	5–10 %

Average atomic density of the glass: $N = 2.3 \times 10^2$ [8].

The coordination radius Si–O: ~1.62 Å [11] is essential for accurate modeling of the glass structure, calculation of bonding energy, and evaluation of its resistance to radiation-induced damage. A supercell with a size of 10–50 nm is modeled. This range was selected based on physical constraints, computational cost, and consistency with experimental data:

a. Physical constraints: Protons with energies of 5–10 MeV have a penetration depth of 5–50 μm [8], but the radius of primary knock-on atom (PKA) cascades is limited to 2–10 nm [9].

b. Minimum size of 10 nm captures the full extent of the damage cascade region, while the maximum size of 50 nm allows for the consideration of defect clustering effects.

c. Numerical limitations of MD simulations: Modeling supercells larger than 50 nm requires excessive computational resources, while sizes below 10 nm lead to distorted results due to boundary effects of the supercell [10].

d. Consistency with experiments: The selected size range is supported by previous studies on radiation damage in glass [12]. Initial temperature: 2500 K → cooled down to 300 K. A temperature of 2500 K is used in the melt-quench method to generate the amorphous structure of borosilicate glass. The actual melting temperature of glass is 1400–1600 K [13], but in molecular dynamics simulations, heating by approximately 1000 K above the melting point is required to break the Si–O, B–O (Fig. 1), and Al–O network structures [14]. Cooling down to 300 K simulates the solidification of the glass at room temperature. In real processes, the cooling rate ranges from 10^4 to 10^6 K/s [15], while in MD simulations it is typically around 10^{12} K/s, due to time scale limitations of the calculations [4]. Energy relaxation is performed for 50 ps at 300 K using the NPT ensemble.
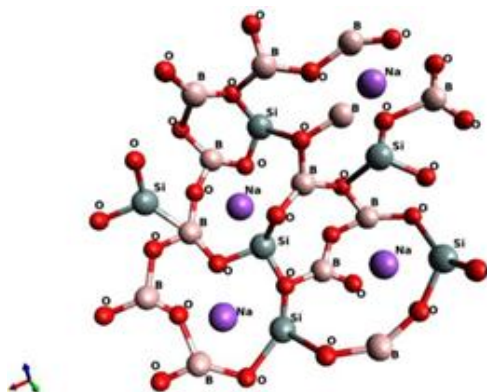
Figure 1. 3D schematic of the borosilicate glass molecule (SiO_2–B_2O_3–Na_2O)

Introduction of Radiation Exposure (Atomic Displacement Process in Borosilicate Glass): To calculate the energy spectrum of displaced atoms, the Kinchin-Pease model [4] is used, which takes into account energy losses during atomic collisions:

$$N_d = \frac{2E_{th}}{0.8 \cdot T_d},$$ (1)

where N_d — number of displaced atoms per primary interaction event, T_d — energy transferred to the recoil atom, E_{th} — displacement threshold energy (~20 eV for glass [16]).

Calculation of Radiation Damage (DPA — Displacements Per Atom): DPA quantifies the average number of displaced atoms per target atom as a result of radiation exposure. It is calculated using the following formula [17]:

$$DPA = \frac{\Phi \cdot \sigma_{tot} \cdot E}{N},$$ (2)

where Φ — fluence (particles/cm²), σ_{tot} — total interaction cross-section (cm²) [18], representing the probability that a particle interacts with a target atom. It includes elastic scattering, inelastic scattering, ionization, and radiation damage formation. E — particle energy (eV), N — atomic density of the glass (atoms/cm³).

Estimation of Vacancy and Interstitial Defect Formation: The defect density *ndn_dnd* — defined as the number of displaced atoms or created defects per unit volume of material — depends on the particle flux and energy:

$$n_d = \Phi \cdot \sigma_d,$$ (3)

where σ_d — displacement damage cross-section [19], indicating how many of the total proton–atom interactions result in atom displacement and defect formation.

Macroscopic Modeling of Glass Mechanics in COMSOL

Following the atomic-level assessment of defects, the next step involved establishing a relationship between the number of defects and changes in mechanical properties. The analysis includes: 1. Utilizing radiation defect density data obtained from LAMMPS simulations. 2. Applying an elastoplastic fracture model to evaluate mechanical degradation. 3. Calculating the reduction in Young's modulus as a function of accumulated damage. 4. Estimating the critical defect concentration at which microcrack formation begins. The parameters of radiation damage are given in Table 2.

T a b l e 2

Initial physical parameters of glass irradiation

Energy of incident protons	1–10 MeV
Fluence of particles	10^{13}–10^{16} particles/cm²
Glass density	$N = 2.3 \times 10^{22}$ atoms/cm³ is consistent with typical values for borosilicate glass
Size of the supercell	10–50 nm (for molecular dynamics simulations)

Material Model Definition: An elastoplastic model with radiation-induced embrittlement is used. Initial Young's modulus of the glass: $E_0 = 70$ GPa [20]. Initial tensile strength: $\sigma_0 = 500$ MPa [21]. To model the degradation mechanism, a dependency of the Young's modulus on DPA is introduced:

$$E_{\text{irr}} = E_0 \cdot \left(1 - k \cdot \text{DPA}\right), \tag{4}$$

where k — degradation coefficient [22]. The strength of the glass was calculated using Griffith's fracture criterion:

$$\sigma_{\text{fract}} = \sigma_0 \cdot e^{-\alpha \cdot \text{DPA}}, \tag{5}$$

where α — radiation embrittlement coefficient [22]. The prediction of microcrack formation was carried out by evaluating the probability of defect growth using the maximum stress criterion. Estimation of critical defect concentration and microcrack initiation:

Maximum stress for failure:

$$\sigma_{\text{max}} = \frac{E_{\text{irr}} \cdot \varepsilon_{\text{cr}}}{1 - \nu}, \tag{6}$$

where $\varepsilon_{\text{cr}} = 0.01$ — critical strain [23], $\nu = 0.23$ — Poisson's ratio [22]. Critical defect concentration DPA_{cr}, at which microcrack formation begins:

$$DPA_{\text{cr}} = \frac{E_{\text{irr}} \cdot \varepsilon_{\text{cr}}}{\sigma_{\text{fract}}}. \tag{7}$$

Results and Discussion

Numerical simulations yielded the following results, which are presented in Table 3.

T a b l e 3

Results of analytical and numerical calculations

Parameter	Value
N_d (number of displaced atoms per interaction)	1098560
DPA (displacements per atom)	$1.15 \cdot 10^{20}$
Proton fluence (particles/cm²) at onset of embrittlement	10^{16}
Proton energy (MeV)	1–10
Total interaction cross-section (cm²)	Energy-dependent, typically $10^{-24} - 10^{-22}$
Defect density (defects/cm³)	$2 \cdot 10^{11}$
Displacement damage cross-section (cm²)	$5 \cdot 10^{-24}$
Initial Young's modulus of glass (GPa)	70
Calculated Young's modulus (GPa)	~60–65 (decrease by 5–15 %)
Initial tensile strength (MPa)	500
Calculated tensile strength (MPa)	Exponentially decreases, down to 250 at DPA > 0.5
Maximum stress at failure (MPa)	487.65 (it is determined from mechanical calculations)
Eirr (irradiation-modified modulus)	66.59
DPA_{cr} (critical DPA threshold)	~0.5 (onset of microcrack formation)

The computational workflow and visualization of radiation damage obtained from the LAMMPS simulation are shown in Figure 2.

```
1  LAMMPS-GUI - Editor - in.borosilicate - *modified*
2
3  # LAMMPS input script for radiation damage in borosilicate glass
4
5  units          metal
6  atom_style     atomic
7  boundary       p p p
8  dimension      3
9
10 # Define simulation box
11 lattice         custom 5.0 &
12                 a1 5.0 0.0 0.0 &
13                 a2 0.0 5.0 0.0 &
14                 a3 0.0 0.0 5.0
15 region         box block 0 10 0 10 0 10
16 create_box     3 box
17 create_atoms   1 random 50000 12345 NULL
18
19 # Potential interaction for borosilicate glass
20 pair_style     tersoff
21 pair_coeff     * * BKS.tersoff Si O B Na
22
23 # Melt-quench method
24 fix            1 all nvt temp 2500.0 2500.0 1.0
25 run            5000
26 fix            2 all nvt temp 2500.0 300.0 1.0
27 run            5000
28
29 # Radiation impact: Proton implantation
30 fix            3 all deposit 10000 1 100 45678 region box vz -1.0 -0.5
31 run            10000
32
33 # Compute displacement per atom (DPA)
34 compute        dpa all damage/atom
35 fix            4 all ave/time 100 1 100 c_dpa file dpa_profile.dat
```

Figure 2. LAMMPS code (radiation damage simulation)

LAMMPS simulations showed that protons with energies of 5–10 MeV generate vacancies, interstitial atoms, and displacement cascades, leading to structural disordering (Fig. 3).
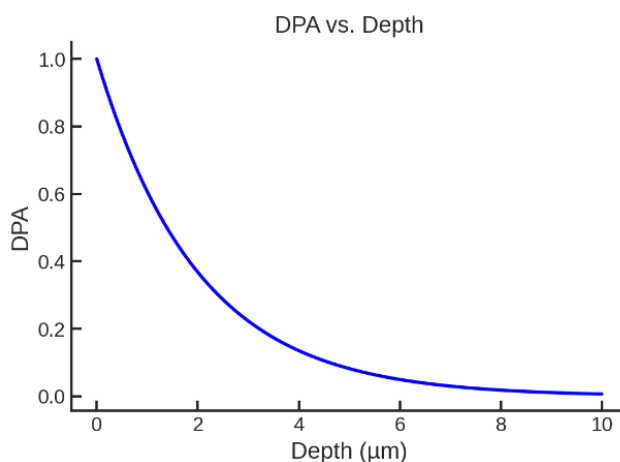
Figure 3. DPA vs. depth — damage zone. Shows the regions within the material,
where radiation damage is concentrated

The highest radiation damage is concentrated in the near-surface layer (at a depth of 0–2 µm), where the DPA reaches its maximum value (close to 1). A damage gradient is observed: as the depth increases (up to 10 µm), the DPA value sharply decreases, indicating attenuation of radiation effects with depth. The penetration depth of radiation defines the critical damage zone, which is primarily located within the first 5 µm of the material, beyond which the intensity of damage significantly decreases (Fig. 4).
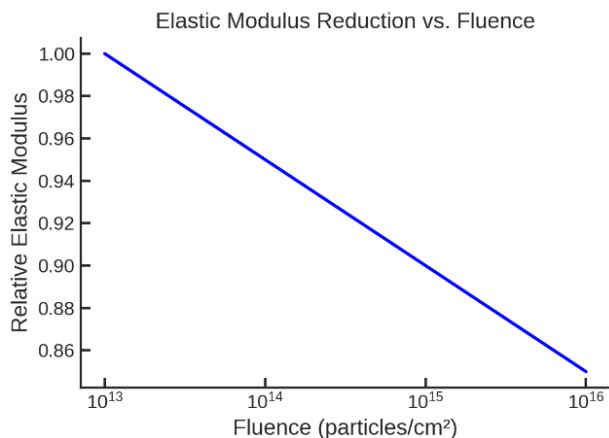
Figure 4. Reduction of Young's modulus vs. fluence — 5–15 % loss.
Confirms a 5–15 % decrease in Young's modulus with increasing proton fluence

The initial value (at low fluence, 10^{13} particles/cm^2) corresponds to a relative Young's modulus of 1.00, representing the unirradiated state of the glass. The final value (at a fluence of 10^{16} particles/cm^2) shows a decrease in relative Young's modulus to approximately 0.86. The reduction is calculated as the difference between the initial and final values: $(1.00-0.86)\times100\,\% = 14\,\%$. Thus, as the fluence increases to 10^{16} particles/cm^2, the Young's modulus decreases by approximately 14 % (Fig. 5).
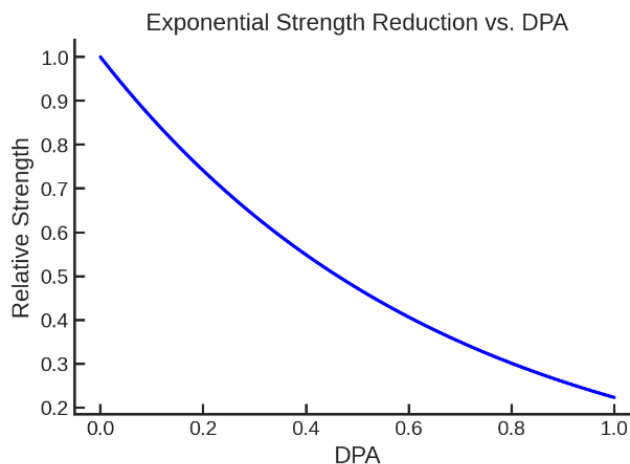
Figure 5. Tensile strength vs. DPA — exponential decay.
Illustrates the exponential decrease in strength at DPA > 0.5

The initial value (DPA = 0) corresponds to a relative tensile strength of 1.0, representing the undamaged state of the glass. Behavior with increasing DPA: At approximately DPA ≈ 0.5, the tensile strength has already dropped to about 0.5 of its original value. At DPA = 1.0, the strength decreases to 0.2 — an 80 % loss. This exponential trend indicates that the curve is strongly non-linear and bends downward, showing accelerated degradation of strength with increasing radiation damage. This means that beyond DPA > 0.5, failure accelerates — the material loses strength much faster than at lower DPA levels. In COMSOL, LAMMPS-derived data were incorporated, and an elastoplastic fracture model was applied. For DPA > 0.5, microcracks begin to form, leading to a critical reduction in strength (Fig. 6).
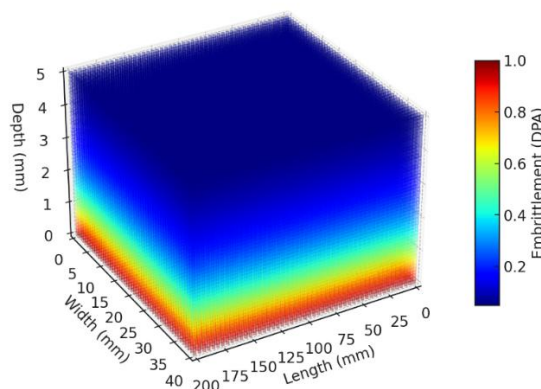
Figure 6. Gradient of radiation-induced embrittlement
in a borosilicate glass sample after proton irradiation (1–10 MeV)

The red and yellow regions (upper layer) indicate a high concentration of radiation damage (DPA ≈ 1.0) near the surface of the sample. The transition from red to blue (at a depth of approximately 1-2 mm) shows a gradual decrease in radiation-induced damage. The blue region (deeper layer) represents an almost complete absence of damage at a depth of 5 mm, confirming the attenuation of the radiation effect in the glass. LAMMPS revealed the formation of radiation-induced defects; COMSOL confirmed a 5–15 % reduction in

mechanical strength; when DPA > 0.5, structural failure begins. A clear quantitative relationship between DPA and the mechanical properties of borosilicate glass was established in the 1–10 MeV energy range.

Conclusion

Numerical simulations have shown that proton irradiation of borosilicate glass in the 5–10 MeV range (within the broader interval of 1–10 MeV) results in the formation of a maximum number of radiation-induced defects (vacancies, interstitial atoms, and displacement cascades), which lead to structural disordering. COMSOL calculations confirmed that when DPA exceeds 0.5, the mechanical strength of the glass decreases exponentially, microcracks begin to form, and the Young's modulus is reduced by 5–15 %. A quantitative relationship between DPA and mechanical properties was established, enabling long-term durability predictions for glass-based materials. However, it is important to note that the simulations were carried out using relatively small linear dimensions, selected to facilitate further mechanical testing under laboratory conditions. To reflect the typical thickness of real borosilicate waste containers, it is necessary to expand the radiation spectrum and particle types considered, in order to capture the full embrittlement mechanism and obtain critically important data for material performance under realistic nuclear waste storage conditions. An analysis of available experimental data shows that, although a number of studies have addressed the radiation resistance of borosilicate glass under gamma and beta irradiation, as well as under high-dose radiation exposure, open-access experimental data on the mechanical properties of borosilicate glass after proton irradiation in the 1–10 MeV range are currently lacking. This makes the present work a novel contribution to the study of radiation-induced embrittlement in glass materials. Therefore, this study was conducted to propose a combined numerical approach for material analysis and to establish criteria for future experimental investigations.

References

1   Carlan, Y., Bechade, J.-L., & Dubuisson, P. (2009). Radiation damage in glassy materials. *Journal of Nuclear Materials*, *386–388*, 430.

2   Wharry, J.P., Swenson, M.J., & Yano, K.H. (2017). Radiation resistance of glass materials. *Journal of Nuclear Materials*, *486*, 11.

3   Liu, X., Miao, Y., Wu, Y., Maloy, S.A., & Stubbins, J.F. (2017). The effect of radiation on borosilicate glasses. *Scripta Materialia*, *138*, 57.

4   Gin, S., Abdelouas, A., Criscenti, L.J., Ebert, W.L., Ferrand K., et al. (2013). Vienna, An international initiative on long-term behavior of high-level nuclear waste glass, *Mater. Today*, *16*, 243–248. https://doi.org/10.1016/j.mattod.2013.06.008.

5   Khassenov, A.K., Bulkairova, G.A., Nussupbekov, B.R., Schrager, E.R., Karabekova, D.Zh., Bolatbekova, M.M., & Zholdasbek, Y.A. (2024). Research of heat conductivity of quartz material. *Bulletin of the University of Karaganda — Physics,* 29, 3(115), 94–100. https://doi.org/10.31489/2024ph3/94-100.

6   Alpyssova, G.K., Afanasyev, D.A., Bakiyeva, Zh.K., Lisitsyna, L.A., Golkovski, M.G., Tussupbekova, A.K., Kissabekova, A.A., & Tuleuov, S.D. (2024). Optical properties of $ZnWO_4$ ceramics obtained by radiation synthesis. *Bulletin of the University of Karaganda — Physics,* 29, 3(115), 51–60. https://doi.org/10.31489/2024ph3/51-60.

7   International Atomic Energy Agency (IAEA). (2019). Spectrum of secondary protons in nuclear reactors and particle accelerators. *IAEA TECDOC-1975*. Vienna: IAEA.

8   International Atomic Energy Agency (IAEA). (2020). Radiation damage in glassy materials. *IAEA TECDOC-1898*. Vienna: IAEA. https://www.iaea.org/publications/search/type/tecdoc-series

9   (2020). Nuclear Materials Database. Simulation of radiation effects in glassy materials.

10   Plimpton, S. (1995). Fast parallel algorithms for short-range molecular dynamics. *Journal of Computational Physics, 117*(1), 1–19.

11   Zeidler, A., Salmon, P.S., Skinner, L.B., Fischer, H.E. (2014). Packing and the structural transformations in liquid and amorphous oxides from ambient to extreme conditions. *Proc. Natl. Acad. Sci. U.S.A, 111*(28), 10045–10048. DOI: 10.1073/pnas.1405660111

12   Delaye, J.-M., Peuget, S., Bureau, G., & Calas, G. (2011). Molecular dynamics simulation of radiation damage in glasses. *Journal of Non-Crystalline Solids, 357*(14), 2763–2768. DOI: 10.1016/j.jnoncrysol.2011.02.026

13   (2005). *ASTM C162-05. Standard Terminology of Glass and Glass Products.* West Conshohocken: American Society for Testing and Materials.

14   Gilard, O., Caussanel, M., Duval, H., Quadri, G., & Reynaud, F. (2010). New model for assessing dose, dose rate, and temperature sensitivity of radiation-induced absorption in glasses. *Journal of Applied Physics*, *108*(9), 093115. ff10.1063/1.3503370ff. ffhal-01288493

15   (2019). *Material Science Handbook. Molecular dynamics and material properties.* Boca Raton: CRC Press.

16 Jolley, K., Smith, R., & Joseph, K. (2015). Borosilicate glass potentials for radiation damage simulations. *Nuclear Instruments and Methods in Physics Research Section B: Beam Interactions with Materials and Atoms, 352*, 140–146. DOI: 10.1016/j.nimb.2014.12.024

17 Was, G.S., Averback, R.S., & Nastasi, M. (2019). *Handbook of Radiation Effects in Materials.* Springer.

18 Iwamoto, Y., Iwamoto, H., Harada, M., Niita, K. (2014). Calculation of displacement cross-sections for structural materials in accelerators using PHITS event generator and its applications to radiation damage. *Journal of Nuclear Science and Technology, 51*(1), 98–107. DOI: 10.1080/00223131.2013.851042

19 Griscom, D.L., Gingerich, M.E., Friebele, E.J. (1993.). Radiation-induced defects in glasses: origin of power-law dependence of concentration on dose. *Physical Review Letters, 71*, 1019–1022. DOI: 10.1103/PhysRevLett.71.1019

20 Doremus, R.H. (1986). Radiation effects in glasses used for high-level nuclear waste immobilization. *Radiation Effects and Defects in Solids, 101*, 235-257. DOI: 10.1080/10420158608206504

21 Jenkins M.L. & Kirk M.A. (2001). *Radiation Damage in Metals.* Cambridge: Cambridge University Press, 402 p.

22 (2002). ASTM C158-02. *Standard Test Method for Strength and Modulus of Glass.* West Conshohocken: American Society for Testing and Materials.

23 Decreton, M., Shikama, T., & Hodgson, E. (2004). Performance of functional materials and components in a fusion reactor: the issue of radiation effects in ceramics and glass materials for diagnostics. *Journal of Nuclear Materials,* 329–333, Part A, 125–132. https://doi.org/10.1016/j.jnucmat.2004.04.012.

Ш.М. Кажыкенов, Г.У. Ерболатова, А.К. Тусупбекова

Боросиликатты шынының радиациялық сынғыштығының кейбір параметрлерін анықтау үшін сандық әдістерді қолдану

Жұмыста боросиликатты әйнектің радиациялық сыну параметрлерін анықтаудың сандық әдісі ұсынылған. Әдіс сәулеленудің белгілі параметрлерін қолдана отырып, сәулеленудің әсерінен материалдың механикалық қасиеттерінің өзгеруін талдауға негізделген: шыны атомдарының σ_{tot} өзара әрекеттесуінің толық қимасы, Ф флюенс және E протондардың энергиясы. Жинақталған зақымдануды сандық талдау үшін DPA (displacements per atom) моделі, ал сандық есептеулер үшін LAMMPS (молекулалық динамика) және COMSOL (механикалық қасиеттерді талдау) қолданылды. Нәтижелер әйнектегі құрылымдық өзгерістерді болжауға және радиацияға төзімділігі жоғары материалдарды жасауға мүмкіндік береді. 1–10 МэВ бөлшектердің энергия диапазоны қарастырылған, радиациялық ақаулар мен серпімділік модулінің төмендеуі арасында корреляция анықталған. Радиациялық зақымданудың шекті мәні (DPAcr), сәулелену дозасына байланысты әйнектің серпімділік модулінің және беріктік шегінің өзгеруі айқындалды. Сәулеленуден кейін материалдың қасиеттерінің өзгеруін сандық сипаттайтын тиімді серпімділік модулі есептелген. Шыны құрылымының сыны бұзылуы флюенстің қандай мәнімен басталатыны анықталды.

Кілт сөздер: радиациялық сыну, өзара әрекеттесудің толық қимасы, DPA, серпімділік модулі, радиацияға төзімділік, ядролық материалдар, модельдеу

Ш.М. Кажыкенов, Г.У. Ерболатова, А.К. Тусупбекова

Применение численных методов для определения некоторых параметров радиационного охрупчивания боросиликатного стекла

В данной работе предложен численный метод определения параметров радиационного охрупчивания боросиликатного стекла. Метод основан на анализе изменения механических свойств материала под воздействием радиации, используя известные параметры облучения: полное сечение взаимодействия σ_{tot} атомов стекла, флюенс Ф и энергию E протонов. Для количественного анализа накопленного повреждения используется модель DPA (displacements per atom), а численные расчёты выполняются в LAMMPS (молекулярная динамика) и COMSOL (анализ механических свойств). Полученные результаты позволяют предсказать структурные изменения в стекле и разработать материалы с повышенной устойчивостью к радиационному воздействию. Рассматривается диапазон энергий частиц 1–10 МэВ, устанавливается корреляция между радиационными дефектами и снижением модуля упругости. Определены пороговое значение радиационного повреждения (DPAcr), изменение модуля упругости и предела прочности стекла в зависимости от дозы радиации. Рассчитан эффективный модуль упругости после облучения, который количественно описывает изменение свойств материала. Установлено, при каком значении флюенса начинается критическое разрушение структуры стекла.

Ключевые слова: радиационное охрупчивание, полное сечение взаимодействия, DPA, модуль упругости, радиационная стойкость, ядерные материалы, моделирование

Information about the authors

Kazhykenov, Shalkar (*corresponding author*) — Master of Science, PhD student, al-Farabi Kazakh National University, Senior Lecturer, D. Serikbayev East Kazakhstan Technical University, Serikbayev Street, 1, Ust-Kamenogorsk, Kazakhstan; e-mail: nuclearshalkar@gmail.com; https://orcid.org/0009-0005-4668-828X

Yerbolatova, Gulnar — PhD, Senior Lecturer, D. Serikbayev East Kazakhstan Technical University, Serikbayev Street, 19, Ust-Kamenogorsk, Kazakhstan; e-mail: e_gulnara77@mail.ru, https://orcid.org/0000-0001-7301-6394

Tussupbekova, Ainura — PhD, Associate Professor of the Department of Radiophysics and Electronics, Physical and Technical Faculty, Buketov Karaganda National Research University, Karaganda, Kazakhstan; e-mail: tussupbekova.ak@gmail.com, https://orcid.org/0000-0001-5299-9977

E.R. Hasanov[1, 2], Sh.G. Khalilova[2, 1✉], A.H. Sultanova[3]

[1]Baku State Uviversity, Baku, Azerbaijan;
[2]Institute of Physics, Baku, Azerbaijan;
[3]Nakhchivan State University, AZ7012, University Campus, Nakhchivan, Azerbaijan

Excitation of Thermomagnetic Waves in Multi-Valley Semiconductors of the GaAs Type

It has been shown that in two-valley semiconductors, in the presence of a temperature gradient, a thermomagnetic wave is excited, which propagates perpendicularly to the temperature gradient. Such an unstable wave is excited at an electric field value where ionization, recombination and generation processes do not occur. Then the total concentration of charge carriers remains constant. The Gunn effect in GaAs was discovered in samples with ohmic contacts. However, obtaining true ohmic contacts in experiments is difficult; therefore, the injection of charge carriers at the contacts must be considered. It is necessary to calculate the impedance of the crystal in the presence of injection and to determine the capacitive and inductive nature of this impedance. The excited wave in GaAs, under the conditions considered, depends on the frequency of hydrodynamic wave. The electric field acts between the valleys The Gunn effect was observed in GaAs at values of crystals of the axes. For other crystallographic orientations, the frequency and growth rate take different values. In our theoretical study, an isotropic sample was used, following Gunn's experiments. Of course, theoretical investigations in anisotropic samples are also of significant scientific interest.

Keywords: thermomagnetic waves, growth, frequency, increment, dynamics, carrier concentration, characteristic frequencies, characteristic electric field, Gunn's effect, semiconductor

✉*Corresponding author*: Khalilova, Shahla, shahlaganbarova@gmail.com

Introduction

The conditions for excitation of thermomagnetic waves in a nonequilibrium plasma were first obtained in the presence of hydrodynamic motions of charge carriers [1]. In this work it was stated that hydrodynamic motions of charge carriers in the presence of a constant temperature gradient ($\vec{\nabla}T$) excite an alternating magnetic field and in this case a so-called thermomagnetic wave with a frequency $\omega_T = -c\Lambda\vec{k}\vec{\nabla}T$ arises in the plasma (where c is the speed of light, Λ is the Nernst-Ettinishausen coefficient, $\vec{k}$ is the wavevector). In [2] the velocity and the thickness of the wave front are estimated, and the inclusion of an external magnetic field affects the thermomagnetic wave profile only slightly.

The reflection wave depends on the initial voltage, magnetic field and fractional parameter in the semiconductor photothermal diffusion medium [3]. Maxwell's equations were applied considering the absence of infinite conducting and bias current medium. In addition, it applies the boundary settings for Maxwell and mechanical stress, diffusion, chemical reaction, and temperature gradient at the interface near the vacuum [3].

Thermomagnetic waves can propagate along the wave vector or perpendicular to the wave vector. Such transverse and longitudinal thermomagnetic waves were theoretically investigated in isotropic and anisotropic conducting media in [4–7]. Of particular interest is the study of transverse and longitudinal thermomagnetic waves in semiconductors. In semiconductors, the flow of charge carriers creates hydrodynamic movements, and an alternating magnetic field is excited in the medium without an external magnetic field (that is $\vec{H}_0 = 0$).

Impurity semiconductors are special media, because in them, considering two types of charge carriers (electrons and holes). The conditions for excitation of thermomagnetic waves require several limiting cases. It is known that in multi-valley semiconductors, unstable states of the medium are ensured by the creation of generators or amplifiers. Of course, the Gunn effect in two-valley semiconductors of the GaAs type is of par-

ticular interest. In GaAs semiconductors, the appearance of thermomagnetic waves can change. Experimental conditions and, of course, the creation of Gunn amplifiers and generators. In this theoretical work, we will investigate the appearance of thermomagnetic waves in two-valley semiconductors in the presence of an external constant electric field and in the presence of a constant temperature gradient. The studies will be carried out at a specific direction of the temperature gradient relative to the wave vector and without an external magnetic field.

In a plasma with a constant temperature gradient, a magnetic field arises. Unlike ordinary plasma, such a plasma has oscillatory properties and thermomagnetic waves are excited and oscillations occur only in the magnetic field. In this case, the wave vector of thermomagnetic waves is perpendicular to the magnetic field or lies in the plane [7]. The speed of thermomagnetic waves is comparable to the speed of sound and the speed of the Alfven wave. These waves are transverse magnetohydrodynamic waves propagating along the lines of force of the magnetic field. Alfven wave oscillations involve not only the electromagnetic field, but also particles of the conducting medium, this is Oscillations in them are possible only in the presence of a magnetic field and a conducting medium that behaves like a single liquid or gas [8].

Electromagnetic oscillations are periodic changes in the field strength E and induction B. Maxwell showed theoretically, and Hertz proved experimentally, that a changing magnetic field generates an alternating electric field, in turn, an alternating electric field generates an alternating magnetic field. This changes (oscillations) in the characteristics of the electromagnetic field occur in space [9]. In semiconductors, the temperature gradient leads to the emergence of a thermoelectric field. In metals, due to the strong degeneracy of electrons, their distribution generally depends very weakly on temperature, and therefore the thermoelectric field is less than in semiconductors in the ratio kT/ε_F (ε_F — Fermi energy), this is by three orders of magnitude. However, the same temperature gradient creates a flow of phonons that implement thermal conductivity; the scattering of electrons on these phonons leads to their "increase", this is to the appearance of a noticeable drift velocity. Because of this, the thermo-emf can increase many times [10]. The concept of magnification was introduced by L.E. Gurevich [11], who applied it to metals in the absence, and later in the presence, of a magnetic field.

Fundamental in the field of kinetics of plasma processes are the works of L.D. Landau, who established the kinetic equation for plasma, and B.I. Davydov, who investigated the properties of plasma in a strong electric field. Due to the peculiarity of Coulomb forces in plasma, collisions with large impact distances are significant, at which the scattering angle and the transferred momentum are small, and therefore the collision integral can be transformed to an integro-differential form [11].

Instability of the hydrodynamic type in a plasma can also arise in the presence of an external magnetic field and a temperature gradient. It was considered in the case when the magnetic field is parallel to the electric field creating a constant ethical current, and in the perpendicular direction there is a temperature gradient. At certain values of the parameters, aperiodic instability occurs in the plasma. The case when the magnetic field is parallel to the temperature gradient and there is no current was also considered. Circularly polarized waves called thermomagnetic waves can propagate in the plasma along the magnetic field [11]. Under certain conditions, these waves become unstable and begin to grow. In a weak magnetic field, the instability is drift, and in a strong field, it is absolute. In L.E. Gurevich and B.L. Gelmont constructed a nonlinear theory of amplifying thermomagnetic waves. Instability, which can be called kinetic, and which is associated with the features of the distribution function of electrons and ions in the plasma, can arise in rarefied inhomogeneous plasma. Yu.A. Tserkovnikov investigated such instability in the presence of a non-uniform external magnetic field, in the case of non-isothermal plasma. In non-isothermal plasma the electron temperature significantly exceeds the ion temperature, and in the presence of a plasma density gradient [11].

When the wavelength of the emerging fluctuations significantly exceeds the Larmor radius, instability occurs within a certain range of carrier concentrations and magnetic field values. In the case of shorter waves, comparable to the Larmor radius, instability arises for all parameter values and is therefore considered "universal" [11].

If a semiconductor is in an external electric field, then the electrons receive a directed motion and drag phonons along with them [11].

Under certain steady-state conditions, the current in solids can be unstable. In this case, increasing oscillations arise.

If a conducting medium is in an external electric and magnetic field, then a new branch of oscillations (longitudinal) appears in its spectrum. These waves are weakly damped at frequencies significantly lower

than the characteristic inverse relaxation times. In the presence of a gradient of any parameter determining the distribution of the field or current, these waves can become unstable and grow like an avalanche. This instability, which is often called a gradient, was observed in one particular case for plasma by Lehnert and theoretically explained by B.B. Kadomizev and A.V. Nedospasov [11]. In semiconductors it was discovered by Yu.L. Ivanov and S.M. [11] and most generally investigated by L.E. Gurevich and co-workers [12], who formulated the above principle and constructed a nonlinear theory for one case.

In the presence of a temperature gradient in a conducting medium, a new type of instability phenomenon is possible. In the case of plasma, it was considered in a special review; in solids, it is possible only in very good conductors at hydrogen and lower temperatures. Under such conditions, weakly damped transverse waves (thermomagnetic) arise, associated with oscillations of the magnetic field. In the presence of an external magnetic field, these waves begin to grow. The work [12] describes an experiment by which it is possible to detect thermomagnetic waves and their amplification.

The theory of fluctuations in a nonequilibrium state, for example, for a system in an external electric field, was developed by V.L. Gurevich [13], using the kinetic equation for correlation functions of a certain type.

Soviet theoretical physicists investigated the phenomenon in semiconductors with a falling volt-ampere characteristic of an N-shaped connection. Such a characteristic can be caused either by the capture of electrons in deep traps, or by the transition of electrons under the influence of an electric field to higher states with lower mobility. The possibility of obtaining high-frequency oscillations gave rise to numerous studies throughout the world. A.F. Volkov and Sh.M. Kogan considered nonlinear oscillations in the case of an s-shaped characteristic. M.I. Iglitsii, E.G. Pel, L.Ya. Pervova and V.I. Fistul investigated oscillations not associated with the space charge, arising in semiconductors with a carrier of both signs, if the differential resistance for one of the carriers is negative [13, 14].

L.E. Gurevich and V.I. Vladimirov [14] investigated the kinetics of plasma with high radiative pressure and showed that the phenomenon of mutual increase of electrons and photons significantly changes the kinetic coefficients. The conditions of thermal instability of the type investigated by A.V. Gurevich also change. A special group of works in plasma kinetics is devoted to the so-called drift approximation, which describes the behavior of a rarefied plasma in an external magnetic field that slowly changes in space or time. In this case, the rapid motion of electrons along Larmor "circles" is accompanied by a slow displacement and change in the radius of these circles due to a change in the magnetic field. Averaging over the fast motion leads to the drift approximation. The theory of plasma oscillations based on this equation was developed by L.D. Landau, who showed that the problem of oscillations should be solved based on a certain initial state of the plasma, that is, its initial distribution function [15–19]. It turned out that even in the absence of collisions, plasma oscillations attenuate, roughly speaking, due to the transfer of wave energy to electrons, whose speed coincides with the phase velocity of the wave. This peculiar attenuation, called Landau attenuation, subsequently became the object of numerous studies.

We will consider excitation of thermomagnetic waves in the above semiconductors (in double-valley) without an external magnetic field and in the presence of a constant electric field. The crystals are under the influence of a constant temperature gradient. The temperature gradient is directed specifically along the external electric field. Between the valleys of the energy gap δ — when compared with the energy eEl obtained from the electric field of charge carriers, where l is the mean free path.

Basic equations of the problem

If the environment is under the influence of an external electric field $\vec{E}$ and a constant temperature gradient $\vec{\nabla} T = const$, then the electric field in the environment has the form:

$$\vec{E}^* = \vec{E} + \frac{[\vec{\upsilon} H]}{c} + \frac{T}{c} \frac{\nabla n}{n} . \tag{1}$$

Equation (1) shows the full effect of the electric field inside the sample. Here $\vec{E}$ is the electric field inside the medium due to the electric charge, $\dfrac{[\vec{\upsilon} H]}{c}$ is the electric field arising due to hydrodynamic movements with $\vec{\upsilon}$ the velocity of the charge carriers, $\dfrac{T}{c} \dfrac{\nabla n}{n}$ is the electric field created due to the redistribution of uneven charges inside the medium. It is known that in GaAs semiconductors the first and second valleys

have an energy gap between them $\Delta = 0.36$ eV. The mobility of charge carriers receiving energy of the order of eEl (l is the mean free path of charge carriers) from the electric field can move to a high energy level if $eEl \sim \Delta$. If we denote the time of transition from the first valley to the second valley τ_{12} and back by τ_{21}, then $\tau_{21} > \tau_{12}$, because the carriers in the second valley after scattering cannot move back to the first valley in an elastic manner. The mobility of charge carriers $\mu_1 \gg \mu_2$ due to the effective masses

$$m_1^* \ll m_2^*. \tag{2}$$

Since in the Gunn effect there was no ionization and generation of charge carriers, the total concentration in the medium was constant, that is

$$n = n_1 + n_2 = const;$$
$$n_1' = -n_2'. \tag{3}$$

The sample under consideration is without impurities and generation and recombination of charge carriers are absent. The external electric field is applied to the crystal in such a way that ionization of atoms is absent, therefore the concentration of charge carriers in the medium is constant.

Considering τ_{21} and τ_{12} the continuity equation in the valleys will have the form

$$\frac{\partial n_1}{\partial t} + \operatorname{div} j_1' = \frac{n_1}{\tau_{12}};$$
$$\frac{\partial n_2}{\partial t} + \operatorname{div} j_2' = \frac{n_2}{\tau_{12}}. \tag{4}$$

Here j_1' and j_2' are the current flux densities in the valleys. Equations (2), (3) and (4) describe the law of transition of charge carriers between valleys. The Gunn effect in two-valley semiconductors was observed at external electric fields of the order of $2 \div 3 \cdot 10^3$ V/cm and therefore at room temperature

$$eEl \gg k_0 T, \tag{5}$$

(k_0 — Boltzmann constant). Equation (5) is the condition of a strong electric field.

In the environment, the current flow density is created by electric current E^* and therefore the current flow density in each valley has the form:

$$\vec{j}_1 = n_1 \mu_1 \vec{E}^* + n_1 \mu_1' \left[\vec{E}^* \vec{H} \right] - \alpha_1 \vec{\nabla} T - \alpha_1' \left[\vec{\nabla} T \vec{H} \right];$$
$$\vec{j}_2 = n_2 \mu_2 \vec{E}^* + n_2 \mu_2' \left[\vec{E}^* \vec{H} \right] - \alpha_2 \vec{\nabla} T - \alpha_2' \left[\vec{\nabla} T \vec{H} \right]. \tag{6}$$

Thus, to obtain the dispersion equation, we must jointly solve the system of equations (4) taking into account (3) and (6). Equation (6) is the flux density of each valley.

Theory

We must find the expression of the electric field $E^{*'}$ from the variable concentration of charge carriers. Therefore, equation (7), (8) will determine the expression E^* from n'.

First, we define $\vec{E}^*$ from (1) as follows

$$\frac{\partial H}{\partial t} - c \operatorname{rot} E^*;$$
$$\vec{H}' = \frac{c}{\omega} \left[\vec{k} E^* \right]; \tag{7}$$

$$J = \vec{j}_1 + \vec{j}_2 = (n_1 \mu_1 + n_2 \mu_2) E^* + (n_1 \mu_1' + n_2 \mu_2') \left[E^* \vec{H} \right] - (\alpha_1 + \alpha_2) \vec{\nabla} T - (\alpha_1' + \alpha_2') \left[\vec{\nabla} T \vec{H} \right]; \tag{8}$$

$$J = \frac{c}{4\pi\sigma} \operatorname{rot} \vec{H}'. \tag{9}$$

Equations (7), (8) and (9) are Maxwell's equation and the expression for the total current.

Substituting (1), (7), (9) into (8) and expanding the vector dedication, we easily obtain j'_1 and j'_2 the equation of continuity of divergence will have the following form (10)

$$E^* = \left[\frac{iT}{e} \vec{k} \frac{n'}{n_0} + \Lambda_0 \beta \vec{\nabla} T \frac{\vec{E}_0 \vec{E}^*}{E_0^2} \right] \frac{1}{\alpha};$$

$$\alpha = 1 + \frac{2\vec{k}\vec{\upsilon}_0}{\omega} + \frac{2\omega_T}{\omega} + i \frac{c^2 k^2}{2\pi\sigma\omega};$$

$$\beta = 2 \frac{d \ln \Lambda}{d \ln E_0^2}.$$

(10)

From (10) it is evident that the propagation of thermomagnetic waves (finite excitation) depends very strongly on the wave vector and on the temperature gradient. We consider the case $\vec{k} \perp \vec{\nabla} T$ because the frequency of thermomagnetic waves has the form

$$\omega_T - c(k\nabla T)\lambda',$$

λ' is the Nerst-Ettinshausen's coefficient. Considering that all variable physical quantities have a monochromatic form after that is

$$(E'^*, n') \sim e^{i\vec{k}\vec{x} - \omega t}$$

after linearization (4) we easily obtain:

$$\vec{k}\vec{j}'_1 = \mu_{10} n_{10} \left(\vec{k}\vec{E}^{*'} \right) + \vec{k}\vec{u}_{10} n' + \frac{2\sigma'_1 c\vec{k}\vec{E}_0}{e\omega} \left(\vec{k}\vec{E}^{*'} \right) + \left(\vec{k}\vec{\upsilon}_{10} n_{10} \delta_1 - \alpha_{10}\gamma_1 \vec{k}\vec{\nabla} T \right) \frac{iT\vec{k}\vec{E}_0}{E_0^2 e\alpha\phi} \frac{n'}{n_{10}};$$

$$\vec{k}\vec{j}'_2 = \mu_{20} n_{20} \left(\vec{k}\vec{E}^{*'} \right) - \vec{k}\vec{u}_{20} n' + \frac{2\sigma'_2 c\vec{k}\vec{E}_0}{e\omega} \left(\vec{k}\vec{E}^{*'} \right) + \left(\alpha_{10}\gamma_2 \vec{k}\vec{\nabla} T - \vec{k}\vec{\upsilon}_{20} n_{20} \delta_2 - \right) \frac{iT\vec{k}}{E_0^2 e\alpha\phi} \frac{n'}{n_{20}};$$

(11)

$$\phi = 1 - \frac{\Lambda_0 \beta \vec{E}_0 \vec{\nabla} T}{\alpha E_0^2}.$$

From (11) the solution to equation (11) is too complicated, and therefore we will consider the following approximations

$$\frac{\mu_{20} n_{20}}{\mu_{10} n_{10}} \cdot \frac{1}{\tau_{12}} = \frac{1}{\tau_{21}}.$$

(12)

The time of transition from the first valley to the second τ_{12} and the reverse τ_{21} transition are different and $\tau_{21} > \tau_{12}$. We consider the case when they are related to the relation (12).

Choosing the direction $\vec{\nabla} T$ and $\vec{k}$ as follows $\vec{k} \perp \vec{\nabla} T$ and substituting (10) into equation (4) we

$$\left[-i\omega^2 - 2i\vec{k}\vec{\upsilon}_0 \omega - 2i\omega_T \omega + \frac{c^2 k^2}{4\pi\sigma}\omega - \frac{\omega}{\tau_{12}} - \frac{2\vec{k}\vec{\upsilon}_0}{\tau_{12}} - \frac{2\omega_T}{\tau_{12}} - i\frac{c^2 k^2}{2\pi\sigma\tau_{12}} + i\vec{k}\vec{\upsilon}_1 \omega + \right.$$

$$\left. +2i\vec{k}\vec{\upsilon}_0\vec{k}\vec{\upsilon}_{10} + i\vec{k}\vec{\upsilon}_1\omega_T - \frac{c^2 k^2}{4\pi\sigma}\vec{k}\vec{\upsilon}_1 \right] \left(\mu_{20} n_{20} \omega + 2ck\mu'_1 n_{10} \right) - \left[i\omega^2 + 2i\vec{k}\vec{\upsilon}_0 \omega + 2i\omega_T \omega - \frac{c^2 k^2}{4\pi\sigma}\omega + \frac{\omega}{\tau_{21}} + \right.$$

$$\left. + \frac{2\vec{k}\vec{\upsilon}_0}{\tau_{21}} + \frac{2\omega_T}{\tau_{21}} + i\frac{c^2 k^2}{2\pi\sigma\tau_{21}} - i\vec{k}\vec{\upsilon}_2\omega - -2i\vec{k}\vec{\upsilon}_0\vec{k}\vec{\upsilon}_2 - 2i\vec{k}\vec{\upsilon}_2\omega_T + \frac{c^2 k^2}{4\pi\sigma}\vec{k}\vec{\upsilon}_2 \right] \left(\mu_{10} n_{10} \omega + 2ck\mu'_2 n_{20} \right) = 0$$

$$\vec{\upsilon}_1 = \mu_1 \vec{E}_0, \vec{\upsilon}_2 = \mu_2 \vec{E}_0$$

From (11) it is clear that the solution to equation (11) is too complicated, and therefore we will consider the following approximations. Equation (11) is the dispersion equation for determining the frequency (13) of the waves arising under the condition (12).

Considering (12), from solution (11) we obtain:

$$\omega_{1,2} = \frac{\tau_{12}}{2\tau_{21}}\left(i\Omega - 4\omega_T - \omega_x\right) \pm \sqrt{\left(\frac{\tau_{12}}{2\tau_{21}}\right)^2 \left(i\Omega - 4\omega_T - \omega_x\right)^2 + \frac{2}{\tau_{21}}\left(2\omega_T 2\vec{k}\vec{\upsilon}_0 + i\frac{c^2 k^2}{4\pi\sigma}\right)}; \qquad (13)$$

$$\Omega = \frac{1}{\tau_{21}} - \frac{1}{\tau_{12}}, \omega_x = 4\vec{k}\vec{\upsilon}_0 + \frac{c^2 k^2}{2\pi\sigma}. \qquad (14)$$

Equation (14) is a characteristic notation. From the analysis of (13) considering (14) we obtain and we will select the imaginary and real parts of the oscillation frequency as follows:

$$\omega_{1,2} = -\frac{i}{2\tau_{21}} - \frac{\tau_{12}}{2\tau_{21}}\left(4\omega_T + \omega_x\right) \pm \left(x + iy\right);$$

$$x = \frac{1}{\sqrt{2}}\left[\sqrt{\Omega_1^4 + \Omega_2^4} + \Omega_1^2\right]^{\frac{1}{2}}, y = \frac{1}{\sqrt{2}}\left[\sqrt{\Omega_1^4 + \Omega_2^4} - \Omega_1^2\right]^{\frac{1}{2}}. \qquad (15)$$

Then from (15)

$$\Omega_1^2 = \left(\frac{\tau_{12}}{2\tau_{21}}\right)^2 \left(4\omega_T + \omega_x\right)^2 - \left(\frac{\tau_{12}}{2\tau_{21}}\right)^2 \Omega^2 + \frac{2}{\tau_{21}}\left(2\omega_T + 2\vec{k}\vec{\upsilon}_0\right);$$

$$\Omega_2^2 - \left(\frac{\tau_{12}}{2\tau_{21}}\right)^2 \cdot 2\left(4\omega_T + \omega_x\right) + \frac{1}{\tau_{21}}\frac{c^2 k^2}{2\pi\sigma}. \qquad (16)$$

In (15) it is to see that one wave is decaying, and the second wave can grow if

$$\frac{1}{\sqrt{2}}\left[\sqrt{\phi_1^2 + \phi_2^2} - \phi_1\right]^{\frac{1}{2}} > \frac{1}{2} \qquad (17)$$

$$\phi_1 = \frac{\tau_{12}^2\left(4\omega_T + \omega_x\right)^2}{4} + 4\tau_{21}\left(\omega_T + \vec{k}\vec{\upsilon}_0\right) - \frac{1}{4};$$

$$\phi_2 = \frac{\tau_{12}^2\left(4\omega_T + \omega_x\right)}{2} + \frac{c^2 k^2 \tau_{12}^2}{2\pi\sigma\tau_{21}}. \qquad (18)$$

Equations (15), (16), (17) and (18) are the distinguished real and imaginary parts of the corresponding quantities. By putting (18) into (15) we easily obtain:

$$\omega = \omega_0 + i\omega_i \qquad (19)$$

In the notation (18) the obtained imaginary and real parts of the frequencies

$$\omega_0 = \omega_T \left\{\frac{\sqrt{2}\tau_{12}}{\tau_{21}}\left[\sqrt{1 + \left(2\tau_{21}\omega_T\right)^2} + 1\right]^{\frac{1}{2}} - \frac{\tau_{12}}{\tau_{21}}\right\}; \qquad (20)$$

$$\omega_1 = \omega_T \left\{\frac{\sqrt{2}\tau_{12}}{\tau_{21}}\left[\sqrt{1 + \left(2\tau_{21}\omega_T\right)^2} - 1\right]^{\frac{1}{2}} - \frac{1}{2\tau_{21}}\right\}. \qquad (21)$$

Equation (20)–(21) define the expression for the part for the increment after theoretical calculation. Analysis (21) shows that for a wave to grow with frequency (20), the inequality must be satisfied

$$8\sqrt{2}\pi\omega_T\sigma\left(\omega_T\tau_{12}\right)^2 > c^2 k^2 \qquad (22)$$

Under the conditions of Gunn's experiment, an increase in thermomagnetic waves is obtained under condition (23). It should be noted that the condition for excitation of thermomagnetic waves in the above-mentioned two-valley semiconductors was investigated for the first time and there is no experimental evidence for the excitation of thermomagnetic waves in two-valley semiconductors.

Using experimental data of the Gunn effect, that is $L = 0.25$ mm, $n \approx 3 \cdot 10^{16}$ cm^{-3} is the length of the sample, it is easy to prove that (22) is well satisfied. When obtaining (20), (21) and (22), it was taken into account that

$$\tau_{12}\omega_T > \frac{1}{4}, \frac{c^2 k^2 \tau_{12}}{2\pi\sigma\tau_{21}} < 2\tau_{12}\omega_T, \tau_{21} > \tau_{12}, \tag{23}$$

which are easily achieved under experimental conditions. Inequality (22) is the condition of excited thermomagnetic waves, inequality (23) is the relationship between the transition times between the valleys.

In our theoretical work, the conditions for observing thermomagnetic waves in two-valley semiconductors of the GaAs type are indicated and corresponding experiments can be carried out.

Results

Thus, in two-valley semiconductors, when charge carriers transition between valleys, a thermomagnetic wave is excited, the wave vector of which is directed perpendicular to the temperature gradient. The frequency of this wave is thermomagnetic in nature. The growth increment of this wave is less than the frequency of the wave. The frequency and growth increment of this wave depend on the times τ_{21} and τ_{12}. Such instability is a purely thermomagnetic instability. The growth criterion of the excited wave is well satisfied when using the data of the Gunn experiment.

Conclusion

For the preparation of high-frequency amplifiers, our theoretical calculation shows an improvement in the quality factor of the devices.

Evaluation of frequencies ω_0 and growth increment ω_1 taking into account the Gunn experiment data shows that the frequency ω_0 of excited waves is of the order of 10^8 Hz, and the growth increment ω_1 of this wave is much smaller, this is 10^7 Hz. It should be noted that the excited thermomagnetic wave propagates with a higher frequency than the frequency of hydrodynamic waves (kv_0) and a lower frequency of electromagnetic waves $\omega_T < ck$. The results of our theoretical work, this is the expression for the frequency, the expression for the increment is valid when the waves propagate perpendicular to the temperature gradient. Of course, under the conditions $k \parallel \nabla T$ of excitation of the corresponding waves and the expression for them as a function of the external electromagnetic field and as a function of the total concentration in the medium will be different. The conditions of excitation of thermomagnetic waves in anisotropic crystals were theoretically investigated in [7]. To obtain the frequencies of current oscillations, it is necessary to calculate the total resistance of the sample, this is the impedance of the crystal.

References

1 Gurevich, L.E. (1963). Thermomagnetic waves and excitation of the magnetic field in nonequlibrium plasmas. *JETP, 44*, 548–555.

2 Chirkova, L.V., Skubnevsky, E.V., Ermagambetov, K.T., & Arinova, E.T. (2016). Nonliner phenomena and instability in semiconductors. *Bulletin of the University of Karaganda — Physics*, 1, 39–45.

3 Gafel, H.S. (2022). Fractional order study of the impact of a photo thermal wave on a semiconducting medium under magnetic field and thermoplastic theories. *Information Science Letter, 11*, 629–638. doi:10.18576/isl/110230

4 Hasanov, E.R., Khalilova, Sh.G., & Maharramov, A.B. (2021). Unstable thermoelectromagnetic waves in conducting media, Sustainable Development Strategy: Global Trends, National Experiences And New Goals. *Proceedings of The First International Scientific Conference,* 517–520.

5 Hasanov, E.R., Khalilova, Sh.G., Mamedova, G.M., Yusifova, K.N., & Akhadova, S.S. (2022). Increasing thermomagnetic waves in conducting media. *Journal of Problems of Energy*, 3, 40–44.

6 Hasanov, E.R., Khalilova, Sh.G., & Mustafayeva, R.K. (2025). Transverse and longitudinal thermomagnetic waves in conducting medi. *Bulletin of the University of Karaganda — Physics*, 3, 51–58. DOI: https://doi.org/10.31489/2025ph3/51-58

7 Hasanov, E.R., Khalilova, Sh.G., & Mustafayeva, R.K. (2024). Excitation of transverse and longitudinal thermomagnetic waves in anisotropic conducting media in the presence of a temperature gradient $\vec{\nabla}T$ without an external magnetic field H. *Bulletin of the University of Karaganda — Physics*, 2, 43–52, DOI: https://doi.org/10.31489/2024ph2/43-52

8 Alfven, G. & Felthammar, K. (1967). *Space Electrodynamics*, 2nd ed. Oxford University Press, 156.

9 Kong, A. (1990*). Electromagnetic Wave Theory*, 2nd ed., John Wiley&Sons, Inc., New York, 677.

10 (1967). *Development of Physics in the USSR. Academy of Sciences of the USSR.* Nauka Publishing House, Moscow, 113–150.

11 Gurevich, L.E. (1946). Thermoelectric Properties of Conductors. *JETP, 16*, 193.

12 Gurevich, V.L. (1964). Features of Electrical Conductivity of Metals at Low Temperatures. *JETP, 47*, 1415.

13 Gurevich, V.L. & Obraztsov, Yu.N. (1957). Effect of the increase in electrons and phonons on thermomagnetic effects in semiconductors. *JETP, 32*, 390.

14 Hideya Nishiyama, HiromichiTsukada, Yukio Matsushima and Shinichi Kamiyama (1997). The effect of an applied magnetic field on non-equilibrium plasma flow along a biased flat plate. *J. Phys. D: Appl. Phys. 30*, 2804. DOI: 10.1007/BF01570182

15 Chirkova, L.V., Ermaganbetov, K.T., Makhanov, K.M., Rozhkova, K.S., Arinova, E.T., & Kurmash, A. (2019). Current instability phenomena in a tunnel diode and electron self-organization processes. *Bulletin of the University of Karaganda — Physics*, 2, 8–13. https://doi.org/10.31489/2019ph2/8-13

16 Abouelregal, A.E., Sedighi, H.M., & Eremeyev, V.A. (2023). Thermomagnetic behavior of a semiconductor material heated by pulsed excitation based on the fourth-order MGT photothermal model. *Continuum Mech. Therm., 35*(1), 81–102. DOI: 10.1007/s00161-022-01170-z

17 Petrov, A.S. & Svintsov, D. (2024). High-Frequency Hall Effect and Transverse Electric Galvanomagnetic Waves in Current-Biased 2D Electron Systems. *JETP Letters, 119*(10), 800–806. DOI: 10.1134/S0021364024600563

18 Hasanov, E.R., Khalilova, Sh.G., Mammadova, G.M., & Mansurova, E.O. (2023). Excitation of unstable waves in semiconductors such as GaAs magnetic fields ($\mu H \gg c$). *IJTPE, 15*, 2, 302–306.

19 Maharramova, A.A. & Hasanov, E.R. (2023). Frequency of transverse and longitudinal thermomagnetic waves in certain anisotropic conducting media. *"Modern Trends in Physics", The 8th International Conference,* 30–31. Baku State University.

Э.Р. Гасанов, Ш.Г. Халилова, А.Х. Султанова

GaAs типті көп аңғарлы жартылай өткізгіштердегі термомагниттік толқындардың қозуы

Екі аңғарлы жартылай өткізгіштерде температура градиенті болған кезде температура градиентіне перпендикуляр таралатын термомагниттік толқын қозғалатыны дәлелденді. Мұндай тұрақсыз толқын иондану, рекомбинация және генерация жүрмейтін электр өрісінің мәнінде қозғалады. Сонда заряд тасымалдаушылардың жалпы концентрациясы тұрақты болады. GaAs-тағы Ганн эффектісі сынамада омдық контактілер болған кезде анықталды. Тәжірибеде омдық контактілерді алу қиын, сондықтан контактілерге заряд тасымалдаушылардың инъекциясын қарастыру қажет. Инъекция болған кезде кристалдың кедергісін есептеп, кедергінің сыйымдылық және индуктивті сипатын анықтау қажет. Қарастырылып отырған жағдайда GaAs-тағы қозған толқын гидродинамикалық толқынның жиілігіне байланысты. Аңғарлар арасында жүзеге асырылатын электр өрісі Ганн эффектісі GaAs-та осьтерінің кристалдарының мәндерінде анықталды. Кристалдық осьтердің басқа мәндерінде жиілік пен өсу өсімінің басқа мәндері болады. Біздің теориялық зерттеуімізде Ганның тәжірибелерінен кейін изотропты үлгі қолданылды. Әрине, анизотропты үлгілердегі теориялық зерттеулер ғылыми қызығушылық тудырады.

Кілт сөздер: термомагниттік толқындар, өсу, жиілік, өсу, динамика, тасымалдаушы концентрациясы, сипаттамалық жиіліктер, сипаттамалық электр өрісі, Ганн эффектісі, жартылай өткізгіш

Э.Р. Гасанов, Ш.Г. Халилова, А.Х. Султанова

Возбуждение термомагнитных волн в многодолинных полупроводниках типа GaAs

Доказано, что в двухдолинных полупроводниках при наличии градиента температуры возбуждается термомагнитная волна, распространяющаяся перпендикулярно градиенту температуры. Такая неустойчивая волна возбуждается при значении электрического поля, при котором не происходит ионизация, рекомбинация и генерация. При этом общая концентрация носителей заряда остается постоянной. Эффект Ганна в GaAs был обнаружен при наличии в образце омических контактов. Длина образца в эксперименте Ганна составляла $L \approx 0,25$ мм. Получение омических контактов в эксперименте затруднено, поэтому необходимо учитывать инжекцию носителей заряда через контакты. Необходимо рассчитать импеданс кристалла при наличии инжекции и определить емкостную и индуктивную природу импеданса. Электрическое поле осуществляет переход между долинами. Эффект Ганна был обнаружен в GaAs при значениях кристаллографических осей. При других значениях кристаллографических осей частота и инкремент роста будут иметь другие значения. В нашем теоретическом исследовании использовался изотропный образец, следуя экспериментам Ганна. Конечно, теоретические исследования в анизотропных образцах представляют научный интерес. В наших работах представлены исследования термомагнитных волн в анизотропных образцах. Однако в наших работах не учитываются переходы между долинами.

Information about the authors

Hasanov, Eldar — PhD in Physics, Associate Professor of Department of Solid State Physics, Baku State University, Leader of Department of Encyclopedia and Terminology, Institute of Physics, Baku, Azerbaijan; e-mail: egasanov065@gmail.com; ORCID ID: https://orcid.org/0009-0009-6900-6148.

Khalilova, Shahla (*corresponding author*) — PhD in Physics, Leading researcher of Department of Encyclopedia and Terminology at Institute of Physics, teacher of Department of Structure of Matter at Baku State University Physics, Baku, Azerbaijan; e-mail: shahlaganbarova@gmail.com; ORCID ID: https://orcid.org/0000-0003-4302-9674.

Sultanova, Aygun — PhD in Physics, Associate professor of Department of General and Theoretical Physics, Nakhchivan State University, Nakhchivan, Azerbaijan; e-mail: aygunsultanova60@gmail.com ORCID ID: https://orcid.org/0009-0006-7406-6055

G.M. Aralbayeva[1], Zh.T. Karipbayev[1✉], A.M. Zhunusbekov[1], A. Tolegenova[1], A. Kakimov[1], Y. Suchikova[2], S. Ubizskii[3], A.I. Popov[4], G.E. Sagyndykova[1]

[1]*Institute of Physical and Technical Sciences, L.N. Gumilyov Eurasian National University, Astana 010008, Kazakhstan;*
[2]*The Department of Physics and Methods of Teaching Physics, Berdyansk State Pedagogical University, 71100 Berdyansk, Ukraine;*
[3]*Lviv Polytechnic National University, S. Bandera Str. 12, Lviv, 79013, Ukraine;*
[4]*Institute of Solid State Physics, University of Latvia, 8 Kengaraga, LV-1063 Riga, Latvia*

Low Temperature Luminescence Behavior of Trace Cr and Fe Impurities in Gd$_3$Ga$_5$O$_{12}$ Single Crystals

This article examines the influence of unintentional Cr^{3+} and Fe^{3+} impurity ions on the luminescent properties of Gd$_3$Ga$_5$O$_{12}$ (GGG) single crystals. The characteristic features of the spectra excited by high-energy synchrotron radiation in the temperature range of 10–300 K are analyzed. It is shown that at 10 K the luminescence is dominated by a narrow-band emission of Cr^{3+} ions arising from the spin-forbidden $^2E \rightarrow ^4A_2$ transition, which indicates weak electron–phonon coupling and high crystalline homogeneity. It is revealed that with increasing temperature the intensity of this transition decreases significantly, while a broadband luminescence emerges, associated with the spin-allowed $^4T_2 \rightarrow ^4A_2$ transition and the contribution of Fe^{3+} ion emission. The temperature evolution of the spectra is shown to result from thermal redistribution of the Cr^{3+} excited-state populations, interlevel state mixing, and partial removal of the spin-forbidden nature of Fe^{3+} transitions due to lattice vibrations. Based on the study, conclusions are drawn regarding the role of impurity centers in energy transfer and nonradiative relaxation processes. The results are of interest both for fundamental photonics and for the development of efficient luminescent materials and optical devices designed to operate over a wide temperature range.

Keywords: gadolinium gallium garnet (GGG), synchrotron radiation, Cr^{3+} ions, Fe^{3+} ions, luminescence, excitation spectra, temperature dependence, energy transfer, electron–phonon coupling, nonradiative relaxation, impurity centers, optical properties

✉*Corresponding author*: Karipbayev, Zhakyp, Karipbayev_zht_1@enu.kz

Introduction

Garnet crystals are widely used in laser technologies, optical sensors, and other photonic applications due to their unique luminescent properties [1–10]. Similar studies of luminescent materials with varying compositions have been reported, for example, for YAGG phosphors with different Al/Ga ratios, demonstrating how modification of crystal composition affects spectral and luminescent characteristics [11]. Chromium and iron are typical impurities that penetrate the lattice at various stages of synthesis. Even small amounts of Cr^{3+} or Fe^{3+} can significantly affect the spectroscopic and luminescent characteristics of the material, as confirmed by similar temperature-dependent luminescence studies in other garnet systems [12]. In GGG, Cr^{3+} exhibit a rich spectroscopic behavior determined by their 3d³ configuration in an octahedral field [13]. At the same time, the luminescent properties of Cr^{3+} are sensitive to a number of factors: temperature, concentration, local environment, and the presence of other impurities. In GGG, Cr^{3+} substitutes for Gd^{3+} in octahedral sites, forming characteristic spectra with sharp ($^2E \rightarrow ^4A_2$) and broad ($^4T_2 \rightarrow ^4A_2$) bands [14]. The authors of [14] demonstrated a sharp decrease in intensity upon heating (by 90–99 % at 300 K) due to the increased probability of nonradiative relaxations.

When Fe^{3+} and rare-earth ions are simultaneously present in the GGG structure, excitation transfer becomes possible, which can be enhanced with increasing temperature, thereby influencing the selectivity and luminescent properties [15]. In [16], it was shown that the spectral position of the deep-red emission band of Fe^{3+} can be modified by adjusting the crystal field strength (CFS). Moreover, it was demonstrated that the thermal response of Fe^{3+} luminescence can be significantly improved by incorporating Cr^{3+} ions, thus enabling thermally activated nonradiative energy transfer $Fe^{3+} \rightarrow Cr^{3+}$. The authors of [16] showed that reducing

the CFS has a favorable effect on the performance of contactless temperature sensing in Fe^{3+}-based luminescent thermometers.

The study of the temperature dependence of the luminescence spectra of these materials is of crucial importance for understanding their optical characteristics and optimizing their applications. The aim of this work was to quantitatively separate and compare the contributions of unintentional impurity luminescence centers Cr^{3+} and Fe^{3+} to the integral luminescence of a $Gd_3Ga_5O_{12}$ single crystal under VUV excitation (160–250 nm) at temperatures of 10–300 K, as well as to determine the mechanisms of thermally controlled redistribution of impurity ion level populations and the energy transfer channels from the host lattice to the impurities.

Methods

The $Gd_3Ga_5O_{12}$ single crystals were grown by the Czochralski method using an iridium crucible. A mixture of argon (98 %) and oxygen (2 %) was used as the growth atmosphere. High-purity oxides Gd_2O_3 and Ga_2O_3 (99.99 wt. %) served as the starting materials. It should also be noted that GGG crystals contain a certain amount (10^{-3}–10^{-4} wt.%) of uncontrolled impurity ions, which is practically difficult to avoid. The samples were prepared in the form of flat plates 0.48 mm thick, oriented in the (111) plane with polished surfaces.

The luminescence studies were carried out using synchrotron radiation at the Superlumi/P66 beamline of the PETRA III synchrotron facility at DESY in Hamburg. This setup has proven to be highly effective for investigating luminescence processes excited in the VUV region [17–21].

The synchrotron radiation provided high-intensity, tunable excitation in the required spectral range, which was selected using a 2-meter monochromator with a spectral resolution of 0.4 nm. This ensured precise excitation of luminescent states in the single crystals. The emitted luminescence from the single crystals was detected using an ANDOR Kymera monochromator, which provided a spectral resolution of 0.2 nm, allowing for accurate detection of luminescence peaks. For sensitive detection over a wide spectral range, a Newton 920 CCD camera (Oxford Instruments, UK) was employed, while photon counting was performed using a Hamamatsu R6358 photomultiplier tube (Hamamatsu Photonics, Japan), particularly effective in the ultraviolet range.

Experiments were conducted at a temperature of 10 K using a helium-cooled cryostat to minimize thermal noise and nonradiative losses. The excitation spectra were corrected against the sodium salicylate signal, ensuring the acquisition of accurate and reliable data across the entire spectral range.

Results and Discussion

The excitation spectra of $Gd_3Ga_5O_{12}$ crystals measured at room temperature for emission wavelengths of 780, 754, and 694 nm (Fig. 1) exhibit characteristic features indicating the influence of unintentional Cr^{3+} and Fe^{3+} impurity ions in the crystal. For the 694 nm luminescence band, starting from approximately 5.5 eV, a sharp increase is observed in the excitation spectrum along with a relatively broad and smooth structure. This energy corresponds to the excitonic transition ($E_g = 5.66$ eV) [22], which is also associated with the excitation of unintentional impurity centers, primarily Cr^{3+} ions, through exciton migration.

In the region around 5 eV, when detecting at 754 nm and 780 nm, an additional peak is clearly visible, which can be unambiguously attributed to the presence of Fe^{3+} ions — a typical unintentional impurity often found in gallium garnets grown under standard conditions.
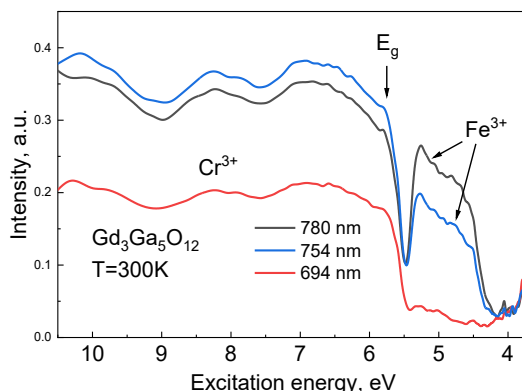

Figure 1. Excitation spectra of the $Gd_3Ga_5O_{12}$ crystal
measured at T = 300 K. $\lambda_{reg} = 780$ nm, $\lambda_{reg} = 754$ nm, and $\lambda_{reg} = 694$ nm

Analysis of the excitation spectra reveals a pronounced influence of Cr^{3+} and Fe^{3+} impurity ions, which manifest themselves as broad excitation bands in the 6–9 eV region and as a distinct peak around 5 eV, respectively. These impurities form additional levels within the band gap, facilitating uncontrolled energy trapping and affecting the luminescence characteristics.

The luminescence spectra of the GGG crystal excited by synchrotron radiation were studied at different temperatures. The emission spectra in the temperature range 300–10 K consist of a broad band spanning 650–870 nm (Fig. 2), which arises from the combined emission of two types of unintentional impurity centers. The component with a maximum around 730 nm is unambiguously associated with the $^4T_2 \rightarrow {}^4A_2$ transition of Cr^{3+} ions, whereas the band peaking at ≈ 775 nm is attributed to Fe^{3+} luminescence [23, 24]. To confirm this, luminescence spectra were recorded at 210 K under excitation at wavelengths $\lambda = 160$ nm and $\lambda = 250$ nm. In Figure 3, the band with a maximum at 775 nm is clearly distinguished, confirming the contribution of Fe^{3+}.

The temperature evolution of the luminescence spectra excited by high-energy quanta of 7.75 eV (160 nm) unambiguously reflects the different behavior of the two unintentional impurity centers — Cr^{3+} and Fe^{3+}. At temperatures below 210 K, the characteristic R-lines of Cr^{3+} begin to appear. At 10 K, the spectrum is characterized by structured lines in the 690–710 nm range, corresponding to the spin-forbidden $^2E \rightarrow {}^4A_2$ transition. As the temperature increases up to 300 K, the narrow structure is suppressed, and a broad symmetric luminescence band of 650–870 nm develops. This is associated with the dominance of the spin-allowed $^4T_2 \rightarrow {}^4A_2$ transition of Cr^{3+} ions and enhanced Fe^{3+} emission, indicating stronger thermal mixing of states and an increased contribution of electron–phonon interaction at higher temperatures.
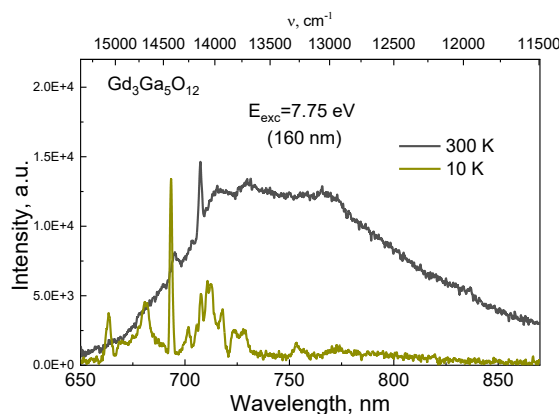

Figure 2. Temperature-dependent luminescence spectra of the GGG crystal
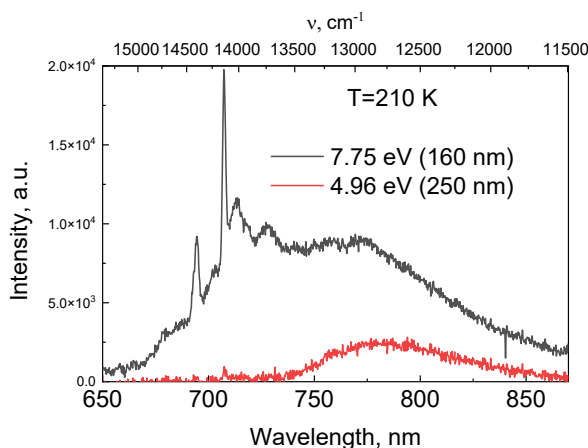

Figure 3. Luminescence spectra of GGG under 160 nm and 250 nm excitation

The experimental results can be explained as follows. Cr^{3+} ions in GGG are characterized by energy levels typical for d^3 ions: $^4A_2$, ^2E, and $^4T_2$. Under excitation with 160 nm radiation in the VUV region, elec-

tronic excitations in the crystal matrix are captured by Cr^{3+} and Fe^{3+} impurity ions. Relaxation of Cr^{3+} occurs via two dominant channels: the narrow-band $^2E \rightarrow {}^4A_2$ and the broadband $^4T_2 \rightarrow {}^4A_2$. Their relative contribution depends on temperature and crystal parameters [25].

Subsequent energy transfer processes occur through phonon-assisted mechanisms and interlevel relaxation, leading to population of the excited states ^2E and $^4T_2$. At 10 K, the spectrum is characterized by structured lines in the 690–710 nm range, corresponding to the spin-forbidden $^2E \rightarrow {}^4A_2$ transition of Cr^{3+} ions occupying octahedral sites of the garnet lattice. The observed linewidth of the R-lines is only a few cm^{-1}, indicating high crystalline homogeneity of the material and weak electron–phonon coupling at low temperature. At cryogenic temperatures, relaxation predominantly terminates at ^2E, resulting in emission with a characteristic narrow spectral structure. Increasing temperature promotes a larger contribution from transitions through $^4T_2$, since thermal lattice expansion reduces the energy gap ΔE between the ^2E and $^4T_2$ levels and enhances their mixing.

In the excitation spectrum of luminescence monitored at 780 nm, a clear band with a maximum at ~5 eV (250 nm) is observed (Fig. 1). However, photons of this energy cannot directly produce emission at 750–780 nm; instead, the energy can be absorbed by defect centers and subsequently transferred to Fe^{3+} ions. Emission at 780 nm was excited only by the 250 nm excitation band, which may be related to charge-transfer transitions involving Fe^{3+} ions at different sites. The increase in luminescence intensity with rising temperature can be explained as follows. The $^4T_1 \rightarrow {}^6A_1$ transition in Fe^{3+} ions is spin-forbidden, since $\Delta S \neq 0$. The broad emission band in the 740–820 nm region has been shown in [26] to correspond to this internal transition of Fe^{3+}. The enhancement of intensity with increasing temperature is explained by the standard mechanism of vibrational and spin-orbit mixing, which grows with the amplitude of lattice vibrations and local symmetry distortions. As temperature increases, these vibrations become stronger, disrupting the local symmetry of Fe^{3+} ions. As a result, the efficiency of orbital mixing increases, leading to an enhanced quantum yield of the Fe^{3+} band. An additional contribution arises from competition with trap states: higher temperatures promote thermal ionization of defects, making Fe^{3+} a more effective acceptor of migrating excitonic energy.
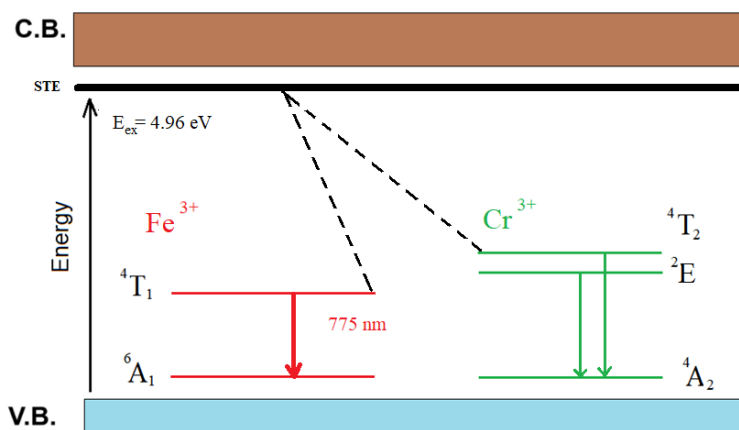
Figure 3. Cr^{3+} and Fe^{3+} centers schematic energy-level diagram in single crystal GGG

Conclusion

The luminescence spectra of unintentional Cr^{3+} and Fe^{3+} impurity ions in GGG under excitation by high-energy synchrotron radiation at 160 nm exhibit a pronounced and systematic temperature evolution. At cryogenic temperatures (~10 K), luminescence is dominated by narrow-band emission associated with the $^2E \rightarrow {}^4A_2$ transition of Cr^{3+} ions, characterized by high spectral resolution. With increasing temperature up to 300 K, a transition to broadband luminescence is observed, governed by the spin-allowed $^4T_2 \rightarrow {}^4A_2$ transition, accompanied by spectral broadening and faster dynamics. These changes are explained by mechanisms of energy transfer from defect centers, thermal redistribution of level populations, and enhanced electron–phonon coupling. The results are important both for understanding fundamental processes in luminescent materials and for the development of highly efficient optical devices operating under varying temperature conditions.

References

1 Jovanić, B., Bettinelli, M., Radenković, B., Despotović-Zrakić, M., & Bogdanović, Z. (2012). Optical spectroscopy of nanocrystalline $Gd_3Ga_5O_{12}$ doped with Eu^{3+} and high pressures. *Materials Chemistry and Physics*, *132*(2-3), 273–277. DOI: 10.1016/j.matchemphys.2011.11.037

2 Elzbieciak-Piecka, K., Sójka, M., Tian, F., Li, J., Zych, E., & Marciniak, L. (2023). The comparison of the thermometric performance of optical ceramics, microcrystals and nanocrystals of Cr^{3+}-doped $Gd_3Ga_5O_{12}$ garnets. *Journal of Alloys and Compounds*, *963*, 171284. DOI: 10.1016/j.jallcom.2023.171284

3 Wollesen, L., Douissard, P.A., Pauwels, K., Baillard, A., Loiko, P., & Brasse, G. … (2025). Microstructured growth by liquid phase epitaxy of scintillating $Gd_3Ga_5O_{12}$ (GGG) doped with Eu^{3+}. *Journal of Alloys and Compounds*, *1010*, 177267. DOI: 10.1016/j.jallcom.2024.177267

4 Kamińska, A., Brik, M.G., Boulon, G., Karbowiak, M., & Suchocki, A. (2010). Spectroscopy of gadolinium gallium garnet crystals doped with Yb^{3+} revisited. *Journal of Physics: Condensed Matter*, *22*(25), 255501. DOI: 10.1088/0953-8984/22/25/255501

5 Bartosiewicz, K., Markovskyi, A., Horai, T., Szymanski, D., Kurosawa, S., Yamaji, A., Yoshikawa, A., & Zorenko, Y. (2022). A study of Mg^{2+} ions effect on atoms segregation, defects formation, luminescence and scintillation properties in Ce^{3+} doped $Gd_3Al_2Ga_3O_{12}$ single crystals. *Journal of Alloys and Compounds*, *905*, 164154. DOI: 10.1016/j.jallcom.2022.164154

6 Kamińska, A., Duzynska, A., Berkowski, M., Trushkin, S., & Suchocki, A. (2012). Pressure-induced luminescence of cerium-doped gadolinium gallium garnet crystal. *Physical Review B*, *85*(15), 155111. DOI: 10.1103/PhysRevB.85.155111

7 Buryi, M., Gaston-Bellegarde, A.M., Pejchal, J., Levchenko, F., Remeš, Z., Ridzoňová, K., Babin, V., & Chertopalov, S. (2023). The role of Er^{3+} content in the luminescence properties of $Y_3Al_5O_{12}$ single crystals: Incorporation into the lattice and defect state creation. *Crystals*, *13*(4), 562. DOI: 10.3390/cryst13040562

8 Mironova-Ulmane, N., Popov, A.I., Antuzevics, A., Krieke, G., Elsts, E., Vasil'chenko, E., Sildos, I., Puust, L., Ubizskii, S.B., & Sugak, D. … (2020). EPR and optical spectroscopy of neutron-irradiated $Gd_3Ga_5O_{12}$ single crystals. *Nuclear Instruments and Methods in Physics Research Section B: Beam Interactions with Materials and Atoms*, *480*, 22–26. DOI: 10.1016/j.nimb.2020.05.027

9 Mironova-Ulmane, N., Sildos, I., Vasil'chenko, E., Chikvaidze, G., Skvortsova, V., Kareiva, A., Muñoz-Santiuste, J.E., Pareja, R., Elsts, E., & Popov, A.I. (2018). Optical absorption and Raman studies of neutron-irradiated $Gd_3Ga_5O_{12}$ single crystals. *Nuclear Instruments and Methods in Physics Research Section B: Beam Interactions with Materials and Atoms*, *435*, 306–312. DOI: 10.1016/j.nimb.2018.01.041

10 Karipbayev, Z.T., Kumarbekov, K., Manika, I., Dauletbekova, A., Kozlovskiy, A.L., Sugak, D., Ubizskii, S.B., Akilbekov, A., Suchikova, Y., & Popov, A.I. (2022). Optical, structural, and mechanical properties of $Gd_3Ga_5O_{12}$ single crystals irradiated with $^{84}Kr^+$ ions. *Physica Status Solidi (B)*, *259*(9), 2100415. DOI: 10.1002/pssb.202100415

11 Tulegenova, A.T., Nogaibekova, G.Zh., Saidazimov, I.A., Vilchinskaya, S.S., & Markhabayeva, A.A. (2024). Spectral Characteristics of Photoluminescence Synthesized in the Field of Radiation YAGG Phosphors with Different Al/Ga Ratio. *Bulletin of the University of Karaganda — Physics*, *4*, 114–122. DOI: 10.31489/2024PH4/114-122

12 Aralbayeva, G.M., Manika, I., Karipbayev, Zh., Suchikova, Y., Kovachov, S., Sugak, D., & Popov, A.I. (2023). Micromechanical Properties of $Gd_3Ga_5O_{12}$ Crystals Irradiated with Swift Heavy Ions. *Journal of Nano- and Electronic Physics*, *15*(5), 05020. DOI: 10.21272/jnep.15(5).05020

13 Orucu, H., Ozen, G., Collins, J., & Di Bartolo, B. (2009). Temperature dependence of the luminescence spectra of garnet crystals doped with chromium ions. *Optical Materials*, *31*(7), 1065–1070. DOI: 10.1016/j.optmat.2007.12.016

14 Lupei, V., Elejalde, M. J., Brenier, A., & Boulon, G. (1994). Spectroscopic properties of Fe^{3+} in GGG and the effect of codoping with rare-earth ions. *Journal de Physique IV*, *4*(C4), 303–306. DOI: 10.1051/jp4:1994478

15 Kniec, K., Ledwa, K. A., Maciejewska, K., & Marciniak, L. (2020). Intentional modification of the optical spectral response and relative sensitivity of luminescent thermometers based on Fe^{3+}, Cr^{3+}, Nd^{3+} co-doped garnet nanocrystals by crystal field strength optimization. *Materials Chemistry Frontiers*, *4*(6), 1697–1705. DOI: 10.1039/D0QM00097C

16 Omelkov, S.I., Chernenko, K., Ekström, J.C., Jurgilaitis, A., Khadiev, A., Kivimäki, A., & Kirm, M. (2022). Recent advances in time-resolved luminescence spectroscopy at MAX IV and PETRA III storage rings. *Journal of Physics: Conference Series*, *2380*, 012135. DOI: 10.1088/1742-6596/2380/1/012135

17 Kalinko, A., Kotlov, A., Kuzmin, A., Pankratov, V., Popov, A. I., & Shirmane, L. (2011). Electronic excitations in $ZnWO_4$ and $Zn_xNi_{1-x}WO_4$ ($x = 0.1$–0.9) using VUV synchrotron radiation. *Central European Journal of Physics*, *9*(2), 432–437. DOI: 10.2478/s11534-010-0128-1

18 Pankratov, V., Popov, A. I., Kotlov, A., & Feldmann, C. (2011). Luminescence of nano- and macrosized $LaPO_4$:Ce, Tb excited by synchrotron radiation. *Optical Materials*, *33*(7), 1102–1105. DOI: 10.1016/j.optmat.2010.12.041

19 Zhunusbekov, A.M., Karipbayev, Z.T., Tolegenova, A., Kumarbekov, K.K., Nurmoldin, E.E., Baizhumanov, M.M., Kotlov, A., & Popov, A.I. (2024). Comparative VUV synchrotron excitation study of YAG:Eu and YAG:Cr ceramics. *Crystals*, *14*(5), 897. DOI: 10.3390/cryst14050897

20 Zhunusbekov, A.M., Strelkova, A.V., Karipbayev, Z.T., Kumarbekov, K.K., Akilbekov, A., Kassymkhanova, R.N., Kassymzhanov, M.T., Smortsova, Y., & Popov, A.I. (2025). Luminescence investigation of BaMgF4 ceramics under VUV synchrotron excitation. *Crystals*, *15*(2), 127. DOI: 10.3390/cryst15020127

21 Ghimire, K., Haneef, H.F., Collins, R. W., & Podraza, N.J. (2015). Optical properties of single-crystal Gd3Ga5O12 from the infrared to ultraviolet. *Physica Status Solidi (B)*, *252*(9), 2191–2198. DOI: 10.1002/pssb.201552115

22 Orucu, H., Ozen, G., Collins, J., & Di Bartolo, B. (2011). Spectroscopy of chromium doped garnets in a wide temperature range. *MRS Proceedings*, *1053*, EE04-01. DOI: 10.1557/PROC-1053-EE04-01

23 Varney, C.R., Reda, S.M., Mackay, D.T., Rowe, M.C., & Selim, F.A. (2011). Strong visible and near-infrared luminescence in undoped YAG single crystals. *AIP Advances*, *1*(4), 042170. DOI: 10.1063/1.3671646

24 Gluchowski, P. & Chaika, M. (2024). Crystal-field strength variations and energy transfer in Cr^{3+}-doped GGG transparent nanoceramics. *The Journal of Physical Chemistry C*, *128*(23), 9641–9651. DOI:10.1021/acs.jpcc.4c01658

25 Somakumar, A.K., Bulyk, L.-I., Tsiumra, V., Barzowska, J., Xiong, P., Lysak, A., Zhydachevskyy, Y., & Suchocki, A. (2023). High-Pressure Near-Infrared Luminescence Studies of Fe^{3+}-Activated $LiGaO_2$. *Inorganic Chemistry*, *62*(31), 12434–12444. DOI: 10.1021/acs.inorgchem.3c01627

26 Müller, R., Mangold, M., Bauer, S., Huber, F., Herr, U., & Thonke, K. (2022). Zeeman spectroscopy of the internal transition $^4T_1 \rightarrow {}^6A_1$ of Fe^{3+} ions in ZnO. *Journal of Applied Physics*, *132*(6), 065702. DOI:10.1063/5.0098499

Г.М. Аралбаева, Ж.Т. Карипбаев, А.М. Жунусбеков, А. Толегенова,
А. Какимов, Я.О. Сычикова, С. Убизский, А.И. Попов, Г.Е. Сагындыкова

Gd₃Ga₅O₁₂ монокристалдарындағы Cr және Fe қоспаларының төмен температуралы люминесценциялық қасиеттері

Мақалада $Gd_3Ga_5O_{12}$ (GGG) монокристалдарының люминесценциялық қасиеттеріне Cr^{3+} және Fe^{3+} иондарының еріксіз қоспаларының әсері қарастырылды. 10–300 K температура диапазонында жоғары энергиялы синхротрондық сәулелену мен қоздырылған спектрлердің сипаттық ерекшеліктері талданды. 10 K температурада люминесценция негізінен Cr^{3+} иондарының спинге тыйым салынған $^2E \rightarrow {}^4A_2$ ауысуынан туындайтын сызықты сәулелену мен анықталатынын көрсетілді, бұл электрон–фонондық байланысының әлсіздігін және кристалдың жоғары біртектілігін көрсетеді. Температура артқан сайын бұл ауысудың интенсивтілігі айтарлықтай төмендеп, кеңжолақты люминесценция пайда болады. Ол спинге рұқсат етілген $^4T_2 \rightarrow {}^4A_2$ ауысуымен және Fe^{3+} иондарының сәулеленуімен байланысты. Спектрлердің температуралық эволюциясы Cr^{3+} иондарының қозған күйлерінің жылулық қайта бөлінуімен, деңгей аралық күйлердің араласуы мен және тор тербелістерінің әсерінен Fe^{3+} ауысуларының спиндік тыйымының ішінара жойылуымен түсіндіріледі. Зерттеу негізінде энергияны тасымалдау және сәулеленбейтін релаксация процестеріндегі қоспа орталықтарының рөлі туралы қорытындылар жасалды. Нәтижелер іргелі фотоника үшін де, кең температура диапазонында жұмыс істейтін тиімді люминесценттік материалдар мен оптикалық құрылғыларды әзірлеу үшін де маңызды.

Кілт сөздер: гадолиний галлий гранаты (GGG), синхротрондық сәулелену, Cr^{3+} иондары, Fe^{3+} иондары, люминесценция, қозуспектрлері, температураға тәуелділік, энергия тасымалдау, электрон-фонондық байланыс, сәулеленбейтін релаксация, қоспаорталықтары, оптикалық қасиеттер

Г.М. Аралбаева, Ж.Т. Карипбаев, А.М. Жунусбеков, А. Толегенова,
А. Какимов, Я.О. Сычикова, С. Убизский, А.И. Попов, Г.Е. Сагындыкова

Низкотемпературное поведение люминесценции примесей Cr и Fe в монокристаллах Gd₃Ga₅O₁₂

В данной статье рассматривается влияние непреднамеренных ионов-примесей Cr^{3+} и Fe^{3+} на люминесцентные свойства монокристаллов $Gd_3Ga_5O_{12}$ (GGG). Проанализированы характерные особенности спектров, возбуждённых высокоэнергетическим синхротронным излучением в температурном диапазоне 10–300 K. Показано, что при 10 K люминесценция определяется узкополосным излучением ионов Cr^{3+}, обусловленным спин-запрещённым переходом $^2E \rightarrow {}^4A_2$, что свидетельствует о слабой электрон-фононной связи и высокой однородности кристалла. Выявлено, что с повышением температуры интенсивность данного перехода существенно снижается, тогда как проявляется широкополосная люминесценция, связанная со спин-разрешённым переходом $^4T_2 \rightarrow {}^4A_2$ и вкладом излучения ионов Fe^{3+}. Доказано, что температурная эволюция спектров обусловлена тепловым перераспределением

населённостей уровней Cr^{3+}, межуровневым смешением состояний, а также частичным снятием спинового запрета переходов Fe^{3+} за счёт колебаний решётки. На основе проведённых исследований сформулированы выводы о роли центров-примесей в процессах переноса энергии и безызлучательной релаксации. Полученные результаты представляют интерес как для фундаментальной фотоники, так и для разработки эффективных люминесцентных материалов и оптических устройств, функционирующих в широком температурном диапазоне.

Ключевые слова: гадолиний-галлиевый гранат (GGG), синхротронное излучение, ионы Cr^{3+}, ионы Fe^{3+}, люминесценция, спектры возбуждения, температурная зависимость, перенос энергии, электрон-фононное взаимодействие, безызлучательная релаксация, центры-примеси, оптические свойства

Information about the authors

Aralbayeva, Gulnara — PhD, Associate professor, Institute of Physical and Technical Sciences, L.N. Gumilyov Eurasian National University, Astana, Kazakhstan; e-mail:aralbayevagulnara@gmail.com; ORCID ID https://orcid.org/0000-0002-6827-5567; Scopus Author ID: 6505898119

Karipbayev, Zhakyp (*corresponding author*) — PhD, Associate professor, Institute of Physical and Technical Sciences, L.N. Gumilyov Eurasian National University, Astana, Kazakhstan; e-mail: Karipbayev_zht_1@enu.kz; ORCID ID https://orcid.org/0000-0003-4066-1826; Scopus Author ID: 56433531200

Zhunusbekov, Amangeldy — Candidate of Physical and Mathematical Sciences, Associate professor, Institute of Physical and Technical Sciences, L.N. Gumilyov Eurasian National University, Astana, Kazakhstan; e-mail: zhunusbekov_am@enu.kz; ORCID ID https://orcid.org/0000-0003-2052-0065; Scopus Author ID: 6508013732

Tolegenova, Akbota — PhD student in Physics and Technical Sciences, Institute of Physical and Technical Sciences, L.N. Gumilyov Eurasian National University, Astana, Kazakhstan; ORCID ID https://orcid.org/0000-0001-7459-1251

Kakimov, Askhat — PhD student in Physics and Technical Sciences, Institute of Physical and Technical Sciences, L.N. Gumilyov Eurasian National University, Astana, Kazakhstan; e-mail: kakimov_ab_2@enu.kz ORCID IDhttps://orcid.org/0009-0005-7511-7443; Scopus Author ID: 58692951700

Suchikova, Yana — Vice-Rector for Research, Doctor of Technical Sciences, Associate Professor, Berdyansk State Pedagogical University (relocated to Zaporizhzhia), Ukraine; e-mail: yanasuchikova@gmail.com; ORCID ID https://orcid.org/0000-0003-4537-966X; Scopus Author ID: 36523907500

Ubizskii, Sergii — Senior Researcher, Associate professor, Lviv Polytechnic National University, S. Bandera Str. 12, Lviv, 79013, Ukraine; e-mail: essfero@gmail.com; ORCID ID https://orcid.org/0000-0001-8898-5374; Scopus Author ID: 6701890955

Popov, Anatoli — Doctor of Physics, Senior Researcher, Institute of Solid State Physics, University of Latvia, Riga, Latvia; e-mail: popov@latnet.lv; ORCID ID https://orcid.org/0000-0003-2795-9361; Scopus Author ID: 7402986699

Sagyndykova, Gibrat — Acting Associate Professor, Candidate of Physical and Mathematical Sciences, Institute of Physical and Technical Sciences, L.N. Gumilyov Eurasian National University, Astana, Kazakhstan; e-mail: gibrat75@mail.ru; ORCID ID https://orcid.org/0000-0001-5792-8799; Scopus Author ID: 58772276200

D.B. Buitkenov[1], N.S. Raisov[1✉], N.Ye. Bazarov[2],
G.T. Tleubergenova[1], A.K. Khassenov[3], D.Zh. Karabekova[3]

[1]Research Center "Surface Engineering and Tribology",
Sarsen Amanzholov East Kazakhstan University, Ust-Kamenogorsk, Kazakhstan;
[2]LLP "PlasmaScience", Ust-Kamenogorsk, Kazakhstan;
[3]Buketov Karaganda National Research University, Karaganda, Kazakhstan

Tribological Performance of Self-Fluxing Ni-Based Coatings Deposited by Gas-Flame Spraying

In the present study, a comprehensive analysis of the microstructure, phase composition, surface morphology, and tribological properties of self-fluxing NiCrFeBSiC alloy coatings produced by flame spraying was conducted. Particular attention was paid to evaluating the influence of different heat treatment regimes — flame heating and furnace heating — on the coating characteristics. X-ray diffraction analysis revealed the formation of the $FeNi_3$ phase, along with Cr_7C_3, $Cr_{23}C_6$ carbides and boride compounds, which significantly affect wear resistance. Goniometric measurements showed that the highest surface hydrophobicity (contact angle of 89.6°) was achieved after furnace heat treatment. Scanning electron microscopy and profilometry studies established that furnace heating provides the densest and smoothest structure with the lowest surface roughness (Ra = 13.388 μm). Tribological tests confirmed that this treatment provides the lowest and most stable coefficient of friction (0.138 ± 0.003), which correlates with the microstructural features of the wear track. The obtained results demonstrate the high efficiency of furnace heat treatment in enhancing the performance characteristics of NiCrFeBSiC-based coatings.

Keywords: self-fluxing alloys, gas-flame spraying, NiCrFeBSiC, heat treatment, steel 45

✉*Corresponding author*: Raisov, Nurmahanbet, nurmakhanbetraisov@gmail.com

Introduction

Structural materials with high performance characteristics capable of operating under severe conditions—such as increased friction, exposure to aggressive environments, and thermal loads—are in great demand. Such service conditions inevitably lead to wear of components, resulting in frequent repairs, replacement of parts, and an increase in production costs, which in turn causes significant economic losses [1, 3].

However, manufacturing components entirely from expensive wear-resistant materials is associated with a sharp rise in production costs and technological difficulties during machining. A rational solution to this problem is the application of wear-resistant coatings or the restoration of worn elements, which makes it possible to significantly extend their service life [1]. Among such solutions, a special place is occupied by coatings made of self-fluxing nickel-based alloys, which have found wide application in mechanical engineering [2, 3]. Thermal spray coatings, including plasma-sprayed ones, based on Ni-Cr-Fe-B-Si-C systems are used to increase the wear resistance of working surfaces of components. NiCrFeBSiC alloys have proven

themselves in service under conditions of intensive friction—in coal boiler components, heat exchangers, turbines, tools, extruders, plungers, rolling mill rolls, and agricultural machinery. These coatings are characterized by high resistance to adhesive wear and corrosion both at ambient and elevated temperatures. To improve their performance properties, the coatings are subjected to remelting after deposition. Due to the presence of boride and carbide phases in their structure, such materials exhibit enhanced wear resistance under abrasive conditions [4, 7].

The formation of the required tribotechnical properties of remelted Ni-Cr-Fe-B-Si coatings is possible only under strictly defined heat treatment regimes (in the range of 1000–1373 K), since these alloys belong to eutectic systems and are highly sensitive to thermal process parameters [5, 6]. Remelting can be carried out by various methods: flame heating, furnace heating, or laser treatment. Although a number of studies [6–10] have examined in detail the structure, properties, and phase transformations during the remelting of self-fluxing NiCrBSiC coatings, issues related to their tribological behavior and wear mechanisms under friction conditions have not been sufficiently addressed. In this regard, the present work is devoted to the investigation of the tribological behavior of NiCrFeBSiC coatings produced by flame spraying followed by remelting.

Materials and methods

As the substrate material, structural carbon steel grade AISI 1045 was selected. This steel is widely used in industry for the production of shaft gears, crankshafts, camshafts, gears, spindles, tires, cylinders, cams, and other normalized, tempered (improved), and surface-hardened components that require increased strength. According to ASTM A331, AISI 1045 steel has the following composition (Table 1).

T a b l e 1

Chemical composition of steel 1045

C	Si	Mn	Ni	S	P	Cr	Cu	Fe
0.42–0.5	0.17–0.37	0.5–0.8	< 0.3	< 0.04	< 0.035	< 0.25	< 0.3	base

A steel rod of carbon steel grade AISI 1045 with a diameter of 50 mm was cut into disks 5 mm thick. The surface was mechanically treated by grinding with abrasive paper up to P600 grit. To improve the adhesion of the applied coating, the disk surfaces were additionally treated by abrasive blasting using electrocorundum (Al_2O_3) with a particle size of 40 μm. After sandblasting, residual abrasive particles and dust were removed by blowing with compressed air. In order to eliminate organic and inorganic contaminants (oils, oxide films), the samples were cleaned in an ultrasonic bath using technical-grade ethanol. The ultrasonic cleaning was carried out for 10 minutes at a frequency of 40 kHz and a solution temperature not exceeding 35 °C. Prior to coating deposition, the samples were preheated to 200–250 °C by flame heating to improve adhesion to the substrate. The surface temperature was monitored using a RoHS-compliant infrared pyrometer, model DT8016E, with a measurement range of –50 °C to 1600 °C and an accuracy of ±2 °C.

The powders have a spherical structure with particle sizes ranging from 100 to 200 μm (Fig. 1).
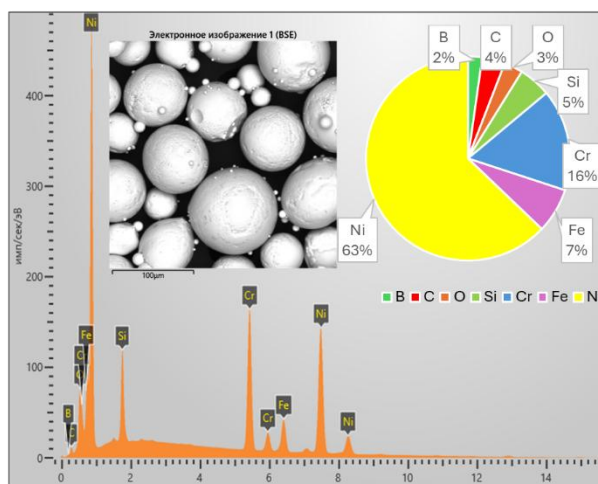

Figure 1. Morphology of self-fluxing NiCrFeBSiC powder

For the coating deposition, a flame spraying unit manufactured by Metal Coat was used, equipped with a 6PM-II powder gun and an MPF700 powder feeder. The general view of the setup and the schematic diagram of the spray gun are shown in Figure 2. The operating principle of this unit consists in melting powder particles by combustion of a gas mixture composed of acetylene and oxygen. Compressed air was used both for powder transport and for cooling the barrel. The air supplied from the compressor passed through a filter integrated into the outlet pressure regulator in order to prevent contamination of the powders with motor oil particles.

The supply of the gas mixture was monitored and controlled by gas flow meters and a compressed-air control unit. In addition, the system included a powder feed adjustment function to reduce material consumption. The particle flow velocity and flame temperature were measured using a high-speed Tecnar Accuraspray 4.0 diagnostic system (11-12).

The spraying parameters were selected in such a way that the porosity of the coatings did not exceed 10 % (ISO/TR 26946:2011). The spraying regime is presented in Table 2.

T a b l e 2

Gas flame spraying parameters for obtaining coatings

Operation gas	Oxygen	25 NLPM
	Acetylene	15 NLPM
Powder carrier gas	Air	37 NLPM
Spraying distance	200 mm	
Spray time	30 s	

The substrate of AISI 1045 steel was preheated by the flame method to a temperature corresponding to low-temperature tempering, 200–250 °C. After preheating, the microhardness of AISI 1045 steel was measured using the Vickers method at 15 different surface points. Before heating, the average microhardness value of AISI 1045 steel was 196.7 ± 5.3 $HV_{0.3}$, while after heating it increased to 298.6 ± 5.7 $HV_{0.3}$.
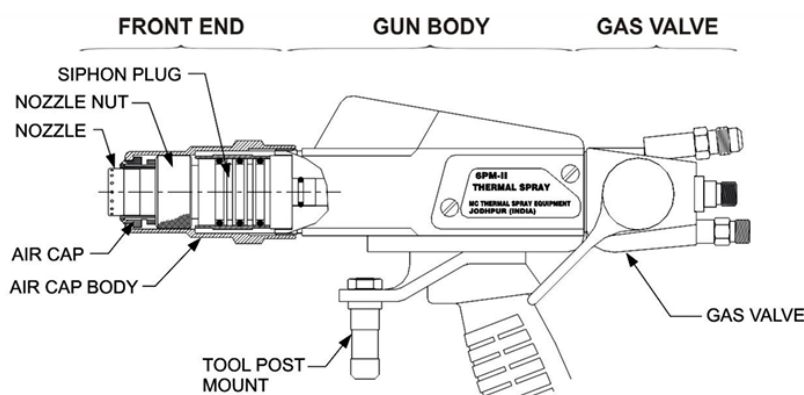

Figure 2. Flame spray gun diagram

The heat treatment of the coatings was carried out by two methods at 1025 °C for 5 minutes: (1) flame heating and (2) furnace heating.

The coating morphology was studied using a SEM 3200 scanning electron microscope (China), equipped with an electron probe attachment for local microanalysis: a Bruker energy-dispersive spectrometer (EDS).

X-ray diffraction (XRD) analysis of the initial powder and coatings was performed on a PANalytical X'PERT PRO diffractometer using CuKα radiation. The diffraction data were collected in the 2θ range of 10–90° with a step size of 0.02° and a counting time of 0.5 s per step.

Tribological tests of the coatings were conducted using a ball-on-disk configuration. As a counter body, a 100Cr6 steel ball with a diameter of 6 mm was used. The applied load was 10 N, sliding speed 5 cm/s, track radius 2 mm, and sliding distance 200 m.

Potentiodynamic polarization curves were recorded on a CorrTest CS310 potentiostat using a three-electrode cell, as shown in Figure 3. The scanning rate was 0.5 mV/s within a potential range of –0.8 V to

+0.8 V. A 3.5 % HCl solution was used as the electrolyte. A platinum mesh served as the working electrode, while saturated silver chloride electrodes were used as both reference and auxiliary electrodes. The current and potential data obtained were processed with the CorrTest CS310 software, which was used to construct polarization curves providing information on corrosion potential, corrosion current, and passivation behavior [9].

Adhesion strength tests were performed in accordance with ASTM C633-15 on a WDW-100kN tensile testing machine, equipped with a self-aligning load application module. For the adhesion test, samples with a diameter of 25.4 mm and a thickness of 7 mm were prepared. Prior to spraying, the samples were subjected to sandblasting and cleaned in an ultrasonic bath with ethanol. The tensile loading rate was 0.020 mm/s [13–17].
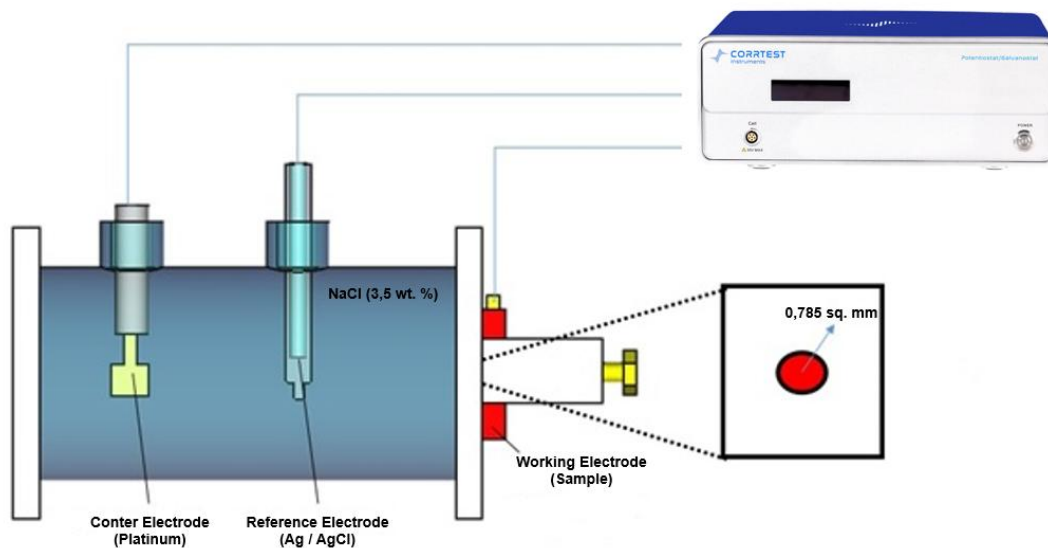

Figure 3. Schematic diagram of the setup Potentiostat CS310
for conducting an electrochemical corrosion experiment [9]

Results and discussion

To study the microstructure and elemental composition of the coating based on NiCrFeBSiC, energy-dispersive X-ray spectral analysis (EDS) was carried out as part of scanning electron microscopy (SEM). The results are presented in Figure 4 in the form of element distribution maps and a summary table of mass fractions.

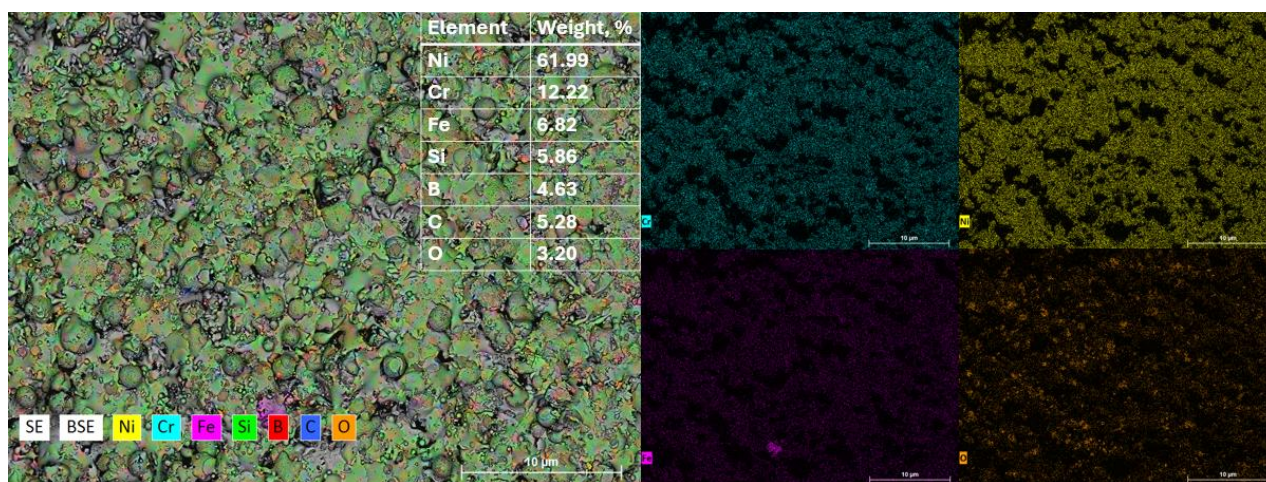| Element	Weight, %
Ni	61.99
Cr	12.22
Fe	6.82
Si	5.86
B	4.63
C	5.28
O	3.20

Figure 4. Map of distribution of elements on the surface of coatings made of self-fluxing NiCrFeBSiC powder

According to EDS analysis, the coating consists of the following elements (wt.%): Ni — 61.99 %, Cr — 12.22 %, Fe — 6.82 %, Si — 5.86 %, B — 4.63 %, C — 5.28 %, and O — 3.20 %. The combined

SEM–EDS mapping shows a uniform distribution of nickel (yellow), chromium (blue), iron (purple), silicon (green), boron (red), and carbon (orange).

Figure 5 presents the XRD patterns of the initial powder and coatings, designated as SF1, SF2, and SF3, which differ in the type of thermal treatment. Coating SF1 corresponds to the as-sprayed layer without additional heat treatment, SF2 represents the coating subjected to flame heating, and SF3 is the coating after furnace annealing.
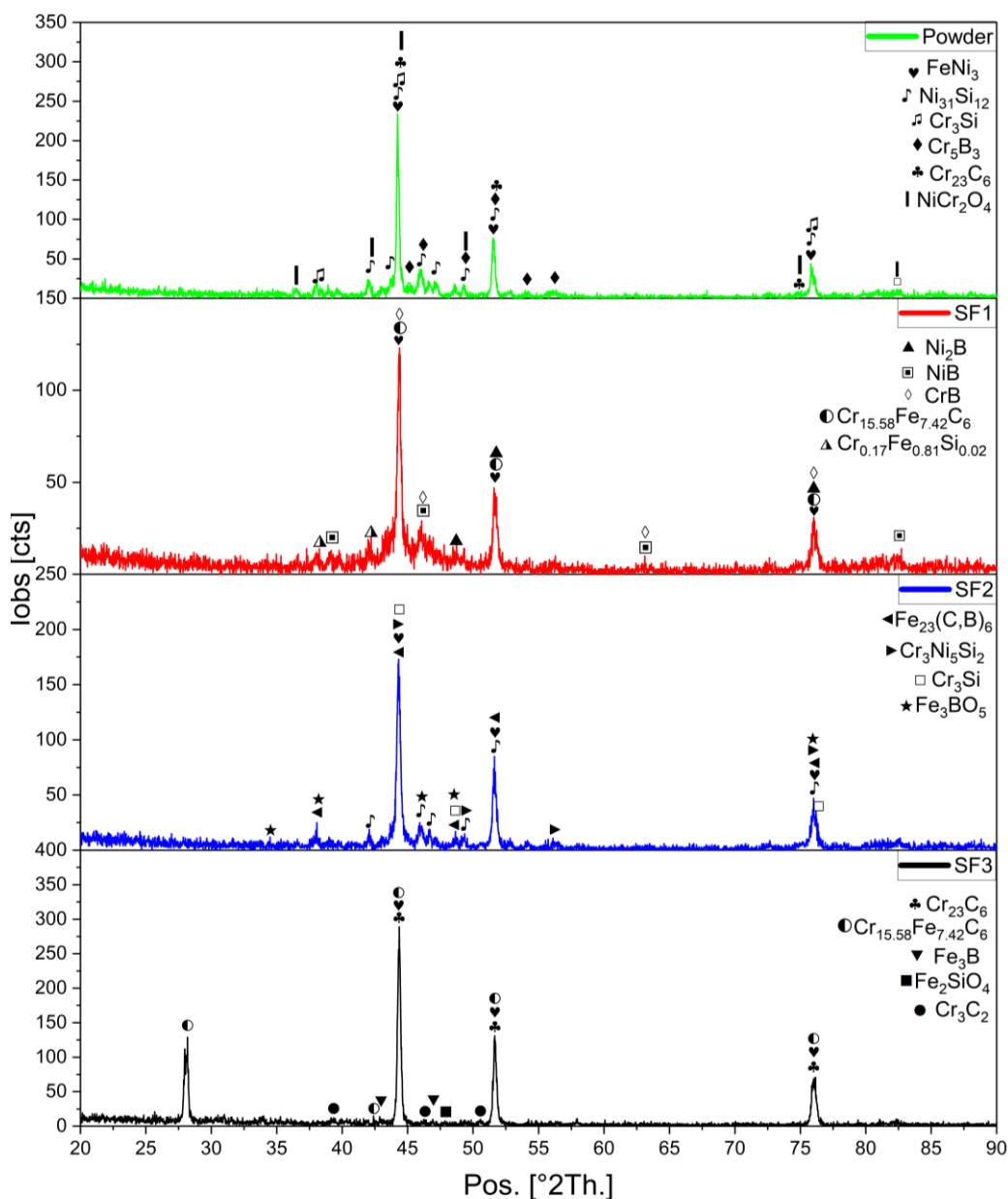

Figure 5. XRD spectra of powder and NiCrFeBSiC coatings: (SF1) without heat treatment, (SF2) after heating with a flame of a gas flame gun, (SF3) after heating in a furnace

Analysis of the diffraction patterns of the initial powder revealed the presence of $FeNi_3$, $Ni_{31}Si_{12}$, Cr_3Si, Cr_5B_3, $Cr_{23}C_6$, and $NiCr_2O_4$ phases, which is typical for nickel-based composite powders with boride–silicide and oxide inclusions. After flame spraying and subsequent heat treatment, significant changes in the phase composition of the coatings were observed [18-19].

In coating SF1, the phases Ni_2B, NiB, CrB, as well as carbide structures of the $Cr_{15.58}Fe_{7.42}C_6$ type and silicide $Cr_{0.17}Fe_{0.81}Si_{0.02}$ were identified, indicating the formation of new compounds during spraying while retaining part of the boride components of the initial powder. Coating SF2, subjected to flame heating, exhib-

ited a more complex phase composition: $Fe_{23}(C, B)_6$, $Cr_3Ni_5Si_2$, Fe_3BO_5, along with residual $FeNi_3$ and Cr_3Si. This suggests active interfacial reactions and diffusion processes enhanced by localized heating.

The SF3 coating, which underwent furnace heat treatment, contained phases such as $Cr_{23}C_6$, $Cr_{15.58}Fe_{7.42}C_6$, Cr_3C_2, Fe_3B, and Fe_2SiO_4 [20–23]. The predominance of stable carbides and borides combined with the minimal content of oxide phases indicates that furnace annealing promotes the formation of thermodynamically stable equilibrium structures, ensuring a dense and ordered microstructure of the coating.

Thus, the post-spraying thermal treatment regime has a decisive influence on the phase composition of the coatings. Flame heating promotes the formation of complex boride–silicide phases, whereas furnace annealing favors the stabilization of carbide structures and the reduction of oxide content, which may positively affect the performance properties of the coatings.

Such phase behavior is consistent with literature data, which note that heat treatment promotes the formation of stable strengthening phases in Ni-based coatings [24–26].

Figure 8 clearly shows that subsequent heat treatment significantly reduces the coating thickness, as well as the number and size of pores. This trend occurs due to more effective particle melting and the filling of pores with molten material [8]. The highest porosity was recorded in sample SF1, which did not undergo any additional heat treatment. The high porosity value indicates the presence of a large number of unmelted particles.

In coating SF2, which was subjected to short-term flame heating, porosity decreased almost 2.5 times compared to the untreated coating. This indicates partial densification of the near-surface layers and the occurrence of self-fluxing under the influence of temperature (Fig. 6b). The lowest porosity was observed in sample SF3, which underwent furnace heating. The furnace provides more uniform and prolonged heating, which promotes active self-fluxing and improved bonding between coating particles. As a result, the structure becomes denser and more homogeneous (Fig. 6c) [24].
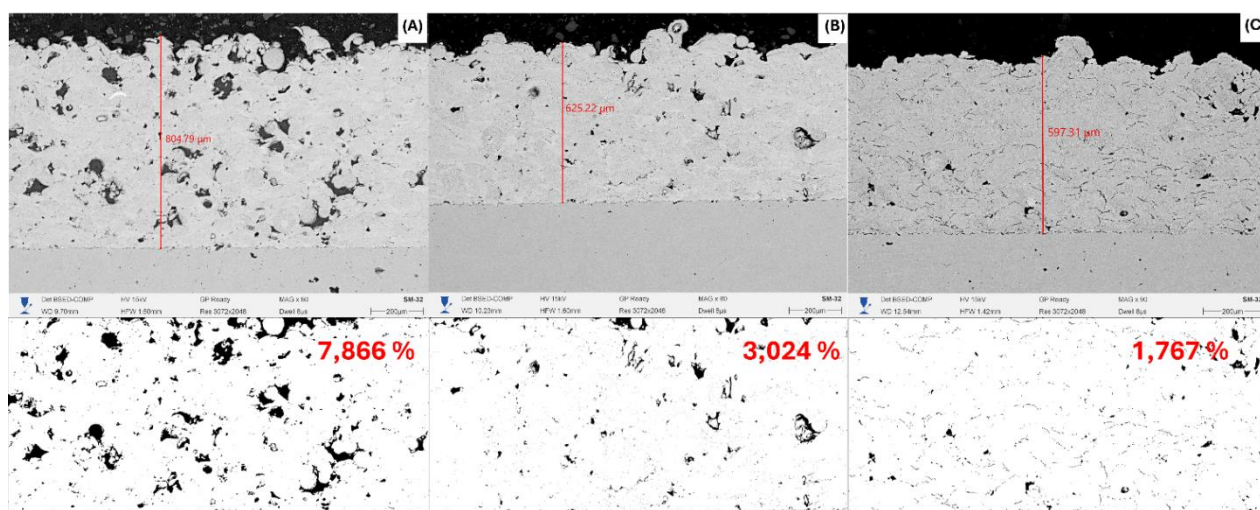

Figure 6. Study of the porosity and thickness of NiCrFeBSiC coatings on a cross section:
(a) without heating — SF1, (b) flame heating — SF2, (c) furnace heating — SF3

For a comprehensive evaluation of the morphology and surface topography of NiCrFeBSi-based coatings subjected to different heat treatment regimes, studies were carried out using SEM and profilometry. Figure 7 shows surface micrographs (top row) and the corresponding surface roughness profiles (bottom row), reflecting the actual height deviations in the selected areas. The SEM images demonstrate the typical microstructure of a thermally sprayed coating, characterized by a dense yet moderately porous structure, which results from the partial melting of particles during spraying [25]. Good interparticle bonding indicates that sufficient temperature was achieved during deposition. A decrease in the Ra parameter from 31.860 μm (as-sprayed) to 13.388 μm (furnace-treated) demonstrates a clear trend towards improved surface quality with the application of heat treatment. The SEM micrographs confirm that thermal treatment promotes densification of the structure, a reduction in porosity, and surface smoothing. The obtained results indicate a significant influence of heat treatment on the morphological and tribological properties of the coatings and highlight the advantages of uniform furnace heating compared to flame heating [26].
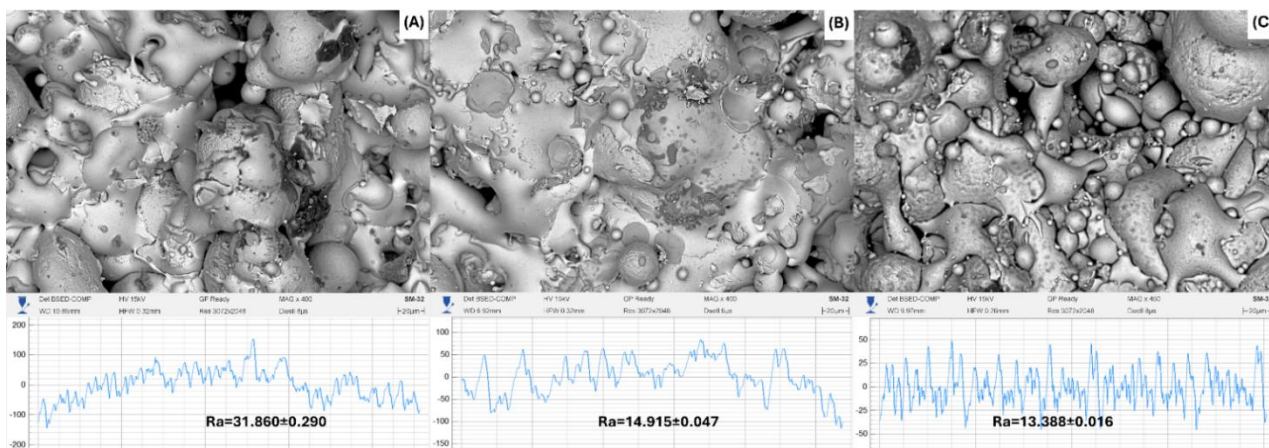
Figure 7. Micrographs of surfaces (top row) and corresponding roughness profile graphs (bottom row):
(*A*) without heat treatment SF1, (*B*) after gas flame heating SF2, (*C*) after heating in a furnace SF3

Tribological tests were conducted to test the wear resistance of the coatings. The results are shown in Figure 8. According to the results of tribological tests with dry friction, it was found that subsequent heat treatment reduces the friction coefficient, thus thermal gas-flame heating and furnace treatment reduced the friction coefficient by 6 times on average for both types of treatment.
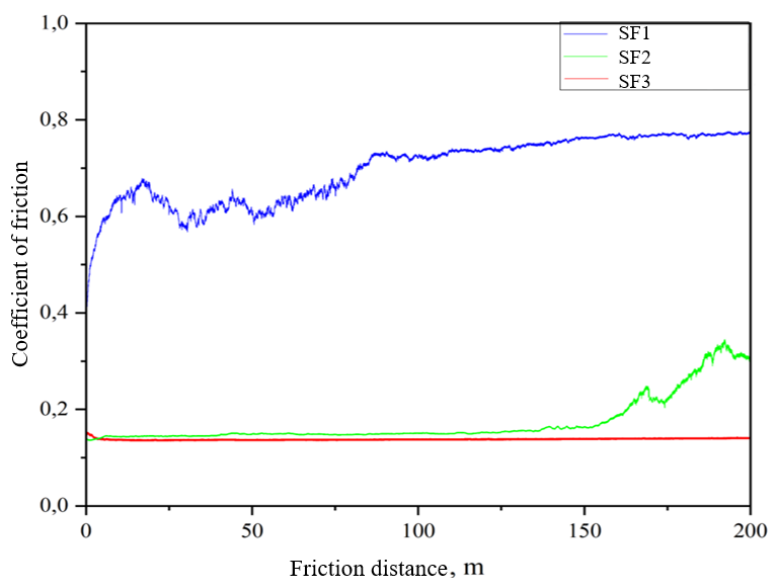

Figure 8. Results of tribological tests of coatings using the "ball-on-disk" scheme under dry friction:
(SF1) without heat treatment, (SF2) after gas-flame heating, (SF3) after heating in a furnace

The most stable and lowest coefficient of friction, $\mu = 0.138 \pm 0.003$, was observed for coating SF3, which underwent furnace heat treatment at 1025 °C followed by slow cooling. The friction coefficient remained nearly constant along the entire wear track, indicating structural uniformity and high quality of the hardened surface, which suggests a reduction in microfractures [27–28]. In the case of flame heating (1025 °C, acetylene–oxygen flame), the coefficient of friction was $\mu = 0.173 \pm 0.050$. Moreover, beginning at a sliding distance of 150 m, an increase in the coefficient of friction was recorded, pointing to a change in the wear mechanism. This trend may be associated with localized densification of the coating structure during flame heating. Although no abrupt fluctuations of the friction coefficient were observed, significant local morphological changes may occur that are not fully reflected in the integral tribometric curve. As shown in [11], under localized temperature spikes and contact with hard inclusions (borides, carbides), plastic deformation of the softer binder matrix can occur, accompanied by strain hardening of the harder particles. To achieve a comprehensive understanding of the wear mechanisms of NiCrFeBSi coatings subjected to different heat treatment regimes, a morphological analysis of the wear track was carried out using scanning elec-

tron microscopy (SEM), as illustrated in Figure 9. This approach was chosen due to the nature of the tribological data obtained and the need for visual confirmation of the proposed processes.
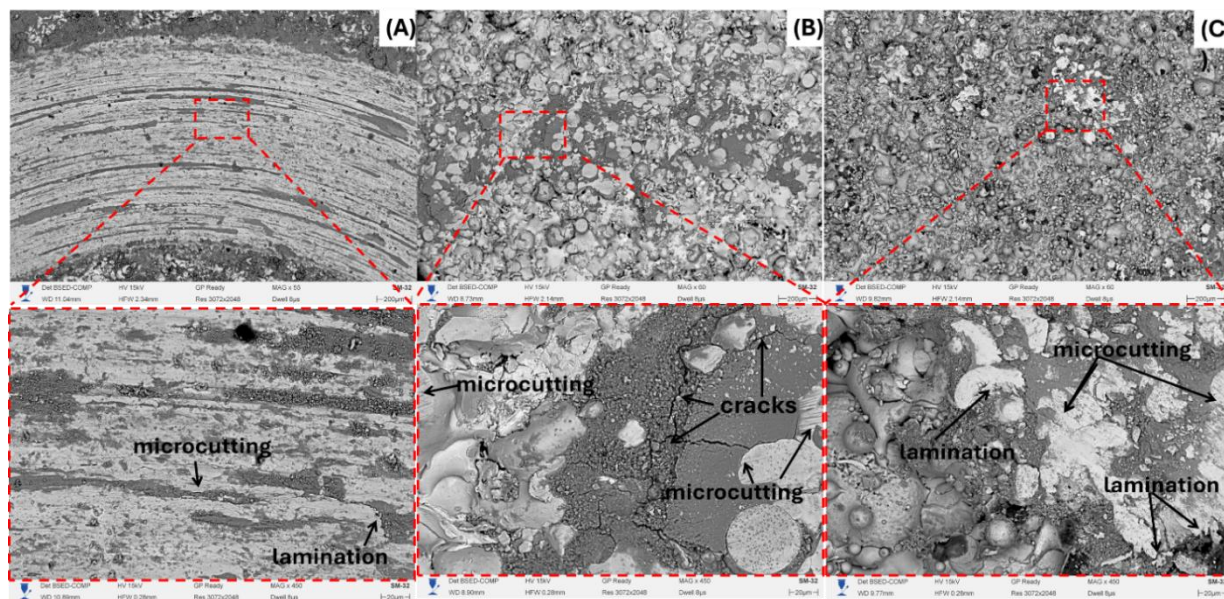

Figure 9. Results of tribological tests using the ball-on-disk scheme under dry friction.
(*A*) without heat treatment SF1, (*B*) after gas-flame heating SF2, (*C*) after heating in a furnace SF3

On the surface of the coating after flame heating, distinct micro-grooves formed during friction, as well as cracks, can be clearly observed. In this context, the micro-grooves result from local abrasive interactions of the counter body with surface inclusions or irregularities of the coating, leading to the removal of microparticles and the formation of elongated traces on the surface. Such areas are often formed in zones where hard phases (carbides, borides) partially protrude above the softer matrix and act as abrasives during sliding. Cracks are formed both along particle boundaries and within the binder phase, indicating a brittle fracture mechanism [29-30].

After furnace treatment, the wear track surface appears more uniform and denser. Although traces of micro-grooves are also present, they are distributed less chaotically and exhibit smaller depth and length. Local layering was also observed, likely occurring along the boundaries of fused particles or between regions with different phase densities. Nevertheless, the overall surface condition confirms a lower degree of wear. This correlates with the low and stable coefficient of friction (0.138 ± 0.003) and indicates a micro-abrasive but plastically adaptive wear mechanism.
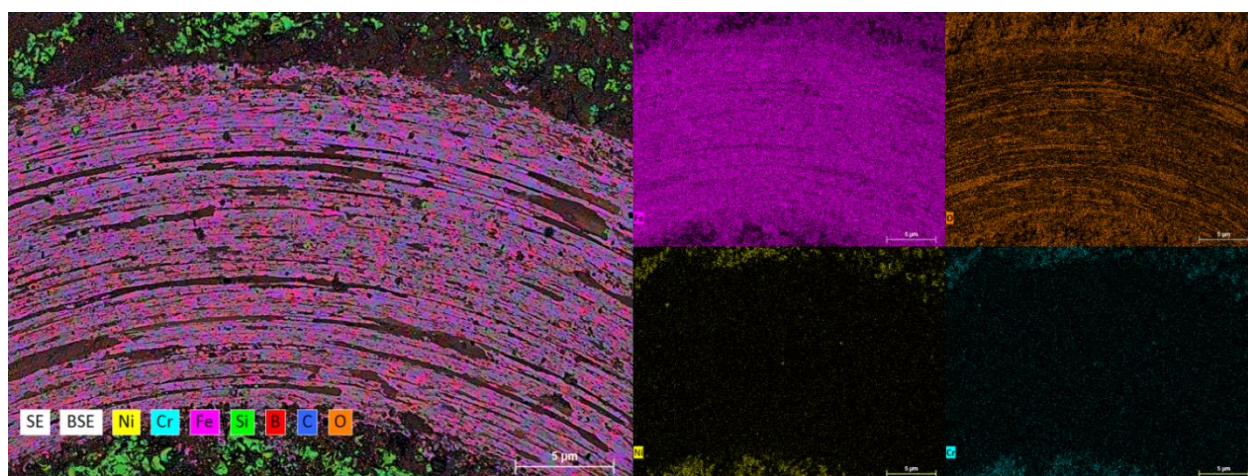

Figure 10. Energy dispersive spectral map (EDS) of the wear track surface of NiCrFeBSi coating
after furnace heat treatment

The presented EDS map confirms that the wear track zone represents the product of intense interaction between the coating and the counter body, accompanied by mechanical damage and thermo-oxidative effects (Fig. 10). The main source of iron in the wear track is the counter body (e.g., a ball made of 100Cr6 steel or an equivalent structural steel). During sliding, especially under localized heating, material transfer from the counter body to the coating surface occurs. The iron worn off from the counter body undergoes surface oxidation, resulting in the formation of iron oxides within the wear track.

The formation of such oxide products of friction is characteristic of oxidative wear, in which oxide films develop on the surface. These films may temporarily reduce the coefficient of friction, but upon their breakdown, they become a source of abrasive particles that accelerate wear [31].

The potentiodynamic curves of all coatings show a significantly higher corrosion potential (Ecorr) compared to AISI 1045 steel (Fig. 11).
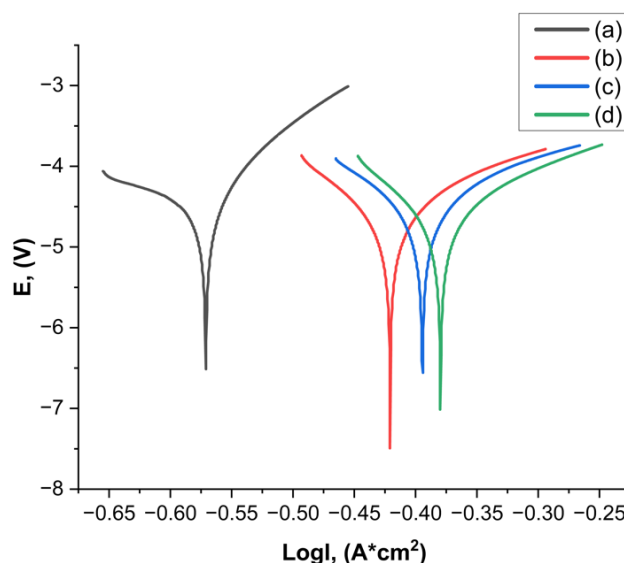

Figure 11. Potentiodynamic curves (*A*) original steel (*B*) without heat treatment SF1,
(*C*) after gas flame heating SF2, (*D*) after heating in a furnace SF3

To describe in detail the corrosion behavior of the samples, the corrosion current was calculated from the slopes of the Tafel sections of the potentiodynamic curves (Table 3).

T a b l e 3

Results of measuring the corrosion resistance of self-fluxing NiCrFeBSiC coatings

Samples	Original Steel AISI 1045	SF1	SF2	SF3
Icorr (A)	0.69218	0.42371	0.39466	0.38963
icorr (A/cm^2)	0.881757962	0.539757962	0.502751592	0.496343949
CR (mm/a)	0.0100873122	0.006174832	0.005751479	0.005678175

The data presented in Table 3 and the potentiodynamic polarization curves show a significant difference in the corrosion resistance of the various types of coatings applied to steel. The table includes key parameters such as corrosion current density (Icorr) and corrosion rate (C.R.), which reflect the materials' behavior in corrosion tests. The coating subjected to furnace heat treatment demonstrates the best performance, with an Icorr value of 0.49634 and a corrosion rate of 0.005678, which are considerably lower compared to other coatings, including AISI 1045 steel and coatings treated by flame heating or left untreated. On the potentiodynamic polarization curve, the plot corresponding to AISI 1045 steel shifts into a more negative potential region, confirming its high corrosion activity. This is consistent with the data in the table, where the corrosion current density and corrosion rate for steel are the highest. In contrast, coatings subjected to subsequent flame heating exhibit improved results; however, their corrosion resistance still remains inferior to that of the furnace-treated coating. Such a combination of processing conditions appears to create a denser and more corrosion-protective surface, which prevents the formation of microcracks and moisture retention, thereby

significantly slowing down the corrosion process. Overall, the coatings treated in the furnace showed the best corrosion resistance among all studied variants, making them the most promising for applications requiring protection against aggressive environments.

The data obtained from the adhesion strength measurements characterize the bonding force between the coating and the substrate (base material), which is one of the key quality indicators of thermally sprayed coatings. The results of the adhesion strength tests are presented in the summary of results (Table 4).

T a b l e 4

**Summary table of the results of the study of the properties
of the characteristics of self-fluxing NiCrFeBSi coatings**

Sample name	Adhesion strength, MPa	Microhardness HV_5GPa	Wettability, º	Friction coefficient	Roughness, µm
SF1	18	528.7±2.3	53.152	0.648±0.070	31.860±0.290
SF2	27	771.6±4.6	79.875	0.173±0.050	14.915±0.047
SF3	34	922.4±5.7	89.603	0.138±0.003	13.388±0.016

The results of contact angle measurements performed using the sessile drop method with an optical goniometer are also presented in Table 4. The data indicate a significant influence of the heat treatment regime on the wettability of the coating surfaces. The lowest contact angle (53.152°) was recorded for the coating without additional heat treatment. This suggests high surface energy and a possible microporous structure that promotes oil wetting. After flame heat treatment, the contact angle increased to 79.875°, which can be explained by densification of the structure, partial sintering of particles, and reduction of surface microroughness. The highest contact angle (89.603°) was observed in the furnace-treated sample, which may be associated with the formation of a more uniform, dense, and possibly oxidized layer with reduced wettability. Thus, it can be concluded that heat treatment reduces wettability, which may be a positive factor for the operation of coatings under oil-lubricated friction conditions.

Figure 12 presents SEM images of indenter impressions obtained from microhardness testing of NiCrFeBSiC coatings subjected to different types of heat treatment. Examination of the impressions made it possible to establish correlations between the type of thermal treatment, the microstructural state, and the local hardness of the material. Figure 12(*A*) shows the indenter impression on the coating without heat treatment. Cracks and depressions in the indentation area are clearly visible, associated with the presence of a pore beneath the surface layer. Such local load-bearing instability leads to a reduced microhardness of 528.7 ± 2.3 HV. The data indicate high brittleness of the coating without additional thermal stabilization. Figure 12(*B*) illustrates the structure of the coating after flame heating. In this case, the structure is denser compared to the untreated sample. The impression has a symmetrical shape, and the number of cracks is reduced. The microhardness is 771.6 ± 4.6 HV, which indicates partial structural stabilization and a reduction in internal stresses. Figure 12(*C*) corresponds to the coating subjected to furnace heating. Here, minimal surface damage around the indentation is observed, with no pronounced cracks or depressions, indicating high structural integrity. This is reflected in the highest microhardness value—922.4 ± 5.7 HV—confirming the effectiveness of furnace heat treatment in improving the mechanical properties of the coating.
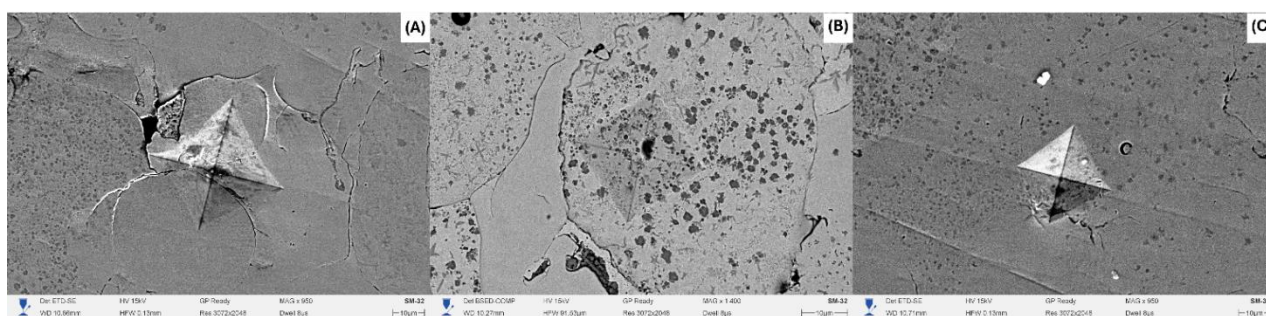

Figure12. SEM images of indenter imprints on NiCrFeBSiC coatings:
(*A*) without heat treatment, (*B*) after flame heating, (*C*) after heating in a furnace

Conclusion

In this study, a comprehensive investigation was carried out on the structural, surface, and tribological characteristics of self-fluxing NiCrFeBSi alloy coatings deposited by flame spraying. It was established that subsequent heat treatment has a significant influence on the formation of the microstructure, phase composition, and performance properties of the coatings. X-ray diffraction analysis revealed the formation of carbide phases (Cr_7C_3, $Cr_{23}C_6$) and intermetallic compounds ($FeNi_3$). Profilometric measurements and SEM micrographs confirmed that uniform furnace heating contributes to a substantial reduction in surface roughness (down to Ra = 13.388 μm), the formation of a dense and homogeneous structure, and the elimination of porosity and defects typical of coatings without additional treatment.

The results of tribological testing showed that the most stable friction characteristics were demonstrated by the coating subjected to furnace heat treatment: the coefficient of friction was 0.138 ± 0.003 and remained constant throughout the entire wear track. In contrast, coatings without heat treatment or treated by flame heating exhibited higher and less stable friction coefficients, accompanied by increased abrasive wear and the formation of microcracks. Elemental analysis of the wear track revealed the presence of wear products in the form of iron oxides originating from the counter body, confirming the contribution of oxidative and adhesive components to the wear mechanism. Thermal treatment—particularly furnace heating—was found to improve the microhardness of the coating by reducing porosity, stabilizing the binder, and enhancing phase distribution. Thus, uniform furnace heat treatment under an optimal temperature regime significantly enhances the service properties of NiCrFeBSi coatings and can be recommended for improving the reliability and durability of protective layers under dry sliding conditions.

Acknowledgment

References

1 Kusumar, Nerlfi. Growney. Third global paint & coatings report, 2016–2021, (n.d.). https://www.coatingsworld.com/issues/2017-09-01/view_market-research/kusumgar-nerlfi-amp-growney-publish-third-global-p/ (accessed May 13, 2025).

2 Pawlowski, L. (2008). *The Science and Engineering of Thermal Spray Coatings*. 2nd ed. John Wiley & Sons, Ltd, UK.

3 Havrlisan, S., Simunovic, K., & Vukelic, D. (2006). Modelling of abrasive wear of Ni-based self- fluxing alloy coatings by the application of experimental design. *Technical Gazette, 23*(6), 1687–1693. https://doi.org/10.17559/TV-20161020210442.

4 García, A., Fern´andez, M.R., Cuetos, J.M., Gonz´alez, R., Ortiz, A., & Cadenas, M. (n.d.). Study of the sliding wear and friction behavior of WC + NiCrBSi laser cladding coatings as a function of actual concentration of WC reinforcement particles in ball-on-disk test. *Tribol. Lett.*, *63*, 41. https://doi.org/10.1007/s11249-016-0734-3.

5 Guo, C., Zhou, J., Chen, J., Zhao, J., Yu, Y., & Zhou, H. (2011). High temperature wear resistance of laser cladding NiCrBSi and NiCrBSi/WC-Ni composite coatings. *Wear*, *270*, 492–498. https://doi.org/10.1016/j.wear.2011.01.003.

6 Górka, J., Lont, A., & Poloczek, T. (2025). The Microstructure and Properties of Laser Cladded Ni Based Self Fluxing Alloy Coatings Reinforced by TiC Particles. *Coatings*, *15*(5), 527. https://doi.org/10.3390/coatings15050527.

7 Wang, Y., Stella, J., Darut, G., Poirier, T., Liao, H., & Planche, M.-P. (2017). APS prepared NiCrBSi-YSZ composite coatings for protection against cavitation erosion. *J. Alloys Compd.*, *699*, 1095–1103. https://doi.org/10.1016/j.jallcom.2017.01.034.

8 Buitkenov, D., Rakhadilov, B., Nabioldina, A., Mukazhanov, Y., Adilkanova, M., & Raisov, N. (2024). Investigation of Structural Phase, Mechanical, and Tribological Characteristics of Layer Gradient Heat-Protective Coatings Obtained by the Detonation Spraying Method. *Materials*, *17*(21), 5253. https://doi.org/10.3390/ma17215253.

9 Sagdoldina, Z., Baizhan, D., Sulyubayeva, L., Berdimuratov, N., Buitkenov, D., & Bolatov, S. (2024). Effect of Electrofriction Treatment on Microstructure, Corrosion Resistance and Wear Resistance of Cladding Coatings. *Coatings*, *14*, 1433. https://doi.org/10.3390/coatings14111433.

10 Xiao, J.-K., Wu, Y.-Q., Zhang, W., Chen, J., Wei, X.-L., & Zhang, C. (2019). Microstructure, wear and corrosion behaviors of plasma sprayed NiCrBSi-Zr coating. *Surf. Coat. Technol.*, *360*, 172–180. https://doi.org/10.1016/j.surfcoat.2018.12.114.

11 Rakhadilov, B., Satbayeva, Z., Ramankulov Sh., Shektibayev N., Zhurerova L., Popova N., Uazyrkhanova G., & Sagdoldina, Z. (2021). Change of 0.34Cr-1Ni-Mo-Fe Steel Dislocation Structure in Plasma Electrolyte Hardening. Change of 0.34Cr-1Ni-Mo-Fe Steel Dislocation Structure in Plasma Electrolyte Hardening. *Materials*, *14*(8), DOI: 10.3390/ma14081928

12 Chen, T., Wu, F., Wang, H., & Liu, D. (2018). Laser cladding in-situ Ti(C, N) particles reinforced Ni-based composite coatings modified with CeO_2 nanoparticles. *Metals*, 8. https://doi.org/10.3390/met8080601.

13 Rakhadilov, B., Buitkenov, D., Sagdoldina, Z., Idrisheva, Z., Zhamanbayeva, M., & Kakimzhanov, D. (2021). Preparation and Characterization of NiCr/NiCr-Al$_2$O$_3$/Al$_2$O$_3$ Multilayer Gradient Coatings by Gas Detonation Spraying. *Coatings*, *11*, 1524. https://doi.org/10.3390/coatings11121524.

14 Houdková, Š., Smazalová, E., Vostřák, M., & Schubert, J. (2014). Properties of NiCrBSi coating, as sprayed and remelted by different technologies. *Surface and Coatings Technology*, *253*, 14–26. doi:10.1016/j.surfcoat.2014.05.009

15 Rakhadilov, B., Pogrebnjak, A., Sagdoldina, Zh., Buitkenov, D., Beresnev, V., & Mukhamedova, A. (2022). Effect of Bilayer Thickness and Bias Potential on the Structure and Properties of (TiZr/Nb)N Multilayer Coatings as a Result of Arc-PVD Deposition. *Materials*, *15*, 7696. https://doi.org/10.3390/ma15217696

16 Kazamer, N., Vălean, P., Pascal, D.-T., Muntean, R., Mărginean, G., & Şerban, V.-A. (2021). Development, optimization, and characterization of NiCrBSi-TiB$_2$ flame-sprayed vacuum fused coatings. *Surface and Coatings Technology*, *406*, 126747. doi:10.1016/j.surfcoat.2020.126747

17 Rakhadilov, B., Sulyubayeva, L., Maulet, M., Sagdoldina, Z., Buitkenov, D., & Issova, A. (2024). Investigation of High-Temperature Oxidation of Homogeneous and Gradient Ni-Cr-Al Coatings Obtained by Detonation Spraying. *Coatings*, *14*, 11. https://doi.org/10.3390/coatings14010011.

18 Dzhurinskiy, D., Babu, A., Pathak, P., Elkin, A., Dautov, S., & Shornikov, P. (2021). Microstructure and wear properties of atmospheric plasma-sprayed Cr$_3$C$_2$-NiCr composite coatings. *Surface and Coatings Technology*, *428*, 127904, ISSN 0257-8972. https://doi.org/10.1016/j.surfcoat.2021.127904.

19 Meiirbekov, M., Ismailov, M., Kenzhegulov, A., Mustafa, L., & Tashmukhanbetova, I. (2024). Study of the effect of combined reinforcement and modification of epoxy resin with rubbers on the impact strength of carbon fiber-reinforced plastic. *Eurasian Journal of Physics and Functional Materials*, *8*(1), 3. https://doi.org/10.32523/ejpfm.2024080103

20 Rojacz, H., Zikin, A., Mozelt, C., Winkelmann, H., & Badisch, E. (2013). High temperature corrosion studies of cermet particle reinforced NiCrBSi hardfacings. *Surf. Coat. Technol.*, *222*, 90–96.

21 Bakhytuly N., Kenzhegulov A.K., Nurtanto M., Aliev A.E., & Kuldeev E.L. (2023). Microstructure and tribological study of TiAlCN and TiTaCN coatings. *Complex Use of Mineral Resources*, *327*(4), 99–110. https://doi.org/10.31643/2023/6445.45.

22 Miguel, J.M., Guilemany, J.M., & Vizcaino, S. (2003). Tribological study of NiCrBSi coating obtained by different processes. *Tribol. Int.*, *36*, 181–187. http://dx.doi.org/10.1016/S0301-679X(02)00144-5.

23 González, R., García, M.A., Peñuelas, I., Cadenas, M., Fernández, M.D.R., & Battez, A. H. (2007). Microstructural study of NiCrBSi coatings obtained by differ ent processes. *Wear*, *263*, 619–624. http://dx.doi.org/10.1016/j.wear.2007.01.094.

24 Fernández, E., Cadenas, M., González, R., Navas, C., Fernández, R., & De Dambor enea J. (2005). Wear behaviour of laser clad NiCrBSi coating. *Wear*, *259*, 870–875. http://dx.doi.org/10.1016/j.wear.2005.02.063.

25 Hemmati, I. (2011). Evolution of microstructure and properties in laser cladding of a Ni–Cr–B–Si hardfacing alloy. *Surf. Eff. Contact Mech*. http://dx.doi.org/10.2495/SECM110.

26 Hemmati, I., Ocelík, V., & De Hosson, J.T.M. (2012). Dilution effects in laser cladding of Ni Cr–B–Si–C hardfacing alloys. *Mater. Lett.*, *84*, 69–72.

27 Reinaldo, P.R. & D'Oliveira, A.S.C.M. (2012). NiCrSiB coatings deposited by plasma transferred arc on different steel substrates. *J. Mater. Eng. Perform.*, *22*, 590–597.

28 Fernandes, F., Cavaleiro, A., & Loureiro, A. (2012). Oxidation behavior of Ni-based coatings deposited by PTA on gray cast iron. *Surf. Coat. Technol.*, *207*, 196–203. https://doi.org/10.1016/j.surfcoat.2012.06.070.

29 Kakimzhanov, D., Rakhadilov, B., Sulyubayeva, L., & Dautbekov, M. (2023) Influence of Pulse-Plasma Treatment Distance on Structure and Properties of Cr$_3$C$_2$-NiCr-Based Detonation Coatings. *Coatings*, *13*, 1824. https://doi.org/10.3390/coatings13111824.

30 Riabinkina, P.A., Bataev, I.A., Batraev, I.S., Ruktuev, A.A., Ulianitsky, V.Y., Tanaka, S., Emurlaeva, Y.Y., Ogneva, T.S., & Bataev, V.A. (2022). An Experimental and Numerical Simulation Study of Single Particle Impact during Detonation Spraying. *Metals*, *12*, 1013. https://doi.org/10.3390/met12061013.

31 Rakhadilov, B., Kakimzhanov, D., Baizhan, D., Muslimanova, G., Pazylbek, S., & Zhurerova, L. (2021). Comparative Study of Structures and Properties of Detonation Coatings with α-Al$_2$O$_3$ and γ-Al$_2$O$_3$ Main Phases. *Coatings*, *11*, 1566. https://doi.org/10.3390/coatings11121566.

Д.Б. Буйткенов, Н.С. Райсов, Н.Е. Базаров, Г.Т. Тлеубергенова,
А.К. Хасенов, Д.Ж. Карабекова

Газды-жалынды бүрку әдісімен алынған өздігінен ағатын никель жабындарының трибологиялық қасиеттерін зерттеу

Жұмыста газды-жалынды бүрку әдісімен жағылған, өздігінен ағатын NiCrFeBSiC қорытпасы негізіндегі жабындардың микроқұрылымы, фазалық құрамы, беткі морфологиясы және трибологиялық сипаттамалары кешенді түрде зерттелді. Әртүрлі жылулық өңдеу түрлерінің — газды-жалынды қыздыру және пеште қыздыру — жабын қасиеттерінің әсеріне ерекше назар аударылды. Рентгендік дифракциялық талдау FeNi$_3$ фазасының, сондай-ақ Cr$_7$C$_3$, Cr$_{23}$C$_6$ карбидтік қосылыстары

мен боридтердің түзілуін анықтады, бұл олардың тозуға төзімділігіне айтарлықтай әсер ететінін көрсетті. Гониометрия әдісімен жүргізілген өлшеулер пеште жылулық өңдеуден өткен жабынның ең жоғары гидрофобтылық қасиетке ие екені айқындалды (жанасу бұрышы — 89,6°). Беткі морфология мен кедір-бұдырлық параметрлері сканерлейтін электронды микроскопия және профилометрия әдістерімен бағаланды, нәтижесінде пештік өңдеу ең тығыз әрі тегіс құрылымды, ең төменгі кедір-бұдырлықпен (Ra = 13,388 мкм) қамтамасыз ететіні анықталды. Өткізілген трибологиялық сынақтар пеште қыздырудан кейінгі жабынның ең төмен және ең тұрақты үйкеліс коэффициентін (0,138 ± 0,003) көрсететінін, бұл тозу ізінің микроқұрылымдық ерекшеліктерімен сәйкес келетінін дәлелдеді. Алынған нәтижелер NiCrFeBSiC негізіндегі жабындардың пайдалану қасиеттерін арттыру үшін пештік жылулық өңдеудің жоғары тиімділігін айғақтайды.

Кілт сөздер: өздігінен ағатын қорытпалар, газды-жалынды бүрку, никель қорытпалары, NiCrFeBSi, жылулық өңдеу, 45 болат

Д.Б. Буйткенов, Н.С. Райсов, Н.Е. Базаров, Г.Т. Тлеубергенова,
А.К. Хасенов, Д.Ж. Карабекова

Трибологическое поведение самофлюсующихся покрытий на основе никеля, сформированных газопламенным напылением

В данной работе проведено комплексное исследование микроструктуры, фазового состава, поверхностной морфологии и трибологических характеристик покрытий на основе самофлюсующегося сплава NiCrFeBSiC, нанесённых методом газопламенного напыления. Особое внимание уделено влиянию различных видов термической обработки — газопламенного нагрева и нагрева в печи — на свойства покрытий. Рентгенодифракционный анализ выявил образование фазы $FeNi_3$, а также карбидных соединений Cr_7C_3, $Cr_{23}C_6$ и боридов, что оказывает значительное влияние на износостойкость. Методом гониометрии показано, что наибольшую гидрофобность поверхности обеспечивает покрытие, подвергнутое термической обработке в печи (контактный угол — 89.6°). Поверхностная морфология и параметры шероховатости оценены с помощью сканирующей электронной микроскопии и профилометрии, где установлено, что печная обработка обеспечивает наиболее плотную и сглаженную структуру с наименьшей шероховатостью Ra = 13.388 мкм. Проведённые трибологические испытания показали, что покрытие после нагрева в печи демонстрирует наименьший и наиболее стабильный коэффициент трения (0.138 ± 0.003), что коррелирует с микроструктурными особенностями трека износа. Полученные результаты свидетельствуют о высокой эффективности термической обработки в печи для повышения эксплуатационных свойств покрытий на основе NiCrFeBSiC.

Ключевые слова: самофлюсующиеся сплавы, газопламенное напыление, никелевые сплавы, NiCrFeBSi, термическая обработка, сталь 45

Information about the authors

Buitkenov, Dastan — PhD, Leading Researcher, Scientific Research Center "Surface Engineering and Tribology", S. Amanzholov East Kazakhstan University, Ust-Kamenogorsk, Kazakhstan; e-mail: buitkenov@gmail.com; ORCID ID: https://orcid.org/0000-0002-0239-5849

Raisov, Nurmahanbet (*corresponding author*) — Junior Researcher, Scientific Research Center "Surface Engineering and Tribology", S. Amanzholov East Kazakhstan University, Ust-Kamenogorsk, Kazakhstan; e-mail: 2002raisov@gmail.com; ORCID ID: https://orcid.org/0009-0007-1698-957X

Bazarov, Nuraly — Researcher, LLP "PlasmaScience", Ust-Kamenogorsk, Kazakhstan; e-mail: bazarov.nuraly@gmail.com, ORCID ID: https://orcid.org/0009-0001-9182-7016

Tleubergenova, Gulim — Engineer, Scientific Research Center "Surface Engineering and Tribology", S. Amanzholov East Kazakhstan University, Ust-Kamenogorsk, Kazakhstan; e-mail: gulh7748@gmail.com, ORCID ID: https://orcid.org/0009-0009-4064-5368

Khassenov, Ayanbergen — PhD, Professor, Buketov Karaganda National Research University, Karaganda, Kazakhstan; e-mail: ayanbergen@mail.ru; ORCID ID: https://orcid.org/0000-0002-5220-9469

Karabekova, Dana — PhD, Professor, Buketov Karaganda National Research University, Karaganda, Kazakhstan; e-mail: karabekova71@mail.ru; ORCID ID: https://orcid.org/0000-0001-8776-4414

M. Ryspayeva✉, I. Berezovskaya

Al-Farabi Kazakh National University, Al-Farabi av., 71, Almaty, Kazakhstan

Numerical Simulation of Turbulent Combustion of Liquid Fuels: Comparative Analysis of Benzene and Tridecane

The work presents a numerical simulation of the combustion process of two liquid fuels (benzene and tridecane) with the application of KIVA-II computational program. The research is focused on evaluation of the effect of fuel mass and spray angle on the combustion process and temperature distribution in a cylindrical combustion chamber. The fuel mass is varied from 5 to 20 mg and the spray angle ranges from 2° to 15°. Temperature fields are analyzed over time to determine heat release characteristics and flame structure for both fuels. The results demonstrate that increasing the injection mass leads to a significant rise in flame height and combustion temperature, which is attributed to enhanced heat energy release. The effect of spray angle is found to be significant only at small values, while at higher values it has little influence on the temperature fields of both fuels. Comparative analysis between benzene and tridecane shows that benzene combustion occurs more intensively and at higher temperatures than the combustion process of tridecane fuel. These findings are essential for optimizing fuel injection parameters and improving the design of combustion systems in internal combustion engines. The results of the study can be applied to enhance combustion efficiency and reduce harmful emissions into the environment.

Keywords: numerical combustion modeling, liquid fuels, benzene, tridecane, mass of injected fuel, spray characteristics, temperature field, concentration fields

✉*Corresponding author*: Ryspayeva, Maiya, mayiya.ryspaeva@kaznu.edu.kz

Introduction

Combustion of liquid fuels is characterized by complex physical and chemical reactions. The process of combustion of liquid fuels can depend on various factors such as initial parameters, chemical properties of a fuel or parameters of turbulence. If one can optimize these factors, it is possible to increase the combustion efficiency and to minimize emissions of harmful substances. In this work the object of numerical research is the combustion process of benzene and tridecane in a closed cylindrical combustion chamber.

The relevance and practical significance of this study are determined by the widespread use of liquid fuels in power plants, in industry and in vehicles. The problem of environmental pollution from combustion products of various fuels and fuel mixtures also remains important. In addition, the processes of combustion and turbulence are complex physical and chemical processes. When modelling it is necessary to take into account multiphase flows with sprays, the presence of chemical reactions and turbulence process.

The importance of modeling the combustion process of liquid fuels is confirmed by modern research. For example, in work [1] it is considered how the injection rate affects the combustion of liquid heptane. The authors conducted the analysis of the concentration fields of reacting substances in the combustion zone of liquid heptane.

In the study [2] the authors analyzed how the excess air ratio affects the combustion and atomization of benzene. As the result of numerical modeling the authors have shown that complete oxidation of the fuel does not occur when rich fuel mixtures burn. This results in increased fuel consumption and reduced combustion efficiency due to the presence of unburned hydrocarbons in the exhaust gases.

The work [3] demonstrates the features of liquid fuel combustion when the initial air temperature in the combustion chamber is changed. A numerical study has allowed to obtain temperature fields of fuel, concentration fields of liquid fuel combustion reaction products for different initial temperatures of the oxidizer in the combustion.

In the article [4] the authors have examined the influence of the temperature on the vortex combustion of liquid fuel. It has been found that flame oscillations appear due to the uneven flow of liquid fuel droplets

at low temperatures. As the result of the analysis the authors have demonstrated that increasing the temperature helps to stabilize and to improve the fuel combustion.

In the work [5] a numerical study of the combustion of fuel mixture of ammonia and hydrogen has been performed to assess the posibility of using this mixture as an alternative fuel. The authors have examined the combustion process of this mixture and have studied the combustion temperature as well as the fuel burning rate. The authors of the article have concluded that the addition of hydrogen improve the combustion process of the mixture by increasing the combustion temperature and by making the process more uniform which helps reduce the emission of harmful substances into the atmosphere.

Study [6] is dedicated to the comparison of various turbulence models. It includes the simulation of do-decane combustion with multiple injections. The numerical experiment has been conducted at different ambient temperatures. The results obtained by the authors have shown good agreement with experimental data.

The scientific novelty of this work lies in the comparative analysis of the influence of spray mass and angle of two different types of fuel (benzene and tridecane) in the combustion chamber using the KIVA-II computational program.

The aim of this study is to identify the optimal combustion conditions for two types of fuel (benzene and tridecane) through numerical simulation by varying the fuel mass and the spray angle of the liquid fuel.

Methods and materials

A mathematical model based on the equations of turbulent flow with fuel spray into a cylindrical combustion chamber has been used for the numerical simulation in this study. This model includes the equations of motion for the liquid phase of the fuel, the mass conservation equations for the various combustion reaction components and the k-ε turbulence model [7].

The mass conservation equation for the component m is expressed as follows [7]:

$$\frac{\partial \rho_m}{\partial t} + \vec{\nabla}(\rho_m u) = \vec{\nabla}\left[\rho D \vec{\nabla}\left(\frac{\rho_m}{\rho}\right)\right] + \dot{\rho}_m^c + \dot{\rho}^s \delta_{m1},\tag{1}$$

where ρ_m is the density of the mixture, ρ is the total density, u is the flow velocity.

The momentum equation in this model:

$$\frac{\partial(\rho\vec{u})}{\partial t} + \vec{\nabla}(\rho\vec{u}\vec{u}) = -\frac{1}{a^2}\vec{\nabla}p - A_0\vec{\nabla}\left(\frac{2}{3}\rho k\right) + \vec{\nabla}\vec{\sigma} + \vec{F}^s + \rho\vec{g},\tag{2}$$

where p is the pressure of the fluid.

The parameter A_0 takes the value 1 for turbulent flow and 0 for laminar flow.

The energy conservation equation:

$$\frac{\partial(\rho I)}{\partial t} + \vec{\nabla}(\rho\vec{u}I) = -p\vec{\nabla}\vec{u} + (1-A_0)\sigma\vec{\nabla}\vec{u} - \vec{\nabla}\vec{J} + A_0\rho\varepsilon + \dot{Q}^c + \dot{Q}^s.\tag{3}$$

The calculation of the heat flux vector J is carried out according to the following relation:

$$\vec{J} = -K\vec{\nabla}T - \rho D \sum_m h_m \vec{\nabla}(\rho_m/\rho),\tag{4}$$

where T is the temperature of the fluid, h_m is the enthalpy of m. $\dot{Q}^c$ is the amount of heat generated by chemical reactions, $\dot{Q}^s$ is the amount of heat supplied to the combustion chamber during fuel injection.

The equations of the k–ε model where k is the turbulent kinetic energy ε is the kinetic energy dissipation rate are calculated using the following formula:

$$\frac{\partial \rho k}{\partial t} + \vec{\nabla}(\rho\vec{u}k) = -\frac{2}{3}\rho k\vec{\nabla}\vec{u} + \vec{\sigma}\vec{\nabla}\vec{u} + \vec{\nabla}\left[\left(\frac{\mu}{\mathrm{Pr}_k}\right)\vec{\nabla}k\right] - \rho\varepsilon + \dot{W}^s,\tag{5}$$

$$\frac{\partial \rho\varepsilon}{\partial t} + \vec{\nabla}(\rho\vec{u}\varepsilon) = -\left(\frac{2}{3}c_{\varepsilon_1} - c_{\varepsilon_3}\right)\rho\varepsilon\vec{\nabla}\vec{u} + \vec{\nabla}\left[\left(\frac{\mu}{\mathrm{Pr}_\varepsilon}\right)\vec{\nabla}\varepsilon\right] + \frac{\varepsilon}{k}\left[c_{\varepsilon_1}\vec{\sigma}\vec{\nabla}\vec{u} - c_{\varepsilon_2}\rho\varepsilon + c_s\dot{W}^s\right].\tag{6}$$

The standard k–ε model was chosen because of its reliable performance for engine turbulent flows. Moreover, it has full integration with KIVA-II code. The standard k–ε model gives reliable results and requires less computational resources. This model is commonly used for spray combustion simulations and it

has shown good performance in previous studies [1–3]. Other models like RNG k–ε model may be applied but they are computationally expensive.

Numerical simulation of liquid fuel combustion has been performed in a cylindrical burner chamber with a height of 15 cm and diameter of 4 cm. Initial conditions of the numerical experiment: air temperature is 900 K, wall temperature is 353 K, pressure is $4{\times}10^6$ Pa.

The computational domain consisted of 600 cells. Parameters are as follows: $nx = 20$ (number of cells along x axis, $ny = 1$ (axisymmetric task usual for cylinder), $nz = 30$ (along z axis, z is a height of chamber). The minimum cell size is 1 mm in the radial direction and 5 mm along z axis. The minimal time step is 1 microseconds. A grid and time step were selected based on established practices in KIVA-II modelling. The mesh and time step were found to provide consistent and stable results [1–3, 7].

The KIVA-II software package has been used for numerical simulation, detailed information about this software is provided in the source [7]. In this article, the authors have examined the combustion of two types of fuel: benzene and tridecane. The fuel mass has been varied from 5 to 20 mg. The influence of the spray angle (from 2° to 15°) has also been studied.

The reaction of benzene combustion producing water and carbon dioxide:

$$2C_6H_6 + 15O_2 \rightarrow 12CO_2 + 6H_2O \tag{7}$$

Benzene is a flammable hydrocarbon with a boiling point of 80,1 °C and a density of 0.7 g/cm³. Benzene is used as a feedstock for engines and has a freezing point of –60 °C [8].

The combustion reaction of tridecane which also results in the formation of water and carbon dioxide:

$$C_{13}H_{28} + 20O_2 \rightarrow 13CO_2 + 14H_2O \tag{8}$$

Tridecane is a colorless liquid from the alkane group with a density of 0.7568 g/ml and it is used as a component of diesel fuel [9].

The formation and oxidation of soot during the fuel combustion are described using a global multi-step chemical reaction [10–12]:

$$C_nH_{2m} + O_2 \xrightarrow{k_q} 2R^* \tag{9}$$

In this reaction, the fuel reacts with oxygen leading to the formation of radical, branching agents and intermediate reaction products.
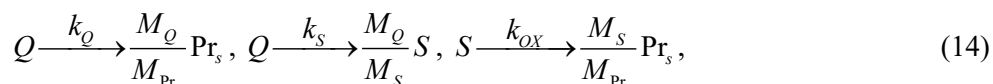
$$R^* + (\Gamma + 1)\left(\frac{1}{m}C_nH_m + pO_2\right) \xrightarrow{k_p} gP + f_1B + f_4Q + R^* \tag{10}$$

$$R^* + Q \xrightarrow{f_2k_p} R^* + B \tag{11}$$

$$B^* \xrightarrow{k_B} 2R^* \tag{12}$$
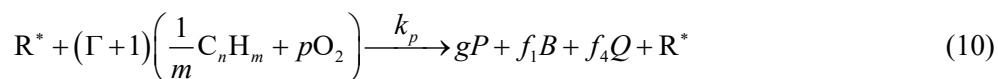
where R^* is radical, B is branching agent, Q is intermediate reaction product.

Coefficients Γ, p, g are formulated as follows:

$$\Gamma = \frac{f_1M_B + f_4M_Q}{\dfrac{M_{RH}}{m} + pM_{O_2}}, \quad p = \frac{n(2 - \lambda) + m}{2m}, \quad g = \frac{n}{m} + 1. \tag{13}$$

The coefficient λ characterizes the ratio between the components of the reaction products $CO / CO_2 = \lambda / (1 - \lambda)$, $\lambda = 0.67$ [10]. The molecular masses of the global components M_B, M_Q are calculated based on the mass balance equation.

During the reaction intermediate compounds are formed and they can be described as follows:

$$Q \xrightarrow{k_Q} \frac{M_Q}{M_{Pr_s}}Pr_s, \quad Q \xrightarrow{k_S} \frac{M_Q}{M_S}S, \quad S \xrightarrow{k_{OX}} \frac{M_S}{M_{Pr_s}}Pr_s, \tag{14}$$

where S defines soot particles (soot), Pr_s is global soot oxidation products, M_S is molecular weight of soot particles.

Results and discussion

The results of the numerical study of the influence of fuel injection mass on the combustion process of liquid fuels are shown in the figures below.

The temperature fields obtained as a result of tridecane combustion simulation are shown in Figure 1 for three time points from the start of the fuel injection. Data analysis has shown that by 4 ms the most of the chamber has warmed up to temperatures above 2000 K.
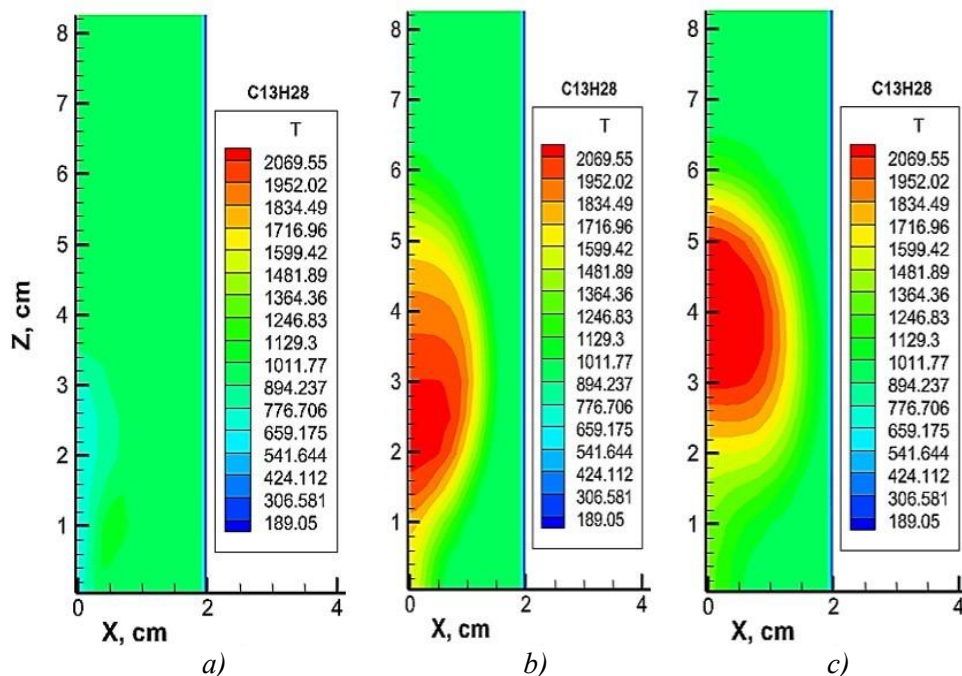

Figure 1. Temperature field during combustion of tridecane for times: *a* — 1.5 ms; *b* — 2.5 ms; *c* — 4 ms

The data in the Figure 2 show the change in temperature in the combustion chamber at three different time intervals for the case of liquid benzene spray. The maximum temperature is observed in the center of the temperature flame and reaches 2385 K. From graphs 1 and 2 it can be seen that benzene burns with a high heat release despite the smaller size of the temperature flame.
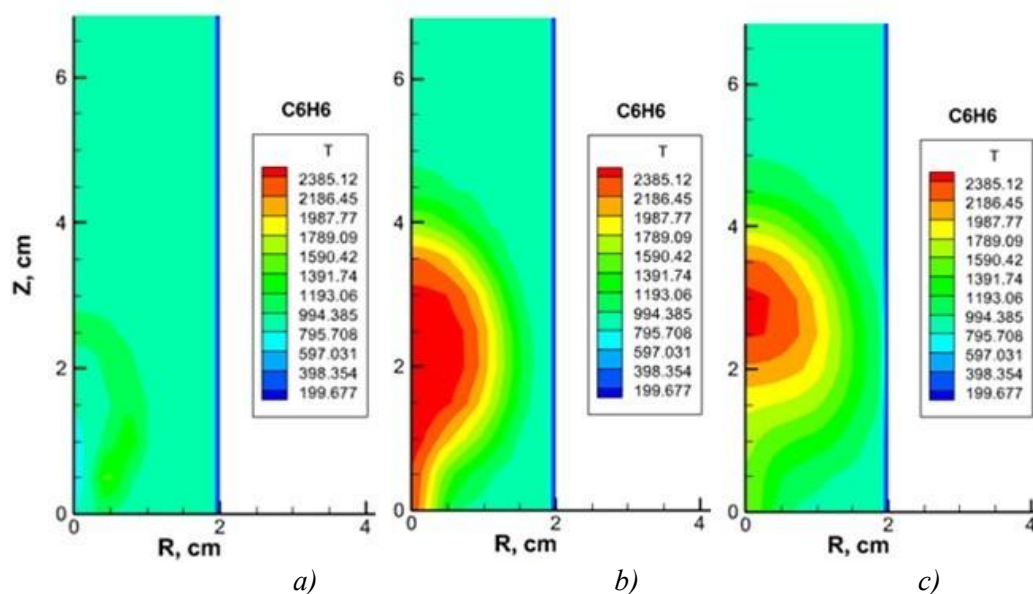
Figure 2. Temperature field during benzene combustion for times: *a* — *t* = 1.5 ms; *b* — *t* = 2.5 ms; *c* — *t* = 4 ms

Figure 3 shows the height of the temperature flame depending in the injection mass of tridecane. The greater the mass of the fuel the greater the height of the temperature flame. The increase in the height of the flame is associated with the increase in the amount of heat released during the fuel combustion. All of this also leads to a raise in the high temperature zone where intense combustion is observed. The graph also demonstrates small fluctuations due to the influence of spray and mixing of the combustion mixture.

The growth in the height of the temperature flame with the raise in the injection mass indicates the increase in the rate of combustion product outflow and the intensity of thermal convection, which is typical for diffusion combustion with the increase in the supplied fuel mass.

Thus, the dependence presented in the Figure 3 demonstrates the characteristic nonlinear dynamics of the temperature development with variations in the mass of the injected fuel which can be used too diagnose the combustion mode and optimize injection parameters in practical fuel supply problems.
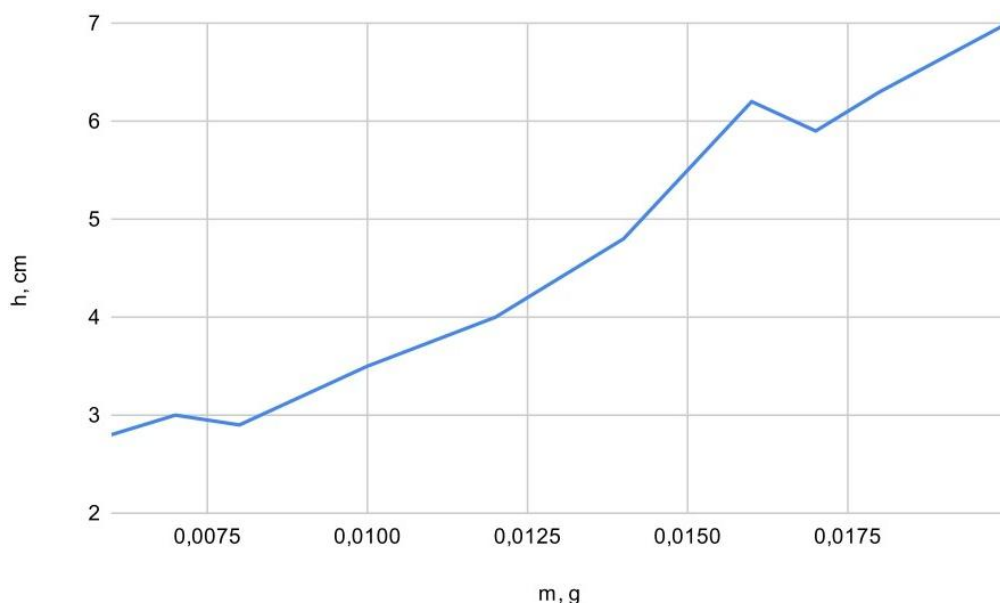
Figure 3. Effect of fuel mass on the height of the temperature flame

Figure 4 shows the effect of tridecane fuel mass on the formation of carbon dioxide in the combustion chamber. At low masses, a sharp increase in carbon dioxide is observed and then the influence of mass is already insignificant. At a mass of 10 to 20 mg the concentration of formed CO_2 stabilizes and this indicates that the limit of its formation during the combustion of tridecane has been reached.
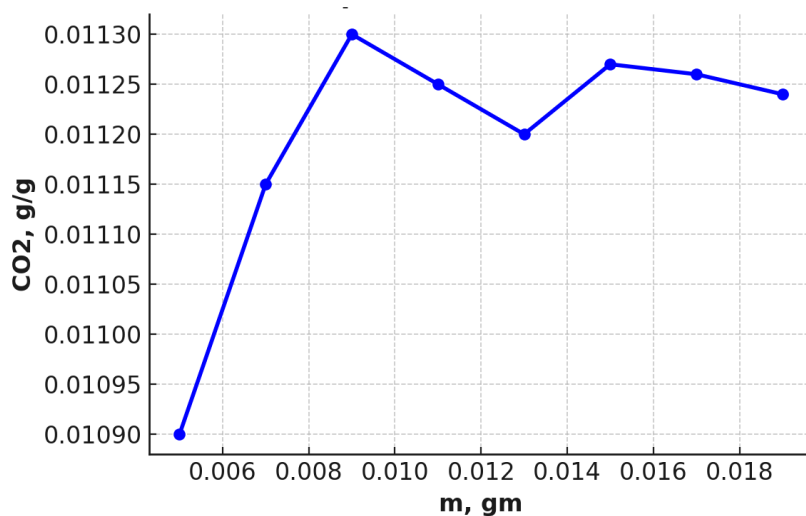
Figure 4. Effect of tridecane mass on carbon dioxide formation

Figure 5 shows how the injection mass of tridecane fuel affects the formation of soot during its combustion. Analysis of graph 5 demonstrates that increasing mass leads to a raise in the amount of soot. At a mass of up to 10 mg, the increase of soot concentration is insignificant; at a mass of more than 10 mg, a sharp increase in soot concentration is observed. Thus, the increase in mass leads to a raise in the formation of soot during the combustion of tridecane.
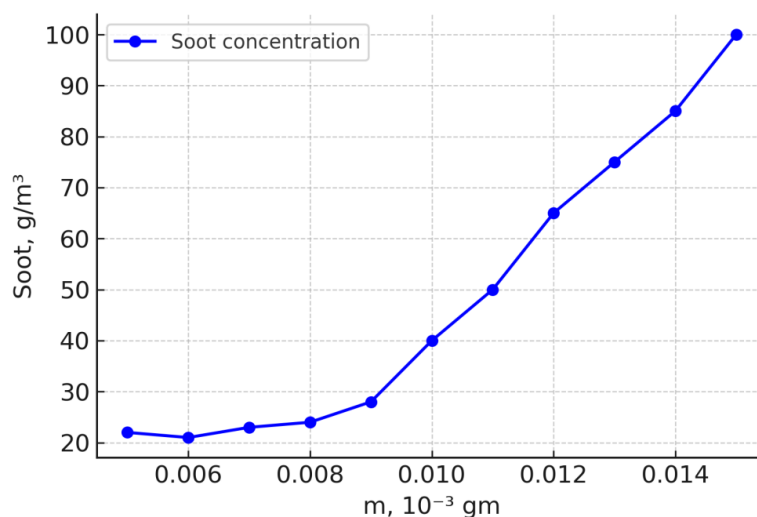
Figure 5. Dependence of the concentration of formed soot on the mass of tridecane injection

To validate the reliability of the simulation results the comparison with the experimental data available in the literature has been done. The calculated ignition time is within reasonable agreement with the experimental results presented in. The comparison confirms that the combustion model accurately reproduces the behavior of tridecane.

The results of the numerical calculation have shown that the optimal injection mass for liquid tridecane is 9 mg according to the graphs 4 and 5. Further increase in fuel mass leads to the raised formation of soot and carbon dioxide, which are harmful products of the chemical combustion reaction. At the same time, the mass of unburned particles also increases and this reduces the efficiency of fuel combustion.

A study on the influence of the spray angle on the combustion process of benzene and tridecane in the combustion chamber has also been conducted. The results of the numerical experiment for benzene (Fig. 6) show that the temperature change occurs at small spray angles. The subsequent increase (5–6°) has virtually no effect on the temperature field in the combustion chamber. It can be concluded that only at low values this parameter can influence the process of atomization and combustion of liquid fuel.
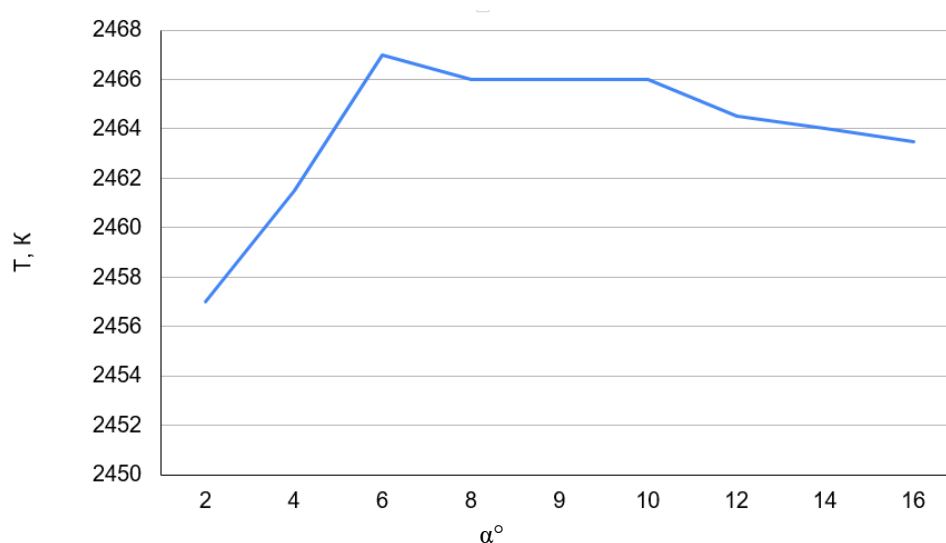
Figure 6. Effect of spray angle α on the maximum temperature during benzene combustion

From the analysis of the graph of the dependence of the maximum temperature during the combustion of tridecane (Fig. 7), it follows that the spray angle has no effect on the process of combustion and temperature changes remain insignificant.

Thus, it can be concluded that the spray angle does not have a significant effect on the process of mixing and combustion of liquid fuel, compared to other processes such as the concentration of fuel and oxidized or turbulence.
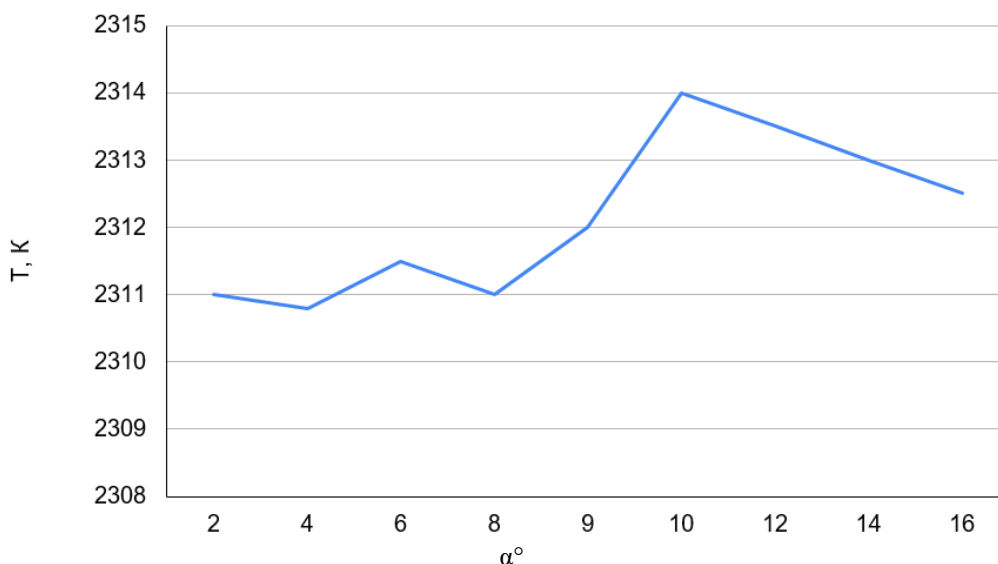

Figure 7. Distribution of maximum temperature for tridecane with changing spray angle α

Conclusion

In this article the authors have performed a numerical calculation of combustion of two types of liquid fuels: benzene and tridecane. A study has been conducted to investigate the influence of fuel mass and spray angle on the process of atomization and combustion of these fuels. Based on the results of numerical experiment the following conclusions can be drawn:

1. With the increase in the mass of fuel injection, a raise in the height of the temperature flame is observed which is associated with the increase in the amount of heat released during the chemical reaction of fuel combustion. There is also an increase in the high temperature zone where the most intense combustion occurs.

2. When adding small amounts of fuel, an increase in the amount of produced carbon dioxide is observed. When the injection mass reaches more than 10 mg, the process of carbon dioxide production stabilizes. Its concentrations remain practically unchanged with a further increase in the mass of fuel supplied to the chamber.

3. The mass of the fuel has a significant impact on the formation of soot in the combustion chamber, with a mass less than 10 mg the increase in soot concentration is insignificant; with a mass of more than 10 mg, a sharp increase in soot concentration is observed.

4. The analysis of the results has shown that the spray angle of liquid fuel droplets from 2 to 15° has little effect on the combustion parameters of the studied types of fuel. However, an increase in the injection mass of these fuels leads to a raise in heat exchange and temperature during the combustion of fuels.

The significance of the presented work is the possibility of practical application of the results for improving combustion and spraying processes in internal combustion engines operating on different types of fuel.

References

1   Berezovskaya, I., Tasmukhanova, A., Ryspayeva, M., & Ospanova, S. (2023). Numerical study of the influence of injection velocity of liquid fuel on the combustion process. *Eurasian Physical Technical Journal, 20*(3(45)), 43–51. https://doi.org/10.31489/2023No3/43-51

2   Shotayeva, E.Zh. & Ryspayeva, M.Zh. (2022). Calculation of the influence of initial parameters on the combustion process of liquid fuel. *Universum: Technical Sciences, 4*(97). https://7universum.com/ru/tech/archive/item/13439

3   Begaly, Z.D. & Ryspayeva, M.Zh. (2022). Modeling of liquid fuel combustion using modern computational technologies. *Universum: Technical Sciences, 3*(96). https://7universum.com/ru/tech/archive/item/13281

4   Hodge, A., Shahin, T., Gejji, R., Philo, J., Lucht, R., & Slabaugh, C. (2024). Fuel temperature effects on combustion stability of a high-pressure liquid-fueled swirl flame. *Journal of Propulsion and Power, 41*, 1–11. https://doi.org/10.2514/1.B39592

5   Huang, H., Zhang, Z., Han, X., & Wu, Z. (2022). Numerical study on the spray and combustion characteristics of ammonia/hydrogen blends in a constant volume vessel. *Energies, 15*(8), 2941. https://doi.org/10.3390/en15082941

6   Zhou, Q., Lucchini, T., D'Errico, G., Maes, N.C.J., Somers, L.M.T., & Lu, X. (2020). Computational modeling of diesel spray combustion with multiple injections. *SAE Technical Paper*, 2020-01-1155. https://doi.org/10.4271/2020-01-1155

7   Amsden, A.A., O'Rourke, P.J., & Butler, T.D. (1989). *KIVA-II: A computer program for chemically reactive flows with sprays*. Los Alamos National Laboratory.

8   NIST Chemistry WebBook, SRD 69. National Institute of Standards and technology https://webbook.nist.gov/cgi/cbook.cgi?Name=benzene&Units=SI

9   Gorokhovski, M. & Borghi, R. (1993). Model of soot formation and oxidation in diesel engines. *Journal of Diesels, Transactions of SAE*, 930075, 3–15.

10 Sabel'nikov, V., Gorokhovski, M., & Baricault, N. (2006). The extended IEM mixing model in the framework of the composition PDF approach: Applications to diesel spray combustion. *Combustion Theory and Modelling, 10*(1), 155–169.

11 Vinkovic, I., Simoens, S., & Gorokhovski, M. (2005). Large eddy simulation of droplet dispersion for inhomogeneous turbulent wall flow. *International Journal of Multiphase Flow, 32*(3), 344–364.

12 Ha, Dong-Myeong. (2012). The Investigation of Compatibility of Combustible Characteristics for n-Tridecane. *Journal of the Korean Society of Safety*, 27.

М. Рыспаева, И. Березовская

Сұйық отынның турбулентті жануын сандық модельдеу: бензол мен тридеканды салыстырмалы талдау

Жұмыста KIVA-II есептік бағдарламасын қолдану арқылы екі сұйық отынның (бензол мен тридекан) жану процесінің сандық модельдеуі ұсынылған. Зерттеу жану процесіне, температураның цилиндрлік жану камерасындағы таралуына отын массасы мен бүрку бұрышының әсерін бағалауға бағытталған. Отын массасы 5-тен 20 мг-ға дейін, ал бүрку бұрышы 2°-тан 15°-қа дейін өзгертілді. Екі отын түрі үшін жылу бөлу сипаттамаларын және жалын құрылымын анықтау мақсатында температуралық өрістер уақыт бойынша талданды. Нәтижелер отын бүрку массасының артуы жалын биіктігі мен жану температурасының айтарлықтай өсуіне әкелетінін, бұл жылу энергиясының бөлінуінің артуымен байланысты екенін көрсетті. Бүрку бұрышының әсері тек аз мәндерде елеулі екені анықталды, ал үлкен мәндерде оның екі түрлі сұйық отынның температуралық өрістеріне әсері шамалы болды. Бензол мен тридекан арасындағы салыстырмалы талдау бензолдың жану процесі жоғары температурада және қарқындылығы жағынан тридеканнан басым болатынын көрсетті. Бұл тұжырымдар іштен жанатын қозғалтқыштарда қолданылатын жану жүйелерінің құрылымын жетілдіру және отын бүрку параметрлерін оңтайландыру үшін маңызды. Зерттеу нәтижелері жану тиімділігін арттыруға және қоршаған ортаға зиянды заттардың шығарылуын азайтуға қолданылуы мүмкін.

Кілт сөздер: жануды сандық модельдеу, сұйық отындар (бензол, тридекан), айдалатын отынның массасы, бүрку сипаттамалары, температура өрісі, концентрация өрістері

М. Рыспаева, И. Березовская

Численное моделирование турбулентного горения жидких топлив: сравнительный анализ бензола и тридекана

В работе представлено численное моделирование процесса сгорания двух жидких топлив (бензола и тридекана) с применением вычислительной программы KIVA-II. Исследование сосредоточено на оценке влияния массы топлива и угла распыла на процесс сгорания, а также на распределение температуры в цилиндрической камере сгорания. Масса топлива варьируется от 5 до 20 мг, а угол распыла – от 2° до 15°. Анализируются температурные поля во времени с целью определения характеристик тепловыделения и структуры пламени для двух видов топлива. Результаты показывают, что увеличение массы впрыска приводит к значительному увеличению высоты пламени и температуры сгорания,

что определяется увеличением выделения тепловой энергии. Показано, что влияние угла распыла значимо только при малых значениях, в то время как при больших значениях оно мало влияет на температурные поля обоих типов жидких топлив. Сравнительный анализ между бензолом и тридеканом показывает, что горение бензола происходит более интенсивно и при более высоких температурах, чем процесс сгорания тридекана. Эти выводы необходимы для оптимизации параметров впрыска топлива и совершенствования конструкции систем сгорания в двигателях внутреннего сгорания. Результаты исследования могут быть применены для повышения эффективности сгорания и снижения вредных выбросов в окружающую среду.

Ключевые слова: численное моделирование горения, жидкие топлива (бензол, тридекан), масса впрыскиваемого топлива, характеристики распыления, температурное поле, поля концентрации

Information about the authors

Ryspayeva, Maiya (*corresponding author*) — PhD, Senior Lecturer, Department of Thermal and Technical Physics, Faculty of Physics and Technology, Al-Farabi Kazakh National University, Almaty, Kazakhstan; e-mail: mayiya.ryspaeva@kaznu.edu.kz, ORCHID ID: https://orcid.org/0000-0003-0850-3107

Berezovskaya, Irina — PhD, Senior Lecturer, Department of Thermal and Technical Physics, Faculty of Physics and Technology, Al-Farabi Kazakh National University, Almaty, Kazakhstan; email: Yryna.Berezovskaya@kaznu.edu.kz;https://orcid.org/0000-0001-8737-9954

A.S. Askarova[1], S.A. Bolegenova[1], Sh.S. Ospanova[1✉],
S.A. Bolegenova[1], G.Y. Baidullayeva[2], A.Z. Nurmukhanova[1]

[1]Al-Farabi Kazakh National University, Almaty, Kazakhstan;
[2]Asfendiyarov Kazakh National Medical University, Almaty, Kazakhstan

Investigation of Dispersion, Breakup, and Combustion Processes of Liquid Fuel Droplets under High Turbulence

In the present study, the processes of breakup, dispersion, and evaporation of gasoline droplets in a model combustion chamber under high turbulence reacting flow were investigated using modern computational modeling methods. The influence of the initial gas temperature in the chamber on spray dynamics, droplet distribution, and thermal characteristics of the flow was analyzed. The results of computational experiments enabled the detailed visualization of the reacting flow, including the temperature, aerodynamic, and concentration characteristics of the fuel–air mixture. It was established that an increase in the initial gas temperature leads to a reduction in the mean droplet size, accelerated evaporation, and enhanced combustion intensity. It was observed that droplets spread over considerable distances from the nozzle while maintaining a relatively uniform radial distribution. As the droplets move upward in the chamber, their temperature gradually increases, reflecting complex interactions with the two-phase flow. The study demonstrated that higher gas temperatures intensify combustion and significantly raise maximum temperature levels. Based on the research conducted, the key role of the initial gas temperature in shaping the spray and flame structure was substantiated, providing a basis for recommendations to optimize the operation of combustion chambers in thermal engines.

Keywords: liquid fuel, droplets, combustion, dispersion, atomization, turbulent flow, gas temperature, spray dynamics, simulation, combustion chamber

✉*Corresponding author*: Ospanova,Shynar, Shynar.Ospanova@kaznu.edu.kz

Introduction

Energy and transportation in the modern world remain largely dependent on hydrocarbon fuels. According to the International Energy Agency, their share of the global energy balance exceeds 80 %, with liquid fuels accounting for a significant portion. Their widespread use is attributed to a combination of high energy properties, ease of transportation, and their ability to be utilized efficiently in various applications. Despite growing interest in biofuels and other alternative energy sources, liquid hydrocarbon fuels remain a leading source of energy, ensuring the stability and efficiency of energy and transportation systems [1].

From an environmental perspective, liquid fuels offer advantages over solid energy sources. Their combustion produces virtually no ash, and pollutant emissions are significantly lower. Specific CO_2 emissions are 73–75 kg/GJ, compared to 90–95 kg/GJ for coal. The SO_2 and particulate matter content in the combustion products of liquid fuels is two to three times lower than that of coal, which complies with international environmental requirements [2].

According to the U.S.Energy Information Administration (EIA), global consumption of oil and other liquid fuels is projected to increase by 19 % between 2025 and 2040, primarily driven by the transportation and industrial sectors [3]. Demand is expected to rise from 95 million barrels per day in 2025 to 104 million barrels per day in 2030 and to 113 million barrels per day in 2040. The main drivers of this growth will be countries outside the OECD, where demand is projected to increase by 1.3 % annually, while in OECD member states, a slight decline is expected [4].

The forecast also indicates that OPEC will maintain or expand its share of global crude oil and condensate production. Renewable energy is expected to remain the fastest-growing source of energy, with an average annual growth rate of 2.3 %. Fossil fuels are expected to continue dominating the global energy mix, accounting for approximately 77 % of total consumption by 2040. Among fossil fuels, natural gas is expected to show the fastest growth, with an average annual increase of 1.4 % (Fig. 1) [5].
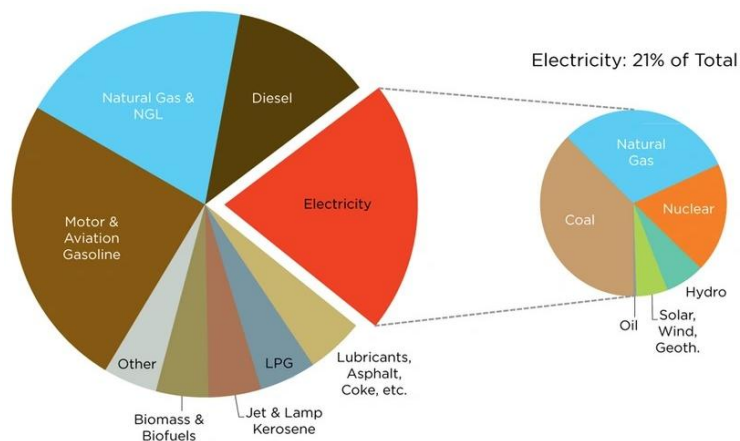
Figure 1. Structure of global energy consumption by fuel type and electricity source

The scientific novelty of the study stems from the need for a more in-depth analysis of the decomposition, evaporation, combustion, and dispersion processes of liquid fuels. The dynamics of droplets and dispersed systems directly determine the completeness of combustion and the efficiency of heating systems, as well as the level of harmful emissions.

The practical significance of the research results lies in their potential use in the design and modernization of power and transport systems. A thorough understanding of liquid fuel dispersion and combustion processes enables the development of more efficient nozzle systems for gas turbine engines, the improvement of combustion chambers in thermal power plants, and the optimization of operating processes in internal combustion engines. Ultimately, this contributes to increased energy efficiency, reduced operating costs, and a reduced environmental impact.

This study aims to comprehensively investigate the physicochemical mechanisms underlying the decomposition, evaporation, combustion, and dispersion of liquid hydrocarbon fuels under various thermodynamic conditions. Particular attention is paid to identifying the factors determining droplet size, evaporation rate, combustion flame formation, and combustion product formation mechanisms. Achieving this goal will enable the development of more accurate models of heat and mass transfer processes, improve the efficiency of liquid fuel use in power and transportation systems, and reduce harmful emissions by optimizing atomization and combustion processes.

Mathematical and geometrical models of the problem

The continuity equation governing mass conservation in a two-phase flow can be expressed as follows [6]:

$$\frac{\partial \rho}{\partial t} + \operatorname{div}(\rho \mathbf{u}) = S_{mass}. \tag{1}$$

The parameter u characterizes the velocity field of the liquid fuel, whereas S_{mass} designates the source term introduced by density variations in the surrounding gas phase induced by evaporation.

The governing relation for momentum conservation in a two-phase flow can be written as follows [6]:

$$\rho \frac{\partial u}{\partial t} + \rho (\operatorname{grad} \mathbf{u}) \mathbf{u} = \operatorname{div} \xi + \rho \mathbf{g} + S_{mom}, \tag{2}$$

In this context, S_{mom} represents the source term corresponding to the local variation of momentum in the gaseous phase because of droplet dynamics.

The governing relation for internal energy conservation can be formulated as follows [6]:

$$\rho \frac{\partial E}{\partial t} = \tau{:}\mathbf{D} - \rho \operatorname{div} \mathbf{u} - \operatorname{div} \mathbf{q} + S_{energy}. \tag{3}$$

The parameter q is the heat flux described by Fourier's law, whereas S_{energy} designates the source term reflecting the internal energy contribution associated with droplet dynamics.

The governing relation for the transport and conservation of component m can be formulated as follows [7]:

$$\frac{\partial(\rho c_m)}{\partial t} = -\frac{\partial(\rho c_m u_i)}{\partial x_i} + \frac{\partial}{\partial x_i}\left(\rho D_{c_m}\frac{\partial c_m}{\partial x_i}\right) + S_{mass}. \tag{4}$$

The parameter ρ_m represents the mass density associated with component m, whereas ρ characterizes the total mass density of the mixture under consideration.

The turbulent structure of the reacting flow is quantified by means of the empirical two-equation k–ε model, which simultaneously resolves the transport equations for turbulent kinetic energy k and its dissipation rate ε [8–10]:

$$\rho\frac{\partial k}{\partial t} + \rho\frac{\partial \overline{u}_j k}{\partial x_j} = \frac{\partial}{\partial x_j}\left[\left(\mu + \frac{\mu_t}{\sigma_k}\right)\frac{\partial k}{\partial x_j}\right]\frac{\partial \overline{u}_i}{\partial x_j} + G - \frac{2}{3}\rho k \delta_{ij}\frac{\partial \overline{u}_i}{\partial x_j} - \rho\varepsilon, \tag{5}$$

$$\rho\frac{\partial \varepsilon}{\partial t} + \rho\frac{\partial \overline{u}_j \varepsilon}{\partial x_j} - \frac{\partial}{\partial x_j}\left[\left(\mu + \frac{\mu_t}{\sigma_\varepsilon}\right)\frac{\partial \varepsilon}{\partial x_j}\right] = c_{\varepsilon_1}\frac{\varepsilon}{k}G - \left[\left(\frac{2}{3}c_{\varepsilon_2} - c_{\varepsilon_3}\right)\rho\varepsilon\delta_{ij}\frac{\partial \overline{u}_i}{\partial x_j}\right] - c_{\varepsilon_2}\rho\frac{\varepsilon^2}{k}. \tag{6}$$

The constant values c_{ε_1}, c_{ε_2}, c_{ε_3}, σ_k, σ_ε, serving as parameters of the computational model, are generally obtained from experimental data.

A droplet tracking model was used in this study, allowing for a detailed description of the dynamics of fuel droplets in a gas flow. This model considers their individual trajectories, evaporation processes, and heat and mass transfer with the surrounding environment. This enables the analysis of the spatial distribution of droplets, their temperature characteristics, and concentrations in the flame, which is key to understanding fuel combustion and evaporation processes.

To more accurately simulate the behavior of the dispersed phase, a droplet collision model was additionally used (Fig. 2). It is based on a probabilistic approach: when droplet trajectories intersect, the probability of their interaction is estimated, allowing for phenomena such as agglomeration (droplet merging) and fragmentation (breakdown into smaller particles) [11]. This significantly improves the accuracy of spray modeling and allows for more accurate predictions of droplet size distribution, evaporation rate, and flame structure formation [12–15].
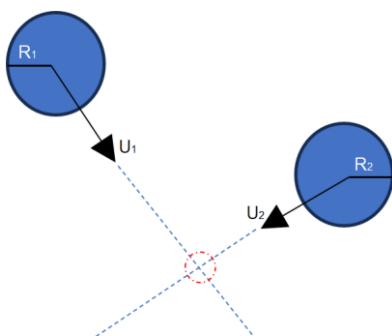
Figure 2. Illustration of the droplet collision model

The study utilized a model of a cylindrical combustion chamber 15 cm high and 4 cm in diameter (Fig. 3), with a liquid fuel injection nozzle installed in the center of its lower base. A real internal combustion engine served as the prototype for the simulated chamber, lending structural and operational realism to the computational model. The initial parameters included a pressure of 80 bar and a droplet radius of 25 μm.

The prediction of ignition delay was performed through an integral analysis using CHEMKIN. For biofuels, a simplified mechanism was employed to allow faster computations, accounting for 144 reactions involving 49 species [16, 17].

The concentrations of combustion products were determined using a model based on the detailed kinetic mechanism of the combustion process.

To predict soot formation during the combustion of hydrocarbon fuels, the global Shell soot model [18] was employed. This model accounts for key processes such as nucleation, particle growth, and agglomeration, as well as hydrocarbon pyrolysis and the formation of polycyclic aromatic hydrocarbons, which play a

central role in soot generation [19, 20]. By using this approach, it becomes possible to estimate soot emissions and optimize combustion conditions, contributing to improved engine performance and reduced environmental impact.
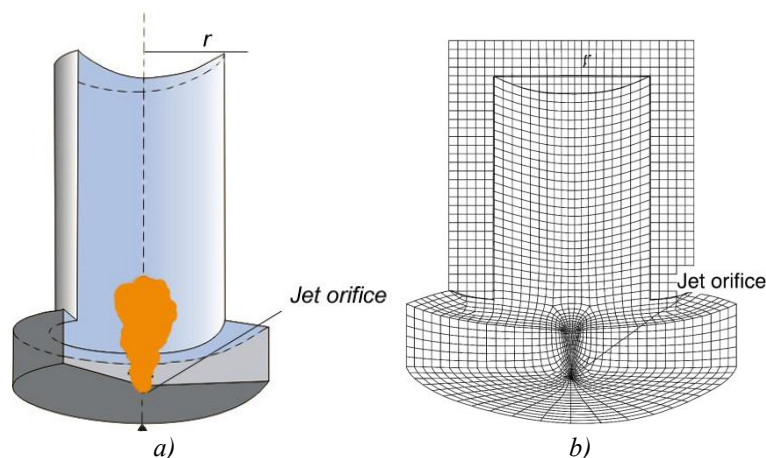

Figure 3. The main structural elements used in modeling the system under study are: *a*) a schematic representation of the combustion chamber geometry; *b*) visualization and discretization of the computational domain

For numerical modeling of the breakup, dispersion, evaporation, and combustion of liquid fuel droplets, the KIVA-3V software package developed at Los Alamos National Laboratory (USA) was employed. This code is designed for three-dimensional simulations of flows in internal combustion chambers and is based on the finite-volume method for solving the Navier–Stokes equations with consideration of turbulence, heat, and mass transfer, and chemical reactions [21, 22].

The KIVA-3V code includes modules for calculating fuel droplet trajectories, evaporation, collisions, and secondary breakup, which allows for a detailed description of the interaction between the dispersed and gaseous phases under conditions of high turbulence. The software package features an adaptive computational grid, flexible boundary conditions, and the capability to vary the thermodynamic parameters of the fuel and oxidizer. The use of KIVA-3V made it possible to obtain detailed distributions of temperature, velocity, and species concentration in the reacting flow, ensuring high accuracy in describing spray and combustion processes under various initial gas temperatures.

This study presents the results of computational experiments aimed at investigating the influence of initial temperature on the processes of breakup, dispersion, combustion, and evaporation of gasoline droplets in a model combustion chamber under conditions of high turbulence. The injection gas temperature varied from 700 to 1500 K, which made it possible to analyze its effect on spray flame formation as well as on the temperature and concentration fields of the reacting flow.

Results and Discussion

Figure 4 illustrates selected results of numerical simulations addressing the radial dispersion of liquid fuel droplets within the model combustion chamber. The analysis of the obtained data reveals that an increase in chamber temperature leads to a reduction in the mean droplet diameter. This trend is primarily associated with enhanced evaporation rates and intensified aerodynamic atomization processes. However, the magnitude of this reduction remains relatively modest, indicating that the geometric transformation of droplets is constrained under the studied conditions.

The spray dynamics of gasoline droplets exhibit characteristic spatiotemporal features in a highly turbulent flow. At 0.8 ms after injection, the droplets attain a penetration height of approximately 1.2 cm above the injector nozzle. In the radial direction, a nearly uniform distribution of droplets is observed up to 0.2 cm from the chamber axis, suggesting a stable atomization regime and well-established spray formation mechanisms.

These results highlight the significance of initial gas temperature in shaping both the evaporation–atomization interplay and the subsequent distribution of reacting phases. Despite the relatively moderate change in droplet size, the findings confirm the strong temperature dependence of spray dynamics, which is critical for predictive modeling of heat and mass transfer processes in advanced combustion systems.

Figure 5 presents the numerical simulation results of the temperature distribution of liquid-fuel droplets in the combustion chamber at 0.8 ms after injection.

The analysis indicates that in the lower part of the chamber, droplet temperatures remain close to 300 K, which is attributed to their recent entry into the flow and the limited time available for heat and mass exchange with the surrounding hot gases. As the spray develops upward, the droplets progressively heat up, reaching maximum temperatures in the range of 500–550 K in the central and upper regions of the chamber.

This distribution highlights the presence of a pronounced temperature gradient caused by the non-uniformity of heat transfer and the variation in droplet sizes. Larger droplets retain lower temperatures due to their slower thermal response, whereas smaller ones rapidly approach equilibrium with the surrounding gaseous medium. Consequently, the droplet temperature field reflects the complex interplay of heat transfer, evaporation, and dispersion processes under turbulent combustion conditions.

a) 700 K   *b*) 1000 K   *c*) 1500 K
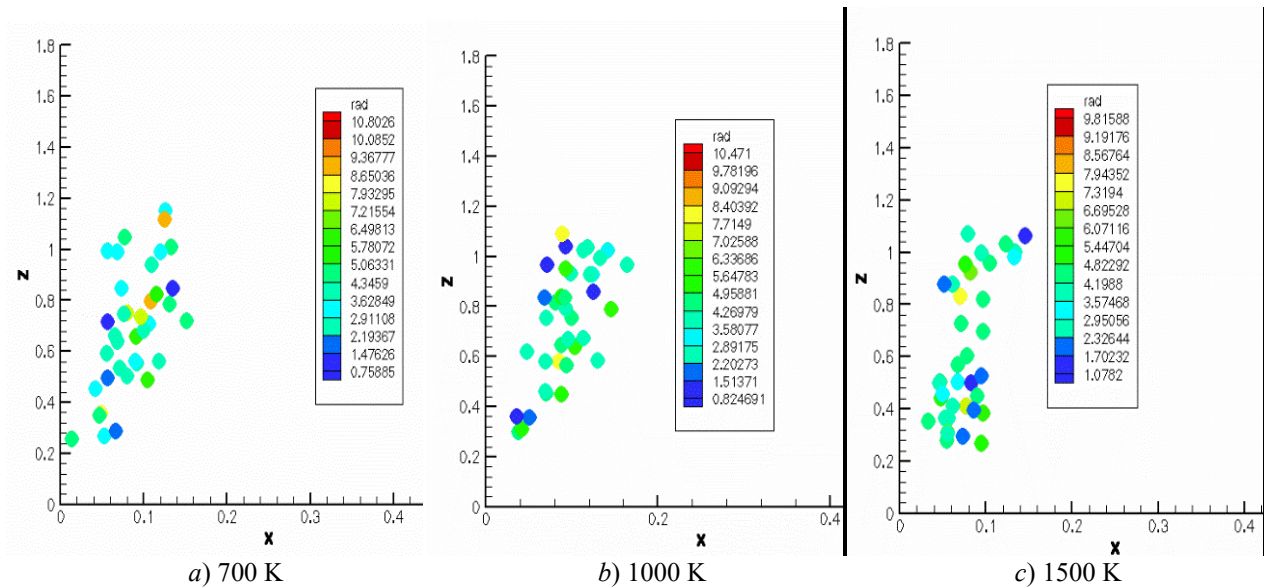
Figure 4. Dispersion of gasoline droplets by size in the combustion chamber space
at *t*=0.8 ms at different initial temperatures of the gas

a) 700 K   *b*) 1000 K   *c*) 1500 K
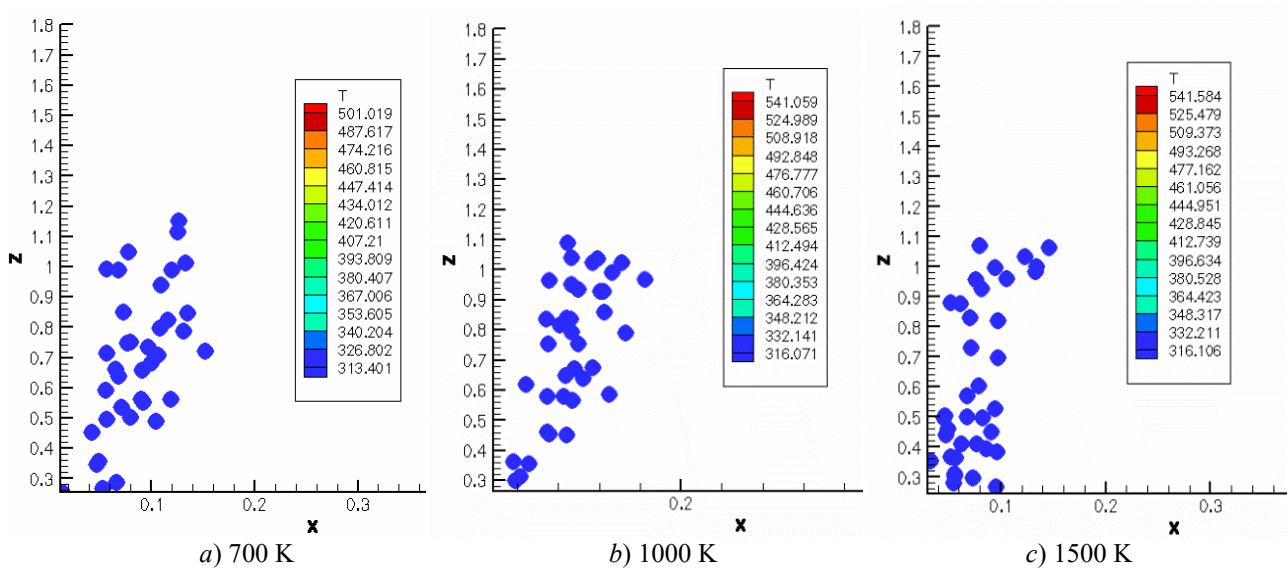
Figure 5. Dispersion of gasoline droplets by specific temperature in the combustion chamber space
at *t* = 0.8 ms at different initial temperatures of the gas

Unlike gasoline spray, which is characterized by relatively rapid heating of small droplets and a more uniform radial distribution within the chamber, diesel fuel spray exhibits greater heterogeneity in both droplet size and temperature. Diesel droplets are typically larger and more viscous, which slows their evaporation and heat exchange with the surrounding gases. As a result, droplet temperatures in the lower part of the chamber remain significantly lower, and equilibrium with the hot medium is reached more slowly than in gasoline sprays.

Additionally, diesel sprays often show a wider range of droplet sizes and more pronounced temperature gradients, affecting the formation of the combustion zone and overall fuel burning efficiency. These characteristics highlight the importance of considering the specific fuel properties when modeling heat and mass transfer processes under turbulent combustion conditions [23, 24].

The analysis of Figure 6 demonstrates that when the oxidizer temperature in the combustion chamber exceeds 800 K, the combustion process becomes significantly more intense. This is accompanied by accelerated ignition, an increased rate of chemical reactions, and more complete fuel oxidation. As a result, a substantially larger amount of heat is released, leading to a pronounced rise in chamber temperature, which in peak values approaches 3000 K.
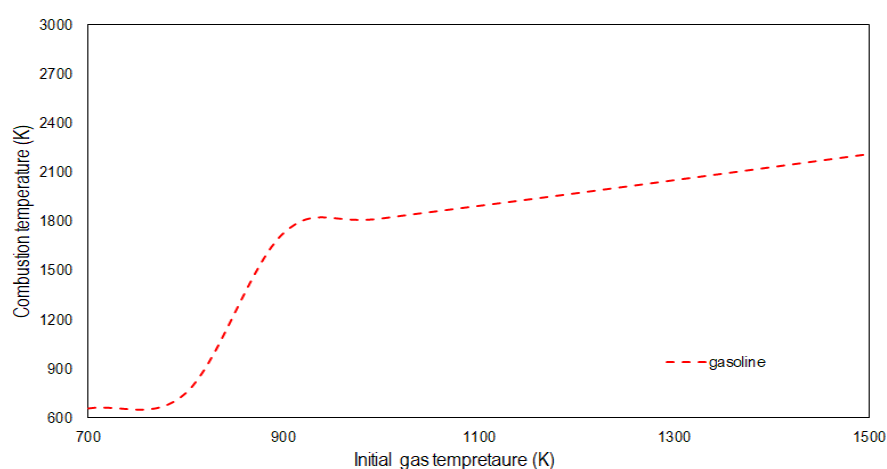
Figure 6. The distribution of the maximum combustion temperature in the combustion chamber,
depending on the initial gas temperature

Particular attention should be paid to the dependence of the maximum temperature on the initial conditions. When the oxidizer temperature increases from 900 K to 1500 K, the maximum flame temperature rises from 1726.09 K to 2208.53 K.This trend highlights the strong sensitivity of the thermodynamic characteristics of combustion to the initial thermal state, which is associated with intensified heat transfer, enhanced fuel droplet evaporation, and accelerated oxidation reactions.

Thus, increasing the initial oxidizer temperature not only strengthens heat release but also contributes to the formation of a more stable and energetic flame, which is of key importance for optimizing combustion chamber performance under conditions of high thermal loads.

Figure 7 presents the results of numerical simulations of nitrogen concentration evolution in the combustion chamber over time. The analysis shows that nitrogen concentration remains relatively stable during the initial phase, when fuel injection has just begun and significant interaction with the oxidizer has not yet occurred.

The most pronounced variations are observed at approximately 1.5 ms, when the injected fuel is fully delivered into the chamber, has evaporated, and chemical reactions are initiated. At this stage, the combustion process is accompanied by the formation of nitrogen oxides, resulting in a noticeable redistribution of concentration fields. These findings indicate that the dynamics of nitrogen concentration are closely linked to the stages of fuel injection, evaporation, and ignition, and may serve as an indicator of pollutant formation intensity during combustion.

Similar insights into the effects of flow dynamics on species distribution can be drawn from [25], where the influence of throttle hole diameters on fluid flow in an inertial hydrodynamic installation was investigated. The results demonstrated that variations in the constriction geometry significantly affect the velocity and

pressure fields, leading to a non-uniform distribution of fluid properties downstream of the throttle. By analogy, in combustion systems, such variations in local flow conditions can influence the mixing and transport of reactants, thereby affecting the spatial and temporal evolution of nitrogen concentration. This emphasizes that both injector geometry and flow constrictions play a crucial role in shaping concentration fields and may impact the intensity and localization of pollutant formation during combustion.

Figure 8 illustrates the gas velocity fields in the combustion chamber at different moments in time. At the initial stage of injection, gasoline droplets enter the chamber with a velocity of approximately 200 m/s, while the gaseous medium remains at rest. Due to the inertial motion of the droplets, the gas is entrained and acquires momentum, resulting in the formation of a high-velocity zone along the spray trajectory.

a) 0.5 ms   *b*) 1 ms   *c*) 1.5 ms   *d*) 1.9 ms
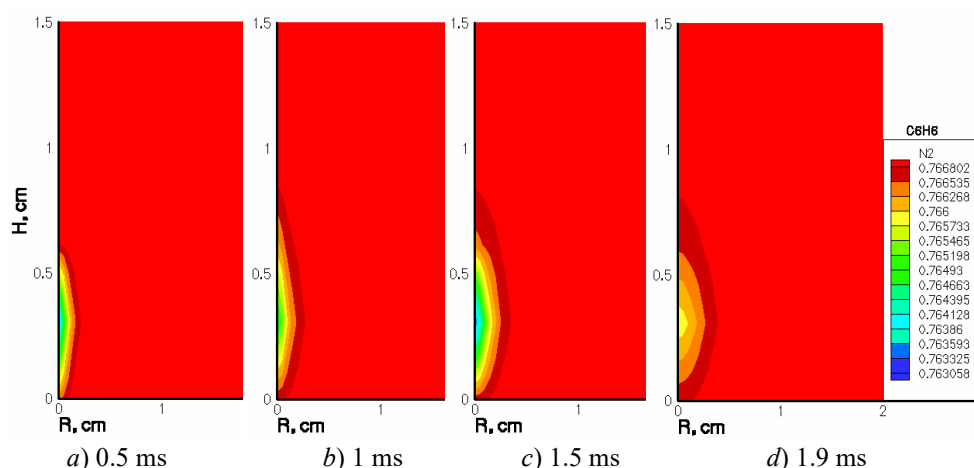
Figure 7. Distribution of nitrogen concentration during gasoline combustion at different time moments

a) 0.8 ms   *b*) 1.5 ms   *c*) 2.0 ms
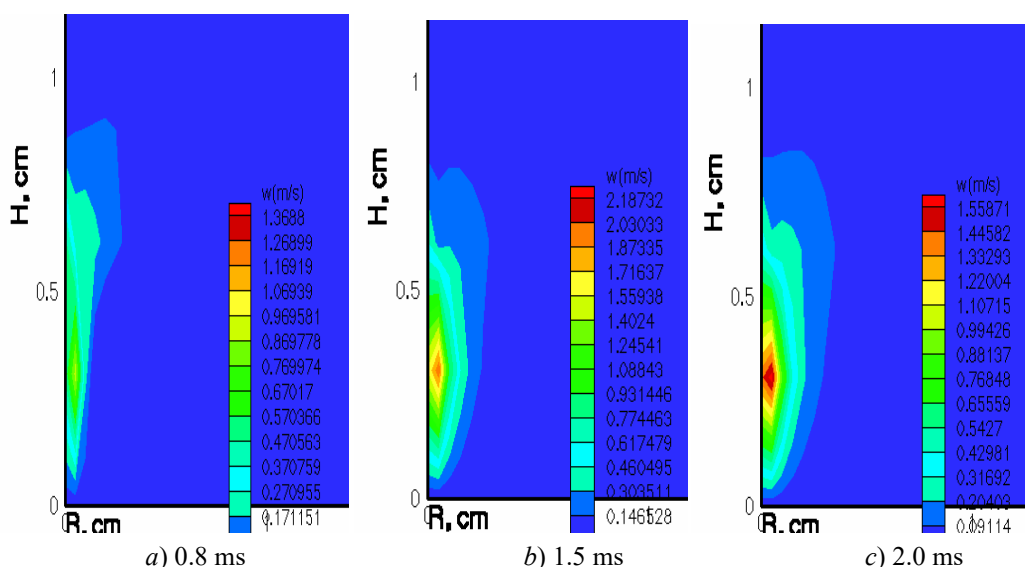
Figure 8. Distribution of gasoline droplet velocities at different time moments

The highest gas velocities are observed in the central axial region of the chamber, where the fuel jet develops. The maximum velocity occurs within a radial distance of about 1 cm from the chamber axis. In the radial direction, the velocity gradually decreases, forming a characteristic flow profile with a distinct high-velocity core and peripheral regions of deceleration.

Compared to biodiesel spray, gasoline droplets heat up and evaporate significantly faster due to their smaller size and lower viscosity. Biodiesel droplets are typically larger, more viscous, and contain oxygenated compounds, which slow down evaporation and delay thermal equilibrium with the surrounding hot gases. Consequently, biodiesel exhibits stronger temperature gradients and a less uniform distribution within the combustion chamber than gasoline [26]. Gasoline, in contrast, achieves more uniform heating and dispersion,

which enhances rapid mixing with air and promotes faster and more efficient combustion, giving it a clear advantage over both diesel and biodiesel in terms of spray dynamics and ignition responsiveness [27].

In addition, the lower surface tension of gasoline promotes more intense breakup of the liquid jet into fine droplets even at moderate injection pressures [28]. This ensures a more uniform spray formation and improves vapor–air interaction throughout the combustion chamber. As a result, gasoline is characterized by a shorter ignition delay and greater combustion stability, especially under transient operating conditions. Fine atomization also contributes to more complete utilization of the injected fuel, reducing the likelihood of locally rich zones that typically lead to incomplete combustion and soot formation.

Furthermore, the chemical composition of gasoline, characterized by a high-octane number and high volatility, provides better controllability of the combustion process. The high-octane number enhances resistance to detonation and allows for higher compression ratios, thereby improving the engine's thermal efficiency. Rapid evaporation of gasoline ensures earlier and more uniform flame front propagation, promoting stable combustion and reducing emissions of unburned hydrocarbons. Compared to heavier fuels, gasoline provides smoother flame development and lower cycle-to-cycle variations, making it particularly effective for high-speed and highly turbulent combustion systems where precise fuel–air mixture formation is critical.

The comparison of the results obtained in the present study with the numerical analysis data of gasoline sprays from the Engine Combustion Network (ECN) Spray G case, performed using the Large Eddy Simulation (LES) method and the Eulerian–Lagrangian framework, shows good agreement in the fundamental patterns of droplet breakup, dispersion, and evaporation [29]. Both studies confirm the key role of initial thermodynamic conditions, such as gas temperature and pressure, in shaping the spray structure and combustion intensity. With an increase in the initial gas temperature, a reduction in the mean droplet diameter and an acceleration of the evaporation process are observed, leading to a more uniform distribution of the fuel–air mixture and higher maximum temperatures in the combustion zone. Unlike the ECN Spray G configuration, which considered early and late injection regimes, the present work analyzed a temperature range from 700 to 1500 K at fixed injection parameters. Nevertheless, the penetration dynamics and radial distribution of droplets show similar trends: at higher temperatures, a stable spray plume with smaller droplets and a pronounced vertical temperature gradient is formed. Thus, the modeling results confirm the universality of the regularities identified within the ECN Spray G framework for various chamber geometries and turbulence conditions, enhancing the reliability of the findings and the validity of recommendations for optimizing spray and combustion processes.

These results demonstrate that the injection process strongly governs the gas-dynamic structure of the flow, determining the intensity of turbulent mixing and establishing the conditions for subsequent combustion.

Conclusions

This study simulated the processes of gasoline droplet breakup, dispersion, evaporation, and combustion in a model combustion chamber at various initial gas temperatures under high turbulence. The results obtained allow the following conclusions:

1. Increasing the initial gas temperature leads to a decrease in the average droplet diameter, which is associated with intensified evaporation and aerodynamic breakup processes, although the change in droplet size remains relatively small;

2. The droplet propagation dynamics demonstrate stable plume formation: at 0.8 ms, the droplets reach a height of up to 1.2 cm and are uniformly distributed across the chamber width to a width of 0.2 cm;

3. A pronounced droplet temperature gradient was established: in the lower zone, the temperature is approximately 300 K, while in the upper regions it reaches 500–550 K, reflecting the influence of droplet size and heat and mass transfer conditions;

4. As the oxidizer temperature increases above 800 K, the combustion process becomes more intense, with the maximum chamber temperature reaching 3000 K.As the initial temperature changes from 900 to 1500 K, the maximum temperature increases from 1726.09 K to 2208.53 K;

5. The nitrogen concentration changes most significantly at 1.5 ms, due to the completion of injection, fuel evaporation, and the onset of a chemical reaction accompanied by the formation of nitrogen oxides;

6. The gas-dynamic flow structure is determined by the injection process: maximum gas velocities are observed near the chamber axis and reach values within 1 cm along the radius, forming a characteristic flow profile with a high-velocity core and deceleration zones at the periphery.

Thus, the study confirms the decisive role of the initial gas temperature in shaping the characteristics of fuel atomization and combustion. The results obtained can be used to improve heat and mass transfer models and optimize the operating modes of combustion chambers in power and transport systems.

The proposed numerical solutions and identified regularities are applicable within the range of parameters characteristic of small-scale model combustion chambers operating under high turbulence. The results obtained describe the behavior of fuel droplets under conditions similar to those occurring in gasoline and diesel internal combustion chambers. The model can also be adapted for the study of biodiesel fuels, considering their specific physicochemical and thermodynamic properties. However, direct extension of the results to large-scale industrial systems requires additional verification and refinement of boundary conditions.

The developed comprehensive model has a universal character and can be applied to a wide range of liquid hydrocarbon petroleum fuels, as well as adapted for simulations involving biofuels. However, variations in the geometry or design features of the combustion chamber, as well as changes in operating conditions, require additional adjustment of the input parameters and refinement of boundary conditions. This approach ensures the reliability and adequacy of the computational results when extending the applicability of the model to broader operating ranges.

The numerical modeling methods implemented in the KIVA-3V software package are reproducible when using similar computational grids, time steps, and turbulence models. Under these conditions, the results can be verified not only by other researchers but also compared with experimental data, demonstrating satisfactory agreement in the main thermal characteristics. This confirms the reliability and physical validity of the applied approach.

The analysis showed that the general trends in spray and combustion characteristics remain consistent under moderate variations in the initial gas temperature and injection velocity. However, with significant deviations of input parameters, the stability of the numerical solution may decrease due to the nonlinear relationship between the turbulence intensity and the evaporation rate of fuel droplets. This relationship is confirmed both by the computational data obtained in the present study and by previously published experimental [13] and numerical works [6, 19], which demonstrate that an increase in turbulence intensity enhances phase mixing, heat and mass transfer, and consequently accelerates droplet evaporation.

To assess the accuracy, stability, and reliability of the obtained numerical results, a series of verification calculations was carried out. Convergence tests with respect to the computational grid and time step were performed, along with a sensitivity analysis of key parameters through sequential variation of input conditions. Calibration of chemical kinetic mechanisms was conducted to reproduce the ignition delay. The reliability of the numerical results was assessed using statistical indicators that characterize the accuracy and internal consistency of the model. In addition, mass and energy conservation were verified, and the influence of input uncertainties was assessed using the Monte Carlo method. The results confirm the stability, physical validity, and reproducibility of the comprehensive model within the range of initial gas temperatures of 700–1500 K, pressure of 80 bar, and mean droplet radius of approximately 25 μm.

The obtained results advance the understanding of the physicochemical mechanisms of breakup, dispersion, evaporation, and combustion of liquid fuel droplets under high turbulence conditions. The identified relationships between the initial gas temperature, spray flame dynamics, and thermochemical characteristics of the reacting flow make it possible to refine heat and mass transfer models and improve the accuracy of combustion parameter predictions. Of particular importance is the revealed role of oxidizer temperature in determining maximum flame temperatures and nitrogen concentration distributions, which contributes to the development of combustion theory and reactive flow modeling.

The findings can be applied in the design and optimization of combustion chambers in power plants and internal combustion engines. It has been shown that higher initial gas temperatures promote more intense combustion and stable flame formation, thereby increasing fuel efficiency and reducing emissions of harmful substances, including nitrogen oxides. The results may serve as a basis for improving fuel injection and atomization systems and for developing more environmentally friendly and energy-efficient combustion technologies.

References

1   Askarova, A., Bolegenova, S., Ospanova, Sh., Bolegenova, K., &Nurmukhanova, A. (2025). Energetic Efficiency of Turbulent Biofuel Combustion for Advanced Bioenergy Technologies. *International Journal of Mathematics and Physics*, *16*(1), 20–28.

2   U.S.Energy Information Administration (EIA) total reports. Retrieved from https://www.eia.gov/totalenergy/reports.php#/T120

3   Usman, O., Iorembe, P.T., Ozkan, O., & Alola, A.A. (2025). The asymmetric effect of household and commercial energy efficiency on U.S. energy-related CO_2emissions. *Innovation and Green Development*, *4*(5), 100293.

4   Hill, A. (2025). The social welfare implications of electrification in the U.S. residential energy market. *Journal of Environmental Economics and Management, 131,* 103136.

5   Report InformasiyaAgentliyi. Retrieved from https://report.az/ru/energetika/eia-mirovoe-potreblenie-zhidkogo-topliva-uvel

6   Askarova, A., Bolegenova, S., Ospanova, Sh., Rakhimzhanova, L., Nurmukhanova, A., & Adilbayev, N. (2024). Optimization of Fuel Droplet Sputtering and Combustion at High Turbulence Flows. *Russian Physica Journal*, *67*, 167–170.

7   Bolegenova, S., Askarova, A., Ospanova, S., Makanova, A., Zhumagaliyeva, S., Nurmukhanova, A., Adilbayev, N., & Shalkar, A. (2024). Simulation of liquid fuel spray formation and distribution in a reacting turbulent flow. *Eurasian Physical Technical Journal*, *21*(2(48)), 22–30.

8   Castaldi, M., Bonheure, M., Eulitz, F., Van Geem, K.M., & Verstraete, T. (2023). Development and application of an implicit density-based solver for chemically reacting flows in OpenFOAM. *Computers & Fluids*, *300*, 106766.

9   Mohsin, H.M., Zhuo, Y., & Shen, Y. (2024). Eulerian-Eulerian-VOF multifluidmodelling of liquid–gas reacting flow for hydrogen generation in an alkaline water electrolyser. *Fuel*, *373*, 132164.

10   Zhapbasbayev, U.K., Bossinov, D.Zh.,Pahomov, M.A., & Sattinova, Z. (2025). Modeling of turbulent non-isothermal flow in a heating network pipe. *Bulletin of the University of Karaganda–Physics*, *30*(2(118)), 67–74.

11   Tretola, G., Navarro-Martinez, S., & Vogiatzaki, K. (2022). Primary break-up characterisation and droplet statistics of multihole sprays using a probabilistic surface density methodology. *International Journal of Multiphase Flow, 152,* 104039.

12   Macpherson, G. B., Nordin, N., & Weller, H. G. (2009). Particle tracking in unstructured, arbitrary polyhedral meshes for use in CFD and molecular dynamics. *Communications in Numerical Methods in Engineering*, *25*, 263–273.

13   Khan, S. B., Alroe, J., Medcraft, C., Sauret, E., Harrison, D., & Ristovski, Z. (2025). Secondary droplet breakup of impaction-pin nozzle: Comparison between experimental and CFD-DPM modelling. *Journal of Aerosol Science*, *190*, 106664.

14   Gorokhovski, M., & Barge, A. (2025). Assessment of fluctuating drag model for a single particle larger than the Kolmogorov length scale. *Physics of Fluids, 37*, 053316.

15   Amanbaev, T.R., Tilleuov, G.E., & Zuparbekova, A. (2021). Mathematical modeling of dispersed media flows in the presence of nucleation, coagulation and phase transitions. *Bulletin of the University of Karaganda–Physics*,*102*(2), 14–24.

16   Ra, Y. & Reitz, R.D. (2008). A reduced chemical kinetic model for IC engine combustion simulations with primary reference fuels. *Combustion and Flame*, *155*, 713–738.

17   Liang, L., Reitz, R. D., Iyer, C.O., & Yi, J. (2007). Modeling knock in spark-ignition engines using a G-equation combustion model incorporating detailed chemical kinetics. *SAE Technical Paper*, 2007-01-0165.

18   Gorokhovski, M. & Borghi, R. (1993). Numerical simulation of soot formation and oxidation in diesel engines. *SAE Transactions*, *102*, 118–130.

19   Tao, F., Golovitchev, V. I., & Chomiak, J. (2004). A phenomenological model for the prediction of soot formation in diesel spray combustion. *Combustion and Flame*, *136*(3), 270–282.

20   Askarova, A., Bolegenova, S., Ospanova, Sh., Bolegenova, K., & Nurmukhanova, A. (2025). Simulation of the effective distribution of biofuel droplets in a reacting flow. *Journal of Machine Engineering*, *25*(2), 123–137.

21   Amsden, A.A. (1997). *KIVA-3V: A Block-Structured KIVA Program for Engines with Vertical or Canted Valves*. Los Alamos, New Mexico, 80 p.

22   Yang, S.L., Siow, Y.K., Teo, C.Y., & Hanjalic, K. (2005). A KIVA code with Reynolds-stress model for engine flow simulation. *Energy, 30*(2–4), 427–445.

23   Bolegenova, S., Askarova, A., Ospanova, Sh., Zhumagaliyeva, S., Makanova, A., Aldiyarova, A., Nurmukhanova, A., & Idrissova, G. (2024). Technology of reducing greenhouse gas emissions for decarbonization and decreasing anthropogenic pressure on the environment. *Physical Sciences and Technology*, *11*(1-2), 64–75.

24   Zhumanbayeva, A.S., Jaichibekov, N.Zh., & Kurmanova, D.Y. (2025). Study of the influence of turbulence models on hydrodynamic and thermal parameters of heat carriers in calculations of heat exchangers. *Bulletin of the University of Karaganda–Physics*, *30*(3(119)), 68–76.

25   Nussupbekov, B.R., Ovcharov, M.S., Oshanov, E.Z., Yesbergenov, U.B., Duisenbayeva, M.S., Tishbekov, A.A., & Amanzholova, M.K. (2023). Determination of the effects of the diameters of the throttle holes on the fluid flow of an inertial hydrodynamic installation. *Bulletin of the University of Karaganda–Physics, 112*(4), 82–90.

26   Askarova, A., Bolegenova, S., Ospanova, Sh., Maxutkhanova, A., Bolegenova, K., & Baidullayeva, G. (2025). Study of thermophysical dynamics in biofuel droplet atomization and combustion. *Eurasian Physical Technical Journal*, *22*(2(52)), 60–69.

27 Yadav, M., Yadav, A. K., & Ahmad, A. (2024). Enhancing combustion and emission characteristics of CI engines through atomization and fuel–air mixing using non-circular orifices: A path towards sustainable biodiesel utilization. *Green Technologies and Sustainability*, *3*(343), 100161.

28 Duronio, F., Zhang, A., Zhao, L., & De Vita, A. (2025). Assessment of an effervescent breakup model for Lagrangian simulations of real fuel sprays. *International Journal of Thermofluids, 25*, 100991.

29 Lien, H.P., Li, Y., Pati, A., Sadiki, A., & Hasse, Ch. (2024). Numerical studies of gasoline direct-injection sprays (ECN Spray G) under early- and late-injection conditions using Large Eddy Simulation and droplets-statistics-based Eulerian–Lagrangian framework. *Fuel, 357*, 129708.

А.С. Аскарова, С.А. Болегенова, Ш.С. Оспанова,
С.А. Болегенова, Г.Е. Байдуллаева, А.З. Нурмуханова

Жоғары турбуленттіліктегі сұйық отын тамшыларының дисперсиясын, ыдырау және жану процестерін зерттеу

Жұмыста модельдік жану камерасындағы жоғары турбуленттіліктегі әсерлесетін ағындағы бензин тамшыларының ыдырау, дисперсиясы және булану процестері заманауи компьютерлік модельдеу әдістерін пайдалана отырып зерттелінді. Камерадағы газдың бастапқы температурасының бүрку динамикасына, тамшылардың таралуына және ағынның жылулық сипаттамаларына әсері талданды. Модельдеу бойынша жүргізілген есептік эксперименттердің нәтижелері әсерлесетін ағынның температуралық, аэродинамикалық және концентрациялық сипаттамаларын қамтитын толық визуализациясын алуға мүмкіндік берді. Газдың бастапқы температурасының өсуі тамшылардың орташа өлшемінің кемуіне, олардың булануын жеделдетуге және жану интенсивтілігінің артуына алып келетіні анықталды. Тамшылар соплодан едәуір қашықтыққа таралып, салыстырмалы түрде біркелкі радиалды үлесуге ие болатындығы байқалды. Камера бойымен жоғары қозғалған сайын тамшылардың температурасы біртіндеп артып, екі фазалы ағынмен күрделі әрекеттесуді бейнелейді. Газ температурасының өсуі жанудың қарқындылығын арттырып, максималды температуралық көрсеткіштердің айтарлықтай жоғарылауына ықпал ететіні дәлелденді. Жүргізілген зерттеу нәтижелері бойынша газдың бастапқы температурасының бүрку мен алау құрылымын қалыптастырудағы негізгі рөлі айқындалып, жылу қозғалтқыштарының жану камераларының жұмысын оңтайландыру бойынша ұсыныстар жасауға негіз болды.

Кілт сөздер: сұйық отын, тамшылар, жану, дисперсия, бүрку, турбулентті ағын, газ, температура, бүрку динамикасы, модельдеу, жану камерасы

А.С. Аскарова, С.А. Болегенова, Ш.С. Оспанова,
С.А. Болегенова, Г.Е. Байдуллаева, А.З. Нурмуханова

Исследование процессов дисперсии, распада и горения капель жидкого топлива при высокой турбулентности

В настоящей работе исследованы процессы распада, дисперсии и испарения капель бензина в модельной камере сгорания в реагирующем потоке при высокой турбулентности с использованием современных методов компьютерного моделирования. Проведен анализ влияния начальной температуры газа в камере на динамику распыла, распределение капель и тепловые характеристики потока. Результаты вычислительных экспериментов по моделированию позволили получить детализированную визуализацию реагирующего потока, включающую температурные, аэродинамические и концентрационные характеристики топливно-воздушной смеси. Установлено, что повышение начальной температуры газа приводит к уменьшению среднего размера капель, ускорению их испарения и усилению интенсивности сгорания. Выявлено, что капли распространяются на значительные расстояния от сопла, демонстрируя при этом относительно равномерное радиальное распределение. При продвижении вверх по камере температура капель постепенно увеличивается, отражая сложное взаимодействие с двухфазным потоком. Доказано, что с ростом температуры газа сгорание становится более интенсивным, а максимальные температурные показатели значительно возрастают. На основе проведенного исследования обоснована ключевая роль начальной температуры газа в формировании структуры распыла и факела, что позволяет формулировать рекомендации по оптимизации работы камер сгорания тепловых двигателей.

Ключевые слова: жидкое топливо, капли, горение, дисперсия, распыл, турбулентный поток, газ, температура, динамика распыла, моделирование, камера сгорания

Information about the authors

Askarova, Aliya — Doctor of Physical and Mathematical Sciences, Professor of the Department of Thermophysics and Technical Physics, al-Farabi Kazakh National University, al-Farabi avenue, 71, 050040, Almaty, Kazakhstan; e-mail: Aliya.Askarova@kaznu.edu.kz; https://orcid.org/0000-0003-1797-1463

Bolegenova, Saltanat — Doctor of Physical and Mathematical Sciences, Professor, Head of the Department of Thermophysics and Technical Physics, al-Farabi Kazakh National University, al-Farabi avenue, 71, 050040, Almaty, Kazakhstan; e-mail: Saltanat.Bolegenova@kaznu.edu.kz; https://orcid.org/0000-0001-5001-7773

Ospanova, Shynar (*corresponding author*) — PhD, Acting Associate Professor of the Department of Thermophysics and Technical Physics, al-Farabi Kazakh National University, al-Farabi avenue, 71, 050040, Almaty, Kazakhstan; e-mail: Shynar.Ospanova@kaznu.edu.kz; https://orcid.org/0000-0001-6902-7154

Bolegenova, Symbat — PhD, Associate Professor of the Department of Thermophysics and Technical Physics, al-Farabi Kazakh National University, al-Farabi avenue, 71, 050040, Almaty, Kazakhstan; e-mail: Bolegenova.Symbat@kaznu.edu.kz; https://orcid.org/0000-0003-1061-6733

Baidullayeva, Gulzhakhan — Candidate of Physical and Mathematical Sciences, Associate Professor of the Department of Normal Physiology with a Biophysics Course, Asfendiyarov Kazakh National Medical University, Tole-bi str., 94, 050012, Almaty, Kazakhstan; e-mail: G.baydullaeva@mail.ru; https://orcid.org/0000-0002-1998-1617

Nurmukhanova, Alfiya — Candidate of Technical Sciences, Senior Lecturer of the Department of Thermophysics and Technical Physics, al-Farabi Kazakh National University, al-Farabi avenue, 71, 050040, Almaty, Kazakhstan; e-mail: alfiyanurmukhanova7@gmail.com; https://orcid.org/0000-0002-0289-3610

CORRIGENDUM

G.K. Alpyssova[1], Zh.K. Bakiyeva[1*], I.P. Denisov[2], E.V. Kaneva[3],
E.V. Domarov[4], A.K. Tussupbekova[1]

[1]Karaganda Buketov University, Karaganda, Kazakhstan;
[2]National Research Tomsk Polytechnic University, Tomsk, Russian Federation;
[3]X-ray Analysis Laboratory, Vinogradov Institute of Geochemistry SB RAS, Irkutsk, Russian Federation;
[4]Budker Institute of Nuclear Physics of the Siberian Branch of the Russian Academy of Sciences Novosibirsk, Russian Federation
([*]Corresponding author's e-mail: shanar83@mail.ru)

Dependence of the Radiation Synthesis Efficiency of Ceramics Based on Tungstates on the Flow Power

Ceramic samples of monocomponent (CaO, MgO, ZnO and WO_3) and two-component ($ZnWO_4$, $MgWO_4$, $CaWO_4$) compositions were synthesized by direct impact of high-energy electron flow on the charge of stoichiometric composition. Radiation synthesis of samples weighing about 50 g is realized in time of 10s without the use of any additional substances to stimulate the process. Systematic studies of the dependence of radiation synthesis of tungstate ceramics on the flux power density have been performed for the first time. It was found that the dependences of synthesis efficiency on the flux power density of monocomponent (CaO, MgO, ZnO and WO_3) and two-component ($ZnWO_4$, $MgWO_4$, $CaWO_4$) ceramic samples have the form of constantly increasing curves. There is a threshold above which the synthesis is realized for all synthesized samples. The effect of mutual influence of charge components on the efficiency of synthesis of two-component systems was found. Synthesis of $ZnWO_4$, $MgWO_4$, $CaWO_4$ ceramics is realized under the same conditions of radiation treatment, while the thresholds of synthesis realization of one-component samples of CaO, MgO and ZnO and WO_3 ceramics differ significantly. It is shown that at all used modes of radiation treatment the formation of ceramics with the same properties are realized. This effect is due to the inhomogeneous distribution of electron flux energy losses in the substance. Synthesis of two-component ($ZnWO_4$, $MgWO_4$, $CaWO_4$) ceramic samples is realized at the same power density above 1,0 kW/cm^2. The radiation synthesis of the $ZnWO_4$, $MgWO_4$, $CaWO_4$ ceramics is mainly determined by tungsten oxide.

Keywords: ceramics; metal tungstate, luminescence; radiation synthesis, X-ray diffraction spectra, EDX analysis, power density, optical properties of ceramics

Introduction

Crystals and ceramics based on tungstate of alkaline-earth and rare-earth metals have found wide application as scintillation materials [1–3]. These materials have high absorption capacity of radiation, are resistant to external factors: temperature, aggressive media. They can be used both for registration of heavy particles, electrons and X-ray radiation [4–7].

Synthesis of these materials from metal oxides with high melting point is difficult. Moreover, the melting point of the main initial component, WO_3 (1473 °C), differs significantly from the melting points of other components, such as MgO (2825 °C), ZnO (1975 °C), CaO (2572 °C). Therefore, the synthesis methods used, most often Czochralski and Bridgman [8–11], are labor-intensive, time-consuming, and require the use of other substances to stimulate synthesis.

Radiation method is promising for the synthesis of ceramics based on metal oxides, fluorides. It realized and described first time in [12–14]. The radiation method showed that the impact of a powerful flow of electrons with an energy of 1.4, 2.5 MeV t power density up to 30 kW/cm^2 on the charge stoichiometric

composition is possible to form ceramics based on metal oxides, including tungstate. It is established that the synthesis is realized by direct impact of the electron flux on the charge in the crucible for a time less than 1 s, with high efficiency, without the use of any additional substances that contribute to the process.

The present work is aimed at studying the dependence of the synthesis efficiency on the radiation ion treatment modes, in particular, on the power density of the electron flux falling on the charge.

Experimental

Radiation synthesis of ceramics was realized by direct impact of a powerful flow of high-energy electrons on the charge. The synthesis of materials was carried out by direct electron beam irradiation using the ELV6 electron accelerator at the facility UNU Stand ELV-6 of Budker Institute of Nuclear Physics, of the Siberian Branch of the Russian Academy of Sciences Novosibirsk, Russian Federation. The ELV-6 electron accelerator provides generation of electron flux with energies in the range from 1.4 to 2.5 MeV and power up to 100 kW. The electron beam output through the differential pumping system has a Gaussian distribution in cross-section. In our experiments, the beam area on the charge surface in the crucible was 1 cm^2. A scanning system was used for obtaining large area samples. The beam was scanned at a frequency of 50 Hz across the mixture surface in the transverse direction of a crucible with a width of 5 cm and a length of 10 cm. The crucible was displaced relative to the scanning beam at a speed of 1 cm/s for the entire length of the crucible. Each elementary section of the charge in the crucible was exposed to the radiation flux for 1 s. The total time of exposure of the electron flux to the treated surface of the charge in the crucible was always 10 s. The synthesis of ceramics was realized only due to the energy of the radiation flux, only from the charge materials, without additives of other materials facilitating the process.

Measurements of dispersity of initial powders used for synthesis of initial powders for obtaining ceramic samples were carried out by laser diffraction method using a laser particle size analyzer Shimadzu SALD-7101.

The X-ray diffraction patterns were obtained using a Bruker D8 ADVANCE (AXS, Berlin, Germany) diffractometer equipped with a scintillation detector.

The luminescence of the synthesized samples (luminescence excitation spectra and luminescence spectra) were measured using a Cary 5000 UV-Vis-NIR spectrophotometer.

Results and Discussion

Mixtures of WO$_3$, MgO, ZnO, CaO starting powders in stoichiometric ratio were prepared for synthesis. All the starting powders were obtained from Hebei Suoyi New Material Technology Co., Ltd, had a purity degree of at least 99,95 %.

It was shown in [15] that the results of radiation synthesis are largely determined by the prehistory of the starting materials, not only their purity but also their particle size distribution. All starting materials have significantly different melting temperatures [16]. In this connection, we investigated the particle size distribution and performed radiation synthesis of each of the starting materials prior to the synthesis of multicomponent ceramics.

The results of the particle size distribution study are shown in Figure 1. The figures show the distribution of particles in the used powders in the form of dependence of the number of particles on their size and dependence of the volume of the particles.

There are two groups of particles with sizes from 0,01 to 1 μm and from 1 μm to 50 μm for all powders. The number of small particles is dominant, but in the total volume of powders their volume is much smaller. Therefore, the synthesis result should be determined mainly by the number of the large particles. The ratio between the number of small and large particles in powders of different composition differs. As follows from the presented results, the distributions of large particles of ZnO and MgO overlap with the distribution of WO$_3$ particles. The size distribution range of large CaO particles is much wider than that of WO$_3$. We can expect a difference in the efficiency of synthesis of ceramics of tungstates of these two groups: a large difference in the size of the initial particles may appear in the express synthesis due to the existence of local non-stoichiometry [14].

The starting materials for the synthesis of two-component metal tungstate ceramics have significantly different melting points: WO$_3$ (1473 °C), MgO (2825 °C), ZnO (1975 °C), CaO (2572 °C), which can affect the efficiency of their synthesis [17]. However, for radiation synthesis, ionization processes play a dominant role in the formation of a new structure from the initial ones, while thermal processes contribute to their efficiency. It seems necessary to study the efficiency of radiation synthesis of ceramics of starting materials. We

have carried out a series of studies of the dependence of the synthesis of ceramics from starting materials on the power density of the radiation flux. The charge for synthesis was simply initial powders of WO_3, ZnO, MgO, CaO. Radiation treatment of the charge was carried out under the conditions mentioned above in the "without scanning" mode. The dependence of the morphology of synthesized samples on the modes of radiation exposure and electron flux power density is shown in Figure 2.
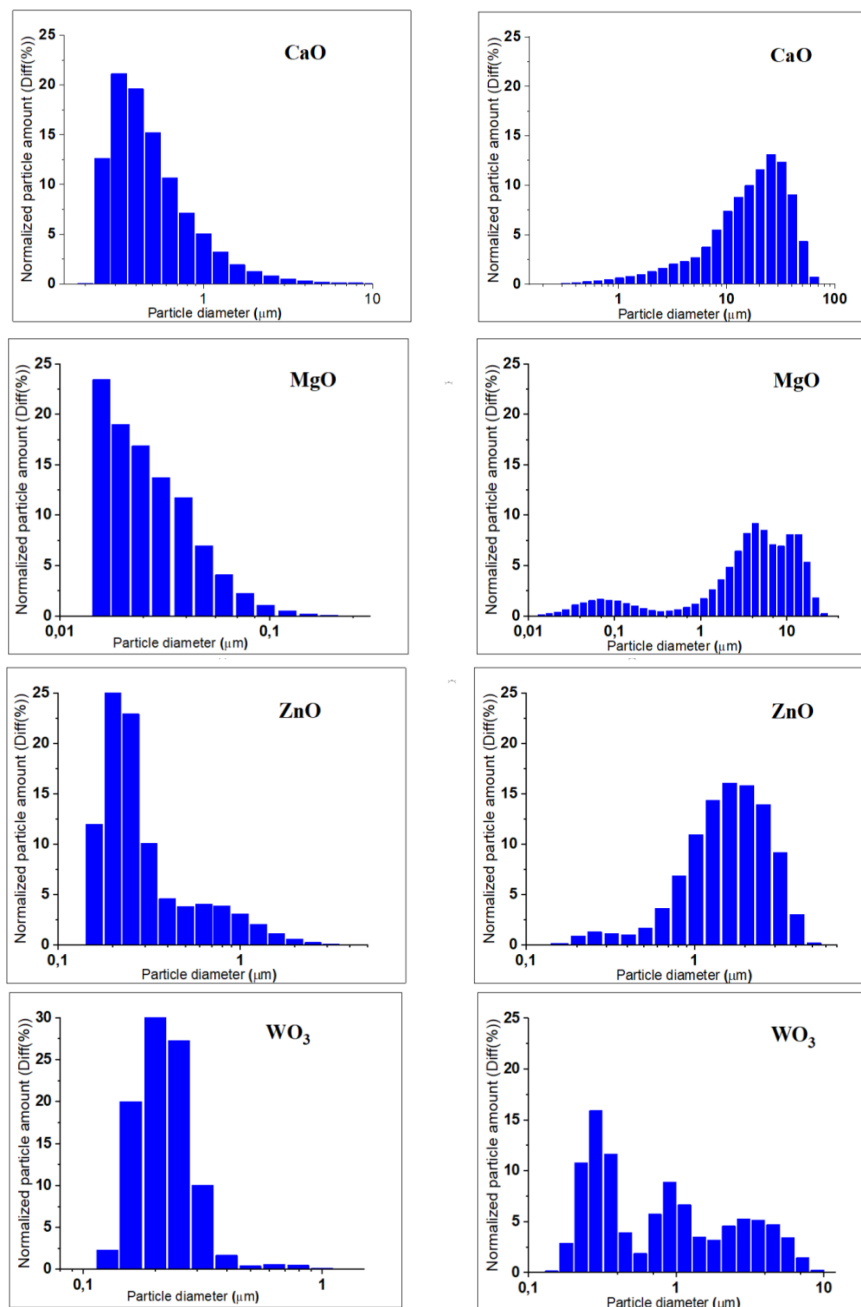
Figure 1. Particle number and volume distribution of the used powders

Figure 2 shows photos of ceramic samples from the initial materials. The value of power density is indicated in the figures. As follows from the presented photos for monocomponent ceramic samples, the dependence of the synthesis result on the electron flux power density is clearly visible. Especially clearly this dependence is seen on the example of WO_3 and ZnO. This dependence is less pronounced in the synthesis of CaO ceramics. Synthesized MgO ceramics has high power densities, but the ceramic samples are formed under the surface of the charge, because the bulk density of the MgO charge ($\rho=0.5$ g/cm^3) is much less than WO_3 ($\rho=2.6$ g/cm^3) and ZnO ($\rho=1.1$ g/cm^3). WO_3 and ZnO differ significantly from MgO and CaO in melt-

ing temperatures. For CaO, a picture of a sample obtained using the "with scanning" mode is given as an example. The synthesis of ceramics from the whole charge in the crucible is realized in this mode. Accordingly, in order to fulfill the equality of absorbed energy in both modes, the power density in the "with scanning" mode is increased by a factor of 5.
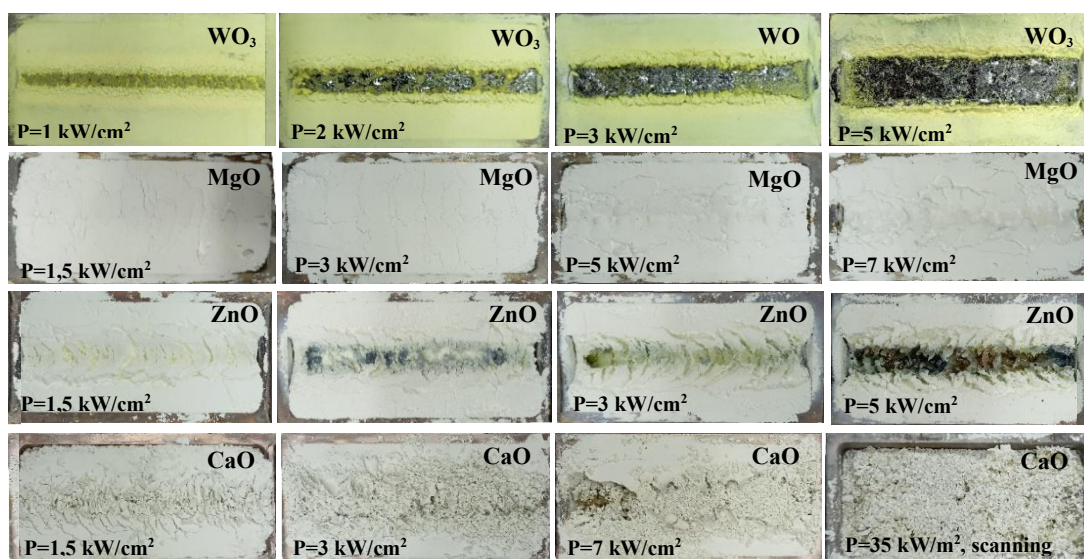
Figure 2. Dependence of morphology of synthesized samples on radiation exposure
modes-electron flux power density

Quantitative dependences of synthesis efficiency on power density in the studied monocomponent compositions are shown in Figure 3. Synthesis efficiency in this work is understood as the weight of the synthesized sample. Such characterization of the process seems to be quite justified: the charge volume in our work is always the same using the same crucibles.
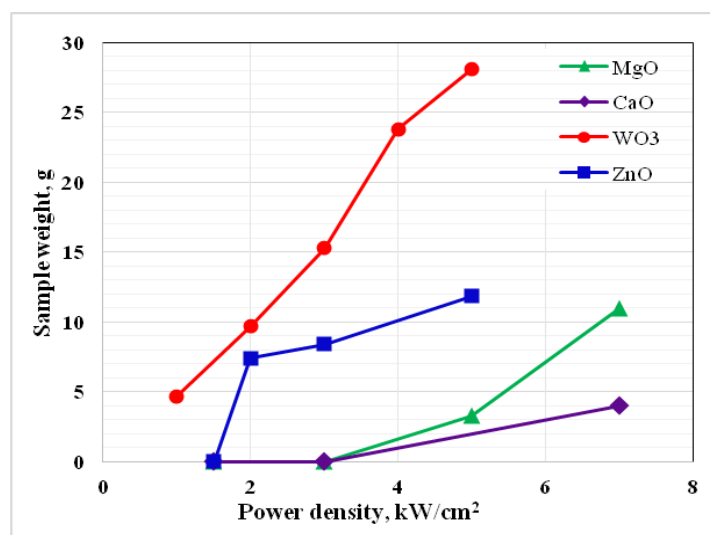
Figure 3.Dependence of ceramic synthesis efficiency from used initial
monocomponent compositions on power density

The synthesis of WO_3 and ZnO ceramics is realized when the power density exceeds 1–1.5 kW/cm^2, whereas for the synthesis of MgO and CaO ceramics, power densities above 2.5 kW/cm^2 are required.

We consider that it is necessary to emphasize the following. To determine the weight of the synthesized sample using the "without scanning" mode, the sample is removed from the crucible and cleaned from the charge adhering to it. This procedure is easily realized when the charge is treated with high power radiation

fluxes. It is impossible to clean the completely porous sample from the charge at low power densities. Therefore, the initial points on the dependences are determined with some error. Nevertheless, the full dependence quite unambiguously indicates that the threshold for the realization of the synthesis of WO_3 and ZnO ceramics is lower than that of MgO and CaO. It is necessary to pay attention to the existence of a constant growth of the sample weight at high power density. The growth of the sample weight is due to the increase of the sample area, as it is clearly seen for WO_3 and ZnO. The growth of the bandwidth of the formed ceramics is due to the fact that the electron beam has a Gaussian distribution. As the integral power of the beam increases, the width of its impact region increases with exceeding the threshold for synthesis, as can be seen from Figure 2.

A charge was prepared from the above described monocomponent metal oxides and radiation synthesis was performed. The charge was prepared from oxide powders in stoichiometric ratio. Table 1 describes the compositions prepared for synthesis, radiation treatment modes used for synthesis, electron flux power density. The sample number means the serial number of the experiment according to the accounting system adopted by the authors. The masses of the charge in the crucible and the yield of the synthesis reaction are also given. Here, the yield of the synthesis reaction is understood as the ratio of the mass of the sample to the mass of the charge used. The synthesis was carried out in the "scanning" mode.

Table 1

Composition of synthesized ceramics when treated with 1.4 MeV electron flow

Sample, №	Sample description	P, kW/cm^2	M$_s$, g	Output, %
623	$ZnWO_4$ (ZnO 26 %), (WO$_3$ 74 %)	15	64,63	91,29
624	$MgWO_4$ (MgO 14,8 %), (WO$_3$ 85,2 %)	15	47,31	97,17
625	$CaWO_4$ (CaO 19,5 %), (WO$_3$ 80,5 %)	15	39,46	73,28
627	$ZnWO_4$ (ZnO 26 %), (WO$_3$ 74 %)	15	62,56	93,36
738	$MgWO_4$ (MgO 14,8 %), (WO$_3$ 85,2 %)	18	36,99	98,8
718*	$ZnWO_4$ (ZnO 26 %),(WO$_3$ 74 %)	22	86,62	90,0
*Note – 718 was obtained at an electron beam energy of 2.5 MeV.				

Figure 4 shows photos of samples of synthesized ceramics in standard crucibles with internal dimensions of 100×50 mm.
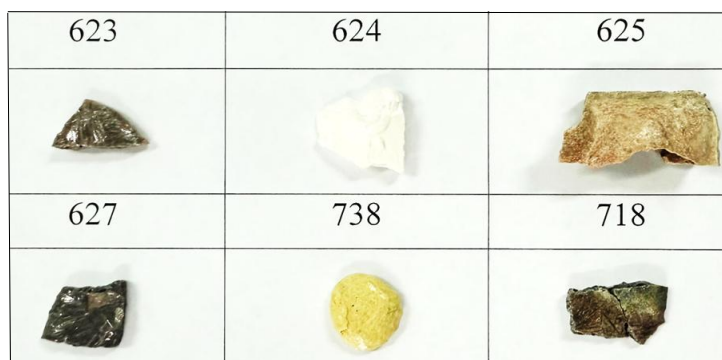
Figure 4. Photos of samples of synthesized ceramics with numbers 623, 624, 625, 627, 718, 738 (Table 1)

The samples have the form of plates similar to solidified molten mass, about 5 mm thick, with a porous structure inside. Not the entire volume of the charge is involved in the synthesis of ceramics. They use three types of crucibles differing in depth: 7, 10 and 14 mm. For each experiment, differing in the composition of the synthesized ceramics, its bulk density, and electron energy, the one is chosen at which the electrons of the beam will be completely absorbed by the charge. Otherwise, atoms (ions) from the crucible will be introduced into the formed ceramics. Therefore, there always remains a layer of unused charge under the formed ceramics. Part of the charge may disappear during radiation treatment, atomized due to charging of particles by the electron beam. This process can be significant at low mass of dielectric particles of initial substances. We take into account in determining the yield of the synthesis reaction the existence of residues of the charge in the crucible and atomization during radiation treatment.

As can be seen in Table 1, the yield of the synthesis reaction in all samples synthesized in the "with scanning" mode has a value ranging from 73 % to 98 %. Two reasons for this difference are possible. CaO (2572 °C) has a melting point higher than ZnO (1975 °C) and WO_3 (1473 °C). But MgO (2825 °C) also has a melting point higher than ZnO and WO_3. Another factor that differentiates the starting materials is the difference in particle size distribution. In the dispersion spectra (Fig. 1), the number and volume of particles with sizes above 10 μmare are much larger in CaO than in WO_3, MgO and ZnO. It seems to us that this characteristic can determines the difference in the yields of the material synthesis reaction. Nevertheless, we do not deny the influence of the difference in melting temperatures on the synthesis process.

Studies of the dependence of the synthesis efficiency of $ZnWO_4$, $MgWO_4$, $CaWO_4$ ceramics in the "without scanning" mode were performed, as well as for monocomponent compositions shown in Figure 3. The results of the studies are presented in Table 2 and Figure 5. The weight of $CaWO_4$, $MgWO_4$, $ZnWO_4$ tungstate ceramics samples was measured during synthesis without scanning at different electron beam power densities with E=1.4 MeV.

Table 2

Efficiency of synthesis of tungstate ceramics

Power P, kW	Weight of $CaWO_4$, g	Weight of $MgWO_4$, g	Weight of $ZnWO_4$, g
1,5	8,74	11,07	9,57
2	12,97	14,55	13,47
3	16,88	18,26	20,14

Weight dependence of $CaWO_4$, $MgWO_4$ and $ZnWO_4$ tungstate ceramics during synthesis without scanning at different electron beam power densities with E=1.4 MeV.
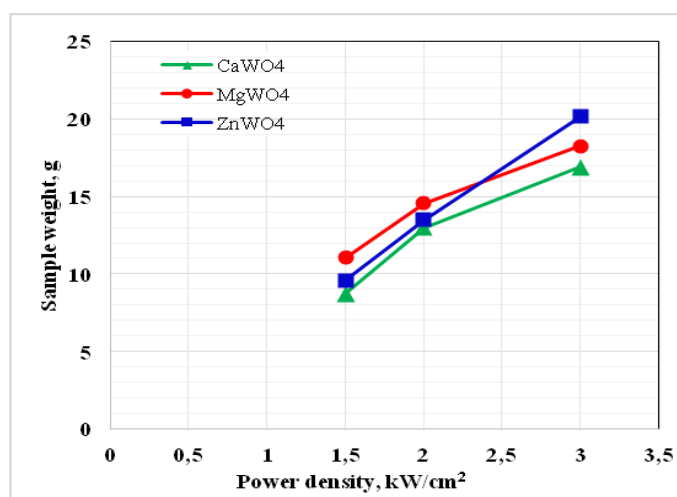
Figure 5. Weight dependence of $CaWO_4$, $MgWO_4$, $ZnWO_4$ tungsten ceramics on electron flux power density

As follows from the presented results, synthesis in all investigated samples of multicomponent ceramics is realized at the same regimes of radiation treatment. We emphasize that ceramics of monocomponent samples is realized at different regimes for CaO, MgO, WO_3 and ZnO. Note that equal conditions of electron beam energy losses during radiation treatment in the "without scanning" mode, for example 1.5 kW/cm^2, corresponds to 7–85 kW/cm^2 in the "with scanning" mode.

The structure of synthesized samples of $ZnWO_4$, $CaWO_4$ ceramics was studied by X-ray diffraction using a Bruker D8 ADVANCE diffractometer (AXS, Berlin, Germany) equipped with a scintillation detector in step-scan mode over a diffraction angle range of 10 to 90° 2θ and CuKα radiation as the source. Details of the research methodology and analysis are described in [15].

The results of the X-ray powder diffraction investigation are presented in Table 3. The qualitative phase analysis and indexing of the diffraction patterns utilized the data from the PDF-2 database (ICDD, 2007) as follows:

- PDF 01-088-0251 "Zinc tungsten oxide ($ZnWO_4$)", symmetry — monoclinic lattice, space group — $P2/c$ (#13), $a = 4.6926$ Å, $b = 5.7213$ Å, $c = 4.9281$ Å, $\beta = 90.632$ °.

- PDF 01-072-0257 "Calcium tungsten oxide ($CaWO_4$)", symmetry — body-centered tetragonal lattice, space group — $I41/a$ (#88), a = 5.243 Å, c = 11.376 Å.

- PDF 01-072-0677 "Tungsten oxide (WO_3)", symmetry — monoclinic lattice, space group — $P21/n$ (#14), a = 7.306 Å, b = 7.54 Å, c = 7.692 Å, β = 90.881 °.

T a b l e 3

The results of the phase composition investigation

Sample	Phase	Degree of crystallinity	Crystallite size	Refined unit cell parameters
$ZnWO_4$	$ZnWO_4$	99.9 ($\pm$5) %	131 ($\pm$15) nm	$P2/c$, a = 4.689(4) Å, b = 5.716(7) Å, c = 4.925(3) Å, β = 90.6(1) °, V = 132.0(1) Å^3
$CaWO_4$	$CaWO_4$ (~86 %)	99.9 ($\pm$5) %	167 ($\pm$35) nm	$I41/a$, a = 5.243(2) Å, c = 11.371(4) Å, V = 312.5(2) Å^3
	WO_3 (~14 %)		114 ($\pm$28) nm	$P21/n$, a = 7.311(2) Å, b = 7.532(2) Å, c = 7.694(2) Å, β = 90.8(1) °, V = 423.6(1) Å^3

The results of the study of $MgWO_4$ ceramics are not presented due to the absence of complete data on this material in our database [18]. As can be seen from the results presented in the table, during radiation synthesis in the samples ceramics formed crystalline phase in the form of crystallites with sizes of 100–170 nm. The dominant phase is $ZnWO_4$, $CaWO_4$ ceramics, with WO_3 as the accompanying phase [19].

The main functional characteristic of metal tungstates is luminescence and its properties [20]. Excitation and luminescence spectra were measured for $ZnWO_4$, $MgWO_4$, $CaWO_4$ ceramics samples [21]. The excitation and photoluminescence spectra were measured on a SM-2203 Solar spectrofluorimeter. Figure 6 shows the excitation and luminescence spectra of $ZnWO_4$, $MgWO_4$, $CaWO_4$.
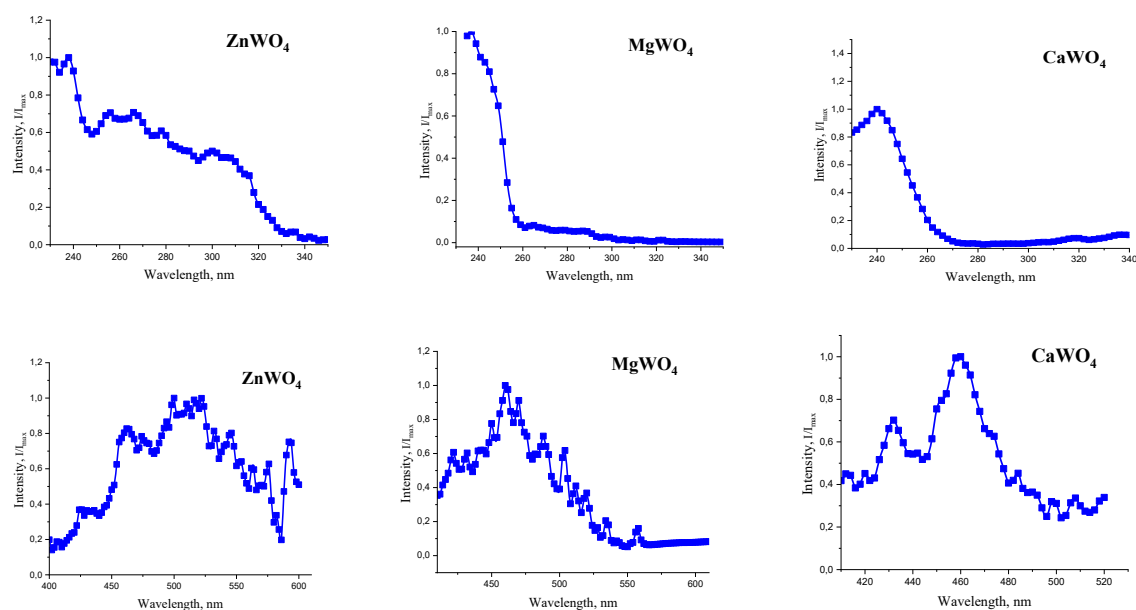
Figure 5. Excitation (top) and luminescence (bottom) spectra of $ZnWO_4$, $MgWO_4$, $CaWO_4$, respectively

In $ZnWO_4$ ceramics luminescence is excited by UV radiation from 230 to 320 nm, in $MgWO_4$ 230–250 nm, in $CaWO_4$ 230–260 nm [22]. The luminescence maxima occur in $ZnWO_4$ at 500 nm, in $MgWO_4$, at 460 nm, in $CaWO_4$ at 460 nm. In general, the spectral characteristics of photoluminescence correspond to those known for crystalline materials [23].

Conclusion

For the first time, systematic studies of the dependence of radiation synthesis of tungstate ceramics on the conditions of radiation treatment have been performed. The dependence of synthesis efficiency on the power density of high-energy electron flux of monocomponent (CaO, MgO, ZnO and WO_3) and two-component ($ZnWO_4$, $MgWO_4$, $CaWO_4$) ceramic samples has been established. It is shown that these dependences have the form of continuously increasing curves. Nevertheless, for all synthesized samples there is a threshold above which the synthesis is realized. The knowledge of thresholds and dependence on the electron flux power density allows us to choose the optimal conditions for the synthesis realization and contributes to the development of ideas about the processes in the charge in the radiation field that ensure the formation of ceramics.

The effect of the mutual influence of charge components on the synthesis efficiency of two-component systems is of interest. Synthesis of $ZnWO_4$, $MgWO_4$, $CaWO_4$ ceramics is realized under the same conditions of radiation treatment, while the thresholds for the synthesis of single-component CaO, MgO, ZnO and WO_3 ceramics samples differ significantly.

It is shown that at all used modes of radiation treatment the formation of ceramics with the same properties are realized. This effect is due to the inhomogeneous distribution of electron flux energy losses in the substance.

Acknowledgements

Funding

References

1   Гринев Б.В. Сцинтилляционные детекторы и системы контроля радиации на их основе / Б.В. Гринев, В.Д. Рыжиков, В.П. Семиноженко. — Киев: Наук. думка, 2007. — 447 с.

2   Grassmann H. Scintillation properties of ZnWO4 / H. Grassmann, H. -G. Moser // Journal of Luminescence. — 1985. — Vol. 33. — Issue 1. — P. 109–113. https://doi.org/10.1016/0022-2313(85)90034-1

3   Глобус М. Пути повышения радиационной стойкости неорганических сцинтилляционных кристаллов для физики высокий энергий / М. Глобус, Б. Гринев, В. Люблянский, Т. Хрупова // Вопросы атомной науки и техники. Сер. Физика радиационных повреждений и радиационное материаловедение. — 2003. — Т. 89. — № 6. — С. 89–97.

4   Nagirnyi V. Energy transfer in ZnWO4 and CdWO4 scintillators / V. Nagirnyi, E. Feldbach, L. Jönsson, M. Kirm, A. Kotlov, A. Lushchik, V.A. Nefedov, B.I. Zadneprovski // Nuclear Instruments and Methods in Physics Research. — 2002. — Vol. 486. — P. 395–398. https://doi.org/10.1016/S0168-9002(02)00740-4

5   Kolobanov V.N. Optical and luminescent properties of anisotropic tungstate crystals / V.N. Kolobanov, I.A. Kamenskikh, V.V. Mikhailin, I.N. Shpinkov, D.A. Spassky, B.I. Zadneprovsky, L.I. Potkin, G. Zimmerer // Nuclear Instruments and Methods in Physics Research. — 2002. — Vol. 486. — P. 496–503. https://doi.org/10.1016/S0168-9002(02)00760-X

6   Mikhailik V.B. Cryogenic scintillators in searches for extremely rare events / V.B. Mikhailik, H. Kraus // Journal of Physics D. — 2006. — Vol. 39. — No. 6. — P. 1181–1191. DOI 10.1088/0022-3727/39/6/026

7   Minoru Itoha. Photo-stimulated luminescence and photo-induced infrared absorption in ZnWO4 / Itoha Minoru, Katagiria Tsuyoshi, Aokia Tomonori, Fujita Masami // Radiation Measurements. — 2007. — Vol. 42. — P. 545–548. https://doi.org/10.1016/j.radmeas.2007.01.049

8   Sarukura N. 4 — Czochralski Growth of Oxides and Fluorides. Handbook of Crystal Growth (2nd ed) / N. Sarukura, T. Nawata, H. Ishibashi, M. Ishii, T. Fukuda. — 2015. — P. 131–168. https://doi.org/10.1016/B978-0-444-63303-3.00004-3

9 Dabkowska H.A. Floating Zone Growth of Oxides and Metallic Alloys / In P. Rudolph (Ed.) / H.A. Dabkowska, A.B. Dabkowski, R. Hermann, J. Priede, G. Gerbeth // Handbook of Crystal Growth: Bulk Crystal Growth: Part A. — 2015. — Vol. 2. — P. 281–329. https://doi.org/10.1016/B978-0-444-63303-3.00008-0

10 Brandle, C.D. Czochralski growth of oxides / C.D. Brandle // Journal of Crystal Growth. — 2004. — Vol. 264. — No. 4. — P. 593–604. https://doi.org/10.1016/j.jcrysgro.2003.12.044

11 Колосов В.Н. Электронно-опосредованные реакции при металлотермическом восстановлении оксидных соединений молибдена и вольфрама / В.Н. Колосов, В.М. Орлов // Докл. РАН. — 2019. — Т. 484. — № 4. — С. 447–450. https://doi.org/10.31857/S0869-56524844447-450

12 Lisitsyn V.M. YAG based phosphors, synthesized in a field of radiation / 6th International Congress "Energy Fluxes and Radiation Effects" IOP Publishing / V.M. Lisitsyn, M.G. Golkovsky, D.A. Musakhanov, A.T. Tulegenova, Kh.A. Abdullin, M.B. Aitzhanov // Journal of Physics Conference Series. — 2018. — Vol. 1115. — No. 5. — P. 5. DOI:10.1088/1742-6596/1115/5/052007

13 Lisitsyn V.M. Formation of Luminescing High-Temperature Ceramics upon Exposure to Powerful High-Energy Electron Flux / V.M. Lisitsyn, L.A. Lisitsyna, M.G. Golkovskii, D.A. Musakhanov, A.V. Ermolaev // Russian Physics Journal. Optics and spectroscopy. — 2021. — Vol. 63. — No. 9. — P. 1615–1621. DOI: 10.1007/s11182-021-02213-9

14 Lisitsyn V. / Radiation Synthesis of High-Temperature Wide-Bandgap Ceramics / V. Lisitsyn, A. Tulegenova, M. Golkovski, E. Polisadova, L. Lisitsyna, D. Mussakhanov, G. Alpyssova // MDPI Journal. Micromachines. — 2023. — Vol. 14. — 2193 p. https://doi.org/10.3390/mi14122193

15 Lisitsyn V. The Optimization of Radiation Synthesis Modes for YAG: Ce Ceramics / V. Lisitsyn, D. Mussakhanov, A. Tulegenova, E. Kaneva, L. Lisitsyna, M. Golkovski, A.M. Zhunusbekov // MDPI Journal.Materials. — 2023. — Vol. 16. — 3158 p. https://doi.org/10.3390/ma16083158

16 Mikhailik V.B. Performance of scintillation materials at cryogenic temperatures / V.B. Mikhailik, H. Kraus // Wiley Online Library. Physica status solidi (b). Review Article. — 2010. — Vol. 247. — P. 1583–1599. https://doi.org/10.1002/pssb.200945500

17 Nikl M. Complex oxide scintillators: Material defects and scintillation performance / . Nikl, V.V. Laguta, A. Vedda // Physica status solidi (b). Feature Article. — 2008. — Vol. 245. — P. 1701–1722. https://doi.org/10.1002/pssb.200844039

18 Mikhailik V.B. Studies of electronic excitons in MgMoO4, CaMoO4 and CdMoO4 crystals using VUV synchrotron radiation / V.B. Mikhailik, H. Kraus, D. Wahl, M.S. Mykhaylyk // Wiley Online Library. Physica status solidi (b). — 2005. — Vol. 242. — Issue 2. — P. R17–R19. https://doi.org/10.1002/pssb.200409087

19 Itoh M. X-Ray Photoelectron Spectroscopy and Electronic Structures of Scheelite- and Wolframite-Type Tungstate Crystals / M. Itoh, N. Fujita, Y. Inabe // Journal of the Physical Society of Japan. — 2006. — Vol. 75. — No. 8. — P. 8. https://doi.org/10.1143/JPSJ.75.084705

20 Ржевская О.В. Оптические и люминесцентные свойства монокристаллов CdWO4 и CdWO4: Mo / О.В. Ржевская, Д.А. Спасский, В.Н. Колобанов, В.В. Михайлин, Л.Л. Нагорная, И.А. Тупицина, Б.И. Заднепровский // Оптика и спектроскопия. — 2008. — Т. 104. — № 3. — С. 407–414.

21 Pankratov V. Luminescence center excited state absorption in tungstates / V. Pankratov, L. Grigorieva, D. Millers, S. Chernov, A.S. Voloshinovskii // Journal of Luminescence. — 2001. — Vol. 94-95. — P. 427–432. https://doi.org/10.1016/S0022-2313(01)00326-X

22 Ovechkin A.E., Luminescence of ZnWO4 и CdWO4 crystals / A.E. Ovechkin, V.D. Ryzhikov, G. Tamulaitis, A. Zukauskas // Physica status solidi (a). — 1987. — Vol. 103. — P. 285–289.

23 Nagirnyi V. Luminescence study of pure and Fe- or Mo-dopped ZnWO4 crystals / V. Nagirnyi, L. Jonsson, M. Kirm, A. Kotlov, A. Lushchik, I. Martinson, A. Watterich, B.I. Zadneprovski // Radiation Measurements. — 2004. — Vol. 38. — P. 519–522. http://dx.doi.org/10.1016/j.radmeas.2004.01.024

Г.К. Алпысова, И.П. Денисов, Ж.К. Бакиева, Е.В. Канева, Е.В. Доморов, А.К. Тусупбекова

Вольфрамат негізіндегі керамиканың радиациялық синтезінің тиімділігінің ағын қуатына тәуелділігі

Монокомпонентті (CaO, MgO, ZnOжәнеWO3) және екікомпонентті (ZnWO4, MgWO4, CaWO4) композицияларының керамикалық үлгілері стехиометриялық құрамның шихтасына жоғары энергиялы электрон дарағының тікелей әсері арқылы синтезделді. Салмағы шамамен 50 г болатын үлгілердің радиациялық синтезі процесті ынталандыру үшін кез келген қосымша заттарды қолданбай 10 с уақыт ішінде жүзеге асырылады. Алғаш рет вольфрамат керамикасының радиациялық синтезінің ағын қуатының тығыздығына тәуелділігі туралы жүйелі зерттеулер жүргізілді. Синтез тиімділігінің біркомпонентті (CaO, MgO, ZnO және WO3) және екікомпонентті (ZnWO4, MgWO4, CaWO4) керамика үлгілерінің ағынының тығыздығына тәуелділігі үнемі өсіп келе жатқан қисықтар түрінде болатындығы анықталды. Барлық синтезделген үлгілер үшін шекті мән бар, оның үстінде синтез жүзеге асырылады. Екікомпонентті жүйелердің синтезінің тиімділігіне шихта компоненттерінің өзара әсерінің әсері анықталды. ZnWO4, MgWO4, CaWO4 керамикасының синтезі бірдей жағдайларда, радиациялық өңдеуде жүзеге асырылады, ал CaO, MgO және ZnO және WO3 керамикасының

біркомпонентті үлгілерін синтездеу шектері айтарлықтай ерекшеленеді. Радиациялық өңдеудің барлық қолданылған режимдерінде бірдей қасиеттері бар керамиканың қалыптасуы жүзеге асырылатындығы көрсетілген. Бұл әсер заттағы электрондар ағынының энергия шығынының гетерогенді таралуына байланысты.

Кілт сөздер: керамика, металл вольфраматы, люминесценция, радиациялық синтез, рентген дифракциясының спектрлері, EDX-талдау, қуат тығыздығы, керамиканың оптикалық қасиеттері.

Г.К. Алпысова, Ж.К. Бакиева, И.П. Денисов, Е.В. Канева, Е.В. Домаров, А.К. Тусупбекова

Зависимость эффективности радиационного синтеза керамики на основе вольфраматов от мощности потока

Синтезированы образцы керамики монокомпонентных (CaO, MgO, ZnO и WO_3) и двухкомпонентных ($ZnWO_4$, $MgWO_4$, $CaWO_4$) составов посредством прямого воздействия потока высокоэнергетических электронов на шихту стехиометрического состава. Радиационный синтез образцов весом около 50 г реализуется за время 10 с без использования любых дополнительных веществ для стимуляции процесса. Впервые выполнены систематические исследования зависимости радиационного синтеза керамики вольфраматов от плотности мощности потока. Установлено, что зависимости эффективности синтеза от плотности мощности потока монокомпонентных (CaO, MgO, ZnO и WO_3) и двухкомпонентных ($ZnWO_4$, $MgWO_4$, $CaWO_4$) образцов керамики имеют вид постоянно нарастающих кривых. Для всех синтезированных образцов имеет место наличие порога, выше которого синтез реализуется. Обнаружен эффект взаимного влияния компонентов шихты на эффективность синтеза двухкомпонентных систем. Синтез $ZnWO_4$, $MgWO_4$, $CaWO_4$ керамики реализуется при одинаковых условиях, радиационной обработки, тогда как пороги реализации синтеза однокомпонентных образцов керамики CaO, MgO и ZnO и WO_3 существенно различаются. Показано, что при всех использованных режимах радиационной обработки реализуется формирование керамики с одинаковыми свойствами. Обусловлен этот эффект неоднородным распределением потерь энергии потока электронов в веществе.

Ключевые слова: керамика, вольфрамат металла, люминесценция, радиационный синтез, спектры рентгеновской дифракции, EDX-анализ, плотность мощности, оптические свойства керамики

References

1   Grinev, B.V., Ryzhikov, V.D., & Seminozhenko, V.P. (2007). *Stsintilliatsionnye detektory i sistemy kontrolia radiatsii na ikh osnove* [Scintillation detectors and radiation monitoring systems based on them]. Kyiv: Naukova dumka [in Russian].

2   Grassmann, H. & Moser, H.-G. (1985). Scintillation properties of ZnWO4. *Journal of Luminescence, 33*(1), 109–113. https://doi.org/10.1016/0022-2313(85)90034-1

3   Globus, M.E., Grinev, B.V., Liubinskii, V.R., Ratner, M.A., & Grineva, T.B. (2003). Puti povysheniia radiatsionnoi stoikosti neorganicheskikh stsintilliatsionnykh kristallov dlia fiziki vysokikh energii [Enhancement of radiation hardness of inorganic scintillation crystals for high-energy physics]. *Voprosy atomnoi nauki i tekhniki. Seriia Fizika radiatsionnykh povrezhdenii i radiatsionnoe materialovedenie — Issues of atomic science and technology. Series: Radiation Damage Physics and Radiation Materials Science, 6*(89), 89–97 [in Russian].

4   Nagirnyi, V., Feldbach, E., Jönsson, L., Kirm, M., Kotlov, A., Lushchik, A., Nefedov, V.A, & Zadneprovski, B.I. (2002). Energy transfer in ZnWO4 and CdWO4 scintillators. *Nuclear Instruments and Methods in Physics Research, 486,* 395–398. https://doi.org/10.1016/S0168-9002(02)00740-4

5   Kolobanov, V.N., Kamenskikh, I.A., Mikhailin, V.V., Shpinkov, I.N., Spassky, D.A., Zadneprovsky, B.I., Potkin, L.I., & Zimmerer, G. (2002). *Optical and luminescent properties of anisotropic tungstate crystals. Nuclear Instruments and Methods in Physics Research, 486*, 496–503. https://doi.org/10.1016/S0168-9002(02)00760-X

6   Mikhailik, V.B. & Kraus, H. (2006). Cryogenic scintillators in searches for extremely rare events. *Journal of Physics D, 39*(6), 1181–1191. DOI 10.1088/0022-3727/39/6/026

7   Minoru, Itoha, Tsuyoshi, Katagiria, Tomonori, Aokia, & Masami, Fujita (2007). Photo-stimulated luminescence and photo-induced infrared absorption in ZnWO4. *Radiation Measurements, 42*, 545–548. https://doi.org/10.1016/j.radmeas.2007.01.049

8   Sarukura, N., Nawata, T., Ishibashi, H., Ishii, M., & Fukuda, T. (2015). *4 — Czochralski Growth of Oxides and Fluorides. Handbook of Crystal Growth* (2nd ed), 131–168. https://doi.org/10.1016/B978-0-444-63303-3.00004-3

9   Dabkowska, H.A., Dabkowski, A.B., Hermann, R., Priede, J., & Gerbeth, G. (2015). Floating Zone Growth of Oxides and Metallic Alloys / In P. Rudolph (Ed.). *Handbook of Crystal Growth: Bulk Crystal Growth: Part A, 2,* 281–329. https://doi.org/10.1016/B978-0-444-63303-3.00008-0

10   Brandle, C.D. (2004). Czochralski growth of oxides. *Journal of Crystal Growth, 264*(4), 593–604. https://doi.org/10.1016/j.jcrysgro.2003.12.044

11 Kolosov, V.N. & Orlov, V.M. (2019). Elektronno-oposredovannye reaktsii pri metallotermicheskom vosstanovlenii oksidnykh soedinenii molibdena i volframa [Electron-mediated reactions during metallothermic reduction of molybdenum and tungsten oxide compounds]. *Doklady Rossiiskoi akademii nauk — Report of the Russian Academy of Sciences, 4*(484), 447–450 [in Russian]. https://doi.org/10.31857/S0869-56524844447-450

12 Lisitsyn, V.M, Golkovsky, M.G., Musakhanov, D.A., Tulegenova, A.T., Abdullin, Kh.A., & Aitzhanov, M.B. (2018). YAG based phosphors, synthesized in a field of radiation / 6th International Congress "Energy Fluxes and Radiation Effects" IOP Publishing. *Journal of Physics Conference Series, 1115*(5), 5. DOI:10.1088/1742-6596/1115/5/052007

13 Lisitsyn, V.M., Lisitsyna, L.A., Golkovskii, M.G., Musakhanov, D.A., & Ermolaev, A.V. (2021). Formation of Luminescing High-Temperature Ceramics upon Exposure to Powerful High-Energy Electron Flux. *Russian Physics Journal. Optics and spectroscopy, 63*(9), 1615–1621. DOI: 10.1007/s11182-021-02213-9

14 Lisitsyn, V., Tulegenova, A., Golkovski, M., Polisadova, E., Lisitsyna, L., Mussakhanov, D., & Alpyssova, G. (2023). Radiation Synthesis of High-Temperature Wide-Bandgap Ceramics. *MDPI Journal. Micromachines, 14*, 2193 p. https://doi.org/10.3390/mi14122193

15 Lisitsyn, V., Mussakhanov, D., Tulegenova, A., Kaneva, E., Lisitsyna, L., Golkovski, M., & Zhunusbekov, A.M. (2023). The Optimization of Radiation Synthesis Modes for YAG: Ce Ceramics. *MDPI Journal Materials, 16*, 3158 p. https://doi.org/10.3390/ma16083158

16 Mikhailik, V.B. & Kraus, H. (2010). Performance of scintillation materials at cryogenic temperatures. *Wiley Online Library. Physica status solidi (b). Review Article, 247*, 1583–1599. https://doi.org/10.1002/pssb.200945500

17 Nikl, M., Laguta, V.V., & Vedda, A. (2008). Complex oxide scintillators: Material defects and scintillation performance. *Physica status solidi (b). Feature Article, 245,* 1701–1722. https://doi.org/10.1002/pssb.200844039

18 Mikhailik, V.B., Kraus, H., Wahl, D., & Mykhaylyk, M.S. (2005). Studies of electronic excitons in MgMoO4, CaMoO4 and CdMoO4 crystals using VUV synchrotron radiation. *Wiley Online Library. Physica status solidi (b), 242*(2), R17–R19. https://doi.org/10.1002/pssb.200409087

19 Itoh, M., Fujita, N., & Inabe, Y. (2006). X-Ray Photoelectron Spectroscopy and Electronic Structures of Scheelite- and Wolframite-Type Tungstate Crystals. *Journal of the Physical Society of Japan*, 75(8), 8 p. https://doi.org/10.1143/JPSJ.75.084705

20 Rzhevskaia, O.V., Spasskii, D.A., Kolobanov, V.N., Mikhailin, V.V., Nagornaia, L.L., Tupitsina, I.A., & Zadneprovskii, B.I. (2008). Opticheskie i liuminestsentnye svoistva monokristallov CdWO4 i CdWO4: Mo [Optical and luminescent properties of CdWO4 and CdWO4 single crystals: Mo]. *Zhurnal Optika i spektroskopiia — Optics and Spectroscopy Journal, 104*(3), 407–414 [in Russian].

21 Pankratov, V., Grigorieva, L., Millers, D., Chernov, S., & Voloshinovskii, A.S. (2001). Luminescence center excited state absorption in tungstates. *Journal of Luminescence, 94-95*, 427–432. https://doi.org/10.1016/S0022-2313(01)00326-X

22 Ovechkin, A.E., Ryzhikov, V.D., Tamulaitis, G., & Zukauskas, A. (1987). Luminescence of ZnWO4 и CdWO4 crystals. *Physica status solidi (a), 103*, P. 285–289.

23 Nagirnyi, V., Jonsson, L., Kirm, M., Kotlov, A., Lushchik, A., Martinson, I., Watterich, A., & Zadneprovski, B.I. (2004). Luminescence study of pure and Fe- or Mo-dopped ZnWO4 crystals. *Radiation Measurements, 38*, 519–522. http://dx.doi.org/10.1016/j.radmeas.2004.01.024

Information about the authors

Alpyssova, Gulnur — PhD, Department of Radiophysics and Electronics, Karaganda Buketov University, University str., 28, Karaganda, Kazakhstan; 100028; e-mail: *gulnur-0909@mail.ru*; ORCID ID: 0000-0002-7164-2188

Bakiyeva, Zhanara (*corresponding author*) — 1st year PhD student, Karaganda Buketov University, University str., 28, Karaganda, Kazakhstan; 100028; e-mail: *shanar83@mail.ru* ORCID ID: 0009-0005-1949-4535

Denisov, Igor — Researcher, Department of Materials Science, National Research Tomsk Polytechnic University, Tomsk, Russian Federation

Kaneva, Ekaterina — PhD, X-ray Analysis Laboratory, Vinogradov Institute of Geochemistry SB RAS, 1A, Favorsky Str., Irkutsk 664033, Russian Federation; e-mail: *kev604@mail.ru* ORCID ID: 0000-0001-7155-6784

Domarov, Evgeny — Researcher, Budker Institute of Nuclear Physics of the Siberian Branch of the Russian Academy of Sciences Novosibirsk, Russian Federation; e-mail: *domarov88@mail.ru*; ORCID ID: 0000-0003-2422-1513.

Tussupbekova, Ainur — PhD, Department of Radiophysics and Electronics, Karaganda Buketov University, University str., 28, Karaganda, Kazakhstan; 100028; e-mail: *aintus_070482@mail.ru*; ORCID ID: 0000-0001-5299-9977

АҚЫЛБЕК ЖҮРСІНҰЛЫ ТҰРМҰХАМБЕТОВ — 80 ЖАСТА

Академик Е. А. Бөкетов атындағы Қарағанды ұлттық университетінің физика факультетінің негізін қалаушылардың бірі, «Қарағанды университетінің хабаршысы. Физика сериясы» журналының алғашқы санынан бастап көп жылдар бойы редакция алқасының мүшесі болып қызмет еткен, физика-математика ғылымдарының докторы, профессор, ҚарМУ-дің Құрметті профессоры және Қазақстан Республикасының білім беру саласындағы Құрметті қызметкері Ақылбек Жүрсінұлы Тұрмұхамбетов сексеннің сеңгіріне аяқ басып отыр.

1946 жылдың 8 ақпанында Қостанай облысының Қарабалық ауданындағы Бөрлі ауылында дүниеге келген Ақылбек Жүрсінұлы жасынанақ білімге құштарлығымен ерекшеленді. Орта мектепті алтын медальмен тәмамдап, Қазақ мемлекеттік университетінің физика факультетіне түсіп, кейін аспирантураны да ойдағыдай аяқтады.

1973 жылдың ақпанында жаңадан ашылған Қарағанды мемлекеттік университетінің физика факультетіне қызметке қабылданып, осы білім ордасында табанды еңбегімен танылды. 2004 жылдың қыркүйек айына дейін Академик Е. А. Бөкетов атындағы Қарағанды мемлекеттік университетінің физика факультетінде абыройлы қызмет атқарып, ғылым мен білімнің дамуына өз үлесін қосты. Университетіміздің алғашқы ректоры Е.А. Бөкетов «Второй в республике» атты мақаласында (Букетов Е.А. Грани творчества. — Алма-Ата: Жазушы, 1977. — С. 75) өзінің ұйымдастырушылық, іскерлік қабілетімен көзге түскен жас маманды ерекше ілтипатпен атап өткен. А.Ж. Тұрмұхамбетов ҚарМУ-дің бай тарихында өзіндік із қалдырды. Әр жылдары теориялық физика, жылу физикасы, жалпы және теориялық физика кафедраларының меңгерушісі болды, факультет деканы қызметін ойдағыдай атқарды. Сол кезеңде Оқу министрлігінің тапсырмасы бойынша өткізілетін «Студент және ғылыми-техникалық даму» атты Бүкілодақтық олимпиаданы республикалық деңгейде ұйымдастырып, басқарды. Негізгі жұмыспен қатар қоғамдық жұмыспен де шұғылдануға тура келді: бірнеше жыл білім және ғылым қызметкерлері кәсіптік одағының Қарағанды облыстық комитетінде Тексеру комиссиясының төрағасы болды. 1980-81 жылдары Одақтық Білім және ғылым министрлігі алғашқылардың бірі ретінде Италияның Турин қаласындағы политехникалық институтке ғылыми іссапарға жіберді. Университетке сіңірген еңбегі еленіп, А.Ж. Тұрмұхамбетовке 2006 жылы Е.А. Бөкетов атындағы Қарағанды мемлекеттік университетінің «Құрметті профессоры» атағы берілді.

А.Ж. Тұрмұхамбетов 2004 жылы отбасылық жағдайға байланысты Қ.И. Сәтбаев атындағы Қазақ ұлттық техникалық университетіне ауысып, университет құрамындағы Жоғары оқу орындарының техникалық пәндер оқытушылары мен инженерлік кадрлардың біліктілігін арттыру және қайта даярлау жөніндегі Республикалық орталықтың директоры қызметін атқарды. Сонымен қатар ол осы кезеңде жалпы және теориялық физика кафедрасының профессоры ретінде ғылыми-педагогикалық жұмысын жалғастырды. Бұл жылдары Қ.И. Сәтбаев атындағы ҚазҰТУ-дың Ғылыми кеңесінің мүшесі болып сайланып, университеттің ғылыми-ұйымдастырушылық жұмысына белсене атсалысты. Сонымен қатар әл-Фараби атындағы ҚазҰУ жанындағы «01.04.14 — Жылу физикасы және теориялық жылу техникасы» мамандығы бойынша докторлық диссертациялар қорғалатын мамандандырылған кеңестің мүшесі ретінде жоғары ғылыми аттестация үдерісіне өз үлесін қосты.

2018 жылдың қыркүйегінде әл-Фараби атындағы ҚазҰУ-дың физика-техникалық факультетінің жылу физикасы және техникалық физика кафедрасына профессор лауазымына қабылданып, 2025 жылдың қыркүйегіне дейін осы қызметті атқарды. Бұл кезеңде қазақ және орыс тілдерінде бакалавриат пен магистратура студенттеріне физиканың жалпы және арнаулы пәндерінен дәріс оқып, ғылыми бағыттағы дипломдық жұмыстарға жетекшілік жасады.

150-ге жуық ғылыми және ғылыми-әдістемелік еңбектердің авторы: оның ішінде қазақ және орыс тілдерінде жарық көрген 2 монография, 2 оқу құралы және 1 оқулық бар.

Жаңа білім стандартына сәйкес оқулық әзірлеудегі жемісті еңбегі үшін Жоғары оқу орындары қауымдастығы тарапынан А. Байтұрсынов атындағы «Саңлақ автор» медалімен марапатталған. Сонымен бірге, оқу және ғылым министрлігі бекіткен, қазақ тілінде жазылған «Механика» оқулығы биыл толықтырылып, түзетіліп, үшінші басылымға дайындалды. Бұл басылымға қатысты «Зияткерлік меншік объектісін мемлекеттік тіркеу куәлігі» алынған. Қазіргі оқу жылында «Механика» пәні бойынша республика көлемінде алғаш рет қазақ тілінде әзірленген бейнедәрістер мен бейнесеминарлар ЖАОК жүйесінде оқу үрдісіне енгізіліп, қолданылып келеді.

1974 жылы кандидаттық диссертация, ал 2002 жылы «Ығысқан ағыстардағы турбуленттік тасымалдаудың құрылымдық заңдылықтары» тақырыбында физика-математика ғылымдары бойынша докторлық диссертация қорғады. 2006 жылы А.Ж. Тұрмұхамбетовке Қазақстан Республикасы Білім және ғылым министрлігінің Жоғары аттестациялық комитетінің шешімімен «Физика» мамандығы бойынша «Профессор» ғылыми атағы берілді. 1997 жылдан бері тұрақты түрде өтіп келе жатқан «Бейсызық жүйелердегі хаос пен құрылымдар. Теория және эксперимент» атты Халықаралық ғылыми конференцияны ұйымдастырушылардың бірі және сол кезден бастап Ұйымдастыру комитетінің тұрақты мүшесі.

2003 жылы Қазақстан Республикасының Ұлттық жаратылыстану ғылымдары академиясының толық мүшесі болып сайланды. Көп жылдар бойы Е.А. Бөкетов атындағы университетте шығып тұратын «Қарағанды университетінің хабаршысы. Физика сериясы» журналының редакция алқасының мүшесі ретінде тұрақты қызмет атқарды. Көп жылғы жемісті еңбек өзінің лайықты бағасын алды. Жоғары оқу орындары басшылығының алғыс хаттары мен грамоталарынан бөлек, «Қазақстан Республикасының білім беру ісінің құрметті қызметкері» төсбелгісімен, сондай-ақ 2011–2014 оқу жылдарында Республикалық конкурста студенттердің үздік ғылыми-зерттеу жұмыстарына жетекшілік жасағаны үшін Қазақстан Республикасының Білім және ғылым министрінің дипломымен, «Тәуелсіз Қазақстанның рухани және әлеуметтік даму жолында қол жеткен табыстары және оның гүлденуіне қосқан зор үлесі үшін» Білім және ғылым министрлігінің Құрмет грамотасымен марапатталды.

Өмірлік серігі — Тұрмұхамбетова Елизавета Таибовна, физика-математика ғылымдарының кандидаты, доцент, қазіргі кезде зейнеткер. Екеуі 58 жыл бірге бір шаңырақта тату-тәтті өмір сүріп келеді, отбасында 3 баланы тәрбиелеп, оқытып, өсірді. Бүгінде немерелерінің қызығын көріп отырған бақытты ата-әже. Жоғары оқу жүйесіндегі кәсіби өтілі (стаж) жарты ғасырдан асқан Ақылбек Жүрсінұлының алдынан мыңдаған шәкірттер өтті, олардың арасынан білім беру саласының майталмандары мен білікті өндіріс мамандары, елімізге белгілі ғалымдар шықты. Ол алдына келген білім алушыларға ғана емес, сонымен қатар өз балаларына да қатаң талап қойып, дұрыс тәлім-тәрбие берді. Соның арқасында үлкен қызы соңғы жылдары Қарағанды және Астанадағы медицина университеттерінің ректоры лауазымында қызмет атқарса; екінші қыз баласы Нью-Йоркте (АҚШ) дүниежүзіне белгілі компанияның маңызды департаментінің басшысы; ал ұлы Алматыда беделді логистикалық компанияның бас директоры. Немерелерінің алды Бостонда (АҚШ), енді бірі Бордода (Франция), Астанада өз мамандықтары бойынша еңбек етуде.

Сонымен қатар, 2024 жылы А.Ж. Тұрмұхамбетовке Білім және ғылым саласының мамандарын кеңінен насихаттау мақсатында өткен республикалық байқау нәтижесінде «Қазақстанның Құрметті профессоры» атағы берілді.

Қазақта «Сексеннен секіріп өт…» деген ақжарма тілек бар. Осы игі ниетпен мерейлі жасқа жетіп, биыл ғана толық зейнеткерлікке қадам басып отырған құрметті Ақылбек Жүрсінұлына ұзақ ғұмыр, мықты денсаулық, баянды бақыт тілейміз.

Ізгі ниетпен,
физика-техникалық факультетінің ұжымы

ЖЫЛУФИЗИКАСЫ ЖӘНЕ ТЕОРИЯЛЫҚ ЖЫЛУТЕХНИКАСЫ
ТЕПЛОФИЗИКА И ТЕОРЕТИЧЕСКАЯ ТЕПЛОТЕХНИКА
THERMOPHYSICS AND THEORETICAL THERMOENGINEERING

CORRIGENDUM

МЕРЕЙТОЙ ИЕСІ
НАШИ ЮБИЛЯРЫ
OUR ANNIVERSARIES